Search for sterile neutrinos in β-decays

Konrad Martin Altenmüller

Joint doctoral dissertation
at the Physics Department of the Technical University of Munich
and the doctoral school N° 576 PHENIICS of University Paris-Saclay
in candidancy for the degree of Doktor der Naturwissenschaften (Dr. rer. nat.)
and Docteur de l'Université Paris-Saclay dans la spécialité Physique des Particules

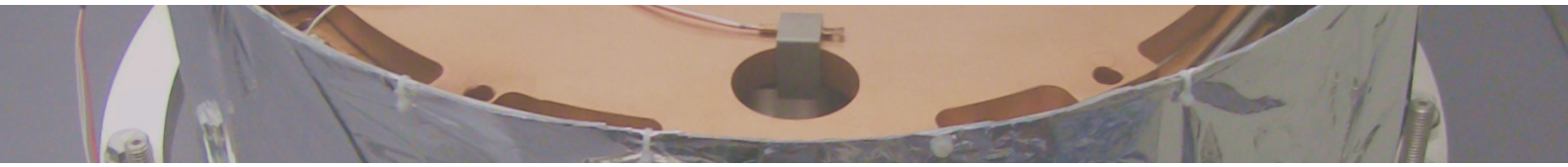

Doctoral supervisors: Prof. Dr. Stefan Schönert (TUM) and Dr. habil. Thierry Lasserre (CEA Saclay, MPI für Physik).

Document compiled on October 21, 2019.

TECHNISCHE UNIVERSITÄT MÜNCHEN

PHYSIK-DEPARTMENT

Search for sterile neutrinos in β-decays

Konrad Martin Altenmüller

Vollständiger Abdruck der von der Falkultät für Physik der Technischen Universität München zur Erlangung des akademischen Grades eines Doktors der Naturwissenschaften (Dr. rer. nat.) genehmigten Dissertation.

Vorsitzender:	Prof. Dr. Andreas Weiler
Betreuer:	Prof. Dr. Stefan Schönert
	Dr. habil. Thierry Lasserre
Prüfer der Dissertation:	Prof. Dr. Bastian Märkisch
	Dr. habil. Laurent Simard
	Dr. habil. Olivier Limousin
	Prof. Dr. Marco Pallavicini
	Prof. Dr. Guido Drexlin

Die Dissertation wurde am 25. Juni 2019 bei der Technischen Universität München eingereicht und durch die Fakultät für Physik am 2. Oktober 2019 angenommen.

Abstract

The work presented in this thesis is about the sterile neutrino search with the two experiments SOX and TRISTAN based on the β-decay. Sterile neutrinos are theoretically well motivated particles that do not participate in any fundamental interaction except for the gravitation. With the help of these particles one could elegantly explain the origin of the neutrino mass, dark matter and the matter-antimatter asymmetry in the universe. As sterile neutrinos can mix with the known active neutrinos, they could be discovered in laboratory searches.

The SOX experiment was designed to search for a sterile neutrino with a mass in the eV-range. This particular mass range is motivated by several anomalous observations at short-baseline neutrino experiments that could be explained by an additional oscillation with a length in the order of meters that arises from an eV-scale sterile neutrino. For SOX it was planned to use the existing Borexino solar neutrino detector to search for an oscillation signal within the detector volume. The neutrinos are emitted from a 5.5 PBq electron-antineutrino source made of the β-decaying isotopes ^{144}Ce and ^{144}Pr, located at 8.5 m distance from the detector center. For the analysis of the signal it is crucial to know the source activity. This parameter is determined by measuring the decay heat of the source with a thermal calorimeter that was developed by TUM and INFN Genova. The decay heat is measured through the temperature increase of a well-defined water flow in a heat exchanger that surrounds the source. The calorimeter was assembled, optimized and characterized. Heat losses were determined through calibration measurements with an electrical heat source. Adjustable measurement conditions and an elaborate thermal insulation allowed an operation with negligible heat losses. It was proven that the power of a decaying source can be measured with $< 0.2\%$ uncertainty in a single measurement that lasts ~ 5 days.
Unfortunately the SOX experiment was canceled after a technological problem rendered the source production with the required activity and purity impossible.

The TRISTAN project is an attempt to discover sterile neutrinos with masses in the order of keV. In contrast to eV-scale sterile neutrinos that are motivated by several anomalies observed in terrestrial experiments, the existence of sterile neutrinos with masses in the keV range could resolve cosmological and astrophysical issues, as they are dark matter candidates. The TRISTAN project is an extension of the KATRIN experiment to search for the signature of keV-scale sterile neutrinos in the tritium β-spectrum. KATRIN itself is attempting to determine the effective neutrino mass by measuring the end point of the tritium spectrum at low counting rates. The KATRIN setup will be modified after the neutrino mass measurements are finished to conduct a differential and integral measurement of the entire tritium spectrum. This project is called TRISTAN. The current detector will be replaced by a novel 3500-pixel silicon drift detector system that has an outstanding energy resolution of a few hundred eV and

can handle rates up to 10^8 counts per second as they occur when the entire spectrum is scanned. Prototype detectors were successfully tested and first tritium data was taken at the Troitsk ν-mass spectrometer to study systematic effects and develop analysis methods. A successful fit of the differential tritium spectrum proved the feasibility of this approach. TRISTAN itself is still at an early stage, but the detector development and systematic studies are well on track and delivered so far encouraging results. The sterile neutrino search is scheduled after the KATRIN neutrino mass program is finished in $\sim$ 2024.

Résumé

Le travail présenté dans cette thèse porte sur la recherche de neutrino stérile à l'aide de désintégrations β dans les expériences SOX et TRISTAN. Le neutrino stérile est une particule hypothétique, solidement établi théoriquement, qui ne prendrait part à aucune interaction fondamentale, gravité mise à part. Étant entendu que le neutrino stérile se mélange avec les neutrinos actifs connus, l'existence de ces premiers peut être étudiée directement en laboratoire.

L'expérience SOX a été conçue pour explorer l'existence d'un neutrino stérile d'une masse autour de l'électronvolt (eV). Un neutrino stérile avec une telle masse permettrait d'expliquer plusieurs anomalies observées à courte distance de sources (quelques mètres) lors de mesures d'oscillations de neutrinos de basses énergies (quelques MeV). SOX avait pour projet d'utiliser le détecteur de neutrinos solaire déjà existant Borexino, et d'observer un signal d'oscillation vers le stérile à l'intérieur même du volume actif du détecteur. La source radioactive de 5.5 PBq et positionnée à 8.5 m du centre du détecteur, émettrait des antineutrinos éléctroniques via la désintégration β du ^{144}Ce et du ^{144}Pr. Une des clés de l'observation de cette oscillation, est la connaissance précise de l'activité de la source. Une telle activité peut être déterminée en mesurant la chaleur dégagée par la source. C'est la raison pour laquelle l'INFN Genova et la TUM ont développé conjointement un calorimètre dédié. La chaleur dégagée par la radioactivité est alors captée par un échangeur puis transmise à un circuit d'eau étroitement contrôlé. Le calorimètre a été assemblé, optimizé puis étalonné avec succès. La perte de chaleur du circuit fut déterminée lors des mesures d'étalonnage grâce à un chauffage électrique. Des variations des conditions expérimentales et une isolation thermique sophistiquée ont permis d'opérer avec des pertes de chaleur négligeables. Il a ainsi été démontré que la puissance thermique de la source pouvait être estimée, en 5 jours seulement, avec une précision supérieure à 0,2 %. Malheureusement, le programme SOX a dû être annulé.

Le projet TRISTAN, quant à lui, tend à démontrer l'existence d'un neutrino stérile avec une masse de l'ordre du kilo-électronvolt (keV). Si le neutrino stérile à l'eV tente d'apporter une réponse aux différentes anomalies observées lors de mesures d'oscillation, le neutrino stérile au keV, en tant que potentiel candidat matière noire. Le projet TRISTAN cherche à mesurer l'empreinte de ce nouvel état de masse sur le spectre du tritium dans le cadre de l'expérience KATRIN. Cette dernière vise à déterminer la masse effective du neutrino (actif) en mesurant l'extrémité du spectre de tritium avec une excellente résolution et un faible taux de comptage. Une fois la mesure achevée, le détecteur de KATRIN sera modifié afin d'effectuer une mesure différentielle et intégrale de l'ensemble du spectre en tritium: c'est le projet TRISTAN. Le détecteur actuel sera remplacé par un nouveau détecteur de silicium à dérive (SDD) de 3500 pixels permettant une résolution de 3 % à 6 keV et pouvant supporter un taux de comptage montant

jusqu'à 10^8 coups par seconde, activité maximum attendue. Un prototype a été testé avec succès et une première mesure de tritium a été réalisé au spectromètre de masse neutrino Troitsk afin d'étudier les erreurs systématiques et de développer des méthodes d'analyses pertinentes. Un premier ajustement cohérent du spectre tritium différentiel acquis lors de cette installation, a démontré la faisabilité du projet. TRISTAN lui-même est toujours en cours de développement mais les caractérisations du détecteur et les études de systématiques sont plus qu'encourageantes pour la poursuite du projet. La première investigation de neutrino stérile avec le détecteur de TRISTAN sur le site de KATRIN est prévue après la mesure de masse, en cours à Karlsruhe, aux alentours de 2024.

Structure of this thesis

This thesis is divided in four parts: the first part is a general introduction to neutrino physics and sterile neutrinos in particular, summarizing theoretical and experimental concepts and the state of the art (chapter 1, page 3).
In the second part the work for SOX is presented: the experiment is introduced in chapter 2 (page 29). Chapters 3 (page 55) to 7 are about the development, characterization and commissioning of the thermal calorimeter to estimate the neutrino source activity.
The third part is about the TRISTAN project, where the experiment itself and the detector system are introduced in chapters 8 (page 111) and 9 (page 125). The characterization of prototype detectors is presented in chapter 10 (page 141), while the analysis of electron data including a tritium spectrum from Troitsk ν-mass is demonstrated in chapter 11 (page 165). Final conclusions and an outlook on the future of sterile neutrino searches are given in chapter 13 (page 227) in part four.

Contents

Part I

Introduction

Chapter 1

Neutrino physics

Neutrinos are among the most abundant particles in the universe, yet many of their properties are still uncertain due to their elusive nature. Neutrinos only interact via the weak force and gravitation and thus very rarely. To study neutrinos, intense sources, large detectors and low background levels are generally necessary, demanding advanced technologies and analysis techniques, which are still improving with each generation of experiments.

Experiments involving neutrinos lead to many advances in physics. Concerning nuclear physics for example, nuclear transitions were explored and the V-A theory for weak interactions was established by discovering that neutrinos have a negative helicity in the Goldhaber experiment. Nuclear form factors were studied by inelastic neutrino scattering off nucleons, which helped to explore quantum chromodynamics. Finally, by observing neutrino interactions in the Gargamelle bubble chamber at CERN the Z-boson was discovered, confirming the electroweak theory (Weinberg-Salam theory) and giving birth to the standard model (SM) of particle physics.
Today, neutrino experiments are focused on exploring physics beyond the SM. Since the discovery of neutrino oscillations, it is known that, in contrary to the predictions of the SM, at least two of the three neutrinos are massive, where they are at least 5 orders of magnitude lighter than the heavier elementary particles. To expand the standard model with a mechanism that explains the neutrino mass and its smallness, experimental input is necessary. Such experimental input is given for example by exploring lepton number violation in neutrino interactions, which is predicted by several theories, including supersymmetry, or by searches for sterile neutrinos and Majorana mass terms, as both are building blocks of the seesaw mechanism. In addition, sterile neutrinos are candidates for dark matter, whose nature is still unknown, despite it constitutes most of the matter in the universe. Since neutrinos do not participate in any interaction stronger than the weak force, they are also suitable to search for even weaker interaction for example by probing the neutrino magnetic moment.
Neutrinos play also an important role in cosmology, as the mass of neutrinos and number of families have a strong influence on cosmological models and the evolution of the universe. Furthermore, neutrinos have a strong impact in astrophysics, as they for example are the main cooling mechanism of heavy stars and thus determine their lifetime. Neutrinos also drive the explosion of core collapse supernovae [FY03].
By observing neutrinos created in nature or man-made objects, one can not only study the properties of these particles, but also learn about their sources. This way the interior of the Sun or the Earth can be probed and the physical processes prevalent in astrophysical objects can be studied.

As a first practical application of neutrino detection, coherent scattering of neutrinos from nuclear reactors off nuclei is emerging as a technique to probe the nuclear fission for nuclear non-proliferation purposes.

In this chapter, a short introduction to neutrino physics is given, where the focus is put on sterile neutrinos, as these are the particles of interest for this thesis. A historic time line of neutrino physics is presented in section 1.1. Section 1.2 recapitulates the status of neutrinos in the standard model. The different natural and artificial neutrino sources are summarized in section 1.3. The concept of neutrino oscillations is presented in section 1.4 and the current status and open questions of neutrino physics are discussed in section 1.5. An introduction to the theory of neutrinos beyond the standard model is given in section 1.6. How the neutrino mass can be measured is presented in section 1.7. Finally, sterile neutrinos and current bounds on their existence are discussed in section 1.8.

1.1 A short history of neutrino physics

A historical overview of neutrino physics and its synergies with the development of the standard model of particle physics can be found in the historical introduction in [FY03]. Here, a summary of the most important experimental milestones is given.

1930 Wolfgang Pauli postulates a neutral particle – at first called neutron – created in the β-decay together with an electron to explain the continuous electron energy spectrum without violating energy conservation. Enrico Fermi established the notion "neutrino" in 1932, after the actual neutron was discovered.

1934 Enrico Fermi publishes his theory of the β-decay, where he already concludes that the neutrinos are massless or very light compared to electrons due to the measured spectral shapes of the emitted electrons [Fer34].

1936 A first indirect verification of the existence of a neutrino is delivered by Aleksander Leipunski, who can show that the recoil of the daughter ions created in the β-decay of ^{11}C is considerably greater than expected without any neutrino emission [Lei36].

1956 Frederick Reines and Clyde Cowan report the results from their experiment in 1953, which confirms the existence of the neutrino [CRH$^+$56]. They detected neutrinos through the inverse beta decay in a scintillator detector by the delayed coincidence technique at a nuclear reactor in Hanford, USA.

1956 The Wu-experiment shows that the weak interaction is not conserving parity. This was confirmed in 1957 by the Goldhaber-experiment, where it was shown that neutrinos exist only with a left-handed helicity, proving the $V - A$ nature of the weak interaction.

1957 Julius Csikai and Alexander Szalay confirm the existence of neutrinos by studying the kinematics of the ^{6}He β-decay in a cloud chamber [Csi57].

1957 Bruno Pontecorvo formulates a theory, where neutrinos can oscillate (into their anti-particle [Pon58]) and sets the foundation for neutrino flavor oscillations.

1962 A group of scientists from Columbia University and Brookhaven National Laboratory discover the muon neutrino in an accelerator experiment and prove that it

is different from the previously discovered (anti-)electron neutrino [DGG$^+$62]. A neutrino beam was produced from decaying pions, which themselves were created by accelerating protons onto a target. The neutrinos produce charged leptons in a spark chamber through charged current interactions. If the muon and electron neutrinos were identical, a similar number of electrons and muons would have been produced, however only muons were observed.

1968 A detector in the Homestake Gold Mine (USA) discovers solar electron neutrinos (mostly ^{8}B-neutrinos). The detector was of the radiochemical type, where a radioactive isotope produced in neutrino interactions ($\nu_e + {}^{37}\mathrm{Cl} \rightarrow {}^{37}\mathrm{Ar} + e^-$) is extracted from the volume and counted [DHH68]. The ν_e-flux was far lower than predicted from solar models, giving rise to the "solar neutrino problem".

1973 In 1973 neutral current neutrino interactions are observed at CERN in the Gargamelle experiment [H$^+$74]. This discovery leads to an unified theory of weak and electromagnetic interactions and the formulation of the standard model of particle physics.

1987 Several detectors discover neutrinos from the supernova 1987A in the Large Magellanic Cloud, which marked the beginning of neutrino astronomy and proved that neutrinos play a major role in these explosions.

199x The radiochemical detectors GALLEX and SAGE detect solar pp-neutrinos, which make up most of the solar neutrino flux, and confirm the existence of the solar neutrino problem by observing a $\sim 45\%$ flux deficit. This discrepancy cannot be resolved by modified solar models, and it becomes clear that massive neutrinos are the only solution [Kir98, GAB$^+$01].

1998 Further evidence of neutrino oscillations is found at the Super-Kamiokande detector that measures a deficit of atmospheric muon neutrinos, depending on their zenith angle and thus on the distance from their origin [Sup98].

2000 Not long after the tau particle was discovered in 1975, the existence of a tau neutrino was established. However, the experimental detection of tau neutrino interactions is achieved only in 2000 with the DONUT experiment [K$^+$01]. A 800 GeV proton beam at Fermilab Tevatron produces charmed mesons in a beam dump, which decay into neutrinos. The tau particles generated in charged current interactions from tau neutrinos were detected via their tracks left in a nuclear emulsion.

2001 The solar neutrino puzzle is resolved by the SNO experiment, which shows that the missing ν_e-flux from the sun is converted into muon and tau neutrinos [A$^+$02], giving the final confirmation that neutrinos oscillate and thus are not massless.

Since then, many more experiments were conducted to increase the knowledge of the neutrino properties, and meanwhile, using neutrinos as probes to study their sources – e.g. the Earth interior and astrophysical objects – has become well established. This list can be hopefully continued in the not so distant future with the determination of the absolute neutrino mass and mass ordering, its nature (Majorana or Dirac), the discovery of the proposed sterile neutrinos and the observation of the cosmic neutrino background, and some unexpected surprises. The open questions of neutrino physics are further discussed in section 1.5.

1.2 Neutrinos in the standard model

The standard model is a quantum field theory that describes the strong, weak, and electromagnetic interactions of the known elementary particles. Only the fourth fundamental force, the gravity, could not be included into an unified theory yet and is separately described by general relativity. The standard model includes the theory of the electroweak interaction, which is the unified theory of the electromagnetic and weak forces, which are necessary to describe neutrino physics. In fact, the observation of neutral current neutrino interactions was an integral experimental evidence to affirm this theory. It is well established by experiments that there are three different types ("flavors") of neutrinos and antineutrinos, which take part in the standard neutral current (NC) and charged current (CC) weak interactions. Each neutrino is paired to one of the charged leptons, such that there are the electron neutrino ν_e the muon neutrino ν_μ and the tau neutrino ν_τ and their antiparticles $\overline{\nu}_e$, $\overline{\nu}_\mu$ and $\overline{\nu}_\tau$. The ν_e e.g. can be created in a charged current interaction only from an electron or from another particle alongside with a positron, or produce an electron.
Neutrinos exist only as left-handed particles or right-handed anti-particles, as measured in the famous Goldhaber experiment. The discovery of neutrino oscillations made it clear that at least two of the three neutrinos are massive, which was not predicted by the standard model. As a consequence, the model has to be extended to explain the observations, for example with right-handed sterile neutrinos. This is further discussed in section 1.6. The number of neutrino species N_ν was measured on one hand by measuring the decay width of the Z^0-boson (or by generally fitting data from electron-positron collisions at LEP and SLC), as the width depends on the possible decay products, which resulted in $N_\nu \approx 3$. On the other hand N_ν was determined though cosmological observations: the number of neutrino species increases the expansion rate of the early universe, and thus affects the time during which the β-equilibrium is maintained (e.g. $\nu_e + n \leftrightarrow p + e^-$). The duration of this equilibrium ultimately affects the neutron fraction and as a consequence the ^{4}He abundance in the universe. While the first approach allows only to determine the number of those neutrino species, which interact weakly (active neutrinos), the cosmological approach is additionally sensitive for sterile neutrinos. Cosmology confirms the three flavor paradigm for active neutrinos, but setting a limit on sterile neutrinos from cosmology is complicated, as it depends on the mass and mixing parameters and the cosmological model. In principle, cosmology allows the introduction of additional neutrinos (see section 1.8) [Par18, FY03].

1.3 Neutrino sources

Neutrinos are everywhere in the universe, coming from a variety of sources. This section is intended to list all major neutrino sources. A plot with the different sources and their respective fluxes is shown in figure 1.1. In this list we start with the natural neutrino sources, ordered from highest flux to lowest:

- **Cosmological neutrinos:** similar to the photon freeze-out, also neutrinos decoupled in the early universe from the plasma, but much earlier – about 1 second after the Big Bang. These neutrinos remain to this day and form a cosmic neutrino background. They are called cosmological neutrinos or relic neutrinos. Their temperature is 1.95 K, which correponds to an energy of $10^{-6} - 10^{-4}$ eV, depending on their mass. Even though they have a large abundance with $340\,\nu/\mathrm{cm}^3$, their low energy made a detection so far not possible. Nonetheless, the outcome of the primordial nucleosynthesis (light element abundance), some features of the

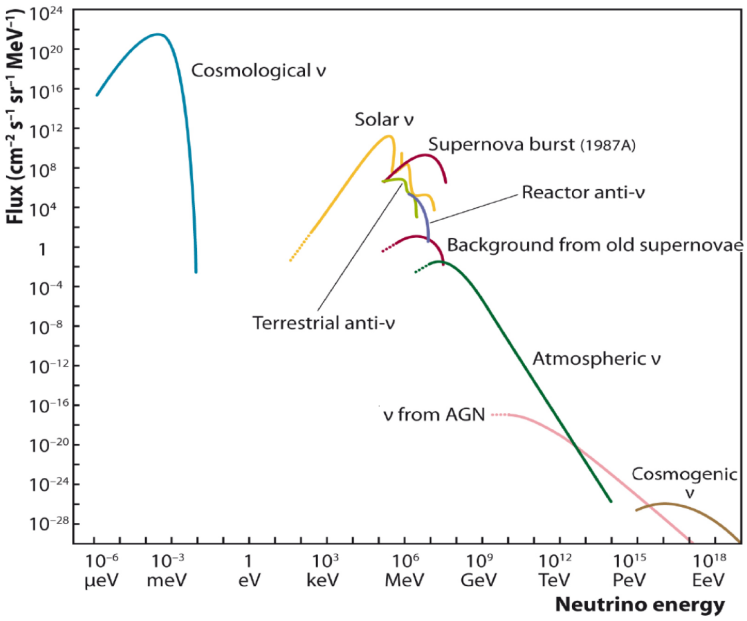

Figure 1.1: Neutrino fluxes at earth from different sources as a function of energy. The plot was taken from [Spi12].

cosmic microwave background and the large scale structure of the universe can be attributed to these neutrinos, giving indirect evidence [FY03, FKMP15]. A direct detection could be possible by capturing them on isotopes with a negative Q-value[1], i.e. radioactive material. An experiment in development is PTOLEMY, which plans to observe relic neutrinos with a 100 g tritium target [B$^+$19]. The signature is a line at the end point of the tritium electron spectrum. Due to the small interaction rate, this effect is not visible in the KATRIN experiment with its 30 μg of tritium in the source (see section 8.3).

- **Solar neutrinos:** ν_e are produced in the core of the sun, predominantly in the pp-cycle of the hydrogen burning. On Earth their flux is $\sim 6 \cdot 10^{10}\,\mathrm{cm^{-2}s^{-1}}$ with a mean energy of $\sim 200\,\mathrm{keV}$. The most precise measurement of the solar neutrino spectrum was performed with the Borexino detector (see section 2.1) [Bor18]. From solar neutrinos one can learn about the physics of the sun and e.g. test the standard solar model and the metallicity problem. Additionally one can study neutrino oscillations including matter effects as the MSW effect (see section 1.4).

- **Supernova neutrinos:** during the neutronization of a collapsing stellar core, large amounts of neutrinos ($\overline{\nu}_e$) are produced that ultimately heat up the matter and drive the explosion of a supernova [Jan11, Jan17]. The first and so far only observed supernova neutrinos from SN1987A arrived at earth with an integral flux of $10^{10}\,\overline{\nu}_e/\mathrm{cm}^2$ (integrated over a few seconds) and energies of $\sim 10\,\mathrm{MeV}$, indicating that the largest part of the gravitational binding energy released in the collapse is radiated within a few seconds in the form of $\sim 10^{58}$ neutrinos with a total energy of $\sim 10^{46}\,\mathrm{J}$ [HKK$^+$87].
  In addition to the occasional neutrino bursts from supernovae in our home galaxy ($\sim$ 2 per century), one expects a continuous flux of neutrinos from supernovae elsewhere in the universe, the so-called diffuse supernova neutrino background

[1] Neutrino capture e.g. on tritium: $\nu_e + {}^3\mathrm{H} \rightarrow {}^3\mathrm{He} + e^-$. The threshold of this reaction is negative as tritium is unstable. The reaction is thus possible for neutrinos of any energy.

(DSNB). The current most stringent limit was derived by Super-Kamiokande: the flux is lower than $3\,\mathrm{cm}^{-2}\mathrm{s}^{-1}$ at $E_{\overline{\nu}_e} > 16\,\mathrm{MeV}$ (< 4 times larger than the expected rate) [B$^+$12]. The DSNB is in reach of the next generation of neutrino detectors [MSTD18].

- **Geoneutrinos:** geoneutrinos are $\overline{\nu}_e$ produced by radioactive isotopes in the earth, mostly by the β-decay of ^{40}K with a maximum energy $Q_\beta = 1.3\,\mathrm{MeV}$ and by β-decays in the ^{238}U and ^{232}Th decay chains. The neutrinos from the uranium and thorium decay chains were observed via the inverse beta decay by KamLAND and Borexino (see section 2.1). Neutrinos from ^{40}K were not observed yet, as their energies are below the inverse beta decay threshold, making a detection above background more difficult. Measuring these neutrinos allows to study the interior of the earth crust. In general these neutrinos have energies of a few MeV and a flux of $\sim 10^6\,\overline{\nu}_e\,\mathrm{cm}^{-2}\,\mathrm{s}^{-1}$ [Bor15a].

- **Atmospheric neutrinos:** when highly energetic cosmic rays collide with the upper atmosphere, charged pions are produced that decay predominantly into muon neutrinos, muons and their anti-particles. The (anti)muons decay in turn into muon and electron (anti)neutrinos [FY03]. Thanks to their high energies that range from a few tens of MeV to hundreds of GeV, these neutrinos could be detected already in 1965 by two groups, despite their low flux of less than $10^{-2}\,\overline{\nu}_e\,\mathrm{cm}^{-2}\,\mathrm{s}^{-1}\,\mathrm{sr}^{-1}$ at 1 GeV ($\hat{=}$ maximum of the spectrum) [A$^+$65, RCJ$^+$65, R$^+$16]. With a detector that can resolve the direction of an interacting neutrino (e.g. Super-Kamiokande) one can study neutrino oscillations by comparing the muon neutrino flux from different zenith angles, i.e. different baselines.

- **High-energy astrophysical neutrinos (AGN and cosmogenic):** the most energetic and rare neutrinos reach us from space with energies up to several PeV, as observed by the IceCube Neutrino Observatory. The flux of astrophysical neutrinos in the 100 TeV–1 PeV range was measured to be $10^{-8}\,\mathrm{GeV}\,\mathrm{cm}^{-2}\,\mathrm{s}^{-1}\,\mathrm{sr}^{-1}$ [Ice14, Ice18]. The source of lower energetic astrophysical neutrinos was linked to active galactic nuclei: in a multi-messenger observation gamma-rays and neutrinos were detected in coincidence and directional agreement with flares of the blazar TXS 0506+056 (detected by IceCube, MAGIC and Fermi). The origin of neutrinos with the highest energies is still not clear, but blazars and astrophysical jets in general are possible sources [A$^+$18a].
  The detection of astrophysical neutrinos opened the field of neutrino astronomy. Neutrinos have the advantage over other high energy cosmic rays that they travel in straight lines unaffected by magnetic fields and do not interact with the CMB as for example gamma rays or protons, for which the universe becomes opaque at energies above several EeV (GZK cut-off) [Mad19]. They allow thus to study the most energetic phenomena in the universe.

There are several man-made neutrino sources:

- **Reactor neutrinos:** the fission products in nuclear reactors produce $\overline{\nu}_e$ through the β-decay with energies up to 12 MeV. In each fission of ^{235}U and ^{239}Pu about 6 neutrinos are produced, such that a 1 GW nuclear power reactor delivers $2 \cdot 10^{20}$ $\overline{\nu}_e$ per second, making it an intense and steady source suitable to study neutrino properties [FY03]. An important systematic effect are uncertainties in the neutrino energy spectrum emitted from an extensive chain of decays. From reactor experiments stems the so-called reactor anomaly, where a reduction of

the observed flux compared to calculations hints at an additional short-baseline oscillation caused by a light sterile neutrino. This will be discussed in more detail in section 1.8.1.

- **Accelerator neutrinos:** a particle accelerator can create a neutrino beam by producing charged pions and kaons, which are magnetically focused and then decay ultimately into electron and muon (anti-)neutrinos with typical energies in the order of GeV. At these energies oscillations are studied with baselines of several hundreds of kilometers. Also, an unexpected appearance of electron neutrinos in the beam was observed at short distances, which hint again at the existence of light sterile neutrinos (see section 1.8.1) [FY03, Sue15].

- **Nuclear weapons:** fission products in nuclear detonations produce $\overline{\nu}_e$ similarly as nuclear reactors. A hydrogen bomb produces in addition ν_e in the fusion process. Cowan and Reines, who detected the first neutrinos ever with the help of a nuclear reactor, initially planned in 1951 to detect neutrinos from a nuclear fission bomb ("project Poltergeist"). The short, intense neutrino burst from a nuclear explosion was considered to be the only source that allows a detection above the background level. It was intended to place a several-ton scintillator detector ~ 50 meters away from a 20-kiloton bomb. The actual neutrino detection was planned to happen during the free fall of the detector down a 50 m deep, sealed and evacuated shaft in order to decouple the system from the blast-induced earth shock. However, after Cowan and Reines realized that the background could be reduced with the delayed coincidence technique, the detection of $\overline{\nu}_e$ from a nuclear reactor became feasible, even though the flux is thousands of times less than from a nuclear explosion [Coo97].

- **Neutrinos from other radioactive sources:** neutrinos are generally produced in β-decays ($\overline{\nu}_e$ in β^-, ν_e in β^+-decays) and in the electron capture process (ν_e). A sufficient quantity of radioactive material can be used to calibrate neutrino detectors as the SAGE and GALLEX experiments [A^+99, A^+06, A^+95, HHK^+14]. To maximize the flux, such a source is placed in the detector or very close to it and thus allows to study short-baseline neutrino oscillations, as they would occur in the presence of an eV-scale sterile neutrino. This concept is used by the SOX project, which plays a major role in this thesis. SOX and its neutrino source are introduced in chapter 2.

1.4 Neutrino oscillations

The description of neutrino oscillations follows the notation of the Particle Data Group [Par18] and is summarized hereinafter. Neutrino oscillations are a consequence of the presence of neutrino flavor mixing: a weakly interacting neutrino (flavor eigenstate), e.g. an electron neutrino, is a superposition of several neutrino states with different masses (mass eigenstates) that propagate through space. These states propagate with different phases, resulting in a changing superposition of the mass eigenstates as a function of the traveled distance, which corresponds to a changing flavor eigenstate. Thus at a certain distance the original electron neutrino can have transformed for example into a muon neutrino.
In mathematical terms: the left-handed fields of the flavor neutrinos $\nu_{\alpha L}$ ($\alpha = e, \mu, \tau$) can be described as superpositions of the left-handed components ν_{jL} of three neutrino

fields ν_j with masses m_j:

$$\nu_{\alpha \mathrm{L}} = \sum_j U_{\alpha j} \nu_{j \mathrm{L}}, \tag{1.1}$$

where $U_{\alpha j}$ is an element of the neutrino mixing matrix U. Within the three neutrino flavor paradigm, when abbreviating $\cos\theta_{ij}$ as c_{ij} and $\sin\theta_{ij}$ as s_{ij}, one can write

$$U = \begin{bmatrix} c_{12}c_{13} & s_{12}c_{13} & s_{13}e^{-i\delta} \\ -s_{12}c_{23} - c_{12}s_{23}s13e^{-i\delta} & c_{12}c_{23} - s_{12}s_{23}s_{13}e^{-i\delta} & s_{23}c_{13} \\ s_{12}s_{23} - c_{12}c_{23}s13e^{-i\delta} & -c_{12}s_{23} - s_{12}s_{23}s_{13}e^{-i\delta} & c_{23}c_{13} \end{bmatrix} \times \\ \times \mathrm{diag}(1, e^{i\frac{\alpha_{21}}{2}}, e^{i\frac{\alpha_{31}}{2}}), \tag{1.2}$$

where θ_{ij} are the mixing angles, δ the Dirac CP violation phase, and α_{21} and α_{31} the two Majorana CP violation phases. The matrix U is also called PMNS matrix to honor its creators Bruno Pontecorvo, Ziro Maki, Masami Nakagawa and Shoichi Sakata. In summary, U is characterized by three angles and three phases. The phases are responsible for the CP violation, but to which extent is depending on whether neutrinos are Dirac or Majorana particles, a question that has not been solved yet by experiments.

The oscillation probability is depending on the mixing angles θ_{ij}, the difference of squared masses between the eigenstates $\Delta m^2_{ij} = m^2_i - m^2_j$, and the neutrino energy E and distance from the source L. As $\Delta m^2_{31} >> \Delta m^2_{21}$, in most applications one can approximate neutrino oscillations as two flavor oscillations. The disappearance or survival probability for a flavor eigenstate ν_α with an energy E at a distance L, where $\nu_\alpha - \nu_\beta$ oscillations are dominating (other oscillations are averaged out), is

$$P(\nu_\alpha \to \nu_\alpha) \approx 1 - \sin^2(2\theta_{ij}) \cdot \sin^2\left(1.27 \frac{\Delta m^2_{ij}\ [\mathrm{eV}^2]}{E\ [\mathrm{GeV}]} L\ [\mathrm{km}]\right), \tag{1.3}$$

while the appearance probability of ν_β is

$$P(\nu_\alpha \to \nu_\beta) = 1 - P(\nu_\alpha \to \nu_\alpha). \tag{1.4}$$

The mixing angles θ_{ij} are related to the PMNS matrix in the following way:

$$\sin^2(\theta_{12}) = \frac{|U_{e2}|^2}{1 - |U_{e3}|^2};\ \ \sin^2(\theta_{13}) = |U_{e3}|^2;\ \ \sin^2(\theta_{23}) = \frac{|U_{\mu 3}|^2}{1 - |U_{e3}|^2}. \tag{1.5}$$

In case of a broad energy distribution and/or large source extension or baseline, the oscillations are washed out and the neutrino flavor conversion is determined by the average probabilities. One is thus not observing an oscillation, but a reduced flux of the flavor neutrino of interest for a disappearance experiment.

The oscillation probabilities are calculated through the wave-packet approach or alternatively by a field-theoretical approach. The derivation with wave packets was first presented by Boris Kayser in [Kay81]. A review that includes in addition the field-theoretical approach can be found in [Zra98]. In text books frequently a simplified calculation is shown, where plane waves are inserted in equation 1.1. Even though the propagation of neutrinos is not properly described by plane waves, one obtains the same formulas as 1.3 when the transition probability is calculated.

The mixing angles and mass differences are conventionally associated with neutrino sources that are most suitable to study them, which is caused by very different L/E factors: θ_{12} is identified as the neutrino mixing that dominates solar neutrinos, while

parameter	value $\pm 1\sigma$	comment
$\sin^2(\theta_{12})$	$0.310^{+0.013}_{-0.012}$	
$\sin^2(\theta_{23})$	$0.580^{+0.017}_{-0.021}$ / $0.584^{+0.016}_{-0.020}$	normal ordering / inverted ordering
$\sin^2(\theta_{13})$	$(2.24 \pm 0.07) \cdot 10^{-2}$ / $(2.26 \pm 0.07) \cdot 10^{-2}$	normal ordering / inverted ordering
Δm^2_{21}	$(7.39^{+0.21}_{-0.20}) \cdot 10^{-5}\,\mathrm{eV}^2$	$m_2 > m_1$ from solar MSW effect
Δm^2_{31}	$(2.53 \pm 0.03) \cdot 10^{-3}\,\mathrm{eV}^2$ / $(-2.51 \pm 0.03) \cdot 10^{-3}\,\mathrm{eV}^2$	normal ordering / inverted ordering
δ/π	$0.94^{+0.18}_{-0.13}$ / $1.24^{+0.12}_{-0.13}$	normal ordering / inverted ordering at 3σ no values are disfavored

Table 1.1: The current knowledge of neutrino oscillation parameters, derived from a global analysis [EGGHC$^+$19, nuf].

θ_{23} is related to atmospheric neutrino mixing, and θ_{13} determines the oscillation observed from reactor neutrinos at $L \sim 1\,\mathrm{km}$. The current measured values of Δm^2_{ij} and $\sin^2(\theta_{ij})$ are listed in table 1.1. It should be pointed out that the oscillations depend only on the squared sinus of the mass difference, the signs of the differences thus have no effect a priori.
An important characteristic of the oscillations is that they are different for a neutrino propagating in vacuum than for one propagating in matter. This effect can be observed with solar neutrinos at high energies, where the survival probability is significantly deviating from the expected vacuum oscillation. Due to the large number density of electrons in the solar plasma, ν_e have a larger cross section for coherent forward scattering than the other neutrino flavors. The ν_e can not only interact via the neutral current, but also through the charged current, which on the other hand is not possible for ν_μ and ν_τ. As a result, the Hamiltonian for electron neutrinos has to be modified with a potential of the form

$$V_{cc} = \sqrt{2} \cdot G_F \cdot N_e, \tag{1.6}$$

where G_F is the Fermi coupling constant and N_e the electron number density. One can view the additional potential like a neutrino refraction index in matter in analogy to the optical theorem. The matter effect in the Sun, called MSW effect (after Mikheev, Smirnov and Wolfenstein) leads to a resonant conversion of ν_e into ν_μ for energies above 2 MeV, e.g. for solar ^{8}B-neutrinos. When formulating the oscillation probabilities, one can show that they depend on the sign of Δm_{12}. Consequently, by observing the matter effects, one could determine that m_2 is larger than m_1 [Sue15].

1.5 Current status and open questions in neutrino physics

In the last years, many experiments were focused on determining the squared mass differences and mixing angles that characterize the neutrino oscillations. A list of the current values is given in table 1.1. The oscillations depend on the squares of the mass difference, such that the sign can not be determined by a single experiment. However, through the MSW matter effect, it is known that $m_2 > m_1$ (see section 1.4). One of the big open questions is the problem of mass ordering, i.e. if m_1 is the lightest neutrino mass eigenstate ("normal ordering") or m_3 ("inverted ordering"). The determination of the ordering would have important consequences for neutrino physics. Once the mass

ordering of the neutrinos is clarified, the uncertainty of the CP-violation δ-phase measurements could be greatly reduced. In addition, the scale of future experiments that search for neutrinoless double beta decay would be defined, as in case of an inverted ordering much higher event rates are expected than for normal mass ordering. Also, a clear lower constraint of the absolute neutrino mass would be set. The mass ordering can be measured in two ways: by observing oscillations in the energy spectrum of reactor neutrinos in the three-flavor framework (i.e. to describe the oscillation probability one has to take all three neutrino species into account) and resolving the tiny difference between Δm^2_{31} and Δm^2_{32}, or by observing matter effects in Earth from atmospheric or accelerator neutrinos, that crossed the planet on a long baseline. Several experiments, using either technique, are in preparation [CDF$^+$13].
In principle, one could also in some cases determine the mass hierarchy, if a result of the sum of neutrino masses is obtained from cosmology, from double beta decay experiments or from single beta decay experiments as KATRIN. This leads to another major open question of neutrino physics – the absolute value of the neutrino mass. This is further discussed in section 1.7.
Also the fundamental question of the neutrino nature – Dirac or Majorana – is of utmost importance. Several experiments explore this question by searching for the neutrinoless double beta decay ($0\nu\beta\beta$), which is only possible if neutrinos are identical with their anti-particles, usually referred to as Majorana particles. A discovery of this decay and the proof that neutrinos are Majorana particles would for example corroborate the seesaw mechanism, an extension of the standard model that can explain neutrino masses and predicts the existence of sterile neutrinos (see section 1.6). The neutrinoless double beta decay is further discussed in section 1.7.
In addition, many experiments search for hypothetical sterile neutrinos that do not interact weakly, but participate in oscillations, and fit to certain experimental observations. Sterile neutrinos with masses $\sim$keV or higher are also dark matter candidates and theoretically well motivated. These particles are of particular interest for this thesis. The search for sterile neutrinos is discussed in detail in section 1.8.
Other research goals in neutrino physics are an improved measurements of oscillation parameters and the determination of the CP violating δ-phase to find out the status of CP symmetry for leptons. The experimental searches are accompanied by the development of theoretical models to explain the origin of neutrino mass and mixing.

1.6 Neutrinos beyond the standard model: neutrino mass and sterile neutrinos in the seesaw mechanism

A review of sterile neutrinos and the seesaw mechanism by Marco Drewes can be found in [Dre13]. This section follows an article by the same author published in [Dre19].
Since the observation of neutrino oscillations it is known that at least two of three neutrinos are massive, despite predictions from the standard model of particle physics. However, their masses are at least 5 orders of magnitude smaller than the next lightest particle, the electron ($m_{e^-} = 511\,\mathrm{keV}/c^2$, $m_\nu < 2\,\mathrm{eV}/c^2$). A popular extension of the standard model to explain neutrino masses and their smallness, and that additionally predicts sterile neutrinos, is the (type I) seesaw mechanism. To generate the mass of a left-handed particle via the Higgs mechanism, the left-handed particle has to couple together with its right-handed partner via a Yukawa coupling to the Higgs field to conserve invariance under Lorentz transformations. Thus the first step is to introduce right-handed neutrinos (ν_R). As the weak interaction does not couple to right-handed particles, these neutrinos are not interacting weakly and are thus called

"sterile". In principle the gauge invariance of interactions demands that left- and right-handed particles have the same mass, but this is not required for neutrinos again for the reason that the weak interaction does not couple to right-handed particles. Thus the right-handed neutrinos can have a mass different from the mass of the left-handed neutrino (ν_L). One can add a Majorana mass M to the right-handed neutrino, which can take any value. Both ν_L and ν_R are connected, since they are now coupling to the Higgs field, and can form superpositions. As a consequence, the mass eigenstate ν of a neutrino is a superposition of both the (massless) left-handed and the (massive) right-handed eigenstates. One can write

$$\nu = \cos\theta_s \nu_L - \sin\theta_s \nu_R, \tag{1.7}$$

where θ_s is the sterile neutrino mixing angle. The mechanism is called seesaw mechanism, since the heavy sterile neutrino ν_R passes a part of its mass to the active observable neutrinos. In addition, the active neutrinos pass their ability to interact weakly to the sterile neutrino. The mixing θ_s is expected to be very small ($<< 1$), such that the neutrino mass is $m_\nu \approx \theta_s^2 M$. In summary, the seesaw mechanism predicts not only sterile neutrinos, but also explains how the neutrino mass is generated and why it is so small (because the mass M is suppressed by θ_s^2). The introduction of sterile neutrinos is not contradicting observations, since its interactions with matter are also suppressed by the factor θ_s^2, resulting in a very small effect.

An additional attractive feature of the seesaw mechanism is that it gives rise to the leptogenesis mechanism, which can explain the matter-antimatter asymmetry in the universe [FY86]. Due to the CP-violation of the weak interaction, which is increased by the Majorana nature, decays of the sterile neutrinos and other interaction lead to the creation of more leptons than anti-leptons. According to theoretical calculations, the inclusion of sterile neutrinos results in exactly the right amount of asymmetry. From a lepton-antilepton asymmetry, a baryon-antibaryon (i.e. matter-antimatter) asymmetry follows due to lepton and baryon number violating processes (sphaleron processes) [Buc14].

A specific variant of the seesaw mechanism that incorporates three sterile neutrinos into the standard model is the Neutrino Minimal Standard Model (νMSM, see figure 1.2). This model is motivated as it can explain cosmological and astrophysical observations. It adds in total 18 new parameters to the standard model: 3 Majorana masses, 3 Dirac masses, 6 mixing angles and 6 CP-violating phases. In contrast to the "ordinary" seesaw mechanism, it is not expected that the Majorana mass scale coincides with the grand unification scale[2]. The mass spectrum is rather defined by cosmological requirements, astrophysical constraints and the observed neutrino oscillations. The lightest sterile neutrino is then assumed to constitute dark matter with a mass $\mathcal{O}(10)$ keV. The motivation for sterile neutrino dark matter and current constraints are discussed in section 1.8.2. The other two sterile neutrinos are used to explain the matter-antimatter asymmetry in the universe through leptogenesis. Their mass is assumed to be $\mathcal{O}(1)$ GeV, required in order to generate the masses of the active neutrinos in combination with a lower bound on their mixing angle from the big bang nucleosynthesis, since these heavy neutrinos have to decay before it starts to affect the observed light element abundances (sterile neutrinos can decay via their mixing into

[2]The grand unification scale is the energy, above which all natural forces (weak, electromagnetic, strong) are expected to become equal in strength and unify to one force. Its value is assumed to be $\sim 10^{16}$ GeV.

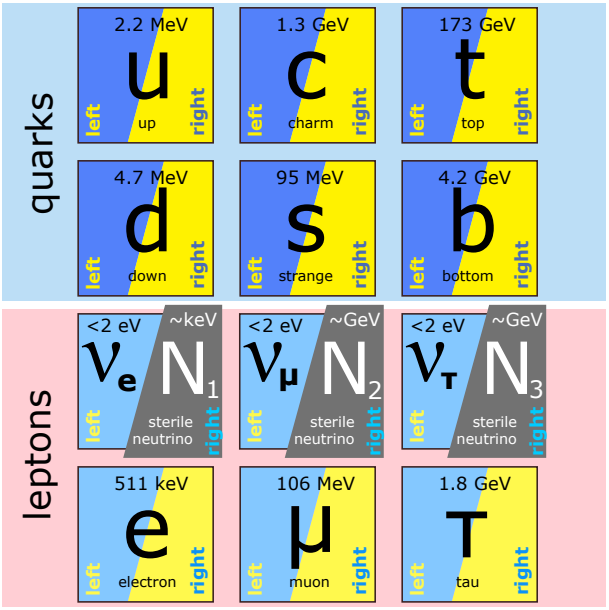

Figure 1.2: The νMSM: in a specific variant of the seesaw mechanism three sterile (right-handed) neutrinos are added to the standard model to explain cosmological and astrophysical observations and neutrino oscillations.

active neutrinos) [Bez08, Gor16, BRS09]. GeV-scale sterile neutrinos are further discussed in section 1.8.3. Due to their small mass, eV-scale sterile neutrinos cannot fully represent dark matter and thus are less motivated by cosmology, but several observations in neutrino oscillation experiments hint at their existence, as it will be shown in section 1.8.1.

1.7 Measurement of the absolute neutrino mass

Since a part of this thesis is about the TRISTAN project, which is an extension of the neutrino mass experiment KATRIN, here a short overview on the experimental challenges to measure the neutrino mass is given. In general there are three complementary approaches to determine the absolute mass of the neutrinos: cosmological observations, measurement of the neutrinoless double beta decay ($0\nu\beta\beta$) rate and electron spectroscopy of the β-decay.

- **Cosmology:** cosmological considerations and observations can give insight on the sum of masses m_Σ of the three active neutrino species (which are relativistic during the photon decoupling):

$$m_\Sigma = \sum_j m_j. \tag{1.8}$$

  At first order, cosmology is not sensitive for neutrino mixing and CP violation. This makes cosmological constraints complementary to terrestrial experiments. The mass m_Σ is proportional to the energy density of neutrinos ρ_ν in the universe. The latter can be derived from the temperature anisotropies of the cosmic microwave background (CMB) together with neutrino decoupling studies within the ΛCDM-model. From this, the current limit yields $m_\Sigma < 0.7$,eV [Par18, Lat16]. This limit can be considered as the most robust one, as the data with minimized systematic effects (e.g. a no assumptions on the microwave background except

for the dipole asymmetry from the Doppler shift) was used.
Only non-relativistic neutrinos affect the CMB anisotropies directly. Neutrinos with sub-eV masses are relativistic during decoupling and thus affect only secondary anisotropies which were created after the decoupling. However, these effects are visible on the entire CMB power spectrum. For example, neutrinos wash out fluctuations on small scales through their free movement, where their so-called free-streaming scale is decreasing with increasing m_j. Including all data from the CMB measured by PLANCK and additional data from other cosmological observations (e.g. Lyman-α data to model the large scale structure) to narrow down the parameters of the universe's evolution and with a complex treatment of the CMB polarization, one can find a limit $m_\Sigma < 0.12\,\mathrm{eV}$. However, this limit has to be used with caution, because it is only valid in the case that there are just three neutrino species and is susceptible to many systematic effects. More information about the derivation of neutrino parameters from cosmological observations can be found in the PDG review "Neutrinos in cosmology" [Par18].

- **$0\nu\beta\beta$:** with neutrinoless double beta decay ($0\nu\beta\beta$) experiments, one is searching for a double beta decay that is not accompanied by a neutrino emission, because the two generated neutrinos annihilated with each other. This is only possible, if neutrinos are Majorana particles. The half-life of this decay, which was not observed yet, is proportional to an "effective Majorana mass" $m_{\beta\beta}$:

$$m_{\beta\beta} = \left| \sum_j U_{ej}^2 \cdot m_j \right| \tag{1.9}$$

The signature of the $0\nu\beta\beta$ is a monoenergetic line at the endpoint of the ordinary $2\nu\beta\beta$ electron spectrum, since all the decay energy is given to the electrons. The detection is very challenging due to the long half-life of the $0\nu\beta\beta$-decay. For example the latest upper limit on the $0\nu\beta\beta$ half-life of ^{76}Ge from the GERDA experiment is $T_{1/2} > 9{\cdot}10^{25}$ years, which is 15 orders of magnitude longer than the age of the universe [GER18, Zsi18]. To detect this decay, one has to construct a detector with minimized background level and maximized target mass. The typical approach is to use a detector that is at the same time the source, e.g. a semiconductor detector made of germanium enriched with ^{76}Ge (e.g. GERDA) or a scintillator made of xenon enriched with the $2\nu\beta\beta$-decaying isotope ^{136}Xe (e.g. KamLAND-Zen [GGH$^+$16]). The current lowest limit on the effective Majorana mass is $m_{\beta\beta} < (0.06 - 0.17)\,\mathrm{eV}$ (90% C.L.) from KamLAND-Zen, depending on theoretical uncertainties in the calculation of the decay rate (nuclear matrix elements). The corresponding lower limit of the half-life is $10.7 \cdot 10^{25}$ years. It should be mentioned that this limit is exceeding the experiment's sensitivity of $5.6 \cdot 10^{25}$ years [GGH$^+$16]. The current best sensitivity is reached by GERDA with $11 \cdot 10^{25}$ y [Zsi18].
From a limit on the effective Majorana mass, one can also derive an upper limit of the mass of the lightest neutrino $m_{\mathrm{lightest}} < (0.18 - 0.48)\,\mathrm{eV}$, which is in this case approximately similar to $\sum m_j$, since we know from oscillation experiments that the mass differences are in the order of 10 meV [GGH$^+$16]. The next generation of experiments is expected to reach a sensitivity such that one would observe the decay in case neutrinos are Majorana particles and their masses are distributed according to the inverted ordering.

- **β-decay (and electron capture):** In the β-decay a tiny amount of the energy is going into the mass of the produced neutrino. One can thus observe a shift

of the maximum electron energy with respect to the calculated full decay energy. The neutrino mass parameter, which is affecting this shift, is the effective electron neutrino mass:

$$m_\beta = \sqrt{\sum_j |U_{ej}|^2 \cdot m_j^2}. \tag{1.10}$$

This is further discussed in section 8.3 in the introduction to the KATRIN experiment, which is scanning the tritium electron spectrum for this effect. From previous experiments an upper limit has been set at $m_\beta < 2\,\mathrm{eV}$ ([K$^+$05, ABB$^+$11]). The experimental challenge here is that to observe an effect smaller than a few eV a detector with an energy resolution in the same order has to be constructed. One approach is to construct an electromagnetic filter to achieve this energy resolution, as used by the KATRIN experiment. Another experiment – PROJECT-8 – aims at determining the tritium spectrum by the radio waves emitted from gyrating electrons in a magnetic field [AE$^+$17].
A related approach is the measurement of an electron capture-spectrum, where the neutrino mass also causes a shift of the end point. In contrast to the β-decay experiments, where actually an effective $\overline{\nu}_e$-mass is measured, the electron capture experiments are sensitive to the effective ν_e-mass. Experiments with this approach use the isotope ^{163}Ho, where the effect of the neutrino mass is enhanced due to the low decay energy. The general principle is to embed the source in an absorber and measure the total deposited energy that is converted into a tiny amount of heat. The ECHO experiment is using magnetic metallic calorimeters [GBC$^+$17], while HOLMES uses transition edge sensors to detect small temperature changes [N$^+$18].
KATRIN started the full scale neutrino mass program in March 2019 and will venture into the region comparable to cosmological limits with a sensitivity of $m_\beta = 0.2\,\mathrm{eV}$. The other projects are still at early "proof-of-concept" stages.

All approaches are complementary. Cosmological limits are strongly depending on models that describe the evolution of the universe and thus have to be cross checked with laboratory measurements. A measurement of m_β could give also input to $0\nu\beta\beta$-decay searches, as for example a sufficient large m_β and a non-observed $0\nu\beta\beta$-decay could together rule out the Majorana nature of neutrinos. On the other hand, a discovery of the $0\nu\beta\beta$-decay would have an major impact on neutrino physics and cosmology, since it shows that neutrinos are Majorana particles and that the lepton number is not conserved.

1.8 Sterile neutrinos

The theoretical motivation of sterile neutrinos was already discussed in section 1.6: the seesaw mechanism extends the standard model with one or more sterile neutrinos, which are heavier then the known active neutrinos. It explains how the active neutrino masses are generated by the sterile neutrinos and explains their smallness. In addition, it delivers with the leptogenesis a mechanism, which describes the origin of the observed matter-antimatter asymmetry of the universe.
Apart from theoretical considerations, some observations of the cosmos and anomalous results from neutrino experiments hint at the existence of sterile neutrinos with certain masses, as discussed in the following.

1.8.1 eV-scale sterile neutrinos

There are three so-called anomalies – an unexpected appearance or disappearance of neutrinos – that hint at the existence of sterile neutrinos with a mass $\mathcal{O}(1)\,\mathrm{eV}$ greater than the active neutrino masses. Such a neutrino would cause neutrino oscillations with a period in the range of meters for an energy in the order of MeV. At this L/E the two flavor approximation is valid, i.e. the standard oscillations can be neglected.

- **LSND and MiniBooNE anomalies:** the first anomaly was observed with LSND at Los Alamos, which detected an unexpected appearance of $\overline{\nu}_e$ in a $\overline{\nu}_\mu$-beam ($E_\nu = \mathcal{O}(10)\,\mathrm{MeV}$) at a distance of 30 m ($L/E = 0.5 - 1.5\,\mathrm{m/MeV}$) from 1993 to 1998. The $\overline{\nu}_e$-beam was produced via the decay of pions and muons, which themselves are created by shooting a 800 MeV proton beam onto a target. In the three neutrino picture, the $\overline{\nu}_e$-fraction in the beam is expected to be 10^{-4}, where the total neutrino flux is derived from simulations. An excess of $\overline{\nu}_e$ was detected at a significance of about $3.8\,\sigma$ that could be resolved by an oscillation introduced by an sterile neutrino with Δm^2_{41} in the range $0.2 - 10\,\mathrm{eV}^2$ and an average oscillation probability of 0.3% [AA$^+$01, GL19]. To cross check these results, the MiniBooNE experiment was started in 2001 at Fermilab, where a ν_μ- or a $\overline{\nu}_\mu$-beam with energies in the range $0.2 - 3\,\mathrm{GeV}$ was aimed at a 800 t-liquid scintillator at 541 m distance ($L/E = 0.2 - 2.7\,\mathrm{m/MeV}$, covering the LSND L/E range). Again an excess of $\nu_e/\overline{\nu}_e$-events was observed at a level of $4.5\,\sigma$, combined with LSND at $6\,\sigma$ significance. The best fit parameters of a sterile neutrino in a two-neutrino oscillation are $\Delta m^2_{41} = 0.041\,\mathrm{eV}^2$ and $\sin^2(2\theta_{41}) = 0.96$ [AA$^+$18]. Currently the MicroBooNE experiment is further investigating this anomaly and will explore, whether the excess is due to background [A$^+$18b].

- **Gallium anomaly**: the two radiochemical solar neutrino observatories SAGE and GALLEX that detected neutrinos via the reaction $^{71}\mathrm{Ga}(\nu_e,\ e^-)^{71}\mathrm{Ge}$ were calibrated with intense ^{51}Cr and ^{37}Ar ν_e-sources [A$^+$99, A$^+$95, HHK$^+$14, A$^+$06]. In both experiments an unexpected disappearance of ν_e was observed at very short distances $\sim 1\,\mathrm{m}$. How the source activity and thus the neutrino flux was determined is shortly described in section 2.4. The measured rate deficit was 16% at a significance of $2.9\,\sigma$. This could be caused by a sterile neutrino with $\Delta m^2 \gtrsim 1\,\mathrm{eV}$ with a mixing $\sin^2(2\theta) \sim 0.1$ (at 90% confidence level, the values depend strongly on cross section calculations) [GLL$^+$12, GGL$^+$16]. Currently the BEST experiment is in preparation to study this anomaly with a ^{51}Cr ν_e-source and a segmented radiochemical detector. If indeed a sterile neutrino is causing the Gallium anomaly, BEST would make a cross-section independent $5\,\sigma$ discovery by comparing the event rates in the detector segments [BCG$^+$18]. First results are expected in early 2020.

- **Reactor anomaly:** after a re-evaluation of $\overline{\nu}_e$-spectra from nuclear reactors alongside with an improved measurement of the neutron half-life it was found that the measured neutrino fluxes were about 7% less than expected at a $3\,\sigma$ significance. Figure 1.3 shows the ratios of the measured number of $\overline{\nu}_e$-events N_{exp} and calculated event numbers N_{calc} for different experiments. Again, an explanation that resolves this discrepancy is a short baseline oscillation due to a sterile neutrino with a $\Delta m^2 \gtrsim 0.5\,\mathrm{eV}^2$ [GL19]. However, also uncertainties of the spectra calculations could account for this anomaly [Hay18]. Especially a still unexplained "bump" at 5 MeV shows that the spectra are not fully understood. The observation of this bump was first published by Double Chooz in 2014 [A$^+$14] and

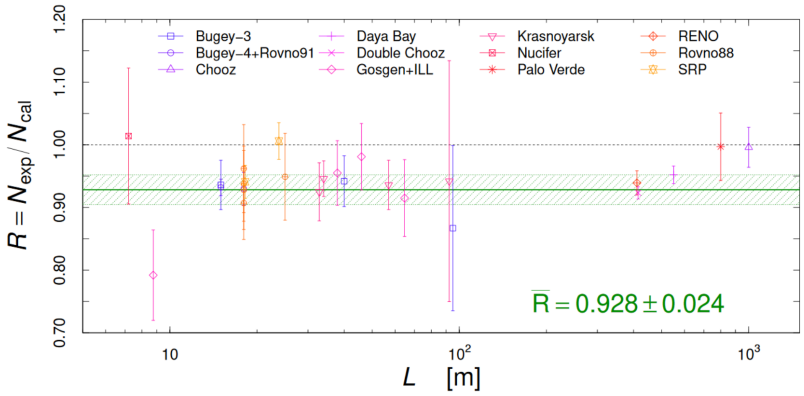

Figure 1.3: The reactor antineutrino anomaly: after a recalculation of reactor $\overline{\nu}_e$-spectra, it became apparent that many experiments measured a number of events N_{exp} that was lower than the calculated number N_{calc}. The plot shows the deficit for different experiments. In average, the measured deficit is about 7% at a significance of 3 σ [GL19].

confirmed by the RENO collaboration at the Neutrino conference 2014 in Boston [C$^+$16]. In 2015 additionally Daya Bay reported the observation of this spectral distortion. [A$^+$16].
To resolve the question of the reactor anomaly, several experiments started taking data at very short distances from nuclear reactors to not only observe a reduced flux, but also an oscillatory pattern depending on distance and energy (which is washed out at larger distances), either by using a segmented a detector (STEREO [A$^+$18d], PROSPECT [A$^+$18e], SoLid [A$^+$17b]), a segmented and movable detector (DANSS [A$^+$18c], Neutrino-4 [S$^+$19]), or a non-segmented detector (NEOS [Siy18]), where only an oscillation in the energy spectrum could be observed. An observation of an oscillation would confirm the sterile neutrino hypothesis. So far Neutrino-4 claimed the observation of an oscillation, which is however in tension with data from PROSPECT. A conclusive picture is still lacking [S$^+$19, Dan18].

The combined data from the anomalies discussed above can be analyzed and a global fit of the 3+1 neutrino picture (one sterile neutrino[3]) can be performed to constrain the parameters of the suspected sterile neutrino. Such a fit from [AGG$^+$16], showing the state of the art shortly before SOX was scheduled for data taking, is shown in figure 1.4. Due to the data selection, open questions concerning systematic effects and the many tensions between the experiments, these global analyses can only be seen as indicative. As one can see, the best fit parameters of a sterile neutrino are $\Delta m^2_{41} \approx 2\,\text{eV}^2$ and $\sin^2(2\theta_{e\mu}) \approx 10^{-3}$ (which translates to $\sin^2(2\theta_{14}) \approx 0.1$). To finally discover or refute the existence of a sterile neutrino, the SOX experiment was conceived: an intense and very compact neutrino source is placed close to the Borexino detector that allows to search for an oscillatory pattern within the detector volume thanks to a good vertex- and energy resolution. This project is introduced in detail in chapter 2.
As of early 2019, several of the above mentioned other short-baseline oscillation experiments delivered results, but could yet not disclose the origin of the anomalies. This is further discussed at the very end of this thesis in chapter 13.

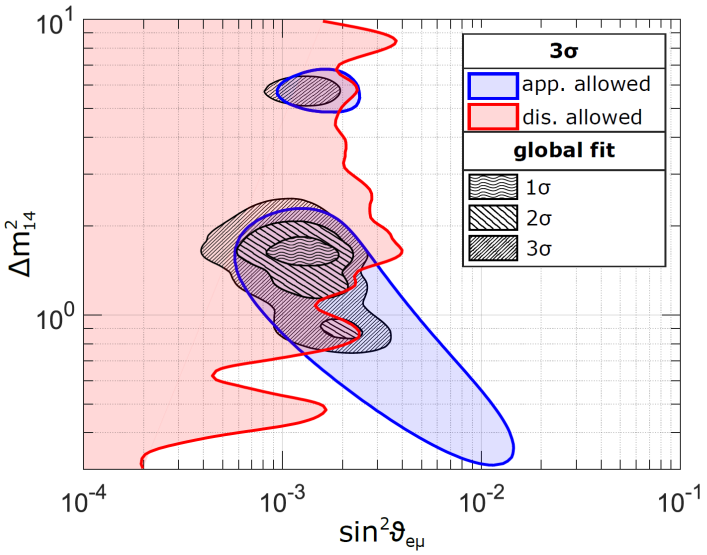

Figure 1.4: A global fit of a sterile neutrino model (3+1) to the short baseline oscillation data from 2016, i.e. shortly before the planned start of the SOX project. Here, the combined fit of the anomalous appearance (app.: LSND / MiniBooNE anomalies) and disappearance data (dis.: gallium- and reactor anomaly) is shown together with the separated $3\,\sigma$ allowed regions as a function of the mass difference Δm^2_{41} and the amplitude $\sin^2(2\theta_{e\mu}) = 4|U_{e4}|^2|U_{\mu 4}|^2$. This plot was adapted from [AGG+16]. As of 2019 more data is available, but a clear exclusion of a sterile neutrino with a eV-scale mass was not achieved yet (see e.g. [GL19]).

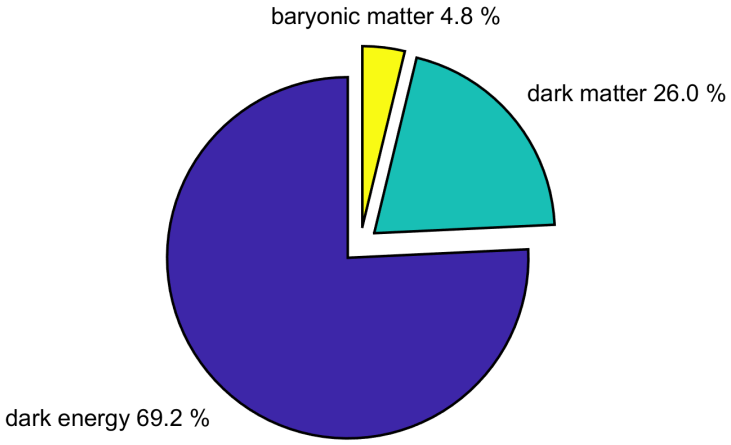

Figure 1.5: The contents of the universe today, according to the latest results from the Planck satellite [Par18]. Only a small fraction of the energy density is made of baryonic matter (i.e. stars etc.), the largest part – dark energy and dark matter – is of unknown nature. Sterile neutrinos are a candidate particle for dark matter.

1.8.2 keV-scale sterile neutrinos and dark matter

The existence of dark matter (DM), i.e. a component of the universe that contributes a large fraction of the mass and the energy density, is well established. Dark matter can be observed indirectly through its gravitational interaction with baryonic (visible) matter. In galaxy clusters the mean kinetic energy of galaxies can be related to the potential (gravitational) energy through the virial theorem. One can see that the mean velocities of the galaxies, as measured through the Doppler shift of spectral lines, are not matching to a potential that is generated by the visible mass, which is determined from the total light output. With a similar approach, one can see that galaxies are rotating too fast. Another famous observation of two colliding galaxies – the Bullet Cluster – shows that the stars of the galaxy are not aligned with the mass, which acts as a gravitational lens. This observation also strongly disfavors non-particle dark matter theories, e.g. modified Newtonian dynamics. The conclusion is that galaxies are embedded in haloes of invisible matter that are much larger than the galaxies themselves. Additional evidence for dark matter is given by measurements of the cosmic microwave background, which is a snapshot of density fluctuations in the early universe 300 000 y after the big bang, where dark matter strongly influences e.g. the amplitudes of the baryonic acoustic oscillations. In addition, measurements of the Lyman-α forest allow to study the large-scale structure of the universe, which, when compared to simulations, can be explained only with dark matter. Within the ΛCDM cosmological model, the exact content of dark matter in the universe can be derived from measurements of the CMB. According to latest results from the Planck satellite, 69.2 % of the universe are dark energy and 30.8 % are matter, where only 4.8 % are baryonic matter (see figure 1.5) [Par18]. As one can see, the matter content of the universe is dominated by dark matter – particles, about which we know nothing so far.

In contrast to eV-scale sterile neutrinos, terrestrial measurements did not discover anomalies that hint at the existence of keV-scale sterile neutrinos, but there are several astronomical and cosmological observations, which suggest the existence of these particles. Most importantly, sterile neutrinos with masses $> \mathcal{O}(1)$ keV are dark matter candidates. Actually, also the known active neutrinos are dark matter since they are massive and invisible, and light sterile neutrinos would be too, but those can only account for a small fraction of the total dark matter. The reason for this is on one hand that neutrinos are Fermions and thus obey the Pauli exclusion principle. Due to this only a finite number of neutrinos can fit into the potential well of a Galaxy, before the phase space is fully populated. This is called the Tremaine-Gunn bound [BRI09]. On the other hand, light neutrinos would behave as hot dark matter (HDM) in the early universe that has a large free streaming length and thus erases density fluctuations on small scales, which contradicts observations. Sterile neutrino dark matter is thoroughly discussed in the white paper [A$^+$17c], which also serves as an reference for this introduction. Sterile neutrinos with keV-masses would act as warm dark matter (WDM), in contrast to heavier dark matter candidates as WIMPs or Axions that are called cold dark matter (CDM). Several observations at galactic scales indicate that dark matter could be indeed warm:

- **Dwarf galaxies problem:**

  While CDM and WDM result in a similar structure formation at large scales, at scales of dwarf galaxies and smaller they produce very much different structures,

[3] There is no theoretical upper limit on the number of distinct sterile neutrinos. Thus also 3+2, 3+3 fits and so on could be performed.

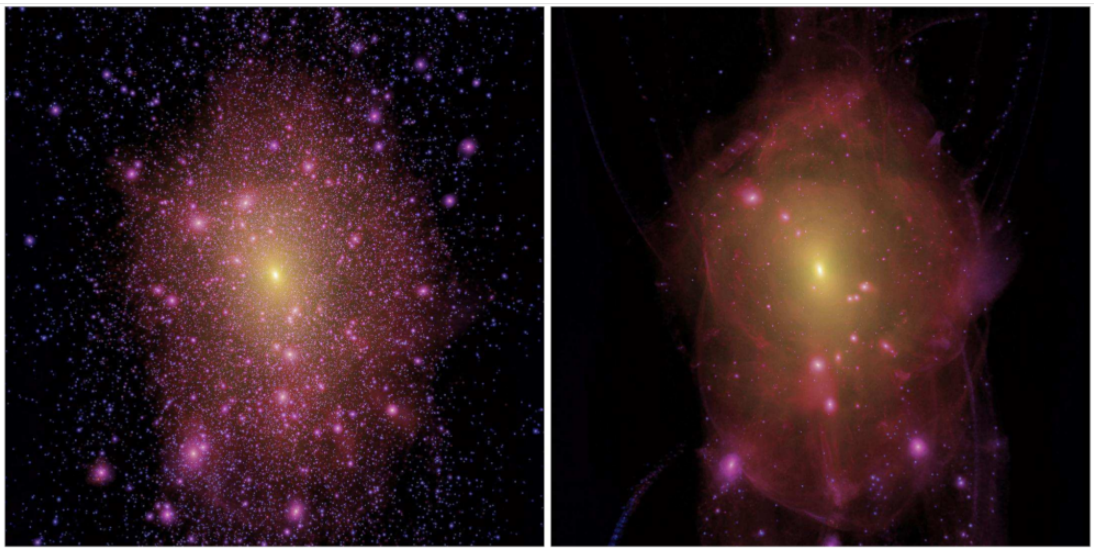

Figure 1.6: N-body simulations of galactic haloes in a cold dark matter (CDM) and warm dark matter (WDM) scenario. **Left:** the CDM simulation. The galactic halo contains a large number of sub-haloes that correspond to satellite galaxies; **Right:** in the WDM scenario a much lower number of sub-haloes is formed [LEF+12].

as warm dark matter tends to wash out small dark matter sub-haloes within a large galactic halo. A plot of simulated galactic haloes in a CDM and a WDM scenario is shown in figure 1.6. As one can see, in case of CDM much more sub-haloes are formed than in the WDM simulation. These sub-haloes represent satellite galaxies. The predicted number of satellite galaxies from a CDM simulation indeed exceeds the observed number by a factor ~ 5. In addition, the number of dwarf galaxies ($M \lesssim 10^{10} M_{\odot}$) in the entire universe is systematically overpredicted by a similar factor. On the other hand, the observations are in agreement with the WDM simulations. These discrepancies are called "dwarf galaxies problem" or "missing satellite problem". However, this problem could be resolved in a CDM scenario through processes that prevent the star formation in sub-haloes and thus makes them unobservable, e.g. heating or winds caused by supernova explosions. Sub-haloes with faint dwarf galaxies can be still observed through weak lensing or the Lyman-α forest: the Lyman-α absorption line of neutral hydrogen in cold gas is observed in the light from quasars. Since the redshift is gradually changing in the line of sight, the line is shifted differently depending on the distance, such that the large scale structure can be mapped. However, these measurements are challenging since many effects have to be disentangled. So far, neither WDM or CDM can be excluded, but lower limits on the mass of sterile neutrino dark matter have been set at a few keV [LEF+12, A+17c].

- **Cusp-core problem:** the Cusp-core problem concerns the inner density profile of galactic haloes. CDM simulations predict a density profile that follows a $\rho \sim r^{-1}$ power-law (a cusp in the center), where r is the radius from the halo center. In large galaxies the profile can be leveled due to baryonic feedback from the formation of bars, discs and bulges. Dwarf galaxies are typically dominated by dark matter and thus a more suitable testing ground. Observations, where the density profile was derived from the rotation of cold gas (hydrogen 21-cm line) or stellar dynamical modeling, show a core-like density distribution that follows a $\rho \sim r^{-0.3}$ law. Simulations show that this could be caused by baryonic feedback,

e.g. supernova winds and bursts of star formation, but it is not clear, if these simulations accurately reproduce the complex physics. On the other hand, WDM would naturally result in core-like density profiles. However, it remains unclear whether WDM is more successful than CDM to reproduce the correct density profile when baryonic feedback is taken into account. In addition, it is disputed whether the density profiles have actually cusps instead of cores [A$^+$17c, BMS18, GBF$^+$18].

- **Too-big-to-fail-issue:** this problem is closely related to the dwarf galaxies and cusp-core problems. It represents the issue that the observed number density and internal kinematics of dwarf galaxies cannot be reproduced by CDM models. Simulations show that sub-haloes in the Milky Way (MW) and Andromeda galaxy are too massive to explain the kinematics of the bright satellite galaxies, which are assumed to be hosted by the most massive sub-haloes. As a consequence one could conclude that the satellites are hosted by less massive haloes and that the most massive sub-haloes are dark. However, they should be too big to fail star formation (hence the name) [BBK11]. This problem could be solved by a reduced virial mass of the galaxies or by tidal stripping, where the host galaxy pulls matter from the satellite due to the gravitational interaction, which ultimately results in a changed dark matter distribution that can account for the observed kinematics. However, also isolated dwarf galaxies show similar kinematics as satellite galaxies and thus constitute indirect evidence against the stripping solution. In addition, simulations predict that the abundance of haloes rises quickly with decreasing halo mass. Observed abundances then restrict galaxy formation to relatively massive haloes, because else there would be too many dwarf galaxies. Nevertheless, as measured from rotation curves via the 21-cm hydrogen line, the host haloes of a large fraction of dwarf galaxies have masses well below this threshold. As the previous mentioned problems, also the too-big-to-fail issue can be possibly solved by baryonic effects: haloes below a certain threshold can lose the majority of their baryonic content due to galactic outflows. Even lighter haloes are unable to accrete gas after the universe re-ionized. Both effects combined result in a different relative abundance of low mass haloes and thus dwarf galaxies. Baryonic processes can also alter the rotation curves, such that the calculation of the halo mass becomes erroneous. The exact contribution of these effects is not clear. WDM would also solve this issue, since it alters the small scale structure formation and reduces generally the abundance of small haloes and results in less dense haloes, which fit to the observed kinematics of dwarf galaxies [A$^+$17c].

In summary, observations on galaxy scale are not in agreement with CDM simulations. However, baryonic matter that is neglected in DM-only simulations could resolve these issues through its gravitational interaction, but the effects of baryonic feedback are hard to estimate. Another solution is WDM, since it levels out small scale structures and thus strongly impacts the abundance, properties and kinematics of dwarf galaxies. Other explanations are for example resonant self-interacting dark matter particles [CGCM19]. In the end, a consistent solution has not been found yet and models for the small scale structure formation of the universe remain disputed and controversial.

Sterile neutrinos as a dark matter candidate can be constrained by X-ray observations. These neutrinos can decay via their mixing with active neutrinos. The main decay branch for sterile neutrinos with masses $< 2{\cdot}m_\mathrm{e}$ is $N \to \nu\nu\bar{\nu}$ and determines the lifetime of the particle. In addition there is a sub-dominant radiative decay $N \to \nu\gamma$ which creates mono-energetic photons. Due to momentum conservation the photon carries half of

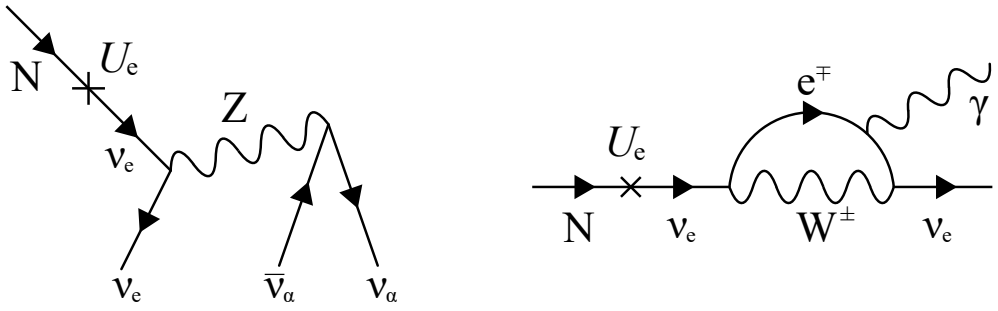

Figure 1.7: Decay channels of a dark matter sterile neutrino N with a mass $m_N < 2 \cdot m_e$. **Left:** the dominant decay into three active neutrinos. **Right:** the radiative decay that results in a mono-energetic X-ray line at an energy $E = 0.5 \cdot m_N$ [A$^+$17c].

the sterile neutrino's energy ($\hat{=}$ mass, since dark matter neutrinos are non-relativistic), which results in an X-ray for a keV-scale sterile neutrino. The Feynman-diagrams of both channels are shown in figure 1.7. The radiative decay can be understood as a sterile neutrino that oscillates into an off-shell active neutrino (i.e. it has a "wrong energy") and thus radiates a photon that couples to a virtual charged lepton or W-boson. Decays at different redshifts would cause a broad line in the diffuse X-ray background. When observing galaxy clusters, the Milky Way halo or dwarf spheroidal satellites, one expects a clear line in the spectrum. Such a line at $\sim 3.5\,\mathrm{keV}$ was observed by XMM Newton in data from galaxy clusters and Andromeda. The line in the Perseus cluster was confirmed by Chandra at $> 3\,\sigma$ significance [BMF$^+$14, BRIF14] and later discovered also in other objects and by the other telescopes Suzaku and NuSTAR (e.g. [CBF$^+$18, IBF$^+$15]). A plot of the line as observed by XMM Newton in Andromeda is shown in figure 1.8. If the line is due to a decaying sterile neutrino, its mass would be $m_s \approx 7.1\,\mathrm{keV}$ and its lifetime $\tau_s = 2 \cdot 10^{20}\,\mathrm{y}$, corresponding to a mixing angle $\sin^2(2\theta) \approx \mathcal{O}(10^{-11} - 10^{-10})$. Other observations, where no line was detected, put upper bounds on the flux [Iak16, CBF$^+$18]. A summary plot of the bounds is shown in figure 1.9. The origin of the line is still unclear and disputed, as it also could be explained by statistical fluctuations, instrumental systematics and uncertain astrophysical lines, especially plasma emission lines [A$^+$17c].
Another interesting study concerning the 3.5 keV excess should be mentioned: the Hitomi satellite did not observe the 3.5 keV line in the Perseus cluster, but it has a larger field of view than XMM and Chandra and thus observes the sum of the diffuse cluster emission, where the line was detected by XMM and Chandra, and the point-like active galactic nucleus (AGN) NGC1275 (Perseus A). Data from Chandra hints at a dip at 3.5 keV in the AGN emission, such that the overall spectrum observed with Hitomi is consistent with the XMM and Chandra data. This behavior – a dip in regions of high dark matter density and a line in less dense regions – could be explained by fluorescent dark matter. This type of dark matter could be made of axions, but not of neutrinos [CDJ$^+$17]. Unfortunately, the Hitomi satellite is not available for further observations, after it was shredded to pieces due to a fatal software error.

A sterile neutrino could be discovered in a laboratory via its effect on the shape of β-decay electron spectra. This is further discussed in section 8.4. So far, laboratory experiments resulted in much weaker bounds than the X-ray observations [DV16]. Some of these experiments were conducted as a response to the observation in 1985 of a distortion in the tritium spectrum that was consistent with a 17 keV neutrino with a 3%-mixing probability [Sim85], which was later rejected. A summary of these bounds

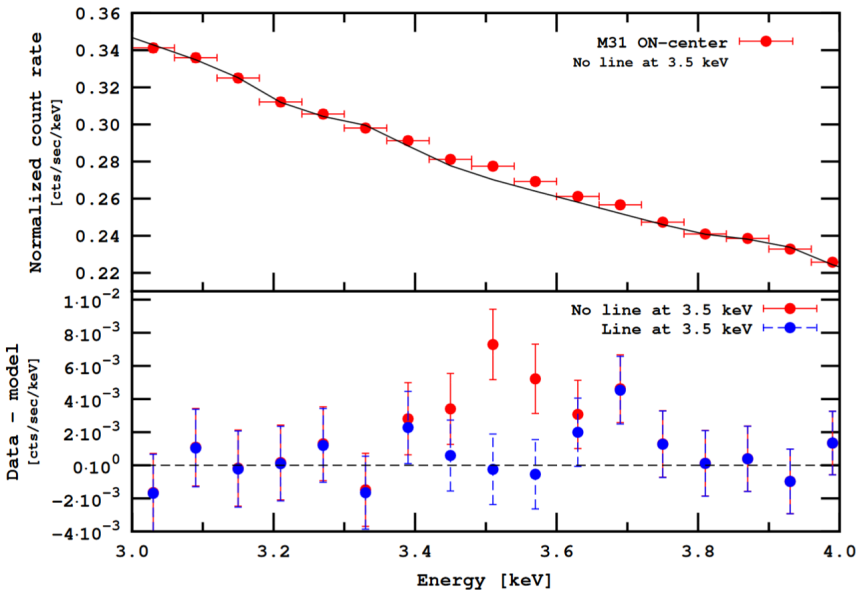

Figure 1.8: The 3.5 keV X-ray line as observed by XMM-Newton in Andromeda [BRIF14]. The bottom plot shows the residuals with and without the line.

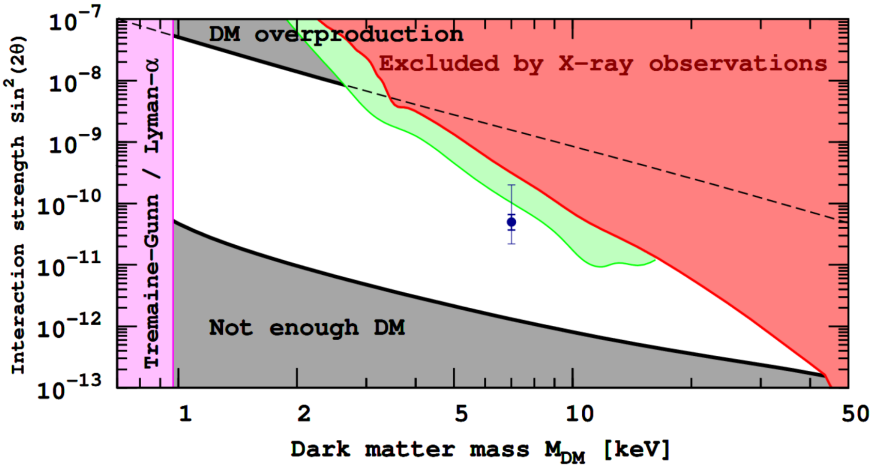

Figure 1.9: The bounds on neutrino dark matter from X-ray observations. A lower mass limit is set by the Tremaine-Gunn bound, the interaction strength has an (model dependent) upper limit to prevent overproduction in the big bang. The bounds set by non-observed lines are shown in different colors for different studies. The data point marks the observed 3.5 keV line. The plot was taken from [BRIF14].

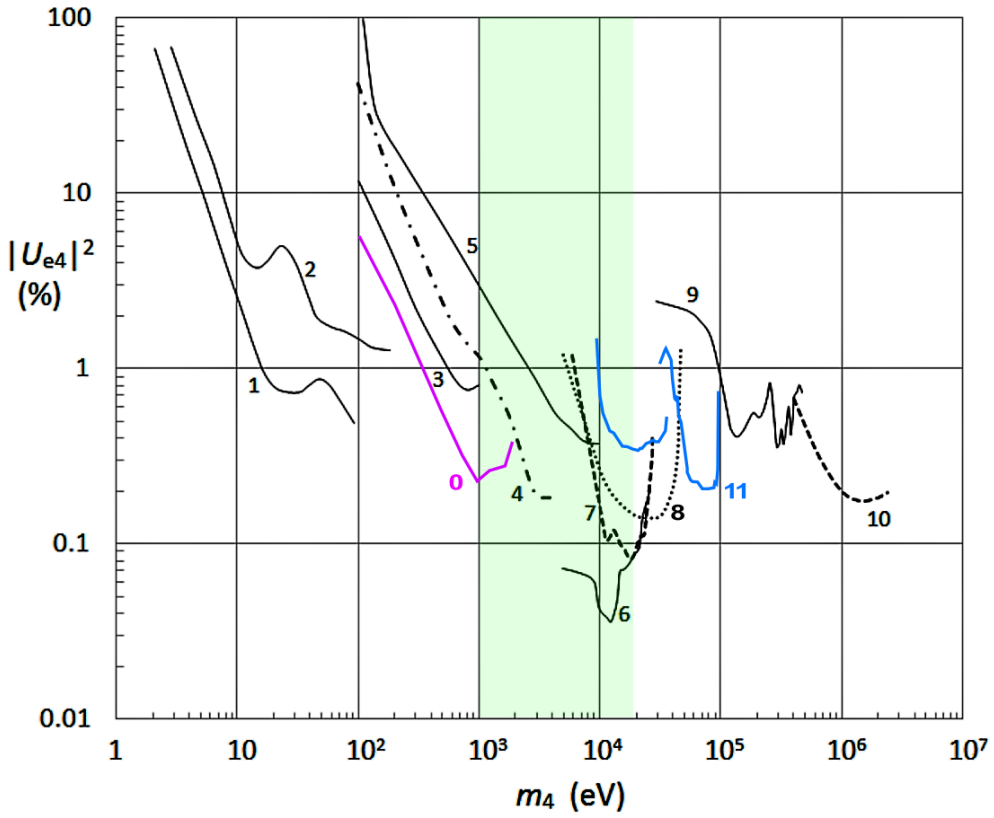

Figure 1.10: A summary of sterile neutrino searches by analyzing the β-spectrum of different isotopes, adapted from [DV16]. All limits correspond to the exclusion at 95% C.L., except for 2) and 9), which are at 90% C.L. In the following, the isotopes used by each measurement are listed: **0)** ^{3}H, Troitsk ν-mass [A$^+$17a]; **1)** ^{3}H, Troitsk ν-mass [BBG$^+$14]; **2)** ^{3}H, Mainz neutrino mass experiment [KSVW13]; **3)** ^{187}Re, [GFGV01]; **4)** ^{3}H, [HDS95]; **5)** ^{3}H, [Sim81]; **6)** ^{63}Ni, [HKP$^+$99]; **7)** ^{63}Ni, [OSS$^+$93]; **8)** ^{35}S, [MAC$^+$93]; **9)** ^{64}Cu, [SCvF83]; **10)** ^{20}F, [DLP90]; **11)** ^{177}Lu, [SOH$^+$96]. The area from 1 to 18.6 keV is marked in green to illustrate the range of the tritium spectrum. Note that at low and high masses stronger limits exist from different laboratory searches, e.g. short baseline oscillation experiments (see section 1.8.1) or searches for a heavy neutrino decay at nuclear reactors (for example [HAF$^+$95]).

is shown in figure 1.10. As one can see, the limits don't venture past a mixing of $|U_{e4}|^2 = \sin^2\theta_{14} = 10^{-4}$, which is ~ 6 orders of magnitude above the X-ray bounds. This is, where TRISTAN joins the game: the goal of this project is to greatly improve the laboratory limits and to scan the parameter space of cosmological interest. The TRISTAN project is presented in chapter 8.

1.8.3 GeV-scale sterile neutrinos and beyond

GeV-scale sterile neutrinos are predicted by the νMSM (see section 1.6). In addition to the keV-scale sterile neutrinos, which serve as dark matter in this model, the GeV-scale sterile neutrinos are necessary to grant the active neutrinos their mass via the see-saw mechanism and for the leptogenesis mechanism that causes the matter-antimatter asymmetry in the universe. Their mixing has an upper bound from the leptogenesis process and a lower bound imposed by the requirement that these heavy neutrinos have to decay before the Big Bang nucleosynthesis (BBN) starts, otherwise they would

change the abundances of light elements in the universe. These particles can be produced in accelerator experiments, for example in the decay of a charged Kaon. The sterile neutrino itself then can decay for example into e^+e^- or $\mu^+\mu^-$-pairs [Bez08]. The expected life time is in the order of µs, requiring a large detector that can detect displaced leptonic jets. A proposed experiment to search for GeV-scale sterile neutrinos up to masses $\mathcal{O}(10)$ GeV and mixing $> 10^{-10}$ is SHiP at the CERN SPS (Super Proton Synchrotron). Current experiments already set bounds on the sterile neutrino's parameters, however, a large region of the allowed parameter space (set by the leptogenesis and the decay before BBN) is still unprobed. A summary of the limits can be found in the SHiP physics paper [SHi16].
It should be mentioned, that dark matter could also be made of a GeV-scale sterile neutrino with a very small mixing angle, making it very challenging to detect [A$^+$17c].

In summary, sterile neutrinos are hypothetical particles that are well motivated by theory, as the seesaw mechanism – an extension of the standard model that explains the origin of neutrino masses – predicts their existence. Sterile neutrinos itself are not interacting weakly, but are still detectable due to their mixing with active neutrinos, such that they take part in neutrino oscillations and can decay.
Sterile neutrinos with eV-scale masses do not solve any cosmological problems, but their existence could explain anomalous observations from neutrino oscillation experiments. The first part of this thesis is about the SOX project, which aimed to ultimately detect or refute these sterile neutrinos with a short-baseline oscillation experiment.
Sterile neutrinos with masses in the order of keV are dark matter candidates. Evidence for their existence is provided by discrepancies of the small scale structure of galaxies within the cold dark matter model and by a possible observation of their decay with X-ray telescopes. The goal of the TRISTAN project, which is covered by the second part of this thesis, is a detection of such a neutrino in a laboratory experiment.

Part II

SOX

Chapter 2

Introduction: the SOX experiment

The SOX (**S**hort distance neutrino **O**scillations at Bore**X**ino) project aimed to search for the signature of eV-scale sterile neutrinos with the Borexino detector by studying the neutrino flux from a strong source located beneath the detector. The vertex- and energy resolution of Borexino makes it possible to look for an oscillatory pattern in space and energy, as it would be present in case of a sterile neutrino with a mass in the eV-range. In addition, by measuring the activity of the source with a calorimeter also a reduced rate can be observed, if the sterile neutrino causes an oscillation at a length that exceeds the detector diameter or that is to small to be resolved.
Among several other experiments that search for eV-scale sterile neutrinos, SOX is a one-of-a-kind experiment since it is the only one that uses a clean, well-defined β-decaying source instead of a nuclear reactor or an accelerator, and uses a detector with high vertex and energy resolution. Reactor or accelerator experiments can deliver data with high statistics, but typically suffer from high background levels and complicated neutrino spectra. Especially by using the proven and famous Borexino detector with its extremely high level of radio-purity, the detection of electron anti-neutrinos emitted from the source can be considered to be background-free.
The Borexino detector is introduced in section 2.1 and the concept of the SOX project is discussed in detail in section 2.2. The anti-neutrino source is described in section 2.3, the activity determination with calorimeters in section 2.4, and spectral measurements to study the neutrino spectrum in section 2.5.
It should be mentioned already here that for a non-scientific unexpected technical problem in the fabrication plant the anti-neutrino source could not be delivered and, since there was only one available manufacturer in the world, the project was unfortunately canceled. The developments presented in this thesis are of potential relevance for future experiments and were published in [ADN+18].

2.1 The Borexino detector

Borexino is a spherical liquid-scintillator detector that is capable of real-time neutrino-spectroscopy and can resolve the position of the neutrino interaction vertex. It was originally built to study solar neutrinos. The detector is described in detail in [Bor09]. The active detecting volume consists of 270 t pseudocumene (PC, an oil with the chemical formula $C_6H_3(CH_3)_3$) with the additive PPO (2,5-diphenyloxazole, $C_{10}H_{10}O_4$, 5 g per liter PC). If a particle deposits energy into this molecular compound, light is emitted through deexcitation. The PPO serves as wavelength shifter, ensuring that the

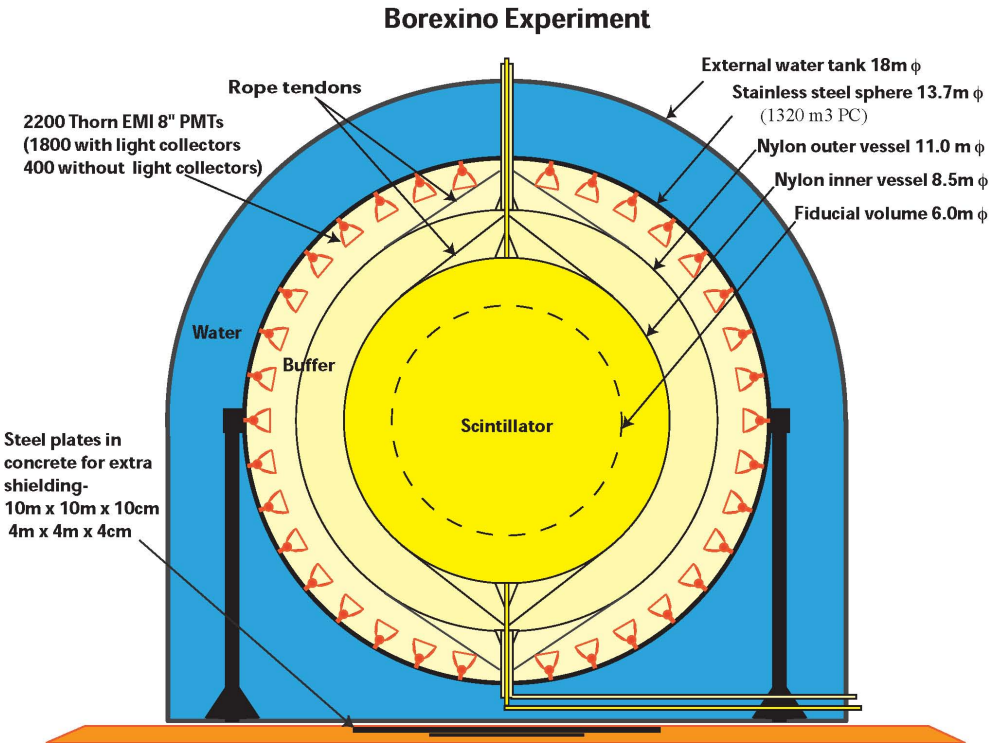

Figure 2.1: A scheme of the Borexino detector: The active volume of liquid scintillator is placed in a nylon balloon that is immersed in a buffer fluid, which itself is divided by a second nylon sphere into two parts. 2200 PMTs are mounted on the stainless steel sphere, which contains the aforementioned components, and detect light emitted in the active volume. The sphere is submerged in a water tank, which is equipped with $\sim$ 200 PMTs and serves as active muon veto and shielding from other external radiation. The detector is located at LNGS below 1400 m of rock that greatly reduce the cosmic muon flux.

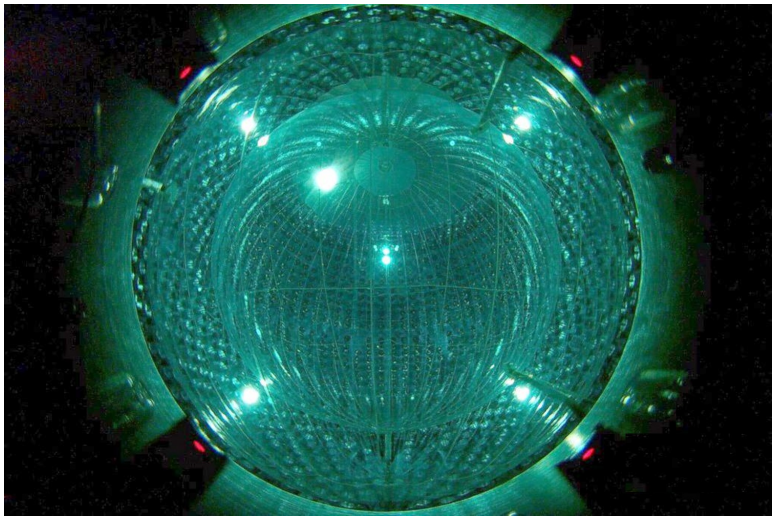

Figure 2.2: A photo of the inner detector: the two nylon spheres are visible, as well as the many PMTs on the inner surface of the stainless steel sphere.

light can travel to the photo multiplier tubes (PMTs) without being absorbed by the PC.
The detector's design is based on the principle of graded shielding ("onion shells"), with the radiopurity of the detector volume increasing from the outside to the inside. A scheme of the detector is shown in figure 2.1. The innermost part of the detector is the active scintillator within a transparent nylon sphere with 4.25 m radius. The nylon is actually not a perfect sphere, but slightly distorted into a shape of a hot air balloon. The next shell of the "onion" is the buffer volume: it is also filled with PC, but instead of PPO dimethylphthalat ($C_{10}H_{10}O_4$) is added that serves as light quencher and thus suppresses the scintillation. This buffer is shielding the active volume from the radioactivity in the stainless steel sphere, that encloses the inner parts of the detector. To prevent migration of radioactive impurities from the steel sphere towards the active volume, especially emanated ^{222}Rn, the buffer is divided into two parts by a second nylon sphere with 5.5 m radius. 2212 PMTs are mounted on the inside of the stainless steel sphere with 6.83 m radius. Most of the PMTs are equipped with light concentrators that reject photons not coming from the active scintillator volume, thus reducing the background by radioactive decays in the buffer or from other PMTs. The 384 PMTs without concentrators allow to study this background and to detect muons that crossed the inactive volume (which can produce spallation neutrons). A photo of the inner detector is shown in figure 2.2. The inner detector, i.e. the steel sphere and everything within, is placed inside a water tank with 18 m diameter and a height of 16.9 m. The water tank serves as passive radiation shield and as an active muon veto – the Cherenkov light emitted by cosmic muons in the water is detected by ~ 200 PMTs, such that events in the inner detector induced by a muon can be discarded during the analysis.
The outermost shell of the onion is a thermal insulation and several water lines welded onto the water tank that actively control and stabilize the detectors temperature. This helps to reduce convective currents in the scintillator and thus prevents the migration of radioactive impurities from regions close to the nylon sphere into the detector center.
The entire detector is located at the Gran Sasso underground laboratory in Italy (Laboratori Nazionali del Gran Sasso, LNGS). The 1400 m of rock (3800 m water equivalent) above the laboratory reduce the cosmic muon flux by a factor 10^6 to ~ 0.4 muons per square meter and hour.
In summary, Borexino's design is driven by the wish to have an extreme radio-purity. Indeed, the experiment achieved unprecedented background levels: for example, one gram of scintillator contains less than $9.4 \cdot 10^{-20}$ g of ^{238}U and less than $5.7 \cdot 10^{-19}$ g of ^{232}Th, a concentration 10 orders of magnitudes smaller than in any natural material on earth [Bor18].

In addition to the aforementioned hardware, the background can be further reduced by software techniques: for the analysis a fiducial volume is defined that excludes events in the active scintillator close to the "dirty" nylon sphere. Some background sources can be removed by searching for coincident events in time and space, for example the so-called threefold coincidence technique for rejecting ^{11}C β^+-decays [B$^+$06]. ^{11}C is produced by spallation of carbon through muons.
While the energy deposition, i.e. detection of solar neutrinos, for which Borexino was mainly built, is caused by neutrino elastic scattering off electrons, the interaction-process of interest for the SOX experiment is the inverse beta decay (IBD):

$$\overline{\nu}_e + p \longrightarrow n + e^+ \tag{2.1}$$

Compared to other neutrino interactions the IBD has the highest cross section (in the order of 10^{-44} cm^2 at a few MeV neutrino energy). However, this interaction is only possible if the $\overline{\nu}_e$'s energy exceeds the threshold $E_{thr} = 1.8$ MeV. The IBD creates two events inside the detector [Sue15]: a prompt signal is caused by the annihilation of the positron and a delayed signal by the neutron capture. Simple kinematics allow us to conclude on the energy of the neutrino $E_{\overline{\nu}_e}$ by measuring the energy deposited by the positron in the scintillator, which we call the visible energy E_{vis}: $E_{\overline{\nu}_e} \approx E_{vis} + E_{thr} - 2m_e c^2 = E_{vis} + 0.778\,\text{keV}$. The second signal is caused by the absorption of the neutron on a proton, forming deuteron and emitting a 2.2 MeV γ ray. The delay between both signals is ~ 200 µs. By acquiring only events with this very characteristic "delayed coincidence", Borexino can detect $\overline{\nu}_e$ background-free. In general, what is detected by Borexino is the number of photo-electrons in each PMT, the number of hit PMTs, and the time of each PMT signal. The number of photo-electrons is proportional to the energy. The exact response was measured in a calibration campaign, where radioactive sources were placed at different position in the inner vessel with the help of an "arm" that can be inserted into the detector. From the timing data one can conclude on the position of the event just by analyzing the time difference of the detection in different PMTs. In the end, Borexino reaches an outstanding energy resolution of 5% and a vertex resolution of 14 cm for neutrinos with an energy of 1 MeV [Bor14].

Borexino started data taking in 2007. The advanced age of the detector left its mark: PMTs are steadily "dieing", as of early 2019 only ~ 1300 of the initial 2200 are still functional. However, this is still sufficient for an excellent performance, and in addition Borexino's background level decreases more and more, such that it is now as low as never before. Meanwhile, Borexino delivered many results. The most important ones are listed in the following:

- **solar neutrinos:** the hydrogen burning of the sun is dominated by the pp-cycle, where effectively 4 protons are turned via several fusion processes into one ^{4}He-nucleus, two positrons and two electron neutrinos with an energy release of 26 MeV. The neutrinos are emitted with a mean energy of ~ 200 keV, which is quite low and thus makes a detection difficult despite the high flux of $\sim 6{\cdot}10^{10}\,\text{cm}^{-2}\text{s}^{-1}$. Other fusion processes that occur with lower probabilities lead to the emission of electron neutrinos at higher energies. Borexino measured the spectrum and fluxes of these neutrinos, except for so-called hep and CNO neutrinos, where only upper limits could be set. This work is presented in [Bor18]. A complete fit of the spectrum from the latest publication is shown in figure 2.3. The measurement of CNO neutrinos, which are produced in a fusion cycle that involves carbon, nitrogen and oxygen nuclei that fuse with protons, is the future goal of Borexino. From a measurement of these neutrinos one can derive the sun's metallicity. However, this measurement is complicated by the low flux and a background from the ^{210}Bi β-decay spectrum. In general, the solar neutrino measurements allow to study the physics of the sun, if the neutrino oscillation mechanisms are assumed to be valid, or to study neutrino oscillations including matter effects as the MSW effect, when the predicted neutrino fluxes from the standard solar model are used;

- **geo-neutrinos:** Borexino detected so-called geo-neutrinos that are $\overline{\nu}_e$ emitted from the ^{238}U and ^{232}Th decay chains in the earth's mantle. In 2056 days of data 24 ± 6 geo-neutrinos were detected. This observation allows to calculate the

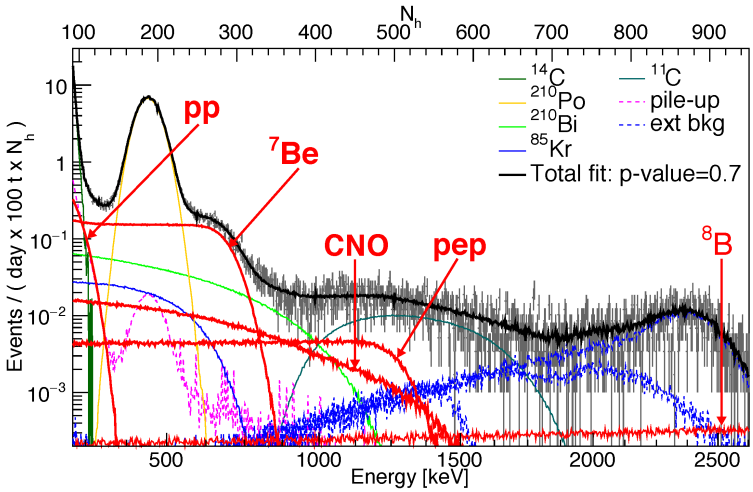

Figure 2.3: The complete fit of the spectrum measured by Borexino as published in [Bor18], including solar neutrinos and background.

thermal power generated in the earth by radioactive decays, which was found to be 23-36 TW. Since the geo-neutrino flux is very low and $\overline{\nu}_e$ are also produced in nuclear reactors, the reactor spectrum had to be included into the analysis, even though no nuclear reactors are operated in Italy [Bor15a];

- **neutrino magnetic moment:** if the neutrino mass is included in the standard electroweak theory, neutrinos are expected to possess a magnetic moment which is proportional to the neutrino mass. Using existing cosmological limits of the neutrino mass, one would expect the magnetic moment to be smaller than $10^{-18}\mu_B$, where μ_B is the Bohr magneton. However, other theories predict a larger magnetic moment which could significantly affect the Borexino data. The neutrino magnetic moment changes the electron recoil spectrum for neutrino detections in Borexino. The data from Borexino was compared to the solar neutrino fluxes measured by radiochemical gallium experiments which are not affected by a neutrino magnetic moment, but no significant deviation was found and the magnetic moment was limited to $\mu_\nu^{\text{eff}} < 2.8 \cdot 10^{-11}\mu_B$ [Bor17c].

- **seasonal modulation of the cosmic muon flux:** the outer detector (the muon veto) was used to measure the muon flux and study seasonal modulations. A positive correlation of the muon flux with the atmospheric temperature and a longer modulation with a ~ 3000 d period were discovered that could be related to the solar activity [Bor19].

Other analyses were looking e.g. for neutrinos from gamma-ray bursts (no detection) [Bor17b], neutrinos in correlation with gravitational waves (no detection) [Bor17a] and the electron's stability was tested [Bor15b]. A complete list of papers published by the collaboration and other Borexino-related research can be found on the official Borexino web-page[1].

2.2 Sterile neutrino search with SOX

The SOX project originated from two parallel efforts: a French group was pursuing together with the KamLAND collaboration a sterile neutrino search by deploying a

[1] http://borex.lngs.infn.it/, retrieved in January 2019.

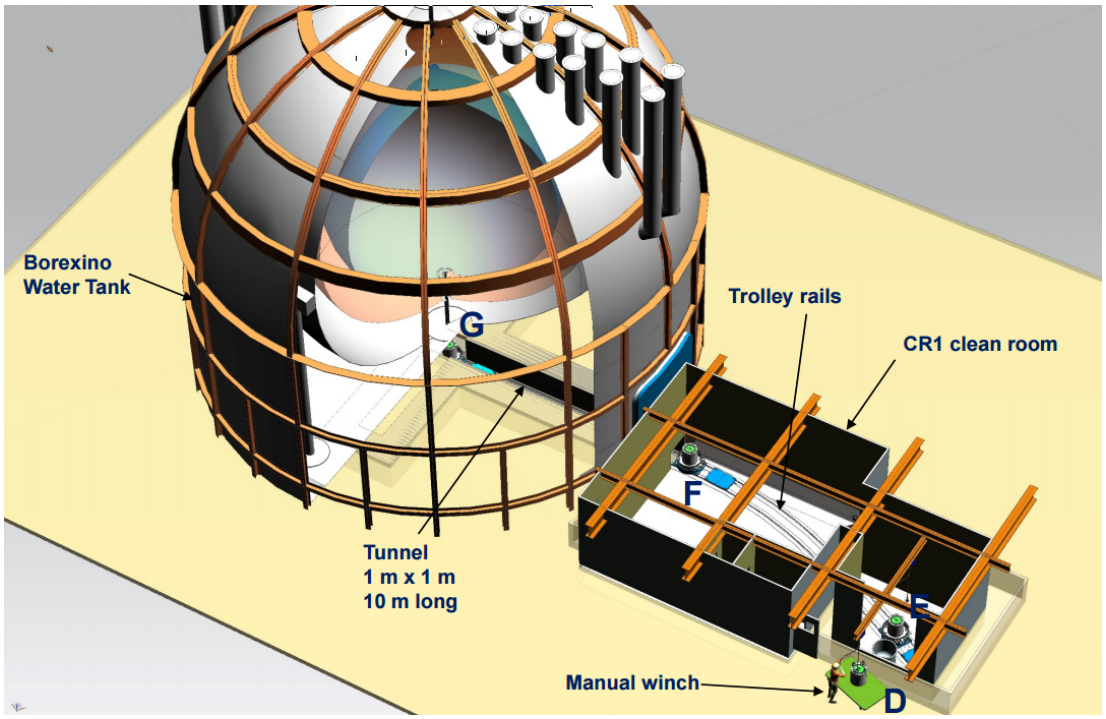

Figure 2.4: A drawing of Borexino with the antineutrino source. Beneath Borexino one can find a tunnel ("the pit"), which is 10 m long and has a cross section of $1 \times 1\,\mathrm{m}^2$. A rail-system allows to move the source from the clean room next to Borexino, where its activity is measured through calorimeters, into the measurement position 8.5 m directly below the detector's center.

Figure 2.5: The insertion of a source mockup into a calorimeter in the clean room (left) and the pit with the rail system (right).

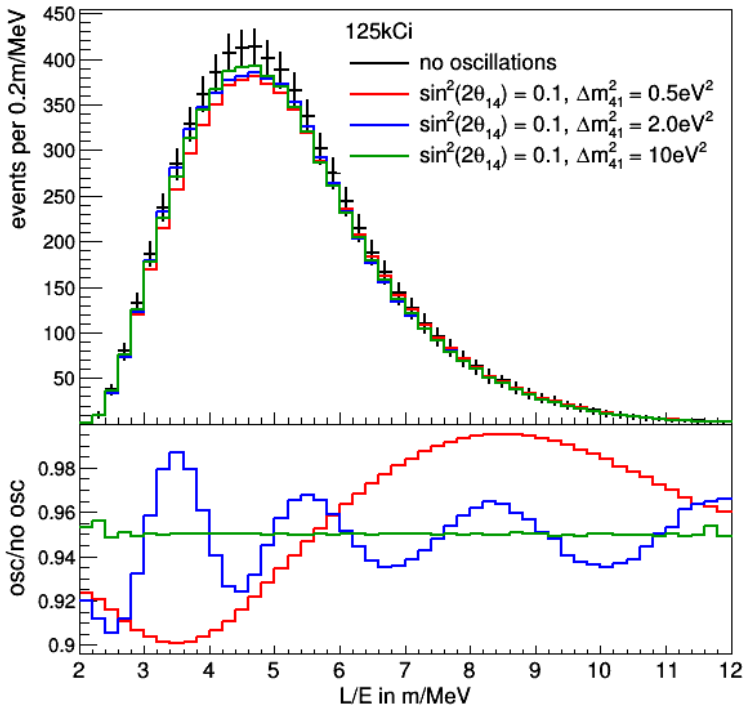

Figure 2.6: The expected oscillation signal in SOX for a 125 kCi (4.6 PBq) source for a sterile neutrino with a mixing angle $\sin^2(2\theta_{14}) = 0.1$ and different masses (Δm^2_{14} between 0.5 and 10 eV^2) as a function of L (distance from the source) over E (neutrino energy). In the top plot the total number of events is shown. The general shape of the histogram is determined by the spherical shape of the detector and the neutrino flux, which is quadratically decreasing with L. In the lower plot one can see the ratio of the signals with oscillations to the signal without any sterile neutrino. For large masses an oscillation is not visible since its period is too short. Instead a reduced rate is observed [Neu16].

^{144}Ce-^{144}Pr anti-neutrino source with an activity of several PBq at the KamLAND detector in Japan [CFL$^+$11, G$^+$13]. The only institution capable of producing such a source was identified to be the Mayak production association in Russia. This project, called CeLAND, could not be realized due to regulatory issues of the souce transportation from Russia to Japan. At the same time the Borexino collaboration explored the possibility to use their detector for a short distance oscillations experiment. These parallel efforts converged in the SOX project. An early concept was published in [SOX13], where it was still discussed to also use a ^{51}Cr-source and place the ^{144}Ce-^{144}Pr-source within the detector. Finally it was decided to use at first a ^{144}Ce-^{144}Pr anti-neutrino source with an activity of 5.5 PBq and to place it in 8.5 m distance directly below the detector center in a small tunnel ("the pit"). The pit has a cross section of $1 \times 1\,\mathrm{m}^2$, and is 10 m long. Beneath the detector center perpendicular tunnels go in both directions for 5 m, giving the pit overall the shape of a "T". A scheme of Borexino with the source is shown in figure 2.4. The source is placed on a carriage such that in can be moved on a rail system into the pit (see figure 2.5). Details about the anti-neutrino source can be found in section 2.3. A ^{51}Cr source would have been an option for a second measurement phase in case the signature of a sterile neutrino was detected.

In case of the existence of a sterile neutrino an oscillation could be observed in space and energy, i.e. the detection rate in the active volume of Borexino would vary depending on the vertex position and neutrino energy apart from geometrical effects. A comparison of the rate in space and energy without and with a neutrino signal ($\Delta m^2_{14} = 0.5 - 10\,\mathrm{eV}^2$, $\sin^2(2\theta_{1,4}) = 0.1$) is shown in figure 2.6. An observation of these so-called wriggles would be smoking-gun signal, i.e. only explainable by a sterile neutrino. Looking for the wriggles is done via a shape analysis. If the sterile neutrino has a larger mass such that the oscillation length becomes too short to be resolved (either due to the detector resolution or because it is washed out due to the source extension) or if the mass is smaller and the oscillation length exceeds the detection volume's diameter, the sterile neutrino signal is more subtle because it appears as an overall reduction of the rate. To perform a rate analysis one has to know the activity of the source and the spectral shape of the neutrino energy. The activity is measured by determining the decay heat generated in the source with thermal calorimeter, as discussed in detail in 2.4. The determination of the source spectrum is presented in section 2.5.

SOX was planned to run for 1.5 years, which is about 2 half-lives of ^{144}Ce. With a 150 kCi (5.5 PBq) source 8638 $\overline{\nu}_e$-events are expected. This quite low number of events is a limiting factor of SOX's sensitivity for a sterile neutrino signal. Much higher statistics could be obtained in other experiments that search for sterile neutrinos in the flux from a nuclear reactor. However, the advantage of SOX is that the detection is background-free and the systematics of Borexino are well understood.
The analysis of the $\overline{\nu}_e$-events can be divided into two components: the shape analysis, where one is studying the relative number of events with respect to L/E, i.e. is looking for wiggles. The other approach is the rate analysis, where one is interested in the total rate to search for a reduced rate caused by the oscillations. In the end, of course both methods are combined to maximize the sensitivity. A plot of SOX's projected sensitivity is shown in figure 2.7[2]. The bands mark the region covered by a source with an activity between 100 and 150 kCi by a rate analysis, a shape analysis or a combined analysis. One can see that the rate analysis is excelling at large Δm^2_{14}, while

[2]The sensitivity study and the plots were done by Birgit Neumair at TUM. A part of this work was published in [Neu16]

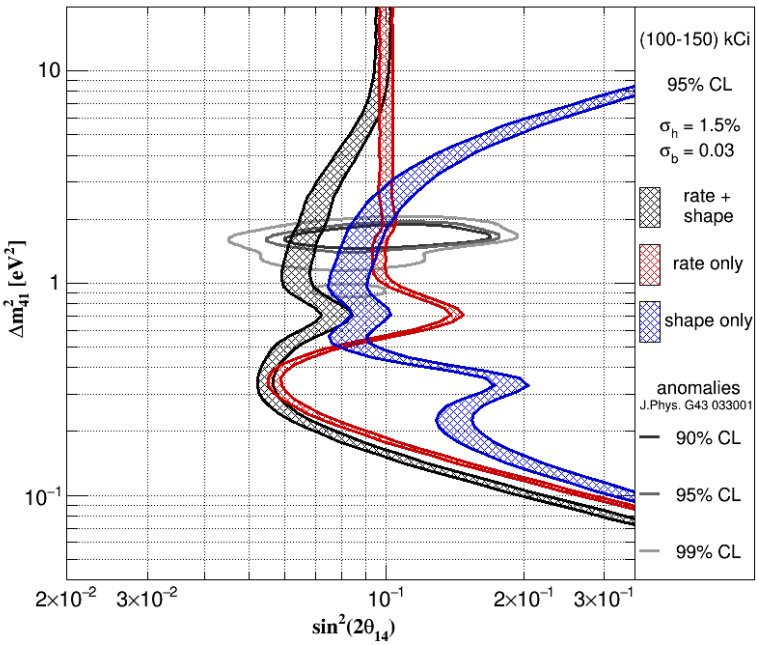

Figure 2.7: The sensitivity of SOX for a rate analysis (red), a shape analysis (blue) or a combined analysis (black). The bands mark the sensitivity for a source activity between 100 and 150 kCi. One can see that the rate analysis is excelling at large Δm^2_{14}, while the shape analysis increases the sensitivity at $\Delta m^2_{14} \sim 1\,\mathrm{eV}^2$, where several periods of an oscillation would be visible in the detector. With the combined analysis the parameter space, where the anomalies suggest a sterile neutrino, is almost completely probed [Neu16].

the shape analysis increases the sensitivity at $\Delta m^2_{14} \sim 1\,\mathrm{eV}^2$, where several periods of an oscillation would be visible in the detector (see figure 2.6 for $\Delta m^2_{14} = 2\,\mathrm{eV}^2$). With the combined analysis and a 150 kCi source the 90% confidence level region found by fitting the anomalies (see section 1.8.1) with a sterile neutrino hypothesis is almost completely covered.
Some systematic uncertainties that limit the sensitivity are the shape of the neutrino spectrum, which is depending on an unknown shape-factor parameter b (see section 2.3 and 2.5), and the knowledge of the source activity, which will be calculated from a measurement of the decay heat. Figure 2.8 shows the sensitivity of SOX in a combined rate and shape analysis for different uncertainties of the parameter b (σ_b), but an perfectly measured source heat. One can see that one requires a measurement of the shape factor, if the anomaly region should be probed, as it will be further discussed in section 2.5. Figure 2.9 shows the sensitivity for different uncertainties of the heat measurement (σ_h), but a well known spectrum. In case of an infinite uncertainty the activity of the source is not known at all such that one can only do a shape analysis. Indeed, the corresponding sensitivity is similar to the one shown in figure 2.7 for the shape analysis. To cover the anomaly region in the parameter space, one has to measure the heat with 1% accuracy, which sets the design goal for the thermal calorimeters, as further discussed in section 2.4.

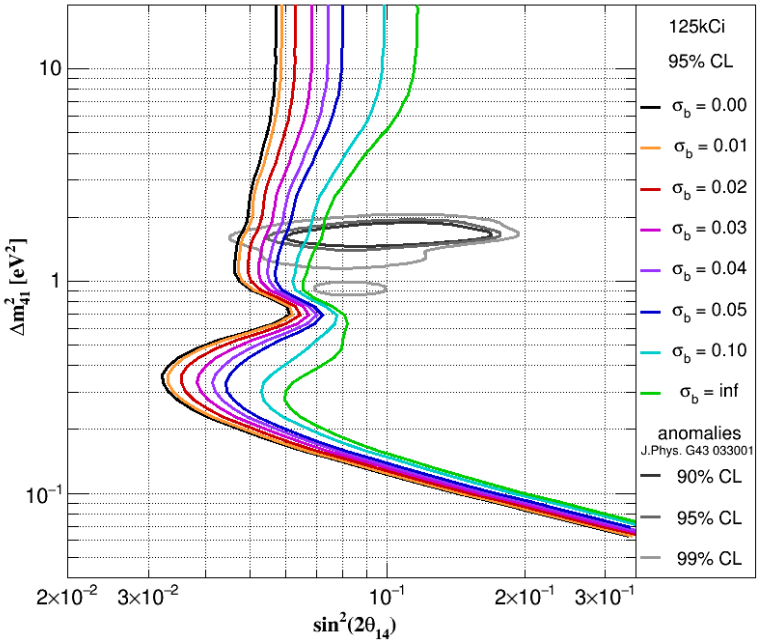

Figure 2.8: SOX's sensitivity in case of an uncertain shape factor parameter b that affects the neutrino spectrum. The parameters space where the existence of a sterile neutrino is suggested by an analysis of the anomalies can only be probed, if σ_b is small. Since previous measurements and calculations of this parameter are not in agreement, a new measurement is required as discussed in section 2.5. The sensitivity study was done by Birgit Neumair at TUM.

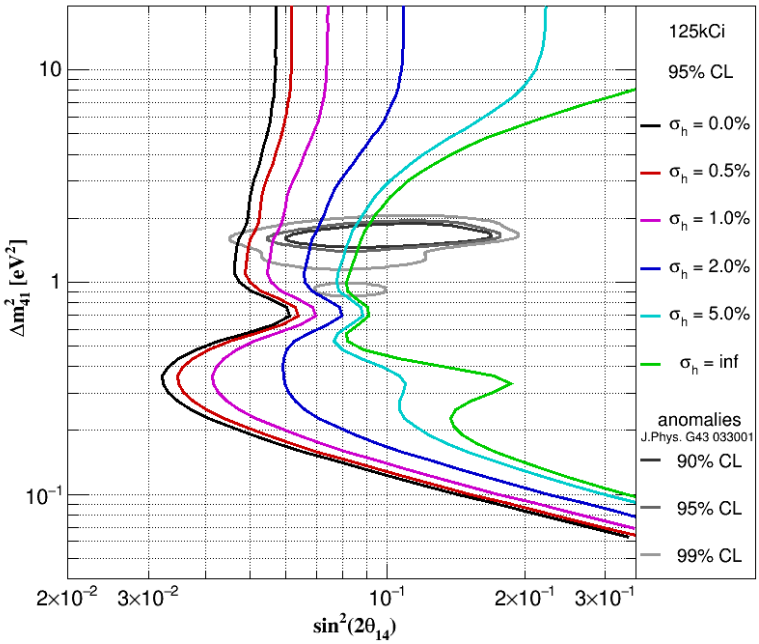

Figure 2.9: The sensitivity of SOX for different uncertainties σ_h of the decay heat that allows us to calculate the source activity. To cover the anomaly parameter space, the calorimeters have to measure the heat with an accuracy better than 1% (see section 2.4). The sensitivity study was done by Birgit Neumair at TUM.

2.3 The antineutrino source

The requirements for the SOX neutrino-source are the following:

- β^--decay with a decay energy Q_β larger than 1.8 MeV to allow the detection of the $\overline{\nu}_e$ in Borexino through the inverse beta decay (IBD);
- an activity of > 100 kCi (3.7 PBq) such that enough data are collected within ~ 1.5 years to ensure a sensitivity for sterile neutrinos that covers the region of the parameter space which is motivated by the anomalies. Several thousand events are necessary to achieve this;
- the lifetime of the isotope has to be long enough to allow the production and transport of the source, which is expected to take several months;
- a high purity that limits the neutrino luminosity from other isotopes and ensures that no significant neutron flux is produced that would lead to an increased background in Borexino and complicate the handling of the source;
- the $\overline{\nu}_e$-spectrum has to be well understood. This is important firstly for the calculation of the activity from the calorimetric measurement, where the mean decay energy (which depends on the spectral shape) has to be known, and for the analysis of the energy dependent oscillations;
- the source has to be small such that oscillations at short lengths are not washed out. In addition it has to fit together with its biological shield into the pit beneath the detector.

The requirement of a decay energy $Q_\beta > 1.8$ MeV and a lifetime of a few month or larger is contradictory, as the decay rate is scaling with the decay energy [CFL+11][3]. As a consequence the source has to consist of a pair of isotopes, where the first isotope has a long life-time and decays into a short-lived isotope with a large decay energy. The most suitable isotope is ^{144}Ce together with its progeny ^{144}Pr, which are both subjected to β^--decay. ^{144}Ce has a half-life of 285 days (lifetime $\tau_{144\text{-Ce}} = 411$ d) that is in the same order as one would expect the duration of a radiochemical source production to be. It decays according to the scheme in figure 2.10 into three different levels of ^{144}Pr with a maximum energy of 0.3 MeV that does not exceed the IBD threshold. However, directly after the Ce-decay, the daughter nucleus ^{144}Pr decays with an half-life $T_{1/2}$= 17 min and with an Q-value of 3 MeV, allowing the inverse beta decay for the emitted $\overline{\nu}_e$. The decay chain then ends at the stable ^{144}Nd. The ^{144}Pr-decay scheme is shown in figure 2.11. A lot of transitions are possible, but only three have branching ratios that are significantly large such that they have to be considered in our application.
Other isotope pairs that fulfill the requirements are ^{106}Ru-^{106}Rh (Q_β(Rh) = 3.54 MeV), ^{90}Sr-^{90}Y (Q_β(Y) = 2.28 MeV) and ^{42}Ar-^{42}K (Q_β(K) = 3.52 MeV). ^{106}Ru and ^{90}Sr are produced in nuclear reactors as ^{144}Ce, however, the chemical extraction of ^{106}Ru is difficult and ^{90}Y (daughter of ^{90}Sr) has a lower Q_β than ^{144}Pr, such that ^{144}Ce-^{144}Pr was deemed most suitable for the antineutrino source [CFL+11].
Another option for the source would be the chromium isotope ^{51}Cr. This isotope does not emit $\overline{\nu}_e$, but mono-energetic ν_e through electron capture. The detection of the

[3] This can be easily seen when the decay rate is calculated according to the Fermi-theory of β-decay, see for example [MK02]. The rate is the integral of the β-spectrum over all possible electron energies. It thus scales with the maximum decay energy (Q-value), assuming constant Fermi functions and matrix elements. In other terms, the Q-value is proportional to the available phase-space, which in turn determines the decay probability.

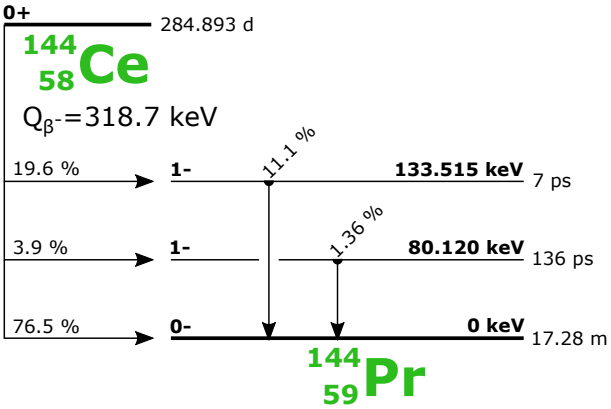

Figure 2.10: A simplified ^{144}Ce level scheme, showing branching ratio, spin, parity, energy and half-life of each level as well as the relative intensities of γ-rays. With an endpoint of $Q_\beta = 319\,\text{keV}$ this decay is not contributing to the neutrino flux detected via inverse beta decay, which has a threshold of 1.8 keV. The isotope's half-life is with 285 days long enough to allow the production of a highly active source. See e.g. [Fir96] for a complete level scheme.

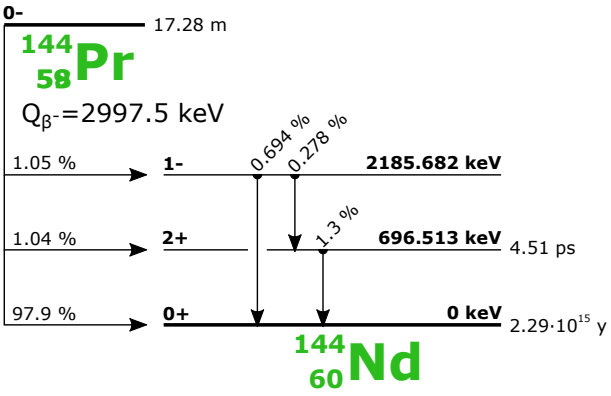

Figure 2.11: A simplified ^{144}Pr level scheme, where the dominating decay branches are shown. See e.g. [Fir96] for a complete level scheme.

	Q-Value [keV]	Branching ratio	Spin and parity	Classification
^{144}Ce branch 1	318.7	76.5%	$0+ \rightarrow 0-$	first-forbidden non-unique
^{144}Ce branch 2	238.6	3.9%	$0+ \rightarrow 1-$	first-forbidden non-unique
^{144}Ce branch 3	185.2	19.6%	$0+ \rightarrow 1-$	first-forbidden non-unique

Table 2.1: The ^{144}Ce decay branches with their transition characteristics.

	Q-Value [keV]	Branching ratio	Spin and parity	Classification
^{144}Pr branch 1	2997.5	97.9%	$0- \rightarrow 0+$	first-forbidden non-unique
^{144}Pr branch 2	2301.0	1.04%	$0- \rightarrow 2+$	first-forbidden unique
^{144}Pr branch 3	811.8	1.05%	$0- \rightarrow 1-$	allowed

Table 2.2: The main ^{144}Pr decay branches with their transition characteristics.

emitted ν_e in Borexino via elastic scattering off electrons is not distinguishable from solar neutrinos and Compton scattering from background processes, requiring a higher activity of the source (in the order of MCi) than for ^{144}Ce-^{144}Pr. A chromium source would have been ready later than the ^{144}Ce-^{144}Pr source such that it was decided to commence the SOX project with the latter. In case the sterile neutrino signature would be observed by SOX, a second phase of the experiment with a ^{51}Cr-source would have been likely.

In summary, the ^{144}Ce-^{144}Pr source produces neutrinos with a sufficient energy thanks to the ^{144}Pr-decay and can be produced with a high activity as it is a commonly produced in nuclear reactors, and it grants a reasonable time for the production due to the large life-time of ^{144}Ce. The dominating decay branches are listed in tables 2.1 and 2.2. One can see, that the 3 MeV-branch of the ^{144}Pr-decay has the largest branching ratio at 97.9%. The transition has no change of angular momentum, but a change of parity, corresponding to a classification of a first-forbidden non-unique transition. The modeling of such transitions is difficult because some approximations (the so-called ξ-approximation) are not accurate, and thus a shape factor is required [Dan68]. The modeling of this shape factor requires the calculation of the nuclear matrix elements, which tend to be very difficult for large nuclei, and results from different groups are not always in agreement. As a consequence it is necessary to measure the β-spectrum of ^{144}Ce-^{144}Pr. This is discussed in greater detail below in section 2.5.
The activity of the source is an important parameter for the analysis in SOX. It will be determined independently with thermal calorimeters that measure the heat released by the radioactive decays. To calculate the source activity from the heat, one needs to know the mean energy per decay, which is also dependent on the spectral shape. Also here the measurement of the shape factor is required to maximize the sensitivity. The calorimetric measurement is further discussed in section 2.4, the development and characterization of a thermal calorimeter is then later a major part of this thesis.

In the following, technical details about the source, its production process and shielding are given. ^{144}Ce is created as a common fission product in nuclear reactors at the level of a few percent and can be extracted from spent fuel rods, if they were stored only for a short period after their removal from the reactor [CFL$^+$11]. The source was ordered from the Mayak Production Association in Russia, the only institution world-wide claiming to be able to produce the required antineutrino generator. The extraction of ^{144}Ce from the fresh nuclear "waste" is done in several steps. In fact, this process is quite complicated, for example it requires to select the proper reactor type and optimize the burning cycle and cooling time to maximize the amount of ^{144}Ce. Here, a simplified summary of the process is given:

- fuel from a VVER-440 reactor is removed after a 4-year cycle and stored in a water pool at the nuclear power plant for at least three years. One ton of the spent nuclear fuel contains then ~ 3 kg of cerium, but only 22.4 g ^{144}Ce which has an activity of 70 kCi. The cerium makes up $\sim 20\%$ of the ~ 13 kg of rare earth elements in the spent fuel [GKST14, KR85];

- the fuel rods are cut into small pieces that are dissolved in an acid. By means of the PUREX-process uranium, plutonium and neptunium are removed from the solution to be recycled for nuclear fuel. The remaining raffinate is highly radioactive waste [GDM$^+$97, BRN$^+$97];

- ^{137}Cs and ^{90}Sr are removed via sorption and the remaining rare earth and transplutonium elements are cleaned from Fe, Ni and Chromium by a chemical process called double oxalate precipitation;

- individual isotopes, including ^{144}Ce are separated through chromatography. The exact process is called displacement complexing chromatography: a column filled by resin grains is loaded with a solution that contains the rare earth and transplutonium elements, which then stick to the resin. Then a so-called displacer is pumped through the column and displaces first the isotope with the weakest adhesion to the resin, then the isotope with the next weakest adhesion and so on [SP54, Fir90, GMC98, KCFP98];

- the obtained cerium is oxidized to create a powder, which is then compressed into pellets that are filled into a hermetic double-walled capsule.

It is obvious that this process to produce a source with the demanded activity requires a very specific infrastructure that is even not common for nuclear reprocessing plants because the separation of radioactive rare earth elements in industrial scales has hardly any market.
A model and drawing of the final source are shown in figure 2.12. The cerium oxide is encased in three individual copper capsules with copper radiators within that help to transport the heat out of the poorly conducting powder. The inner temperature is expected to be lower than 600°C. The three copper capsules are then sealed within two stainless steel cylinders. The entire capsule has a height and diameter of 15 cm. The expected activity of the source at delivery at LNGS was 150 kCi (5.5 PBq).
Since radioactive contaminants in the source could contribute to the heat, the neutrino spectrum and the dose of the SOX personnel, purity constraints were set to the source manufacturer. A first constraint was put on the heat released by impurities, which has to be smaller than 1‰ of the heat released by the ^{144}Ce-^{144}Pr-decay. In addition, concerning the radiation protection, the activities of gamma-emitting impurities have to be

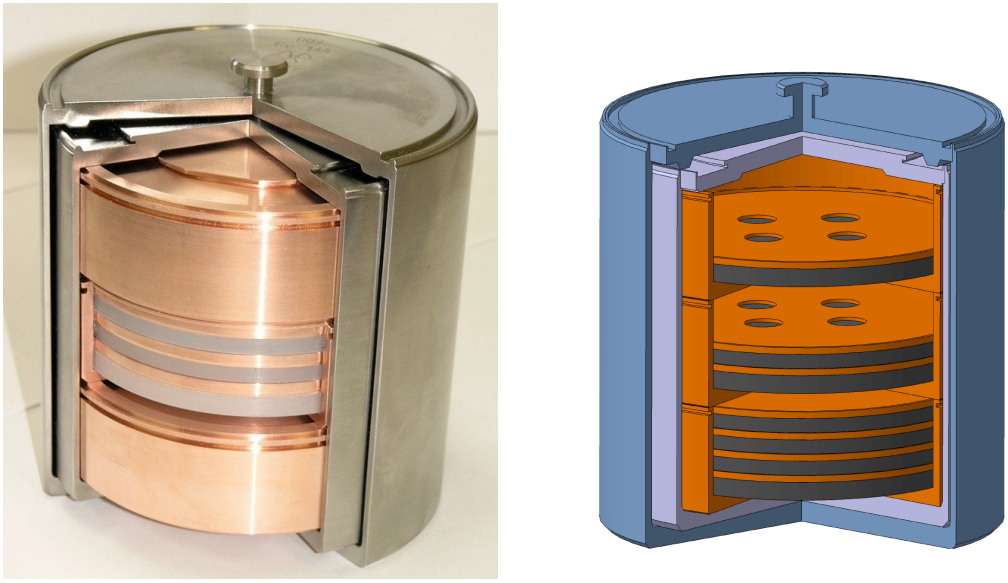

Figure 2.12: The source capsule: to the left a photo of a mockup, to the right a cutaway-drawing. The cerium oxide powder is compressed into pellets that are put into three individual copper capsules with radiators within for helping the heat to escape. The copper capsules are then sealed in a doubled steel cylinder.

smaller than 10^{-3} Bq per Bq ^{144}Ce activity, such that the contributions from contaminants in the source can be neglected for the calculation of the dose. A third constraint was set on the neutron emitter ^{244}Cm by the LNGS administration for scientific reasons to prevent any background source for the other underground experiments close to the Borexino detector: its activity should be at maximum 10^{-5} Bq per Bq of ^{144}Ce activity.

Since the ^{144}Ce-^{144}Pr-decay also produces γ-rays (see the level schemes in figures 2.10 and 2.11), the source has to be encased into a thick biological shield. The requirements for this shield are set by the most energetic gamma ray, which originates from the 2 186 keV deexcitation for the decay branch number 3 in table 2.2 that has an relative intensity of 0.7%. Using a 19 cm thick tungsten shield with a radiation length of about 1.29 cm at 18 g/cm^3 density, an attenuation of $3 \cdot 10^7$ is imposed onto the 2 186 MeV γ-ray. It was calculated by the collaboration that with such a shield the γ-radiation dose from a 5.5 PBq source is less than 120 µSv/h on the surface, and at 1 m distance < 7 µSv/h, which is low enough to allow manual work close to the source for a limited time without exceeding legal exposure limits. The high attenuation also allows the approximation that all the radiation emitted by the ^{144}Ce source is absorbed inside the shield and thus converted into heat, which is important for the calorimetric activity measurement (see section 2.4).
The tungsten shield is produced by Xiamen Tungsten Co., Ltd. in China and actually made of the alloy HWNF50, which is made of 95% tungsten, 3.5% nickel and 1.5% iron. The density of the finished shield was measured to be 18.25 g/cm^3, resulting in a total weight of $\sim$ 2.5 tons. A scheme of this shield is shown in figure 2.13. It is 541 mm high and has a diameter of 538 mm. Access to the inner volume is granted by a massive tungsten plug which is locked by an upper cap. A handling crown with eye-bolts can be screwed on top for moving the shield. Corrosion and drop tests verified the safety of the tungsten alloy. The drop test was performed to ensure that the shield can resist a fall from 3 m height, which is important for the removal of the source from the transport container at LNGS, where it has to be lifted with a crane. A photo of the shield at

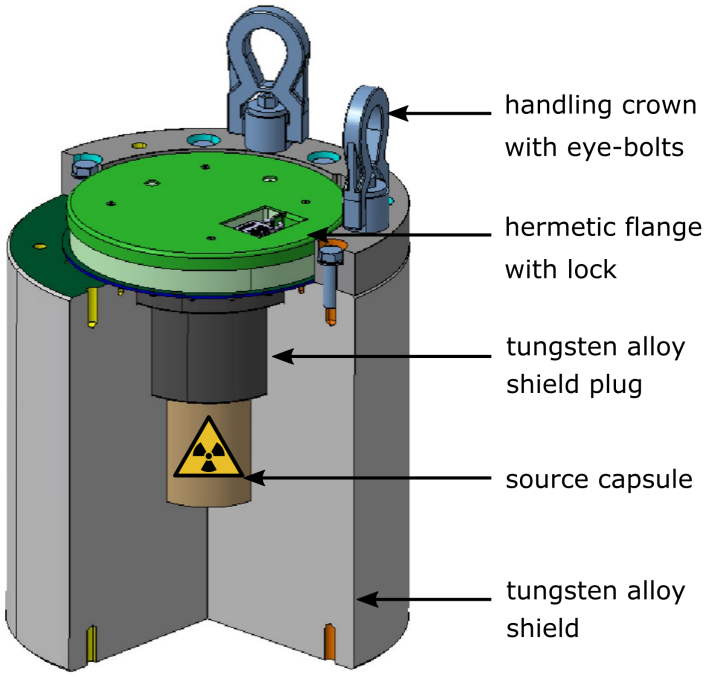

Figure 2.13: A scheme of the tungsten alloy biological shield.

LNGS is shown in figure 2.14.

2.4 The source activity determination with thermal calorimeters

In the SOX project the experimental sensitivity to the sterile neutrino oscillations depends critically on the accurate knowledge of the ^{144}Ce-^{144}Pr source activity and of the spectral energy distribution of the anti-neutrinos emitted in the decay (see figures 2.8 and 2.9). The determination of the activity could be done by direct γ-spectroscopy or by a calorimetric measurement. However, the former is not feasible due to safety reasons (the measurement would have to be done without the biological shield) and would probably not meet the requirement to measure the source activity with 1% accuracy. It was therefore decided to follow the calorimetric approach. If the β-spectrum and thus $\langle E \rangle$, the heat released on average by each individual decay of ^{144}Ce and the daughter isotope ^{144}Pr, are well known, the measurement of the thermal power P yields naturally a measurement of the activity A:

$$A = \frac{P}{\langle E \rangle}. \tag{2.2}$$

The decay heat is expected to be 218 W per PBq activity (see table 2.3 in section 2.5), thus a 5.5 PBq source will generate about 1200 W of heat.
Two thermal calorimeters were constructed that measure the heat released by the source through the temperature increase of a fluid. The redundancy of the calorimeters is due to the historical development of SOX as an union of the two different sterile neutrino projects at KamLAND and Borexino. Because of the high importance of an accurate activity measurement, the redundancy was maintained for SOX. One calorimeter was designed and built by CEA Saclay, of which a scheme is shown in figure 2.15. The

Figure 2.14: The tungsten alloy shield at LNGS during a source handling test.

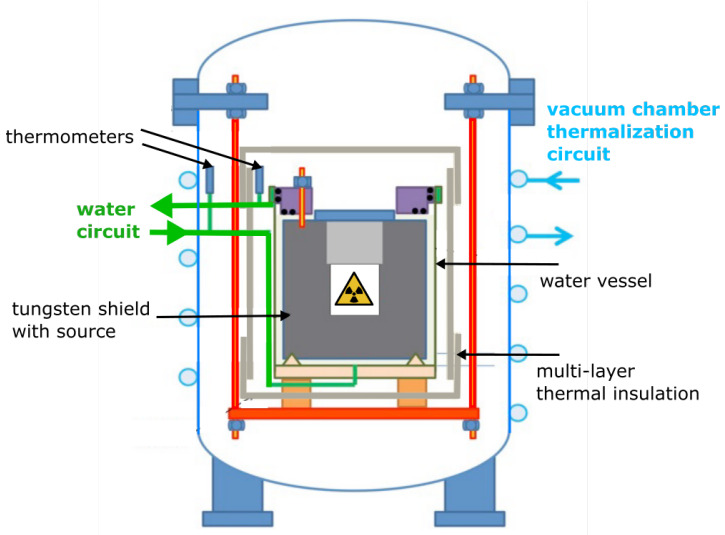

Figure 2.15: The CEA calorimeter. The source is submerged together with its shield in a bath where degassed water is steadily flowing through. The heat of the source is measured by the temperature increase of the water. To avoid heat losses the vessel is placed in a vacuum. It is thermally decoupled from the environment through a long suspension structure and a multilayer insulation that blocks thermal radiation. A secondary water circuit allows to heat up the vacuum chamber to minimize heat gradients for heat loss suppression.

other calorimeter was a joint development of Technical University of Munich and INFN Genova and is called TUM-Genova calorimeter. A major part of this thesis is about the development and calibration of this calorimeter (see chapters 3 to 5). The calorimetric measurements would have been performed in the Borexino clean room before and after the insertion of the source into the tunnel under the detector. After arrival of the source, the first measurement would have been done with the CEA calorimeter, and directly afterwards a second measurement with the TUM-Genova calorimeter was planned. During SOX data taking the source would remain in the TUM-Genova calorimeter, which is mounted on a carriage and can be moved into the pit. Due to the size constraints the vacuum chamber and a few other components have to be removed before moving the setup into the pit, but a low precision measurement can be continued anyways. Also, the water circuit of the calorimeter has to be maintained to cool down the source.
The calorimeters were designed to measure the activity with an uncertainty smaller than 1%. This means that one has also to consider the uncertainty of the power-activity conversion, which is due to an error on the mean energy per decay $\langle E \rangle$ caused by an uncertain shape factor of the ^{144}Pr-electron spectrum. Since previous measurements and calculations of the spectrum are not in agreement, a new effort to determine the shape factor is necessary, as described in the next section. With the proposed spectrometry the uncertainty on the power-activity conversion would be a few per-mill. As it is later reported in chapter 5, the TUM-Genova calorimeter can determine the heat with 0.2% uncertainty, guaranteeing that the 1% accuracy goal on the activity can be achieved.

At this point it is interesting to look how thermal calorimeters are used in science and technology and how the previous experiments SAGE and GALLEX determined their source activity:

- **SAGE / GALLEX:** the experiments that lead to the "gallium anomaly" are the radiochemical solar neutrino detectors SAGE and GALLEX, which were calibrated with ^{51}Cr (SAGE and GALLEX) and ^{37}Ar-sources (only SAGE). The strength of these ν_e-sources was measured (independently from the neutrino flux) in the following way:

  - to determine the activity of a 517 kCi ^{51}Cr-source SAGE used a thermal calorimeter with thermopile sensors that convert the decay heat ($\mathcal{O}(100\,\mathrm{W})$) into electricity. The uncertainty of a single measurement was 2%. This error was reduced by fitting the decay function to multiple measurements. The calorimetric measurement was cross checked by direct counting of the γ-radiation and by mathematically modeling the process of chromium irradiation at the Aktau fast-neutron reactor [A$^+$99]. The total uncertainty of the activity was found to be 1.2%.
    For a second calibration with a 409 kCi ^{37}Ar source (initial strength) the same calorimeter was used. The activity could still be measured quite precisely (0.5% uncertainty) in combination with other measurements, as of the gas volume and isotopic composition of the argon and direct counting [A$^+$06].
  - GALLEX was calibrated two times with ^{51}Cr-sources, whose activity was determined by combined measurements in a similar fashion as for SAGE: through γ-counting of source samples, by a thermal calorimeter that measures the rate of heat increase in an isolated chamber (9% uncertainty for

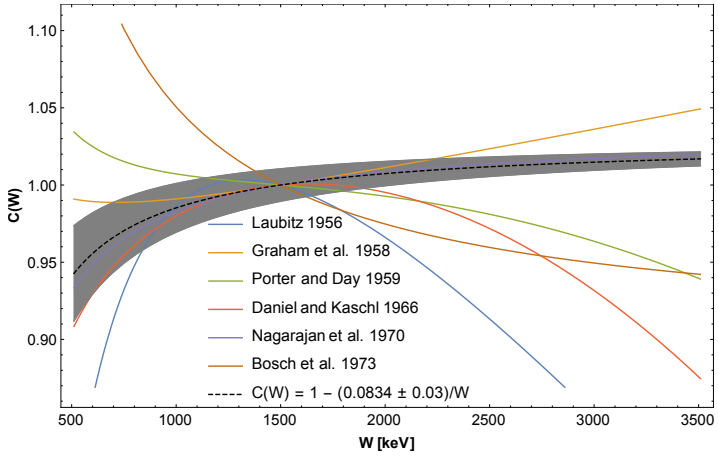

Figure 2.16: The different measured shape factors for the ^{144}Pr main branch from the literature ([Lau56, GGE58, PD59, DK66, NRVR71, BBC$^+$73]) and one calculated by Juoni Suhonen (black dashed line) together with an error band, as it could be achieved with a new measurement. As one can see, a new measurement is required since the previous ones are not in agreement.

the second calibration), by measuring the content of the stable chromium progeny ^{51}Va after the source almost completely decayed, and via a measurement of the neutron flux at the Siloé reactor at CEA Grenoble and mathematical modeling. The activity was found to be 63.4 ± 0.5 PBq (1.7 MCi) for the first source, and 69.1 ± 0.6 PBq (1.9 MCi) for the second, the uncertainty of the activity was between 0.8 and 0.9% [A$^+$95, HHK$^+$14].

- **Nuclear waste characterization:** nuclear waste is stored differently depending on the generated decay heat. Calorimeters are used (or in development) to characterize low level nuclear waste with a heat generation in the order of µW [GJGM18] as well as highly radioactive waste, where a package produces several hundred Watt of heat [RFB$^+$18]. The measurement uncertainties of calorimeters used for this application are with a few % too large for SOX.

- **Isothermal microcalorimeters:** these instruments are used in laboratories to measure the heat produced in chemical, biological or physical processes, e.g. to measure the metabolism of cells [BWGD10] or to determine the activity or mean energy of radionuclide samples [Gun64, Col07]. Typically the heat, which can be less than a µW or as large as ∼1 W, is measured with a thermoelectric device. Microcalorimeters accept samples with dimensions in the order of cm. Obviously these devices are not suitable for SOX.

This is not a complete list, but it should illustrate that the measurement of several hundred Watt of heat emitted in a large source with a sub-percent accuracy is not a common practice and requires a novel approach and R&D efforts.

2.5 Spectral measurements of the ^{144}Ce-^{144}Pr source

The experimental sensitivity to refute or to discover sterile neutrino oscillations depends critically on the accurate knowledge of the ^{144}Ce-^{144}Pr source activity and of the spectral energy distribution of the $\overline{\nu}_e$ emitted by the ^{144}Ce progeny ^{144}Pr (see figures 2.8 and 2.9). As mentioned in section 2.3 the main decay branch of ^{144}Pr (0-) to the ground

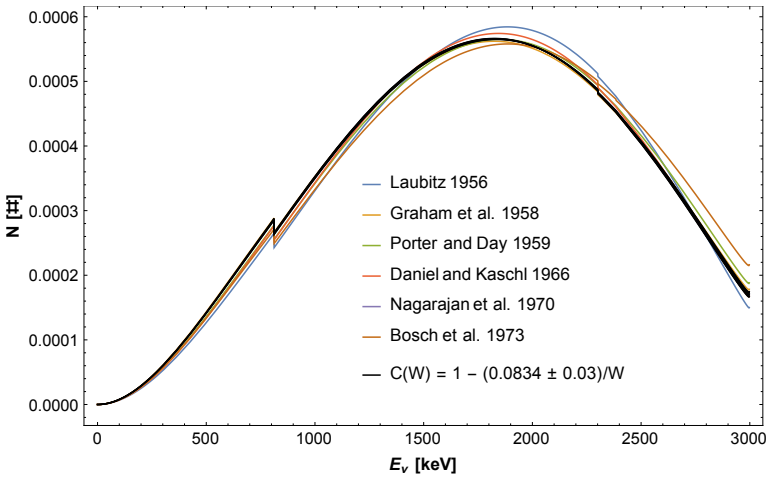

Figure 2.17: Neutrino spectra, modeled with the different shape factors. The large spread causes an error on the mean energy per decay that affects the calculation of the activity from the calorimetric measurement, and also on the interaction rate within Borexino, thus affecting the analysis in two ways. The black band shows the calculated shape factor together with the expected measurement uncertainty of the PERKEO III project.

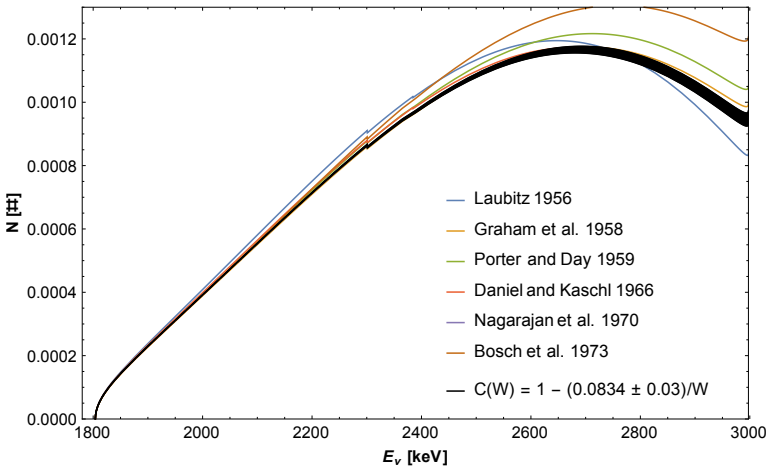

Figure 2.18: The neutrino spectra multiplied with the IBD cross section, i.e. the positron spectra for different shape factors. Due to the E^2-dependence of the cross section, the initial spread of the neutrino spectra (see figure 2.17) is increased even more. The integral of these curves is proportional to the $\overline{\nu}_e$-detection rate in Borexino. The uncertain shape factor causes a rate uncertainty of 9%.

state of ^{144}Nd (0+) is a first-forbidden non-unique transition. Its spectral shape deviates from the allowed one by a shape factor $c(W) = 1 + b/W$, with the total energy W and a parameter b accounting for the first-forbidden character of the decay. The shape factor was measured between 1956 and 1973 by several groups with contradictory results [Lau56, GGE58, PD59, DK66, NRVR71, BBC$^+$73]. For SOX, J. Suhonen carried out a theoretical nuclear structure calculation[4] and derived $c(W) = 1 - 0.0843\,\mathrm{mc}^2/W$. Biases or uncertainties of the theoretical calculations are difficult to asses, thus requiring experimental precision measurements. The different shape factors are plotted in figure 2.16, showing the large spread.

In the following, we consider the shape factor of Suhonen, $b_{\mathrm{Suh}} = 0.0843$ as benchmark value. As explained further below in detail, a new measurement campaign was planned, where the targeted experimental uncertainty of b was $\sigma_b = 0.03$ (absolute). The uncertainty of the shape factor affects the sensitivity of SOX in two ways: it imposes an uncertainty on the cross section for the neutrino detection in Borexino, and it causes an error when calculating the source activity from the decay heat. To assess the size of the uncertainties, the spectra were modeled according to the Fermi-theory and with an approximated Fermi-function from [SV83] and then modified with the different shape factors. Details about these calculations can be found in the Master's thesis [Alt15].
The calculated electron anti-neutrino spectra, which are the mirrored beta spectra, are displayed in figure 2.17 for the different values for the shape factor found in the literature. The discontinuities in the anti-neutrino spectrum at 812 keV and at 2301 keV are due to the beta decays to excited states in the daughter isotope ^{144}Nd, see table 2.2. Given the E^2-dependence of the cross section for the inverse beta decay (IBD), uncertainties of the shape factor have a strong impact on the positron energy spectrum and the integral interaction rate. The positron spectrum, which is similar to the interaction rate per energy interval, is calculated by multiplying the neutrino spectrum N_ν with the IBD cross section σ (see [Alt15]). These spectra are shown in figure 2.18. The black line corresponds to the benchmark value b_{Suh} and its width to the target experimental uncertainty of the new measurement. Taking the contradicting literature values of the shape factor b at their face values, one obtains a difference in the interaction rate (the integral of the positron spectra) of 9%, far beyond the 1% accuracy targeted for the SOX experiment.
Concerning the other impact of the shape factor in the SOX analysis, the heat-activity conversion from the calorimetric measurements, one can calculate that the thermal power release per PBq activity ranges from 213 to 220 W for the different literature values of b.

In summary, the unknown shape factor enters twice in the overall rate uncertainty: first in the determination of the source activity from the measurement of the generated heat by the ^{144}Ce-^{144}Pr source, and second, through energy dependence of the IBD cross section. Consequently, a new measurement of the shape factor is necessary for SOX. Several exploratory measurements were performed that could not determine the shape factor with a satisfying accuracy. These measurements are listed in the following:

- TUM: in a setup developed at Technical University of Munich a thin source sample is placed above a plastic scintillator detector with an PMT. A multi-wire-chamber in between source and scintillator helps to veto photons from the β-particles. The analysis of the data was not continued after the cancellation of SOX;

[4] J. Suhonen, University of Jyväskylä, Finland, priv. communication to S. Schönert, 2015

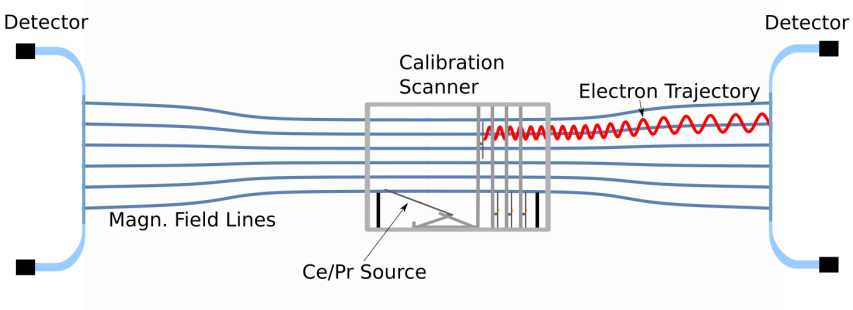

Figure 2.19: A scheme of the spectrometer based on PERKEO III. The source is placed in the center of an elongated vacuum chamber together with calibration sources. A magnet guides the electrons to a plastic-scintillator detector. In case of backscattering the electrons can be detected by a second detector at the other end of the chamber.

- CEA: another measurement was prepared at CEA Saclay, using two plastic scintillator detectors in a "sandwich"-configuration around the source. The source is dissolved in a liquid that is filled in a small drilled hole into the scintillator. A publication of the results is in preparation;
- Moscow: calculations of the ^{144}Pr-spectrum were performed alongside with measurements at Kurchatov Institute and MEPhI in Moscow, again with a plastic scintillator. Final results on the shape factor were not published due to uncertainties in the setup's response function [AKL$^+$17];
- Saint Petersburg: instead of a scintillator, the spectrometer at Petersburg Nuclear Physics Institute uses semiconductor detectors. A large Si(Li)-detector absorbs the electrons, and a second thin Si(Li)-detector is used to detect coincidences for background-rejection. The setup was also used for a sterile neutrino search in the 0.01-1 MeV mass range in the ^{144}Ce-^{144}Pr decay spectrum [DDL$^+$18]. Due to a not understood detector response a measured shape factor was not published.

The project proposed to measure the shape factor with an unprecedented accuracy was based on the PERKEO III spectrometer [MAD$^+$09], which is used to study deviations of the neutron decay spectrum as for example predicted by the Fierz-interference term. The expected shape distortion is similar to the form of the ^{144}Pr-shape factor. Results from this project indicated that the uncertainty of $\sigma_b = 0.03$ can be achieved for the ^{144}Pr-measurement [Sau18]. The spectrum would be measured in the range from 400 to 1500 keV. This project was described in a proposal[5] to request funding from ANR and DFG, which unfortunately was denied.
The setup consists of a large vacuum chamber with a very thin source sample in the center. Strong magnets (normal-conducting) are placed around the chamber whose fields guide the emitted electrons to a scintillating detector. The maximum field strength is 0.15 T. To reduce the systematic impact by backscattering the field decreases adiabatically to 0.09 T at the detector such that the electrons' maximum incident angles are reduced from 90° to 50°, which lowers the backscattering probability. In addition, a second detector is placed at the other end of the spectrometers to detect backscattered electrons, if they were not reflected before on the magnetic field gradient. A drawing of the setup is shown in figure 2.19.
One has also to consider that the two other decay branches to exited states of ^{144}Nd

[5] ANR-DFG 2016 NLE proposal "Precision measurements of the ^{144}Pr electron anti-neutrino spectrum for sterile neutrino search in CeSOX"

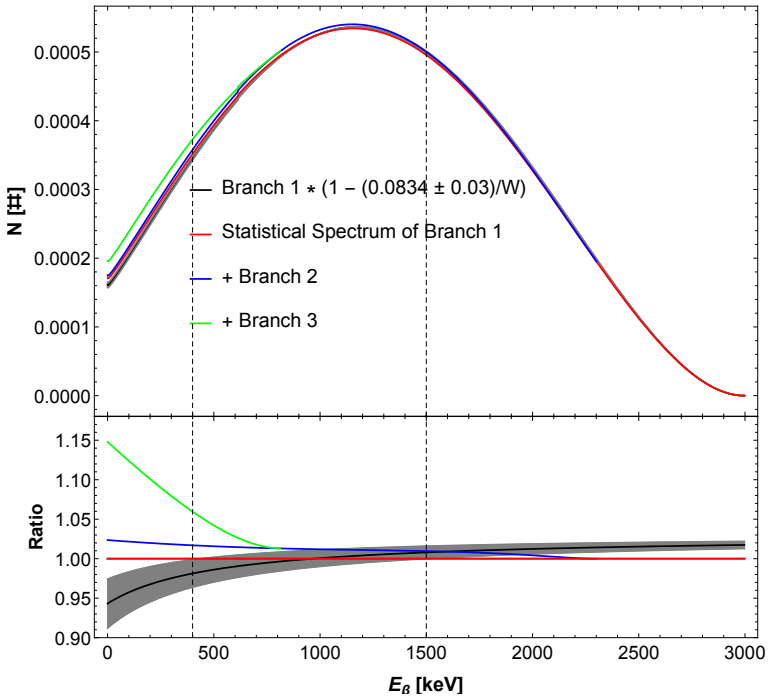

Figure 2.20: The top plot shows the different branches of the ^{144}Pr-decay. On the bottom the ratio of the branches with respect to the statistical spectrum without any shape factor are shown. One can see that the decay branches distort the spectrum by the same amount as the shape factor (calculated by Suhonen), thus these branches have to be measured and considered in the analysis as well. The energy region for the measurement is marked by the dashed vertical lines.

(see table 2.2 on page 41) could interfere with the determination of the shape factor. How these decay branches affect the spectrum is shown in figure 2.20. The branches to the excited states have an impact of similar size as the expected shape factor, however with an opposite sign, thus they could mimic a statistical shape (a spectrum without shape factor) if not considered in the analysis. To measure all three dominant decay branches, an additional set of detectors would be placed close to the source in order to detect the gammas from decays to exited states. Preparatory background measurements and a study to determine whether CsI-scintillator detectors are fast enough to be used in the gamma-tagging array instead of the much more expensive $LaBr_3$-detectors were conducted, as described in section 2.5.1.
In addition the project included also the production of a very thin source, the measurement of the ^{144}Pr γ-lines, and the determination of the branching ratios to cross-check literature values.

With the proposed measurement of the shape factor parameter b with an uncertainty of 0.03 the 1%-accuracy goal on the SOX activity and interaction rate respectively would have been achieved, as shown in table 2.3, where the variation of critical parameters is shown.
The sensitivity of SOX for $\sigma_b = 0.03$ can be found in figure 2.7 on page 37. The uncertainty of the heat / activity in this plot is 1.5% which is more than the expected uncertainty of the actual measurement (heat measurement and heat-activity conversion), because it also contains other Borexino systematics as the error of the fiducial volume size.
In the end, the spectrometry project was canceled after the stop of SOX.

b	$\mathbf{S} = \int \mathbf{N}_\nu \cdot \sigma \mathrm{d}\mathbf{E}$	$\Delta\mathbf{S}/\mathbf{S}$	$\Delta\mathbf{R}/\mathbf{R}$	**decay heat per PBq**
$b_{\mathrm{Suh}} = -0.0843$	$4.609 \cdot 10^{-44}\,\mathrm{cm}^2$	-	-	218.4
$b_{\mathrm{Suh}} + \sigma_b$	$4.643 \cdot 10^{-44}\,\mathrm{cm}^2$	$+0.73\%$	$+0.94\%$	219.0
$b_{\mathrm{Suh}} - \sigma_b$	$4.575 \cdot 10^{-44}\,\mathrm{cm}^2$	-0.74%	-0.95%	218.0

Table 2.3: Uncertainties of critical parameters for SOX considering the determination of the shape factor with an uncertainty $\sigma_b = 0.03$ on the benchmark shape factor parameter b_{Suh}. **S**: inverse beta decay cross section per decay of ^{144}Pr; $\Delta\mathbf{S}/\mathbf{S}$: variation of the predicted interaction rate; $\Delta\mathbf{R}/\mathbf{R}$: variation of the predicted interaction rate taking the uncertainty of the heat-activity conversion from the calorimetric measurement into account. With the proposed accuracy of the spectral measurement the 1%-accuracy goal on the activity / interaction rate can be achieved. In the last column the decay heat per PBq activity is listed. It contains also the energy released by the cerium and assumes that all γ-rays are absorbed within the biological shield.

2.5.1 Detectors for the γ-tagging

A technology that could be suitable for the γ-tagging in the PERKEO-III spectrometer was developed at TUM: an array of CsI-scintillators read out by avalanche photodiodes (APDs) that were designed for the CALIFA calorimeter at FAIR [BGW+15]. These detectors were considered as an option for the γ-tagging array since they were already characterized and are quite inexpensive (in contrast to LaBr-scintillators). Other options, apart from the very fast LaBr-crystals, are high purity germanium detectors. However, their integration into the setup would be very difficult due to their size including a cooling system. The draw-back of the CsI-scintillators is a slow response of the crystal. To detect the electron-γ-coincidence one would then have to use a rather large time window that could lead to a poor signal to noise ratio, if many random coincidences are detected due to the background.
To study this issue preparatory measurements were performed with an CsI-detector array from the CALIFA project. The array consists of 9 individual crystals with the dimensions $3 \times 4 \times 5\,\mathrm{cm}$, each read out by one APD. The goal of the measurements with this detector was to determine the random coincidence rate by measuring the γ-background at the proposed location for the spectrometer in the energy region of the most intense γ-lines of ^{144}Pr which are at 696, 1489 and 2185 keV. Afterwards the time window was determined by emulating the PERKEO plastic scintillator with a NaI-detector and determining the time difference between the detection of coincident events in this detector and the CsI-crystals.
In a first step the detectors were calibrated with ^{22}Na, ^{60}Co and ^{137}Cs sources. From the calibration data also the resolution of the CsI-detector was determined, which is between $\sim$20 and 35 keV in the region of interest. Then the background measurement was carried out at the Physics Department of TUM for 50 minutes without any dedicated shielding. The rates observed in the energy windows of the ^{144}Pr-lines plus / minus the energy resolution (σ), averaged over the 9 crystals, are listed in table 2.4 alongside with the energy resolution.

For the coincidence measurement a ^{22}Na-source was placed between the CsI-detector and a NaI-detector, as pictured in figure 2.21. The ^{22}Na-decay produces positrons, whose annihilation emits two gamma-rays in diametrical directions. By selecting only events at 511 keV, one can search for the detection of a γ-ray pair in both detectors that was emitted from the positron-annihilation. Here the NaI-detector gives the start signal since it is much faster than the CsI-detector. The mean time difference of such

^{144}Pr branch	γ-energy [keV]	energy resolution (σ) [keV]	backgr. rate [s^{-1}]
2	696.5	19.9 ± 1.2	1.89 ± 0.11
3	1489.2	26.9 ± 1.5	0.50 ± 0.06
3	2175.7	33.0 ± 1.8	0.07 ± 0.01

Table 2.4: The dominant transitions to excited states of the ^{144}Pr-decay. For each γ-line the energy resolution (σ) of the CsI-detector was interpolated from calibration data. The background rate was measured in an energy window of the line energy plus / minus the resolution for 50 minutes.

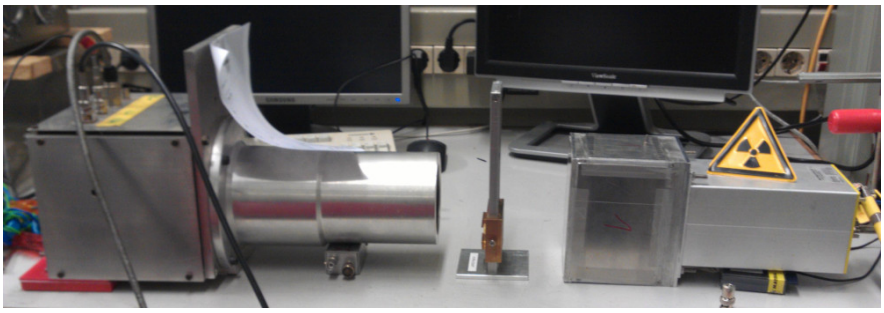

Figure 2.21: The setup for the coincidence measurements with a ^{22}Na-source. The NaI-detector, which gives the start signal, is placed on the left, the CsI detector on the right.

events was found to be ~ 145 ns, which is lower than expected. Now the resulting time difference is used for the window size for the random coincidence calculation. The rate of random coincident r_{rc} events is

$$\Gamma_{\mathrm{rc}} = \Gamma_{\mathrm{plastic}} \cdot \Gamma_{\mathrm{bg}} \cdot \Delta t, \tag{2.3}$$

where r_{bg} is the background rate, r_{plastic} the expected signal rate in the spectrometer's plastic scintillator and Δt the time window, which is assumed to be similar to the time difference measured before. Further it is assumed that the rate in the plastic scintillator is $r_{\mathrm{plastic}} = 3 \cdot 10^3\,\mathrm{s}^{-1}$ and the rate of real coincidences r_{signal} (i.e. a detected electron from branch 2 or 3 in the plastic scintillator and the corresponding γ in the CsI-detector) is $1\,\mathrm{s}^{-1}$, when the branching ratio and the solid angle is considered. In addition for the measurement of the 696 keV-line 80 electron detections are expected in the γ-tagger (these values were used in the proposal for the ^{144}Pr-spectrometry with PERKEO III[6]). Taking the γ-background into account (see table 2.4) one obtains a background rate $r_{\mathrm{bg}} = 82\,\mathrm{s}^{-1}$. The random coincidence rate is then according to equation 2.3 $r_{\mathrm{rc}} = 0.036\,\mathrm{s}^{-1}$. If the signal rate, which is the rate of real coincidences of $1\,\mathrm{s}^{-1}$, is divided by the result, one obtains the signal to background ratio of 28.03, which is larger than the minimum desired ratio of 10. This preparatory measurement thus is encouraging to proceed studying the possibility of a CsI-detector array for the spectrometer. For conclusive results it was planned to do Monte-Carlo-simulations. After all, these efforts became obsolete with the cancellation of SOX.

[6]ANR-DFG 2016 NLE proposal "Precision measurements of the ^{144}Prelectron anti-neutrino spectrum for sterile neutrino search in CeSOX"

Chapter 3

The TUM-Genova thermal calorimeter for SOX

The sensitivity of the SOX project for a sterile neutrino depends on the knowledge of the source activity. The development and characterization of the TUM-Genova calorimeter for the activity determination via a measurement of the decay heat is presented in the next chapters. This chapter gives an overview about the calorimeter concept (section 3.1), thermal simulations that helped us to study the calorimeter's behavior (section 3.2) and the technical configuration of the apparatus (section 3.3). In chapter 4 the analysis of the calorimeter data is explained, and the final results of the characterization and calibration are presented in chapter 5.
The work presented here and in the following chapters was partially published in [ADN+18].

3.1 Concept of the experimental apparatus

The calorimeter was designed with following goals: allow an activity measurement of the antineutrino source with an error smaller than 1 %, while the system is operated in constrained space in the pit below the Borexino detector. The latter requires a compact design for the calorimeter. Thus, the design is strongly dependent on the layout of the antineutrino source, which is described in chapter 2, section 2.3, and the dimensions of the pit. Concerning the source, in the end only the shape of the biological shield is important, which is a cylinder with 538 mm diameter and a height of 618 mm. The complete calorimeter then has to fit into a pit of $1 \times 1\,\mathrm{m}^2$ cross-section.
As discussed in section 2.5, the source is expected to produce 218 W per 10^{15} decays (1 PBq). In the beginning of the SOX project the 5.5 PBq source then produces a power of 1200 W. At the end of the measurement after ∼1.5 years, two half-lives of ^{144}Ce will have passed, such that the power is reduced to 300 W. These values mark the range in which the calorimeter will operate and where the projected accuracy has to be ensured.

It was decided to follow the approach of a flow calorimetric measurement, i.e. the power is measured by the temperature increase of a fluid that flows through a heat exchanger that is directly in contact with the heat source. Another common design for thermal calorimeters are thermo-electric devices, however, the flow calorimetric measurement is preferred because it is neither affected by temperature inhomogeneities on the surface of the source shielding nor by the uncertainty of the thermal conductivity of the materials. The calorimeter concept is shown in figure 3.1. A copper heat ex-

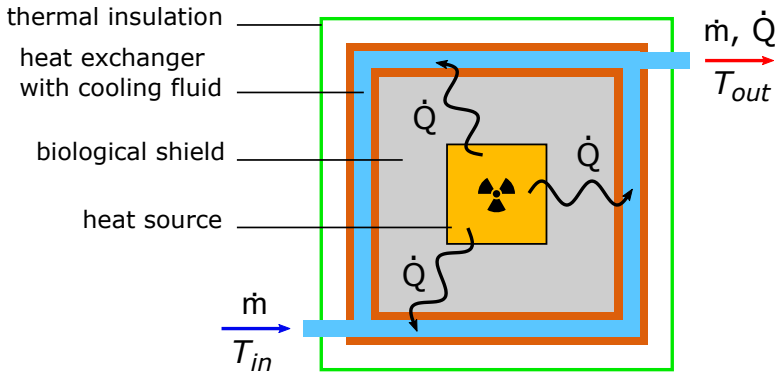

Figure 3.1: The concept of the flow calorimetric measurement: the heat source with its biological shield is inserted into a heat exchanger. A fluid with a well defined mass flow $\dot{m}$ is extracting the heat $\dot{Q}$ from the system. A measurement of the inlet and outlet temperatures T_{in} and T_{out} then yields an estimation of the source power. To ensure that a heat transfer is possible only via the mass flow, the system has to be thermally insulated.

changer completely encases the source and the biological shield. Heat generated by the anti-neutrino source in the center diffuses through the shield and is then removed by the fluid passing through the heat exchanger. The whole system is thermally insulated such that heat can be transported only via the liquid. If no phase transition occurs and in steady state conditions, the energy balance can be written as:

$$P_{\text{source}} = \dot{m} \cdot [h(p, T_{out}) - h(p, T_{in})] + P_{\text{loss}} \tag{3.1}$$

where P_{source} is the power generated by the source, h the specific enthalpy of the cooling fluid as a function of the temperature T and pressure p and $\dot{m}$ is the fluid mass flow. The first term on the right side of the equation is the power transferred to the fluid, which is measured from the parameters of the cooling fluid, while the second one, P_{loss} describes the heat leak through the thermal insulation (positive) and heat that is generated through other processes (negative). The main source of the latter is friction of the circulating fluid. If P_{loss} is negligible or well known, the measurement of the mass flow and of the inlet and outlet temperatures at a known pressure allows us to precisely determine the source power.
Since the measurement accuracy is required to be better than 1 %, both the temperatures and the mass flow must be measured with an accuracy in the order of 10^{-3}. To calculate the power from the measured parameters, the thermal properties of the fluid must be well known. Hence a natural choice is deionized water, whose enthalpy function is precisely tabulated in the literature. The estimation of the measurement uncertainties will be further discussed in chapter 4.

We can also set some requirements for the choice of the optimal mass flow range from analytical considerations: an upper limit on the mass flow is set to prevent the temperature difference $\Delta T = T_{out} - T_{in}$ from becoming too small. A too small temperature difference could decrease the accuracy of the measurement. The temperature difference has to be at least three orders of magnitude larger than the thermometer sensitivity. For example thermometers with 0.01 K sensitivity demand a ΔT in the order of a few tens of K. In addition, an upper limit on the mass flow is necessary to keep the heat generated by friction small. This was calculated in [FMP+16]. The power of a fluid gained (or lost) due to a pressure change is $P = \Delta p \cdot \dot{m}$. The pressure drop due to friction is given by the Darcy-Weisbach equation [Bro02]. Both formulas together yield:

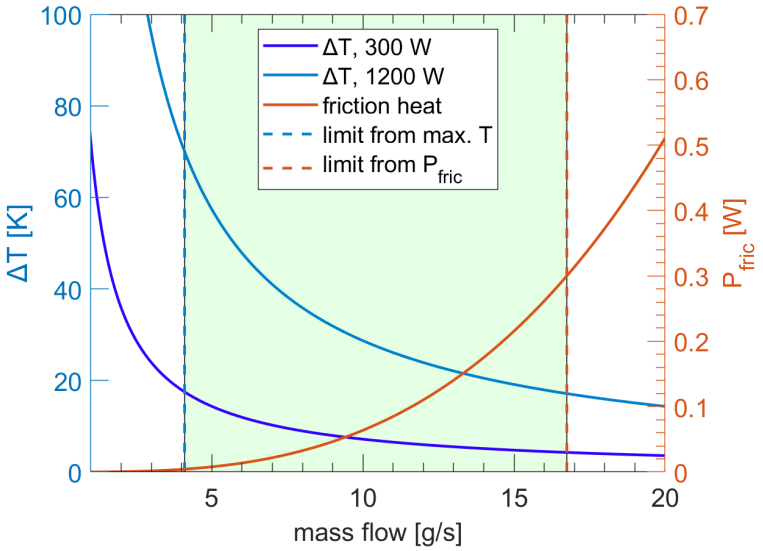

Figure 3.2: The optimum region for the mass flow. In blue (left scale) $\Delta T = T_{\text{out}} - T_{\text{in}}$ as a function of the mass flow for two values of the source power (1200 W and 300 W). In red (right scale) the power generated from friction in the water pipe as a function of the mass flow accordingly to equation 3.2. The blue vertical dashed line represents the lower limit on the mass flow, set by the maximum $\Delta T = 70\,\text{K}$, which prevents the water from boiling, while the red dashed line marks the upper limit, imposed by the maximum allowed friction heat ($P_{\text{fric}} < 0.3\,\text{W}$). The green area marks the optimum range for the mass flow.

$$P_{fric} = \frac{8 \cdot \dot{m}^3 \cdot \lambda \cdot L}{\pi^2 \cdot D^5 \cdot \rho^2} \tag{3.2}$$

where λ is the friction coefficient (Darcy friction factor), related to the roughness of pipes, ρ is the density of water and D and L are the pipe inner diameter and length, respectively.
The lower limit is imposed on the mass flow by the requirement to avoid a phase change of the water, i.e. the outlet temperature has to be well below 100°C ($\Delta T < 70$°C). In addition the mass flow has to be sufficient to ensure a turbulent flow. A turbulent flow is required for a constant water temperature throughout the pipe cross section to improve the heat exchange and avoid errors of the temperature measurement. If a flow is turbulent or not can be estimated from its Reynolds number Re:

$$Re = \frac{v \cdot D}{\eta} = \frac{4 \cdot \dot{m}}{\pi \cdot D \cdot \rho \cdot \eta}, \tag{3.3}$$

where v is the flow speed and η the temperature dependent kinematic viscosity of the fluid. In our application we expect a kinematic viscosity between $0.4 \cdot 10^{-6}\,\text{m}^2/\text{s}$ ($T = 70$°C) and $1 \cdot 10^{-6}\,\text{m}^2/\text{s}$ ($T = 15$°C). For the pipe diameter of 6 mm and a mass flow of 10 g/s the Reynolds number is in the range of 2100 to 5300. The critical Reynolds number, from which on a flow is regarded as turbulent, is $Re_{\text{crit}} = 2320$. As one can see, at low temperatures and low mass flows the flow might be laminar. However, as later will be shown, vortex generators in front of the thermometers ensure a turbulent flow.
In figure 3.2 the behavior of ΔT and of P_{fric} are shown as a function of the mass flow for two different source powers, $P = 1200\,\text{W}$ and $P = 300\,\text{W}$. The optimum region for the mass flow is marked in green. The lower limit is set by $\Delta T < 70$°C, the upper limit

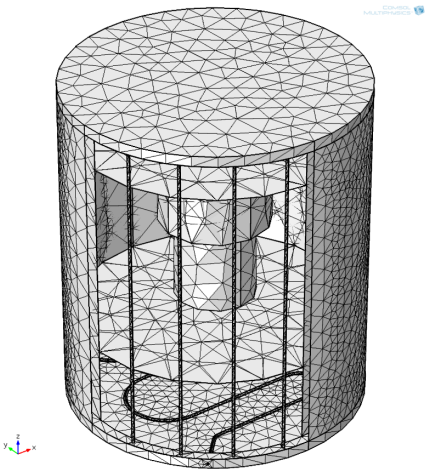

Figure 3.3: The mesh of the COMSOL model for the calorimeter simulations. A part of the model was removed to reveal the inner structure of the system, as the water pipes in the bottom and lateral parts of the heat exchanger, the segmented biological shield, and the capsule in the center that contains the radioactive material and acts here just as an uniform heat source. To simplify the simulation, the pipes, which are designed as a single serpentine throughout the heat exchanger, are not physically linked to each other in the model, but mathematically connected (boundary similarity function in COMSOL).

is set by the friction heat, which is required to be smaller than 0.3 W (1‰ of 300 W). To calculate P_{fric}, one has to estimate the friction coefficient λ. For a turbulent flow a simple empirical approximation is the following equation from Blasius:

$$\lambda = \frac{0.3164}{Re^{0.25}}, \tag{3.4}$$

For Reynolds numbers between 2100 and 5300 we obtain a friction coefficient from 0.037 to 0.047. For the plot the value in the middle $\lambda = 0.042$ is used. The other parameters for the friction heat are taken from the final design: $L = 14.5\,\mathrm{m}$ (length of the pipe in the heat exchanger), $D = 6\,\mathrm{mm}$ (pipe inner diameter). From the plot one can see that for a source power of 1200 W a mass flow between 4 and 17 g/s should be used. For lower powers, one can reduce the flow to even lower values if the sensitivity of the thermometer requires a larger ΔT. However, one has to observe carefully if the mass flow becomes laminar and if the performance of the calorimeter is changed.

3.2 Finite elements simulations in steady and transient state

The design of the calorimeter was guided by thermal finite element simulations, executed with ANSYS [ANS] and COMSOL Multiphysics [COM]. These simulations were used to find the optimum water path through the heat exchanger and to estimate heat losses. The source inside the tungsten alloy biological shield surrounded by a copper heat exchanger with an embedded water coil was simulated in a 3-dimensional model. The mesh of the COMSOL model is shown in figure 3.3. The mesh displays, how the model is divided into small elements (finite element method), where the heat equation (or the Navier-Stokes equation for the water in the pipes) is iteratively solved with the boundary conditions from each element. It can be seen that the mesh is quite

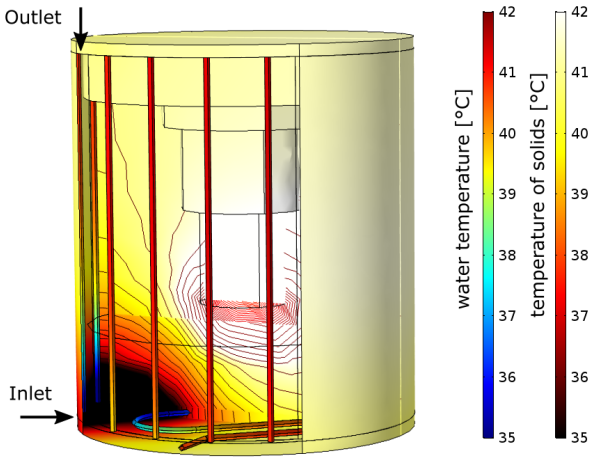

Figure 3.4: The simulated temperature distribution for $P = 1000\,\mathrm{W}$, $\dot{m} = 10\,\mathrm{g/s}$ and $T_{\mathrm{in}} = 15.5\,^{\circ}\mathrm{C}$. The temperatures of the heat exchanger, the shield and source (color scale from red to white) and of the water line (color scale from blue to red) are displayed. A cut plane showing the isothermal lines with 0.5 K steps evidences the big gradient between the shield and the inner part of the source. A large gradient close to the water inlet in the bottom plate is visible. Except close to the inlet area the temperature of the heat exchanger is homogeneous around 42°C, while a maximum temperature of about 120°C is reached in the source capsule.

coarse. However, smaller elements would have increased the computing time such that parameter scans become unfeasible, without leading to different results. Most of the modeled geometry is made of metals with high thermal conductivities that don't allow the formation of large temperature gradients on small scales. Small gradients as they occur in this model are accurately simulated within a coarse mesh.
The simulations were carried out under the assumption that he heat production in the source is uniform in the whole CeO_2 volume. Also the absorption of γ- and X-rays from the ^{144}Ce decay chain in the biological shield (i.e. an extension of the heat production into the shield) was neglected.

In a first study the temperature distribution on the surface of the heat exchanger was simulated and the path of the water pipes was optimized in order to achieve a homogeneous temperature on the outer surface of the heat exchanger. A homogeneous temperature is desired to minimize heat losses and to make them easier to estimate. The simulations have shown that the smallest heat gradients on the exchanger can be obtained when the water flows firstly through a pipe embedded in the bottom part and secondly through a serpentine in the lateral parts. This is shown in figure 3.4. For this result, a constant heat source of 1000 W was simulated in thermal equilibrium (steady state) with a mass flow of 10 g/s. The inlet temperature of the water is $T_{\mathrm{in}} = 15.5\,^{\circ}\mathrm{C}$. Here one can see that the largest heat gradient, from 15.5 °C to $\sim$ 40 °C, occurs in the bottom part of the heat exchanger close to the water inlet. On most of the heat exchanger surface the temperature stays between 40 °C and 42 °C. In addition, one can see through the cut model also the simulated temperature distribution in the biological shield and in the heat source. The color scale of the plot is saturated for temperature above 42°C, but the maximum temperature in the source is 120°C. The contour lines mark similar temperature values in 0.5 K steps.

Additional simulations were conducted to understand the thermodynamic behavior of the system and to estimate the heat losses. Following aspects were studied with dedicated simulation models that were optimized for fast computing to allow some parameter sweeps:

- the temperature distribution on the surface of the copper heat exchanger was simulated for different combinations of source power and mass flow value. For each case the radiative heat losses were calculated, assuming an isotropic thermalized vacuum tank and taking multiple layers of super-insulator foil into account. With 20 layers of super-insulator at the sides and 10 layers above and below the heat exchanger, the radiative heat transfer was estimated to be always smaller than 30 mW;

- it was verified that an asymmetric contact pressure between the source capsule and the biological shield has no significant impact on the temperature distribution in the outer parts of the source and the heat exchanger;

- the heat losses due to the residual air at the pressure of 10^{-3} mbar, as in the condition without a running turbo-molecular pump, were simulated (the calorimeter will be operated under vacuum). The heat losses were found to be in the order of a few hundred mW. For example in case of a "cold" vacuum tank at 15°C and a heat exchanger with a temperature distribution that meets 40°C at the sides and 70°C at the top, the convective heat loss is 0.6 W. This value is 0.06% of the 1000 W applied power and thus much lower than the accuracy goal of the calorimeter.

More details about these simulations can be found in [Alt15].

Finally, the model was validated through time-dependent simulations: the response of the outlet water temperature to a constant applied power was simulated and it was found that 99.9% of the maximum temperature of the outlet water is reached after about 2 days. This implies that measurements will take about 3 days, since after attaining thermal equilibrium the stability of the measurement has to be observed for about one day. Also the exponential decaying power was simulated: as the source decays with $\tau_{\mathrm{Ce}} = 411$ days, the heat is decreasing accordingly and a thermal equilibrium of the system is never reached. The diffusion of heat in the massive radio-protection shield causes a delay between power generation and measurement, dependent on the thermal diffusivity of components and on the radioactive source decay time.This was quantitatively studied with ANSYS finite element simulations, carried out at INFN Genova [FMP+16, ADN+18]. The simulations were performed assuming an initial source power P_0 of 1000 W, decaying exponentially with the ^{144}Ce lifetime and neglecting any possible heat loss. Figure 3.5 shows the result of the simulation: after an initial transient, which lasts nearly 2 days, the measured value follows the same simple exponential law as the generated power, with a time delay t_{d}. By fitting the simulated data, it was found that $t_{\mathrm{d}} \sim 0.2$ days, which affects the measured power by less than 0.1%. Note that in this simulation the system was at thermal equilibrium before turning on the mass flow, resulting in the beginning in a very high measured power due to the overheated setup.

In summary, the simulations helped to determine the optimum water path inside the heat exchanger and allowed us to study heat losses from radiation and convection. It was also verified that an asymmetric contact of the heat source within the biological

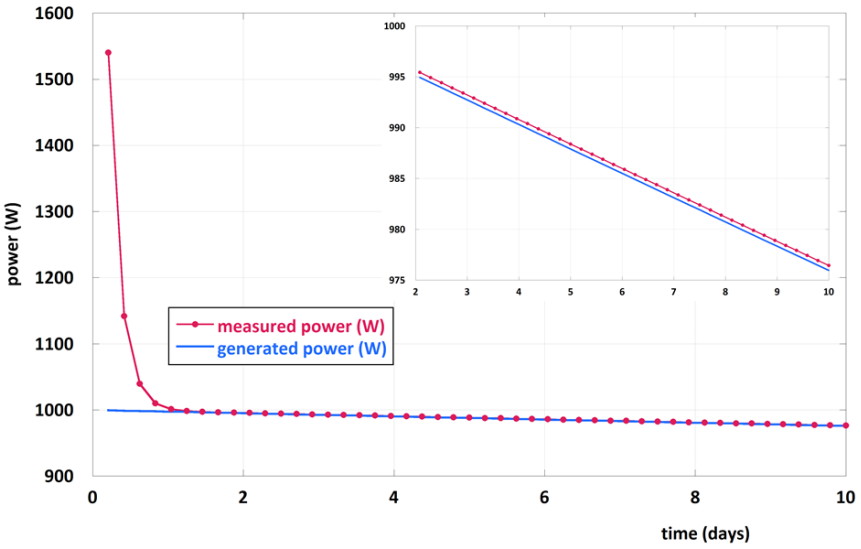

Figure 3.5: A time dependent simulation of the measurement with a decaying heat source from [FMP+16, ADN+18]. The blue line shows the heat generated by the source, while the red line marks the measured power as a function of time. After an initial transient of nearly 2 days, the measured power follows the same simple exponential law as the source power with a delay of $t_d \sim 0.2$ days. This delay is due to the thermal diffusivity of the system. The mass flow (i.e. the cooling of the source) was turned on at $t = 0$, such that the system is overheated in the beginning and an increased power is measured.

shield does not affect the temperature distribution in the heat exchanger. In addition time dependent simulations gave a clear indication that the flow calorimeter can precisely measure the source activity in about 3 days of measurement, if the heat losses are minimized.

3.3 Technical description

3.3.1 Mechanical description

The design of the calorimeter is described in the following. In general, the concept of the mechanical design is to envelop the shielded source inside a copper heat exchanger with a good thermal contact and also to insulate it from the external environment at the same time. The main part of the calorimeter is placed within a cylindrical vacuum chamber with 83 cm height and a maximum diameter of 92 cm. The main components are, from the inside out (see figure 3.6):

- a stainless steel flange bolted to the top of the source shield, which ensures a tight separation between the source and the vacuum in the chamber, see figure 3.7. The space between this flange and the shield is at atmospheric pressure, which is monitored to ensure the tightness;
- a copper heat exchanger, consisting of two semi cylindrical shells (20 mm thick), a bottom platform and a circular lid, see figure 3.7. The lateral shells can be tightened around the tungsten shield with 10 screws on each side. Inside the two lateral parts and the bottom platform of the heat exchanger a small stainless

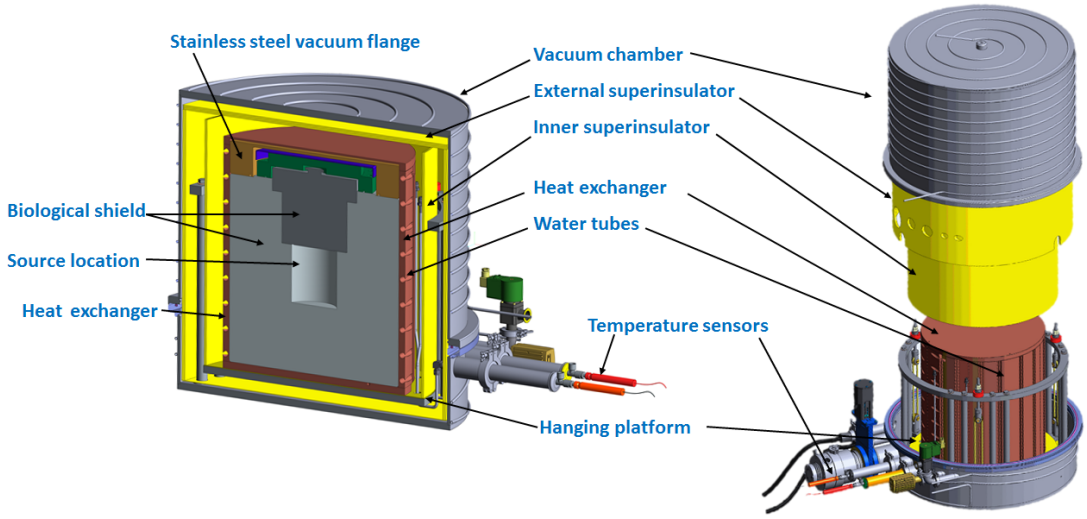

Figure 3.6: A cut-away and an exploded view of the calorimeter. In the cut-away, one can see, how the biological shield with its plug and closing flange is encased in the copper heat exchanger. The heat exchanger is surrounded by an large "tube" of 10 layers of super-insulator to attenuate thermal radiation heat transfer. The heat exchanger and the super-insulator are then placed on a stainless steel platform that is suspended with Kevlar ropes from a support structure, as can be seen in the exploded view. All the previously mentioned components are then completely enveloped with another 10 layers of super-insulator foil. The entire system is placed in an evacuated chamber in order to prevent heat losses through convection. A secondary water circuit is flowing through an coil soldered on the vacuum chamber that allows us to control its temperature (thermalization). By matching the chamber temperature with the temperature of the inside components, all heat losses can be further reduced. Photographs of the systems to reduce heat losses are shown in figures 3.8 and 3.9.

steel serpentine pipe (6 mm inner diameter) for the cooling water is brazed into the copper. The three separate pipes are connected with VCR fittings. The total length of the pipe in the heat exchanger is approximately 14.5 m;

- a stainless steel platform on which the source with the copper heat exchanger is placed. This platform is kept suspended by three pairs of Kevlar® ropes with 0.3 m length from a stainless steel support directly mounted inside the vacuum chamber, as shown in figure 3.8. Kevlar® was chosen since it has a high tensile strength and a low thermal conductivity ($k = 4\,\mathrm{W/m{\cdot}K}$) [kev]. This suspension suppresses heat losses from the heat exchanger to the environment through thermal conduction;

- a first stage of a cylindrical thermal radiation shield, composed of 10 layers of super-insulator Coolcat 2 NW (double-side aluminized mylar with non-woven polyester spacer material), surrounding only the lateral side of the copper heat exchanger and placed on the suspended platform, see figure 3.8;

- a second stage of a thermal radiation shield, made of 10 layers of the same type of super-insulator material as above and completely covering the support structure and the heat exchanger (figure 3.9). It is built as a removable "hat" structure, covering the setup from the sides and from the top, together with a fixed base of super-insulator foil, placed on the floor of the vacuum chamber under the platform. An auxiliary structure prevents the super-insulator from touching the extruding suspension links of the steel platform, which could induce heat losses through conduction.

The stainless steel vacuum chamber is divided by a 923 mm flange into two parts: a lower part with several vacuum ports and feedthroughs for the pump system, the sensors cabling and the water pipes, and a top part (the bell) that can be lifted to allow access to the inner apparatus. The flange is closed alone by the weight of the bell, such that an overpressure in the tank due to a leak in the water circuit could escape before reaching dangerous levels. A stainless steel pipe (8 mm inner diameter) for a secondary water circuit is soldered onto the external surface of the vacuum chamber. This water line allows us to actively control the temperature of the vacuum tank: by heating the vacuum chamber to a temperature that matches the temperature of the heat exchanger, heat losses due to conduction, radiation and convection can be minimized.
In the end the vacuum chamber was too large to entirely fit into the pit under Borexino, so it was decided to do a high precision measurement in front of the pit entrance just before the start of the Borexino data taking (and possibly at the end and maybe in the middle of the measurement), and then to move the calorimeter without the bell and the super-insulator into the pit and continue measuring with lower precision due to more heat losses. In order to easily transport the 2.5 ton-setup under the Borexino detector, the bottom part of the vacuum chamber is sitting on a rail system that connects the far end of the pit with the clean room in front of the pit entrance, on which it can be moved with a winch system.

In conclusion the calorimeter design was driven by the minimization of any heat loss: conduction heat losses were reduced thanks to the Kevlar rope suspension system, convective heat transfer was suppressed by operating the system in a vacuum, and thermal radiation was attenuated by several layers of super-insulator foil placed between the copper heat exchanger surface and the external vacuum chamber (20 layers on the sides and 10 layers on the top and on the bottom). In addition all heat losses were further reduced by the thermalization of the vacuum tank.

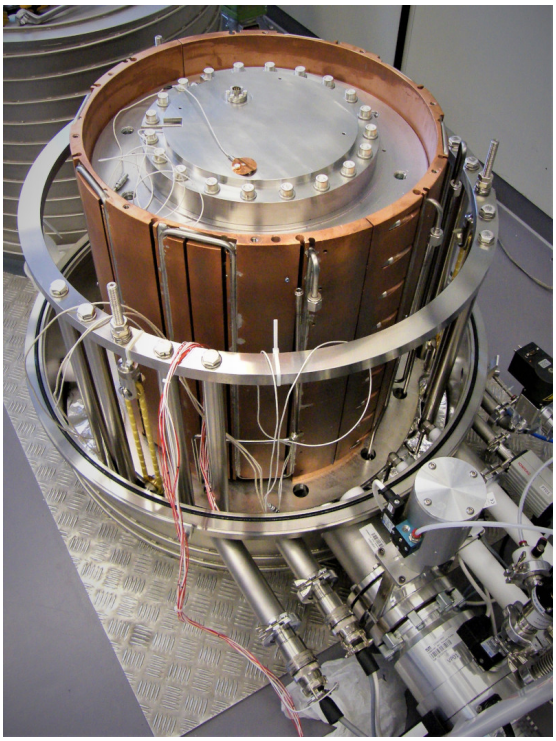

Figure 3.7: The heat exchanger. The top lid was removed to show the shield within (here only an aluminum mockup) with its closing flange on top. The serpentine pipe for the cooling water - brazed into grooves on the outer side of the heat exchanger - is clearly visible. The cabling is for temperature sensors and the power supply for the electrical mockup heat source.

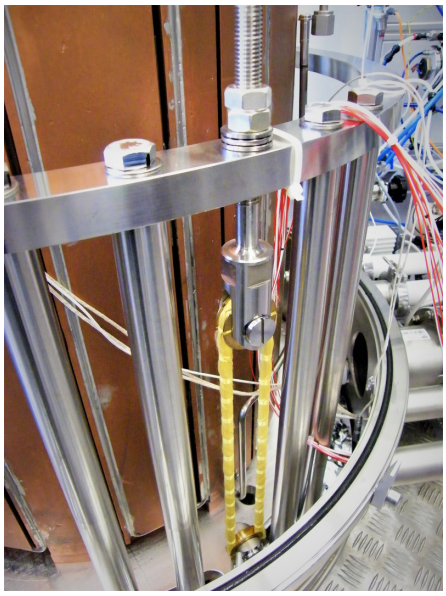

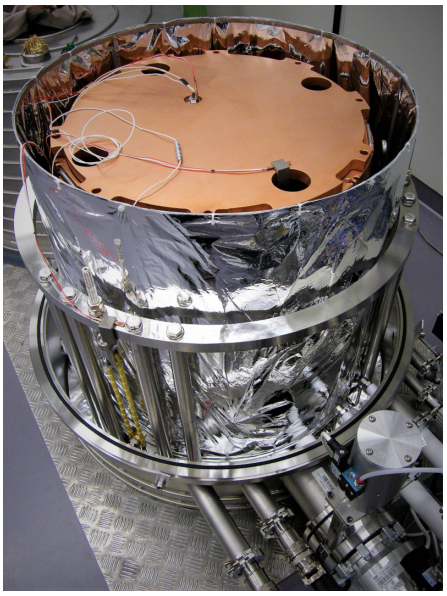

Figure 3.8: Left: a close up view on one of the 3 pairs of kevlar ropes that suspend the stainless steel platform together with the heat exchanger and source that weight $\sim$ 2.5 tons. The poor thermal conductivity of Kevlar helps to minimize heat losses. **Right:** the inner super-insulator shield is placed around the heat exchanger to minimize radiative heat transfer.

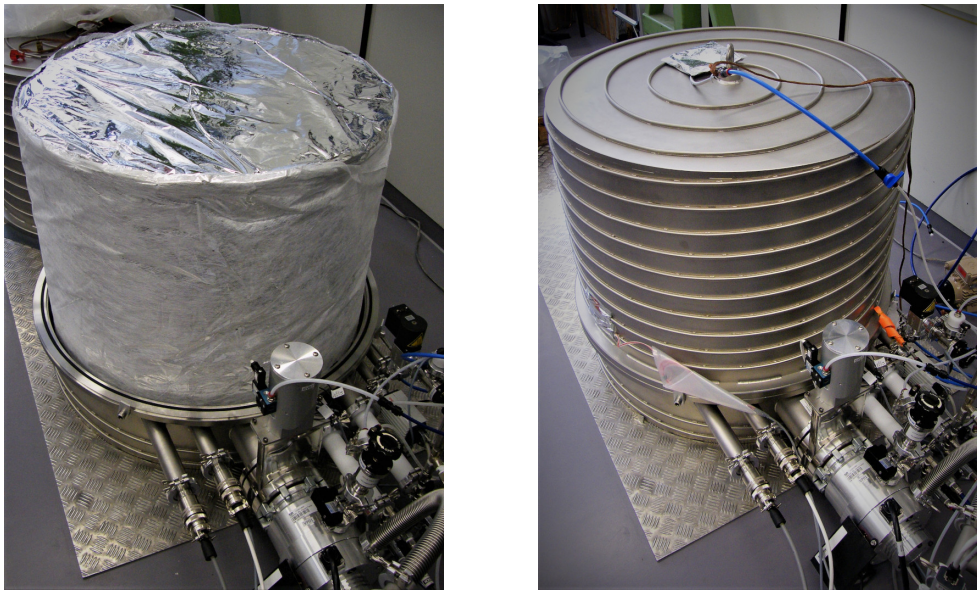

Figure 3.9: Left: the outer super-insulator shield completely envelopes the heat exchanger and support-structure and further attenuates radiative heat transfer. **Right:** the system is operated in a vacuum chamber to prevent heat losses through convection. An independent water circuit in a pipe coil soldered onto the chamber allows us to minimize the temperature difference between the chamber and the inside components to further suppress heat losses.

3.3.2 Instrumentation and control systems

The source power is obtained via eq. 3.1 from the water mass flow $\dot{m}$ and temperature T measurements. Two mass flow meters and two temperature sensors were chosen with an accuracy as high as possible. Each parameter is measured once before the water enters the vacuum chamber, and a second time after exiting it. The mass flow meters (Micro Motion Coriolis Elite Sensor) measure $\dot{m}$ with an accuracy of 0.05% for values between 1.4 and 30 g/s. The configuration of one sensor at the beginning and another one at the end of the water line allows us also to detect any possible leakage in the circuit. Regarding the temperature measurement, two Semi-Standard Platinum Resistance Temperature sensors (PRTs, model 935-14-61) are read out by the high precision 923 milliK thermometer by ISOTECH, whose stability is 7 ppm. The final precision of the temperature measurement is 3 mK, which is guaranteed by the UKAS certification for each sensor. The precision of the two sensors was also checked against each other by performing a measurement in a container with water. The difference between both measured temperatures was indeed smaller than 3 mK during a measurement of a few hours. The two sensors are immersed in the water line just before the entrance and after the exit of the heat exchanger for measuring T_{in} and T_{out} respectively. It is important that the temperature of the water is immediately measured as it enters or exits the heat exchanger, because else it would be affected by the external environment. Therefore the PRTs are inserted in custom made tubes that are directly attached to the vacuum chamber ports, as shown in figure 3.10. These tubes connect the inner stainless steel pipe, coming from the heat exchanger, with the external water line. They are made of the plastic Ertacetal. This poorly thermal conducting material was chosen in order to minimize any conduction heat losses to the external environment and to the vacuum chamber itself. In the tubes directly before the thermometers 3D-printed vortex generators are inserted that ensure a homogeneous water temperature across the pipe

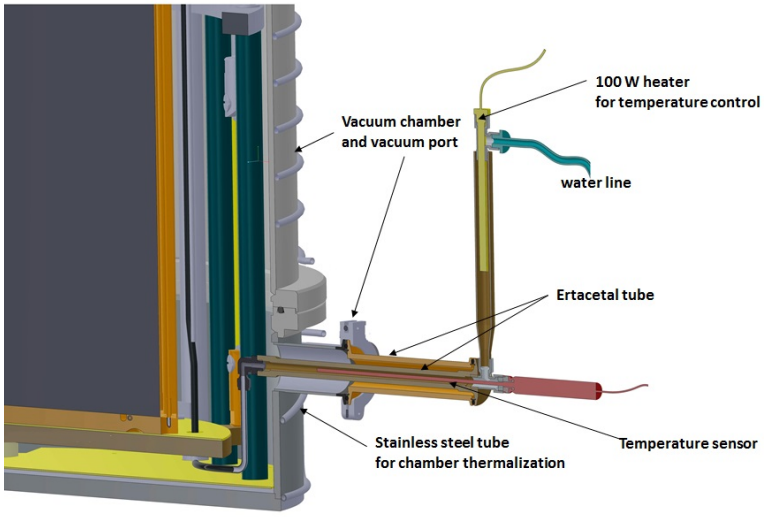

Figure 3.10: Detail of the connection between the water line and the vacuum chamber. To minimize the thermal contact between the water and the external chamber a custom-made Ertacetal tube is used. The tube consists actually of two parts, the inner tube with the water and the temperature sensor (red) and the outer tube, which isolates the inner tube with vacuum. In total two of these connectors are used for the water inlet and outlet. Here the inlet is pictured, where also a 100 W heater for the temperature control is attached.

diameter.

A scheme of the entire water loop is shown in figure 3.11. The water is pumped and cooled by the chiller (Huber Unichiller 025T), which circulates water at 3 bar and at a temperature of about 15°C and has a cooling power of 3 kW. The chiller's inlet and outlet are connected with an adjustable bypass line to reduce the water pressure in the line, when a lower mass flow is required. The stability of the pumping rate and temperature is limited, an additional stabilization is required to prevent the chiller fluctuations from disrupting the thermal equilibrium. Therefore, a proportional valve (Samson Type 3510-1) that is commanded by a proportional-integral-derivative (PID) feedback loop based on the mass flow value acquired by the flow meter, is stabilizing the flow. The feedback loop allows the valve to react on fluctuations in the mass flow by adjusting the throughput. The temperature is stabilized in a similar way: a 100 W-heater is placed in the water circuit just in front of the inlet thermometer (see figure 3.10), to which it is connected with a PID feedback loop. Thereby the mass flow is tunable in the range of $2 - 15$ g/s with an oscillation (induced by the valve regulation) of 0.3% around the average value, while the temperature is stabilized within 0.015°C in the $13 - 18$°C range. The period of the fluctuations is typically ~ 1 minute.

In addition a conductivity-meter (Swansensor RC U) monitors the purity of the water in the range of 0.005-1000 µS/cm with an accuracy of 0.5% at 25°C up to 20 µS/cm. The conductivity was found to be around 5 µS/cm during the entire characterization and calibration campaign of the calorimeter. This instrument was installed to detect changes in the water quality that could effect the thermal properties and thus falsify the measurements.
The water pressure was measured with a SICK PBS pressure sensor (0 - 10 bar range and $\sigma_p = 0.1$ bar accuracy) at the inlet to and outlet from the vacuum chamber.

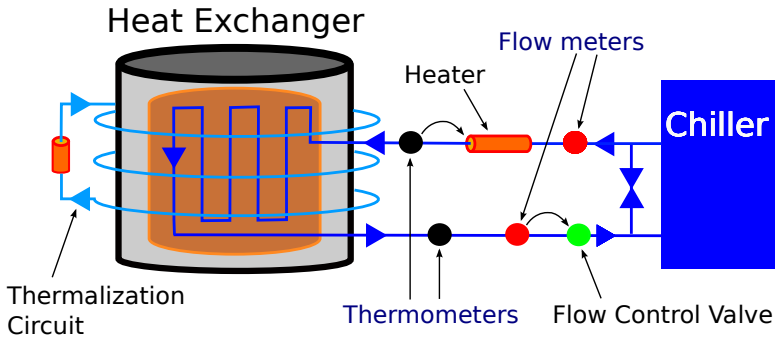

Figure 3.11: Scheme of the water loop: a chiller is cooling and pumping the water; a 100 W heater and a valve in feedback-loops with the temperature and mass flow acquisition stabilize the water temperature and the flow speed respectively. An independent water circuit with a 1.5 kW heater controls the temperature of the vacuum tank.

In addition to the main water circuit, an independent water loop is used to thermalize the vacuum camber in order to further reduce heat losses. This secondary water circuit is powered by a gear pump that generates a high mass flow of $30-40\,\mathrm{g/s}$. The high mass flow guarantees a small temperature gradient on the chamber. The temperature of the water is actively controlled by a 1.5 kW-heater accordingly to the temperature measured on the chamber itself by a Resistance Temperature Detector with an accuracy of 0.5 °C. For measurements at room temperature (15-20 °C) the chamber temperature was kept stable within 0.5 °C for temperatures in the range of 20-33 °C. The temperature gradient between the top and the bottom of the vacuum chamber was found to be a few °C.

Throughout the setup temperature sensors (RTDs) with 0.5 °C accuracy each were placed. They are located on the vacuum chamber, on the copper heat exchanger, on the platform, on the support structure and on the top of the copper lid. Data from these sensors are essential for the optimization of the measurement conditions and minimization of heat losses.

The vacuum pumping system consists of a scroll pump (SCROLLVAC SC 15 D) and a turbo molecular pump (TURBOVAC 361) by Oerlikon Leybold Vacuum, which is connected through a gate valve to a CF100 port of the vacuum chamber. These pumps ensure a pressure $\sim 10^{-5}$ mbar in all conditions of measurement and thus suppress any convective heat transfer within the calorimeter. Pumping down requires some time because the mylar between the layers of the super-insulator foil is out-gassing slowly. The pressure inside the chamber is monitored by an electronic vacuum pressure gauge (IONIVAC Combi Transmitter ITR 90) in the range from $5 \cdot 10^{-10}$ to 10^{3} mbar, while the pressure in the pre-vacuum between the two pumps is acquired by a THERMOVAC Transmitter TTR 91. An additional pressure sensor is located close to the plug of the biological shield: it constantly monitors the atmospheric pressure in the small volume between the stainless steel flange and the top surface of the shield (see figure 3.6) to guarantee that the inner part of the shield is not affected by the pumping system.

Finally three load cells monitor the strain on the Kevlar ropes that suspend the 2.5 tons of source, shield and heat exchanger.

3.3.3 Data acquisition and safety systems

All the sensors are acquired by a National Instrument CompactRIO (NI 9068) Real Time Series device, through a proper National Instruments module or a serial communication. The CompactRIO Real Time Series device is a networked hardware platform with an embedded processor and a real-time operating system that communicates through an ethernet connection to the host computer. It can run many loops at the same time on a stable platform optimized for real-time performance. This allows us to assign a higher priority to the mass flow and the temperature control loop, which requires a fast response, and as well the main sensor acquisitions (1 read-out per second). A lower priority and lower frequency (1 read-out every 3 seconds) was chosen for the acquisition of the monitoring sensors. For each acquired value the corresponding time stamp is saved with 0.1 s precision. This data rate and precision is sufficient for the calorimeter operation, since a measurement takes days and the response time to changes for example in the ambient temperature is in the order of hours.

The system is completely controlled by a LABVIEW software that deals with the acquisition of all the data, runs the three PID feedback-loops for the mass flow stabilization, the T_{in} stabilization and the vacuum chamber thermalization, and handles the chiller and vacuum system control. It also controls the electrical heaters when an electrical heat source is installed in the calorimeter for testing purposes (see next section 3.3.4). However, for safety purposes, the software is hardware controlled by a programmable logic that monitors a short digital signal sent with a constant frequency from the CompactRIO: in case the signal is interrupted, the power supplies of the heaters are switched off.
In addition several automatic safety procedures are implemented to alert the user in case of a hazardous situation and to put the system in a safe condition. The implemented emergency operations are:

- switching off the turbo pump in case of a too-high pressure inside the vacuum chamber;
- switching off the power supply in case of high temperatures or in case of zero mass flow;
- switching off the chiller pump and the gear pump for the secondary circuit in case of a low water level inside the tanks of both loops or in case of leakage.

3.3.4 Electrical source for calibration

In order to characterize and calibrate the calorimeter before the activity measurement of the ^{144}Ce-^{144}Pr source an electrically powered mockup of the source was built. The source capsule is replaced by a copper cylinder with similar dimensions, equipped with 6 electrical heaters to simulate the heat released by the radioactive material. The power of the electrical heat source can be set to a constant or to any function of time, thereby allowing simple measurements of heat losses at constant power or to simulate the source decay.
The mockup copper cylinder is inserted either in the tungsten alloy shield (the same that would have contained the radioactive source) or in an aluminum shield of the same size, specifically built for the calibration measurements. The tungsten alloy shield was available only for a short period after its production and before the transport to Mayak in Russia for the source insertion. Thus the first measurements to estimate heat losses

were performed with the aluminum shield. The final estimation of the calorimeter sensitivity was then done with the actual biological shield, where the electrical mockup simulated the decay of the radioactive source. For such measurements with a time-dependent power the material-dependent thermal diffusivity determines the response time of the system, hence it is preferred to use the tungsten alloy shield.
Since the resistance of the electrical heaters changes with temperature and is even in steady state measurements not stable at a per thousand level, the applied voltage was continuously adjusted in order to keep the power constant within 0.05 W (less than 0.01% for $P > 500\,\mathrm{W}$) or to reproduce accurately the exponential function.
The released power was determined by an electrical measurement: the current was estimated from the amplified voltage drop through a precise and stable shunt resistor (100 mΩ), while the voltage was measured just close to the feedthrough on the top of the stainless steel flange inside the vacuum chamber, thus ignoring the voltage drop due to the cable resistance outside the shield. Both voltages were acquired by two NI-PXI 4071 multimeters, whose error is of the order of 0.25 mV for 100 V. In conclusion, with the assumption that the set power is totally released into the system (the heat released from the cable resistance inside the vacuum chamber is negligible) the global accuracy on the set power was dominated by the current measurement accuracy, which is due to the accuracy on the shunt resistor calibration, and was estimated to be around 0.04%.

Chapter 4

Analysis of the calorimeter data

In this chapter the method to analyze the calorimeter data is described. Over a time period of typically a few days the temperature and mass flow of the water are measured at a known pressure at the inlet – where the water enters the pipe in the vacuum chamber – and at the outlet – where the water pipe exits the chamber. The temperature difference is then proportional to the source power. The challenges of the analysis are first to determine the period, where the calorimeter is "thermalized", i.e. it is at thermal equilibrium or steadily following the source decay, and then to calculate the uncertainty of the measured power. In general the power transferred to the water can be calculated from the data taken with the calorimeter according to following equation:

$$P = \dot{m} \cdot [h(T_{\text{out}}, p_{\text{out}}) - h(T_{\text{in}}, p_{\text{in}})] \,. \tag{4.1}$$

Here, $\dot{m}$ is the mass flow and h the specific enthalpy of water. The enthalpy is a function of temperature $T_{\text{in / out}}$ and pressure $p_{\text{in / out}}$, measured at the inlet and outlet respectively. The pressure was not constantly monitored, but measured only sporadically for different mass flows at inlet and outlet, as its value is not expected to change. For the mass flow an average of both mass flow meters was taken.
The power was calculated according to equation 4.1 for all data points in a measurement, such that the time-dependent power in 1 s steps is obtained. Later an average was taken over the evaluation period, where the power is stable. This average was then regarded as final value for the measured power, called here P_{meas}.

The enthalpy function $h(T, p)$ was released by the International Association for the Properties of Water and Steam [Int18]. Here the "IAPWS-95" formulation for general and scientific use was used, in contrast to the industrial formulation from 1997, which uses simplified equations for faster calculation. The IAPWS-95 release is a collection of analytical functions for the thermodynamic water properties that were validated through measurements. In the analysis software a MATLAB® implementation of IAPWS-95 from [Jun09] was used. The code was modified by the author to accept vector input in order to make full use of MATLAB's optimization for matrices and vectors.

An important issue with the analysis is the decision, when the system is considered to be at thermal equilibrium. After the source is inserted in the calorimeter, there will be a transient phase where the temperature of the system and the outlet water changes continuously. After this phase a thermal equilibrium is eventually reached and the temperature of the outgoing water is constant. In theory the thermal equilibrium is only asymptotically approached, while in reality fluctuations of the measurement conditions as the environmental temperature cause small changes in the "thermal equilibrium"

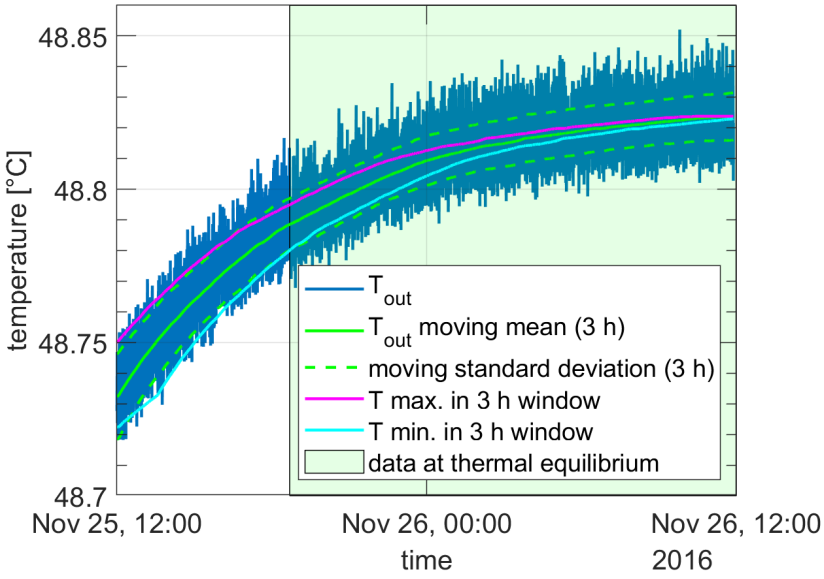

Figure 4.1: The selection of the data at "thermal equilibrium" (green), which decides the final power value. The stability region is defined as this region of the data, where the minimum and maximum of the moving mean of the outlet temperature in a 3 h window are smaller than the bounds set by the moving standard deviation. The condition can be made stronger if required, however it does not change the estimated power significantly.

such that the data is moving around the stable value. One has to define a stability condition, which determines the period, where the power is averaged to obtain P_{meas}. The equilibrium condition, which is described in the following, is imposed on the outlet water temperature, but it could also be applied to the point-wise evaluated power or the temperature difference. Since both the inlet water temperature and the mass flow are very stable, the same period of stable data will be found.
The outlet water temperature T_{out} is filtered with a moving mean over a 3 h-time window. In addition the moving standard deviation is calculated over the same period. The stability condition is fulfilled, when the minimum and maximum of the moving mean in the same time window are within the bounds of the moving standard deviation, i.e. if the fluctuations of the average temperature in a three hour window are smaller than the fast oscillations around the local mean. This is shown in figure 4.1. The region of stability is marked by the green area. On a first glance the data does not look very stable, however, the change of temperature in the stable region is less than 0.05 K in $\sim$ 18 h. The analysis code also checks, if the condition holds true for the inlet water temperature. For very stable data, the condition can be made stronger by increasing the time window and / or requiring the extrema of the moving mean to be within the moving standard deviation bounds multiplied with a factor < 1. However, in the measurements presented in this thesis, the change of the measured power was small compared to the measurement uncertainty, when the condition was made more strict.

The equilibrium condition described above can be used for measurements with constant source power. Transient data from a decaying source can be analyzed in a similar way. In this case, the system is stable when the time-dependent power follows the exponential decay of the source with exactly the same decay constant. To select the stable data, it is multiplied with an inverse exponential decay function to obtain a

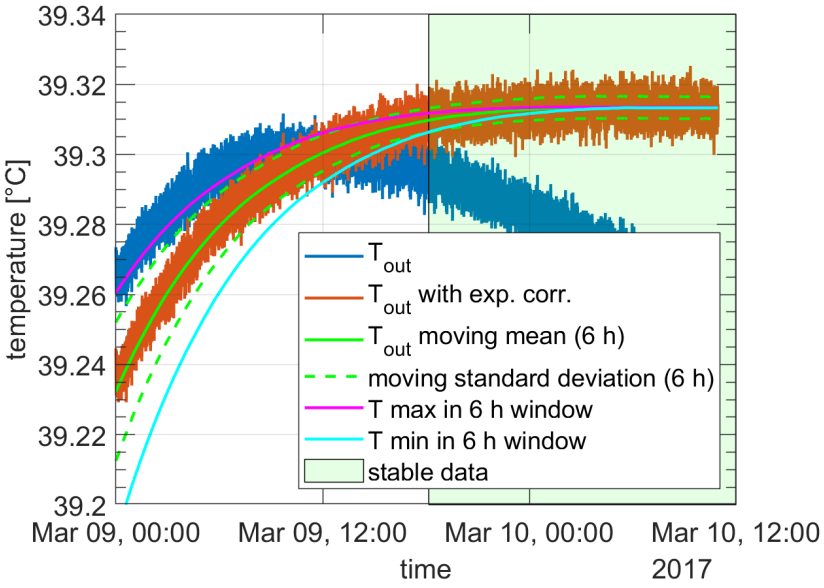

Figure 4.2: The selection of the stable region (green) for transient temperatures from a decaying source. The temperature vector (blue) is exponentially corrected (see equation 4.2) to obtain a constant temperature value (orange), on which the same condition as for the steady state data is imposed. For t_0 March 9, 12:00 was chosen.

constant outlet temperature, on which then the stability condition is applied for the data selection. The function to obtain the constant temperature is

$$T_{\mathrm{out},t_0}(t) = T_{\mathrm{in}} + (T_{\mathrm{out}}(t) - T_{\mathrm{in}}) \cdot \exp\left(\frac{t - t_0}{\tau}\right), \tag{4.2}$$

where T_{in} is the averaged inlet temperature, which is exactly the set value, $T_{\mathrm{out}}(t)$ the vector of measured outlet temperature, t_0 the start time and τ the decay time. The resulting T_{out,t_0} is then a vector of the temperature at time $t = t_0$, calculated from each data point according to the exponential decay. This approach requires that the decay constant is known, which is true for measurements with the ^{144}Ce source ($\tau = 411\,\mathrm{d}$) and with the electrical mockup. After the stability region was found, again an average over the exponentially corrected point-wise calculated power is taken. The resulting P_{meas,t_0} corresponds to the power transferred to the water at time t_0. Exemplary original temperature data and the corrected vector with the region of stability are shown in figure 4.2.

In order to evaluate the accuracy of P_{meas}, the uncertainty of the calculated enthalpy σ_h has to be considered with the correct propagation of the measurement errors of pressure σ_p and temperature σ_T, and also the mass flow measurement uncertainty $\sigma_{\dot{m}}$ has to be taken into account. The sizes of these uncertainties are:

- $\sigma_h = 100$ J/kg (in the $T - p$ region of interest) [Int03];
- $\sigma_p = 0.1\,\mathrm{bar}$;
- $\sigma_T = 0.003\,\mathrm{K}$;
- $\sigma_{\dot{m}}/\dot{m} = 0.05\%$.

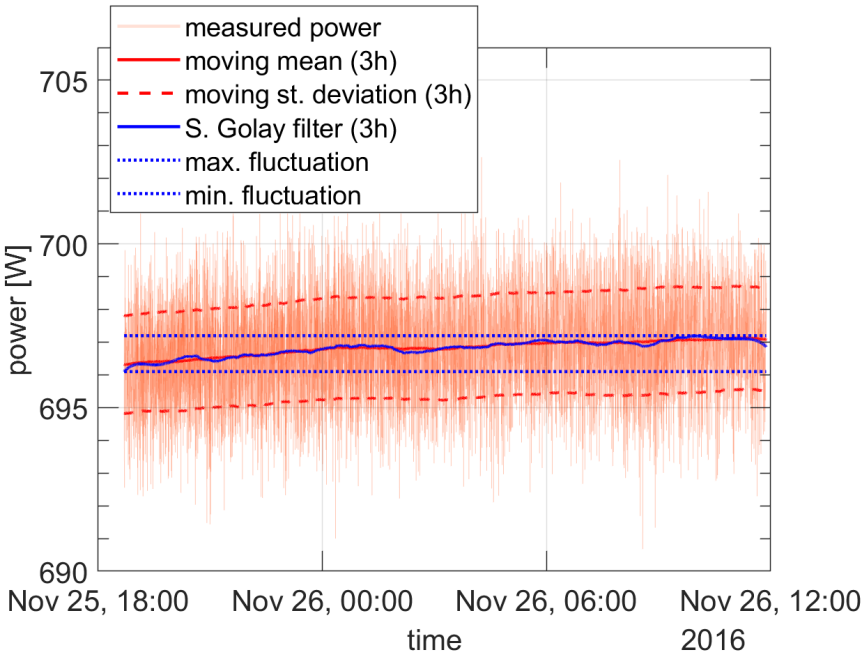

Figure 4.3: The point-wise calculated power in the period of thermal equilibrium. The value is fluctuating around a non-stable value, which causes an uncertainty of the measurement. The blue curve shows data after applying a 5th-order Savitzky-Golay filter. Note that it is alternating more than the moving average on the same time scale (3 h). The maximum and minimum values of the filtered data are used as an error ($\sigma_{P,\text{fluct.}}$) in the analysis.

In addition, an uncertainty due to temperature and mass flow fluctuations has to be added: the system is only stable to a certain extent, even when the equilibrium condition is fulfilled. Figure 4.3 shows the equilibrium region of the point wise evaluated power during a measurement. One can see at a first glance a high frequency oscillation of the power around a mean value. One can also see that the mean value of the oscillations is not stable, but is alternating on timescales $\mathcal{O}(1\,\text{h})$. The change of the mean is modeled by applying a 5th-order Savitzky-Golay filter to the data with a time window similar as for the choice of the thermal equilibrium period (see above, typically 3 h). In figure 4.3 one can see that this filter shows more fluctuations than a simple moving mean on the same time window. Finally, the maximum and minimum value of the measured power in the evaluated time window after applying the filter are used as an error $\sigma_{P,\text{fluct.}}$. The error bars thus can be asymmetric, but typically the upper and lower error bars have the same sizes.

By quadratically adding the uncorrelated errors, one obtains the total uncertainty of the power P_{meas}:

$$\sigma_{P_{\text{meas}}} = \sqrt{\dot{m}^2 \cdot \left(\sigma_{h,\text{in}}^2 + \sigma_{h,\text{out}}^2\right) + \frac{\sigma_{\dot{m}}^2}{\dot{m}^2} \cdot P^2 + \sigma_{P,\text{fluct.}}^2}, \tag{4.3}$$

where

$$\sigma_{h_{\text{in/out}}} = \sqrt{\left(\sigma_p \cdot \left.\frac{\partial h}{\partial p}\right|_{T_{\text{in/out}}}\right)^2 + \left(\sigma_T \cdot \left.\frac{\partial h}{\partial T}\right|_{p_{\text{in/out}}}\right)^2 + \sigma_h^2}. \tag{4.4}$$

For the partial derivatives of the enthalpy function, which in fact consists of many nested functions, linear approximations were used. The resulting error is usually in the

range of 1-2 W for a temperature difference of a few tens of degrees. For a source power of 1000 W this is an uncertainty of $\approx 0.2\%$ and thus satisfies the design goal. This error describes the accuracy of the measurement itself, not of the calorimeter as a whole since heat losses are an additional systematic. In the following section 5 it will be shown how heat losses are minimized such that they are smaller than the measurement error. The error $\sigma_{P_{\text{meas}}}$ is thus the final uncertainty of the source power, when the system is operated in an optimized condition.

The contribution of the instrumental errors to the measurement uncertainty are very small. The error from the fluctuations is dominating together with the uncertainty of the enthalpy function. It should also be mentioned that the dependence of the enthalpy on the pressure is very weak. The pressure drop between inlet and outlet is ~ 1 bar, but one can also use an average of both pressures or a rough estimate in equation 4.1, as the resulting difference will be negligible compared to the overall error.
The enthalpy error can be dropped in case of very small enthalpy differences. For enthalpy differences smaller than 10 000 J/kg, the relative error is 0.1% [Int03]. An enthalpy difference of 10 000 J/kg corresponds to a temperature difference $\Delta T < 2.5\,K$, which occurs for a source power of 100 W with a 10 g/s mass flow or a power of 50 W at 5 g/s. Measurements with such low powers were not performed. However, this error can be used when different measurements are compared. If the parameters of the inlet mass flow are unchanged and the difference in the outlet enthalpy is smaller than 10 000 J/kg, which holds true for several sets of measurements, one can use this smaller error. One then obtains a more accurate value of the power difference between to measurements. The absolute error of the measured power still has to be calculated with the larger error.

Some aspects of this analysis method are arbitrary, which are the determination of the error from fluctuations and the condition to select stable data. To avoid a selection bias, another analysis was performed by Lea Di Noto of INFN Genova with a different error calculation that took fluctuations of the outlet temperature into account instead of variations of the point-wise evaluated power, and with a different stability region selection that was based on the time derivative of the temperature data. Also the analysis of the decaying data was done differently by fitting the exponential function. The results of both analyses were always in agreement.
In the following chapter the results of the calorimeter calibration are presented. The measurements were analyzed according to the method described in this chapter.

Chapter 5

Results of the calorimeter calibration

In this chapter the results from the calorimeter characterization and calibration with the electrical mockup source are presented. The goals of the measurements were to get an understanding of the calorimeter's behavior, i.e. to quantify heat losses under different measurement conditions, to optimize the calorimeter operation in order to minimize heat losses, and to finally prove that the heat of a decaying source can be measured with the projected uncertainty. Again, the results of this work were partially published in [ADN+18], but there are small differences, because the data here was analyzed as described in chapter 4, while in the paper also the analysis by the co-author Lea Di Noto was taken into account. However, the final results and conclusions are the same.

5.1 Setup and measurements

The calorimetric measurements with the electrical heat source can be separated in three different phases:

phase 1: measurements with the aluminum shield at Technical University of Munich. These measurements were performed mostly in summer 2016. The goal was to improve the setup, for example to find the best parameters for the flow and temperature stabilization feed-back loops, position of RTDs (temperature sensors for monitoring the heat distribution in the system), and to estimate heat losses and optimize the measurement conditions. This phase was concluded with a blind measurement with constant source power, where it was proven that the calorimeter satisfies the accuracy goal ($< 1\%$);

phase 2: measurements with the aluminum shield at the final measurement position in the clean room at Borexino end of 2016 / beginning of 2017. Here mostly measurements with constant source power were done to find the optimum measurement conditions.

phase 3: measurements with the actual tungsten alloy biological shield in the Borexino clean room in the first half of 2017. The focus here was put on transient measurements (i.e. a source with a varying power), since the time response of the system depends on the thermal diffusivity of the shield. In a blind measurement, where the electrical source simulated the decay of the ^{144}Ce-^{144}Pr antineutrino generator, it was proven with the two independent analysis methods that the heat can be measured with the desired accuracy.

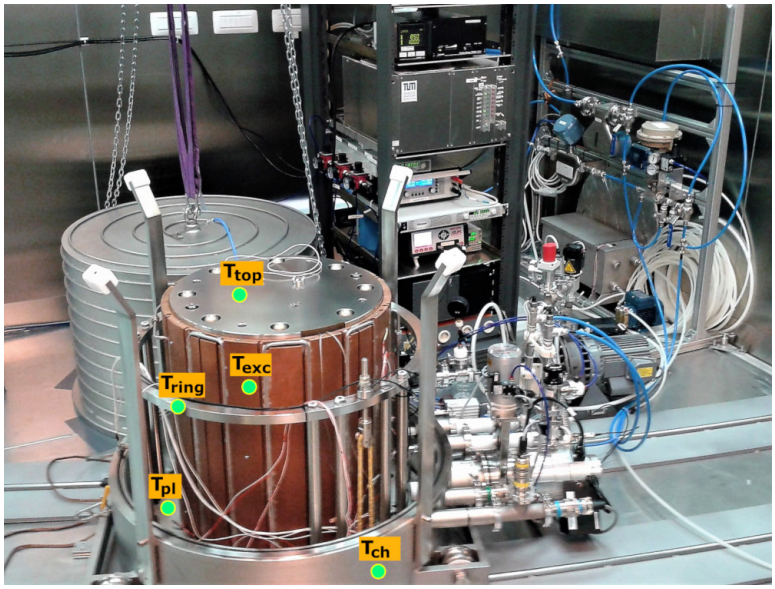

Figure 5.1: The positions of the RTDs to monitor the temperature distribution in the calorimeter.

Additional tests were performed at LNGS to train the handling of the calorimeter together with the radioactive source, as well as measurements without vacuum and super-insulator (as at the final source position in the pit). The results presented here are based mostly on phase 2 and 3, since in the first phase the setup can not be regarded as final due to frequent changes in the hardware and control software. In some measurements, the setup was deliberately put into a non correct configuration in order to study heat losses or examine the impact of unforeseen problems, e.g. poor vacuum, introduction of a thermal link, missing super-insulator and a not entirely closed heat exchanger.

Crucial for measurements are the RTDs, which are placed throughout the setup to monitor the temperatures at several points, and thus allow us to correlate heat losses with the temperature distribution and to optimize the measurement conditions. Following temperatures are monitored by the RTDs:

- T_{exc}: the temperature on the lateral surface of the copper heat exchanger;
- T_{pl}: the temperature of the stainless steel platform, where the heat exchanger is placed on;
- T_{ring}: the temperature of the support structure, that suspends the platform with the heat exchanger by three pairs of Kevlar ropes. The support itself is mounted onto the bottom of the vacuum chamber with several steel columns;
- T_{ch}, the temperature of the vacuum chamber;
- T_{top}, the temperature on the top of the steel flange that is mounted onto the shield.

The position of the temperature sensors are marked on the photo in figure 5.1.

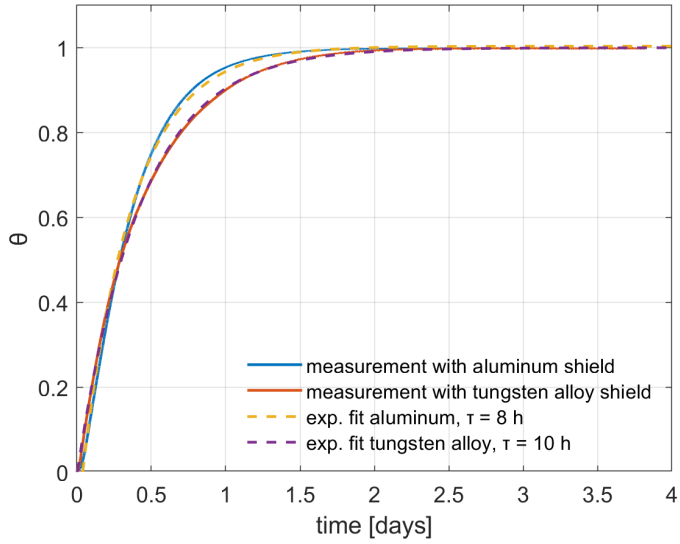

Figure 5.2: The time response of θ, the normalized ΔT to a power step function, fitted with an exponential function (see equation 5.1) for measurements with the aluminum and tungsten shield. It can be seen that the time for the constant for tungsten is larger: to reach 99.9% of final temperature, it is necessary to wait 2.9 days with the tungsten, while for the aluminum its only 2.3 days. One can conclude that a single measurement takes 3 to 5 days, because after the thermalization the stability of the system has to be verified.

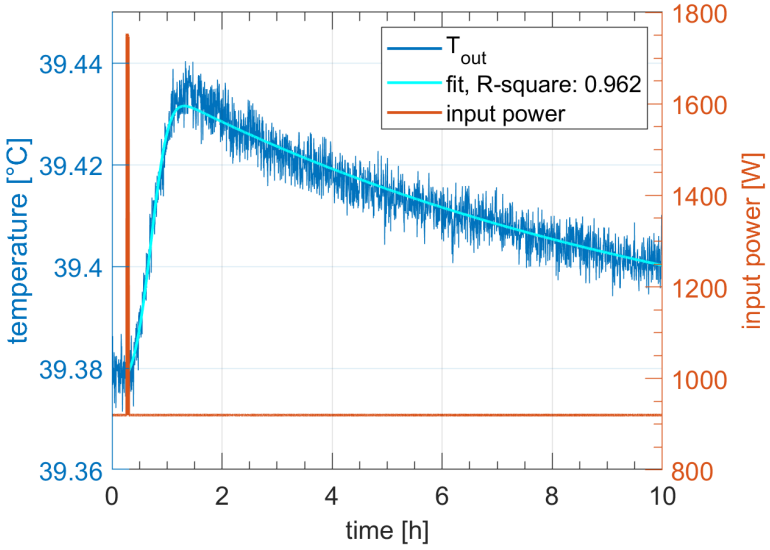

Figure 5.3: The temperature response (left axis) to a δ-like input power function (right axis). The temperature reaches after $\sim 1\,\mathrm{h}$ a peak and then follows an exponential with the same time constant $\tau_{\mathrm{th}} = 10\,\mathrm{h}$ as the calorimeter response to a step function. The response was fitted with equation 5.4. The coefficient of determination (R-square) of the fit results is 0.962.

5.2 Time response of the calorimeter

Due to the finite thermal diffusivity of the calorimeter, a change of the source power is observed in the measurement of the water temperature as a delayed, time-dependent function – the time response. The difference between measurements with the aluminum and the tungsten alloy shield can be shown nicely by looking at the time response to a step function of the source power. Figure 5.2 shows θ, the difference between the outlet and inlet water temperature ($\Delta T = T_{\text{out}} - T_{\text{in}}$), normalized to unity, after the power was turned on in the calorimeter, which was before at room temperature. Data from measurements with the aluminum shield and the tungsten alloy shield are plotted there as a function of time. The data were fitted using the exponential function

$$\theta(t) = 1 - e^{-t/\tau_{\text{th}}}, \tag{5.1}$$

where τ_{th} is the thermal time constant of the system (according to the solution of the heat diffusion equation, see [ADN+18]). When the aluminum shield was used, the time constant $\tau_{\text{th}}^{\text{Al}}$ was found to be about 8 h, and for the tungsten shield $\tau_{\text{th}}^{\text{W}} \approx 10\,\text{h}$. The thermalization time t_{th}, i.e. the time between turning on / inserting the source and starting the measurement at stable conditions, can be defined as $t_{\text{th}} = -\ln(0.001) \cdot \tau_{\text{th}}$. At this time, the temperature has reached 99.9% of its maximum, thus the error is $<1‰$ from then on. The resulting thermalization time are 2.3 days for aluminum, and 2.9 days for the tungsten alloy. This difference is due to the thermal properties of the aluminum and tungsten that influence the heat propagation time from the inner heat source to the water pipe. In summary, a single measurement takes between 3 and 5 days, because after the thermalization phase, the measurement has to be continued to monitor the stability over a time equal to a few τ_{th}.

The time response of a system to a changing temperature can be approximated analytically by equating the internal energy loss of a body with the heat loss on the surface (Newton's law of cooling, see e.g. [LNS04]):

$$-\rho \cdot c_{\text{p}} \cdot V \cdot \frac{\text{d}\Delta T}{\text{d}t} = h \cdot A \cdot \Delta T(t), \tag{5.2}$$

where ρ is the density, c_{p} the specific heat capacity, V the volume of the body, A the outer surface and h the heat transfer coefficient, which was assumed in [ADN+18] to be $15\,\text{W/m}^2$ (determined through finite element analysis). The solution of this differential equation is the above fitted exponential (equation 5.1), and the time constant τ_{th} is then

$$\tau_{\text{th}} = \frac{\rho \cdot c_{\text{p}} \cdot V}{h \cdot A}. \tag{5.3}$$

If we insert $V/A = 0.1\,\text{m}$ (using the dimensions of the shield) and the textbook thermal properties of the materials, for both shields time constants $\sim 5\,\text{h}$ are obtained. Comparing this to the measured values of 8 and 10 h, it can be concluded that the heat transfer coefficient is smaller than assumed.

When data is taken with a decaying source, due to the time response the measured power will follow the generated power with a delay t_{d}. To estimate t_{d}, we first look at the response of the calorimeter for a δ-like function. Figure 5.3 shows such a measurement with the tungsten shield. The power spike of 800 W was put on top of a running stable measurement at 920 W source power. One can see that the measured power (in the plot the outlet temperature is shown, which is proportional to the measured power,

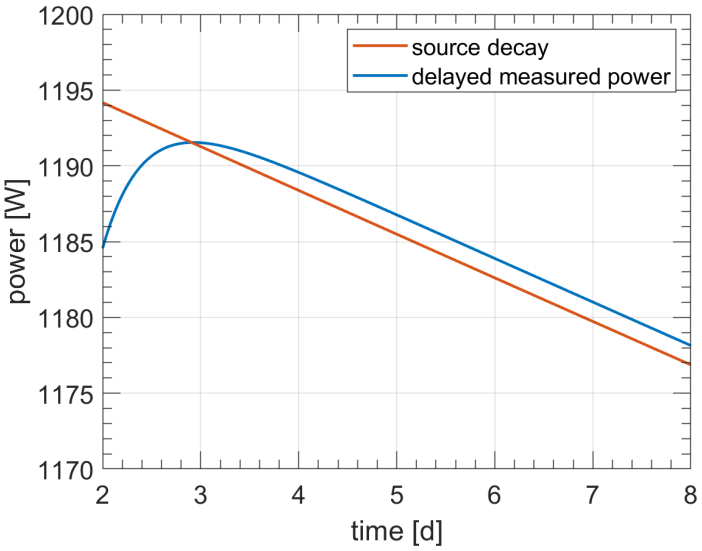

Figure 5.4: An exponential decay function convolved with the calorimeter response to a δ-like input power. The resulting curve corresponds to the power measured with the calorimeter (blue), which follows the decaying power of the source (red) with a delay of 0.45 days.

but shows less fluctuations) increases and reaches an maximum after $\sim 1\,\mathrm{h}$ and then slowly decays back to the original value. This function can be fitted with an exponential multiplied with an error function:

$$T_{\mathrm{out}}(t) = T_0 + \Delta T \cdot \exp\left(\frac{-t}{\tau_{\mathrm{th}}}\right) \cdot \left[0.5 + 0.5 \cdot \mathrm{erf}\left(a \cdot (t-b)\right)\right], \tag{5.4}$$

where the fitted parameters are the original temperature in steady state $T_0 = 39.38°\mathrm{C}$, the temperature increase $\Delta T = 0.06°\mathrm{C}$, the time constant of the exponential $\tau_{\mathrm{th}} = 10.21\,\mathrm{h}$, similar to the time constant for the step response with tungsten (see figure 5.2), and the parameters for the error function $a = 2.83$ and $b = 0.43$. This function is then normalized and convolved with a decay function with the 411 days decay time of ^{144}Ce. The result is shown in figure 5.4. The convolved function, which models the measured power, follows the actual source power with a delay of $t_{\mathrm{d}} = 0.45\,\mathrm{d}$. This corresponds to a deviation of the measured power of 0.11%. This is smaller than the typical measurement error for steady state measurements and in the order of the heat losses.
The time delay was also analytically approximated in [ADN+18] and found to be 0.4 days, which is well in agreement with the empirical estimation presented here.

5.3 Measurements with the aluminum shield

The measurements with the aluminum shield were mostly conducted with a constant heat power in order to optimize the measurement conditions and to determine heat losses. Following the analysis method described in chapter 4 the measured power P_{meas} was obtained and compared to the electrically measured power P_{set}. The heat loss is then the difference: $P_{\mathrm{loss}} = P_{\mathrm{set}} - P_{\mathrm{meas}}$. A positive loss means that heat was transferred to the external environment without detection, while a negative value is due to heat

Run №	P_{set} [W]	$\dot{m}$ [g/s]	T_{in} [°C]	T_{exc}[°C]	T_{ch}[°C]	ΔP [W]
3 4/5	500	5.0	15.5	25.9	15.1	-0.5 ± 0.8
3 5	500	5.0	15.5	25.8	21.8	-0.6 ± 0.8
3 6	700	5.0	15.6	31.9	22.1	0.2 ± 0.8
3 7	700	5.0	15.5	31.7	15.3	1.5 ± 0.9
3 8	700	6.3	15.5	27.3	15.4	0.3 ± 1.0
3 9	700	6.3	15.5	27.4	15.4	1.4 ± 1.0
3 10	920	8.3	15.5	26.9	15.4	1.9 ± 1.3
3 11	920	8.3	15.5	26.9	15.3	0.7 ± 1.3
3 12	920	9.2	15.5	25.2	15.1	0.4 ± 1.4
3 16	729	5.0	16.1	26.1	37.6	-3.2 ± 0.9
3 17	729	5.0	15.8	25.5	27.1	-1.2 ± 0.8
3 18	729	5.0	15.7	25.2	21.3	-0.2 ± 0.8

Table 5.1: List of measurements from the second phase to optimize the conditions of operation. All measurements were conducted with a constant source power.

entering the system, e.g. when the ambient temperature is higher than the temperature inside the calorimeter.

5.3.1 Minimization of heat losses: optimization of the measurement conditions

The optimization of the calorimeter was done through calibration measurements, while using several values of source power, water mass flow and external vacuum chamber temperatures. These measurements are listed in table 5.1. During these measurements the setup was in the regular configuration, with both super-insulation radiation shields in place and with a residual air pressure of $\sim 5 \cdot 10^{-5}$ mbar in the vacuum chamber. At early stages of the measurements in the first phase it became already clear that the heat losses can be correlated to the temperature distribution within the calorimeter, most strongly with the temperature difference between the heat exchanger and the vacuum chamber $T_{\text{exc}} - T_{\text{ch}}$. A plot of the relative heat loss $P_{\text{loss}}/P_{\text{set}}$ with respect to $T_{\text{exc}} - T_{\text{ch}}$ from measurements in phase 2 (final setup at LNGS) is shown in figure 5.5. The correlation is clearly visible and illustrated with a linear fit. The color and markers of the data points refer to different electrical powers and mass flow values and the run numbers are added next to each data point. However, the value of the set power and the mass flow do not seem to affect the heat losses significantly. This is evident for example in the data around $T_{\text{exc}} - T_{\text{ch}} = 10°\text{C}$, where the error bars of all measurements are overlapping. In general, with exception of run 16, where the vacuum chamber was heated to almost 40°C, the losses are always smaller than 0.3%. In the green marked region where $0°\text{C} < T_{\text{exc}} - T_{\text{ch}} < 11°\text{C}$ the heat losses are compatible with zero, considering the measurement error.
Even though in the data of plot 5.5 the mass flow value does not seem to have an effect on the heat losses, it plays an important role, since the mass flow determines the outlet temperature T_{out} and thus also T_{exc}. $T_{\text{exc}} - T_{\text{ch}}$ cannot be adjusted only through the temperature of the vacuum chamber, since the chamber is exposed in a clean room with $\sim 15°\text{C}$ ambient temperature and can be heated only to a certain extent. In conclusion, by choosing a proper mass flow and chamber temperature one can ensure that the temperature difference between the heat exchanger and the vacuum chamber is in the range of $0 - 11°\text{C}$. In this case the heat losses are in the same order as the

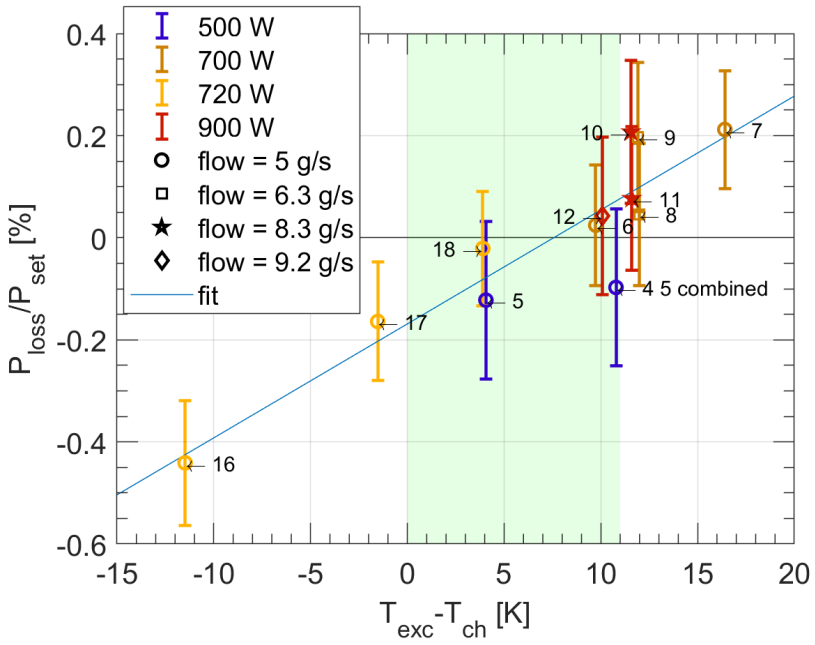

Figure 5.5: Heat losses plotted with respect to the temperature difference between the heat exchanger T_{exc} and the vacuum chamber T_{ch}. A correlation is clearly visible and verified trough a linear fit. The color and markers of the data points refer to different electrical powers and mass flow values and the run numbers are added next to each data point. When $0°\text{C} < T_{\text{exc}} - T_{\text{ch}} < 11°\text{C}$ (green zone), the heat losses are in the same order as the measurement error and thus can be neglected. By adjusting the mass flow and the chamber temperature this condition can be achieved for every measurement.

measurement error and can be neglected.
In the plot of figure 5.5 one can wonder, why the heat losses are not minimized for $T_{\text{exc}} - T_{\text{ch}} = 0$. Here one has to consider that T_{exc} is the temperature of the heat exchanger measured at one point, but the temperature is not homogeneous across the surface.

The measurements from phase 1 and 2 were also used to optimize the parameters for the flow and temperature control . Data that shows the reduction of fluctuations in the water mass flow and temperature by the stabilization are shown in figures 5.6 and 5.7. The stabilization was achieved by steering the valve or the heater through a proportional-integral-derivative (PID) controller that depends on the measured mass flow and temperature. In the plots the y axis shows a similar interval for unstabilized and stabilized data. Except for oscillations around the mean, no major fluctuations of the stabilized data are visible.

5.3.2 Study of the radiation losses without the inner super-insulator stage

In order to study the radiation losses, the inner stage of the super-insulator was removed for a set of measurements and the heat losses obtained with and without the super-insulator stage were compared to each other. This measurement might seem unnecessary, because there is no reason, why the radiation shield should be missing in the real measurement. However, the determination of the radiation losses allows us to see if the calorimeter behaves in a predictable way and helps us to fully understand the

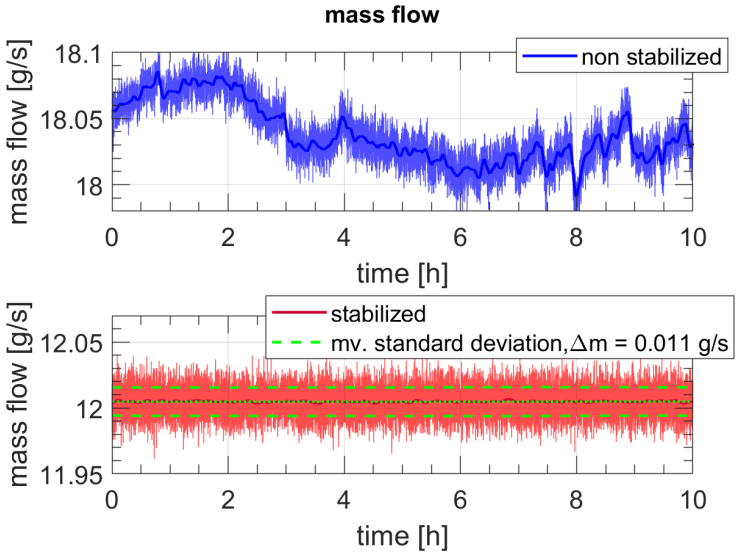

Figure 5.6: The stabilization of the mass flow: in the non-stabilized data in the top plot one can see in addition to the short oscillations around the local mean instabilities on the scale of hours due to non-constant pumping from the chiller. To prevent these flow instabilities from disrupting the thermal equilibrium of the calorimeter, the flow is stabilized by a valve that is connected to one of the flow meters through a feed-back loop. The resulting flow is shown in the bottom plot. The flow is now very stable. The moving standard deviation of the oscillations is 0.01 g/s.

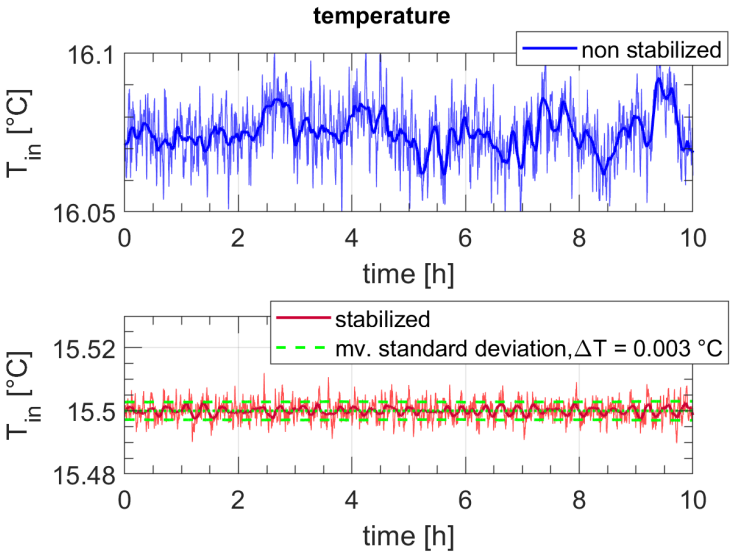

Figure 5.7: The stabilization of the temperature: the fluctuating water temperature as it leaves the chiller is shown in the top plot. In the bottom plot the temperature stabilized with a heater, which is controlled by the inlet thermometer via a feed-back loop, is shown. The fluctuations are reduced, the standard deviation of the oscillations is a few mK.

Run №	comment	P_{set} [W]	$\dot{m}$ [g/s]	T_{in} [°C]	T_{exc}[°C]	T_{ch}[°C]	ΔP [W]
2 27	w/o SI	920	6.3	17.0	45.0	41.0	2.1 ± 1.3
2 28	w/o SI	920	6.3	17.0	44.9	32.0	4.2 ± 1.2
2 30		920	6.3	17.0	45.1	41.0	-0.4 ± 1.2
2 31		920	6.3	17.0	45.1	34.3	0.3 ± 1.8

Table 5.2: List of measurements from the first phase to study radiation losses. Run 27 and 28 were performed with the inner super-insulator stage removed. The measurements consist of two pairs with and without super-insulator, but with matching vacuum chamber temperatures T_{ch}.

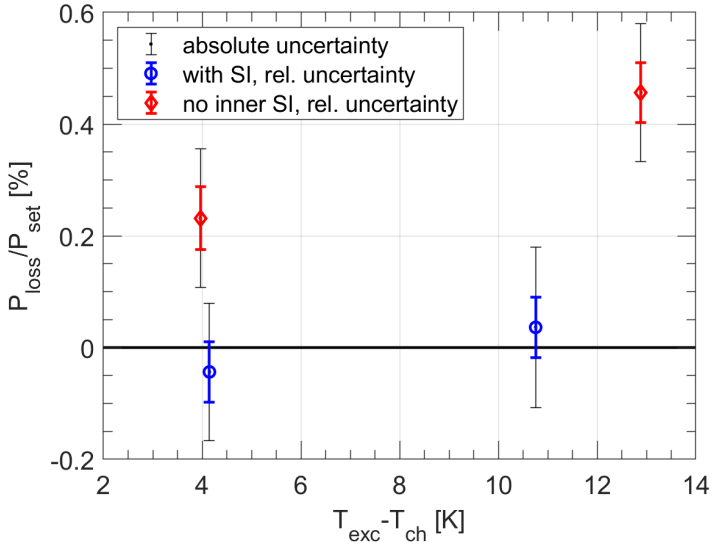

Figure 5.8: Heat losses for measurements in standard configuration (blue) and without the inner super-insulator stage (red). While for the data with the radiation shield the losses are compatible with zero, the heat losses are significantly increased when the super-insulator is removed. The absolute error is displayed by the black error bars, the colored error bars are the relative errors when the results are compared to each other.

apparatus.
The list of measurements for this study is shown in table 5.2. In figure 5.8 the heat losses $P_{\text{loss}}/P_{\text{set}}$ are shown as a function of the difference of the temperatures $T_{\text{exc}} - T_{\text{ch}}$. In addition to the ordinary measurement error (black), the relative uncertainties are shown, where the error of the enthalpy function was neglected (as described in chapter 4). This is possible, if the enthalpy difference of the compared measurements is small, which is true in this case. Note that this error allows only a comparison between the measured heat losses, the absolute error is the black error bar, which includes the error of the enthalpy function.

There are two pairs of measurements, each consisting of one run in standard configuration, and one without the inner super-insulator stage. Within each pair a similar $T_{\text{exc}} - T_{\text{ch}}$ was set[1]. One can see that the data with super-insulator shows heat losses

[1]For run 28 and 31 (see table 5.2) the chamber temperature is not exactly the same (32.0°C vs 34.3°C). These measurements are from the first phase of measurements, which were conducted at TUM, where the ambient temperature is varying strongly in contrast to the very stable LNGS environment. The variations complicate the temperature control of the vacuum chamber.

compatible with zero, as expected since the calorimeter was operated in the optimum conditions ($0°C < T_{exc} - T_{ch} < 11°C$, see the previous section). When the super-insulator is removed, the losses are significantly increased to 0.2 and 0.5%, where the increase is stronger for the larger $T_{exc} - T_{ch}$.
In absence of the inner radiation shield the losses are due to the heat transferred to the support structure, which is enclosed together with the heat exchanger within the outer super-insulator. The highly specular/low absorption super-insulator foil reflects the thermal radiation from the heat exchanger onto the support structure. This effect is visible by observing the temperatures measured by the RTDs shown in figure 5.9, in particular the temperature T_{ring} measured on the ring of the support structure. For each pair of measurements the temperature T_{exc}, T_{ch} and T_{pl} are similar, while T_{ring} is by $\sim 5°C$ increased when the radiation shield is removed (white area in the plot).

In absolute values, without super-insulator the radiative heat losses can be as big as $\sim$4 W (see table 5.2). They can be theoretically quantified by approximating the transferred power between the heat exchanger and the outer super-insulator to the support structure with the following relation calculated for infinitely long concentric cylinders or spheres [RS92]:

$$Q = \frac{A_2 \cdot \sigma \cdot (T_1^4 - T_2^4)}{1/\epsilon_1 + 1/\epsilon_2 - 1}, \tag{5.5}$$

where the inner surface (support structure, denoted with index 1) is diffusely emitting and the outer surface (super-insulator, index 2) is specular. The specular super-insulator surface reflects the thermal radiation from the copper and it is therefore regarded to have the temperature and emissivity of the copper heat exchanger. Using textbook-emissivities (sand-blasted copper: $\epsilon_1 = 0.74$, electropolished steel: $\epsilon_2 = 0.07$), the surface $A_2 = 0.6\,m^2$ and inserting the temperatures from the measurements we obtain $Q \approx 1.5$ W, which is in the same order of magnitude as the measured value.
In summary these measurements have verified the importance and functionality of the super-insulator shield and also showed that we understand the thermal behavior of the apparatus.

5.3.3 Study of the heat losses at higher residual pressure

A set of measurements was performed at an increased residual air pressure by switching off the turbomolecular pump, using only the scroll pump, to study heat losses by convection. These measurements are relevant, because it is possible that a good vacuum cannot be achieved during the measurement with the antineutrino source. The source activity will be first determined by the CEA calorimeter, where the shield is in contact with water (see section 2.4). Even though it should be cleaned before the insertion into the TUM-Genova calorimeter, there might be some corrosion that greatly increases the outgassing and prevents us from reaching low pressures.
With the turbo pump turned on a pressure $\sim 10^{-5}$ mbar or lower was achieved, while it was $\sim$ 2-3 $\cdot 10^{-3}$ mbar when the turbo pump was off.
In figure 5.10, the losses P_{loss} observed at high and low pressure are shown as a function of $T_{exc} - T_{ch}$ for two pairs of measurements, where each pair of data was taken with similar source power and chamber temperature. The data is also listed in table 5.3. When $T_{exc} - T_{ch}$ is in the optimum range, which is true for the first pair of data at $T_{exc} - T_{ch} = 11°C$, the heat losses are in agreement with zero even at high pressure, when the absolute error (black error bar) is considered. When one takes the relative error for comparing both values into account (the error of the enthalpy function is reduced,

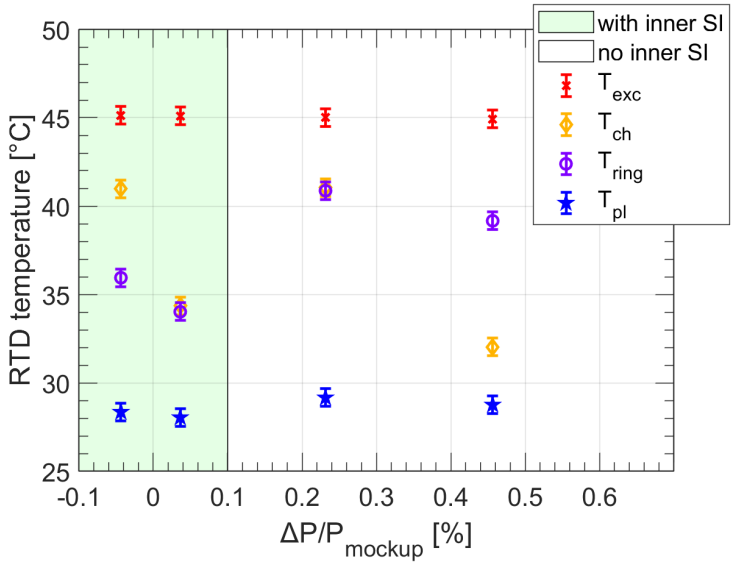

Figure 5.9: The temperature distribution within the calorimeter for measurements with (green area) and without inner super-insulator (white area). Due to the missing radiation shield, heat is transferred from the calorimeter to the support structure (the ring), as it is confirmed by the increased T_{ring} in the white area.

Run №	pressure [mbar]	P_{set} [W]	$\dot{m}$ [g/s]	T_{in} [°C]	T_{exc}[°C]	T_{ch}[°C]	ΔP [W]
3 2	$1.9 \cdot 10^{-3}$	700	5	15.5	32.0	15.3	3.2 ± 1.0
3 3	$1.5 \cdot 10^{-3}$	500	5	15.5	25.9	15.1	0.5 ± 0.8
3 4/5	$< 10^{-5}$	500	5	15.5	25.9	15.1	-0.5 ± 0.8
3 7	$< 10^{-5}$	700	5	15.5	31.7	15.3	1.5 ± 0.8

Table 5.3: List of measurements from the second phase to study convection losses.

see chapter 4), the convection effect is clearly visible as both errors do not overlap and the separation of both data points is 1 W. This is in agreement with simulations that predicted a convective heat loss of 0.6 W under similar measurement conditions (see section 3.2). For the measurements at higher source power $T_{\text{exc}} - T_{\text{ch}} = 16.5°\text{C}$ is out of the optimum range and both data at low and high pressure show heat losses, which are increased by 1.7 W in case of high pressure.
The change of the losses as a function of the pressure is not as strong as the dependence on the temperature difference $T_{\text{exc}} - T_{\text{ch}}$. The measurements performed with a bigger value of $T_{\text{exc}} - T_{\text{ch}}$ and with the turbo-pump on have bigger heat losses than the measurements performed with the turbo off at smaller values of $T_{\text{exc}} - T_{\text{ch}}$.
We can conclude that also in the case in which a low pressure cannot be achieved due to surface outgassing or other unexpected problems, the convection losses can be reduced down to $< 0.2\%$ by setting proper values of T_{ch} and mass flow such that $T_{\text{exc}} - T_{\text{ch}} < 11°\text{C}$.

5.3.4 Conclusions from the stationary measurements

In conclusion, many measurements with a constant source power inside the aluminum shield were done in order to calibrate the system, to optimize the measurement conditions and to estimate the heat losses. It was shown that the heat losses can be reduced

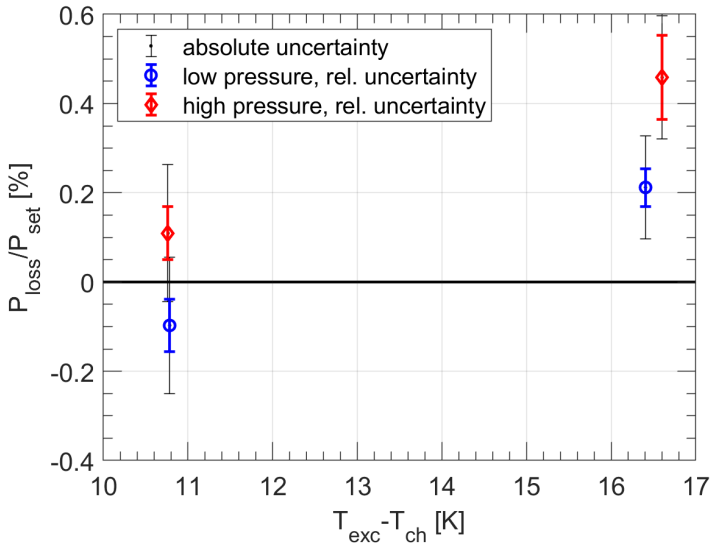

Figure 5.10: P_{loss} as obtained with the turbomolecular pump on ($p \sim 10^{-5}$ mbar, blue data) and off ($p \sim 10^{-3}$ mbar, red data) as a function of $T_{\mathrm{exc}} - T_{\mathrm{ch}}$, the difference of the temperature between the copper heat exchanger. When the condition $0°\mathrm{C} < T_{\mathrm{exc}} - T_{\mathrm{ch}} < 11°\mathrm{C}$ for minimal heat losses is fulfilled, losses are negligible even at high pressure.

Run №	P_{set} [W]	$\dot{m}$ [g/s]	T_{in} [°C]	T_{exc}[°C]	T_{ch}[°C]	P [W] (Genova analysis)	P [W] (TUM analysis)
2 23	729	5	17	45.8	32.3	728.4 ± 1.1	727.9 ± 1.4
2 24	729	5	17	45.8	34.7	727.2 ± 1.1	727.8 ± 1.0
2 25	729	5	17	45.8	41.0	-	728.3 ± 1.1

Table 5.4: Three subsequent measurements were analyzed blindly through two independent methods, one by Lea di Noto of INFN Genova (Genova analysis) and one by the author (TUM analysis). Both analysis used different enthalpy functions, stability conditions and error calculations. In the Genova analysis the data from run 25 was not stable enough to qualify for analysis. In the end both results are in agreement with each other and the set power, and thus it was proven that the calorimeter can determine the heat released by the source with 0.2% accuracy.

close to negligible values if $T_{\mathrm{exc}} - T_{\mathrm{ch}}$ is set between 0 and 11°C by adjusting the mass flow and the vacuum chamber temperature, even when only a moderate vacuum pressure of $\sim 10^{-3}$ mbar can be established.

As a confirmation of the previously discussed results a stationary 'blind' measurement was performed, where the power applied to the electrical heater (ranging between 700 W and 900 W) was hidden until the analysis was completed. The data was analyzed with two independent analysis, one by the author, following an earlier version of the method described in 4, and another one by Lea di Noto of INFN Genova. Differences are the enthalpy function, selection of the stability region and error calculation. The average value of the measured power, combined from both analyses, was $P_{\mathrm{meas}} = (727.9 \pm 1.3)$ W, whilst the applied power was revealed to be $P_{\mathrm{set}} = 729.0 \pm 0.3$ W, resulting in an agreement within 0.2 % for measurements with constant power. The individual results are shown in table 5.4.

Run №	comment	P_{set} [W]	$\dot{m}$ [g/s]	T_{in} [°C]	T_{exc} [°C]	T_{ch} [°C]	ΔP [W]
4 1		920	9.2	15.5	36.3	27.6	-0.2 ± 1.4
4 2		920	9.2	15.5	36.3	25.8	0.0 ± 1.4
4 9	no exc.-lid	920	9.2	15.5	43.6	25.5	0.9 ± 1.4
4 14	exc. opened	720	9.2	15.5	34.1	25.5	-0.8 ± 1.4
4 17	thermal link	920	10.0	15.5	33.2	25.2	-0.7 ± 1.5
4 19	thermal link	945	5.0	16.0	54.6	26.1	3.5 ± 1.1
4 20		905	11.0	15.5	31.2	26.0	-1.3 ± 1.6

Table 5.5: Steady state measurements with the tungsten shield: here the measurements from the third phase to optimize the conditions of operation are listed. All measurements were conducted with a constant source power. A few measurements were conducted with a non-standard configuration, as noted in the comment column.

5.4 Measurements with the tungsten alloy shield

In the last measurement phase, the electrical source was installed into the tungsten biological shield. First the previous results were verified with stationary measurements. A list of these measurements is shown in table 5.5, and $P_{\text{loss}}/P_{\text{set}}$ as a function of $T_{\text{exc}} - T_{\text{ch}}$ is plotted in figure 5.11. To simulate problems as they could occur during the source insertion for a few measurements a thermal link was inserted. The thermal link was a piece of plastic that connected the support structure with the platform, on which the heat exchanger and the shield with the source are placed. A contact like this could happen in a real measurement if the setup is slightly tilted. Another measurement was conducted with the heat exchanger not fully closed around the shield. The shield with the source is inserted into the heat exchanger by opening the lateral copper shells on one side. After the shield is slided in, the 10 screws are closed. Although no problems were experienced, it might happen that the screws block or the shells get deformed such that the closing cannot be completed. With the radioactive source the procedures will not allow to fix this issue, such that the measurement has to be commenced with the heat exchanger opened. However, in both cases the heat losses and the temperature distribution were not affected significantly. The heat losses are around zero when the condition $0°\text{C} < T_{\text{exc}} - T_{\text{ch}} < 11°\text{C}$ that was derived from the measurements with the aluminum shield is fulfilled.

One difference between measurements with the aluminum and the tungsten shield is that the temperature of the heat exchanger T_{exc} is different (at least at the position of the RTD). E.g. run 12 from the aluminum data (see table 5.1) and run 1 with the tungsten (see table 5.5) were both performed with a source power of 920 W and a mass flow of 9.2 g/s, but with aluminum the heat exchanger temperature was found to be 25°C while it was 36°C with the tungsten shield. To fulfill the condition for minimal heat losses $T_{exc} - T_{ch} < 11°\text{C}$ one has to accordingly increase the chamber temperature. However, the chamber temperature can be kept at maximum at a temperature of $\sim 30°\text{C}$ due to the cool underground environment. As a result the mass flow has to be large enough to ensure that $T_{\text{exc}} < 41°\text{C}$, which ultimately puts a limit on the enthalpy difference $\Delta h \approx P/\dot{m}$. The heat exchanger temperature is typically a few degrees below the outlet water temperature. With an inlet water temperature of 15 - 16 °C, the limit on ΔT is then $\sim 25°\text{C}$, resulting in the limit $P/\dot{m} < 0.11\,\text{J/kg}$. Figure 5.12 shows T_{exc} as a function of $P/\dot{m}$ for measurements with the aluminum and tungsten shield. First,

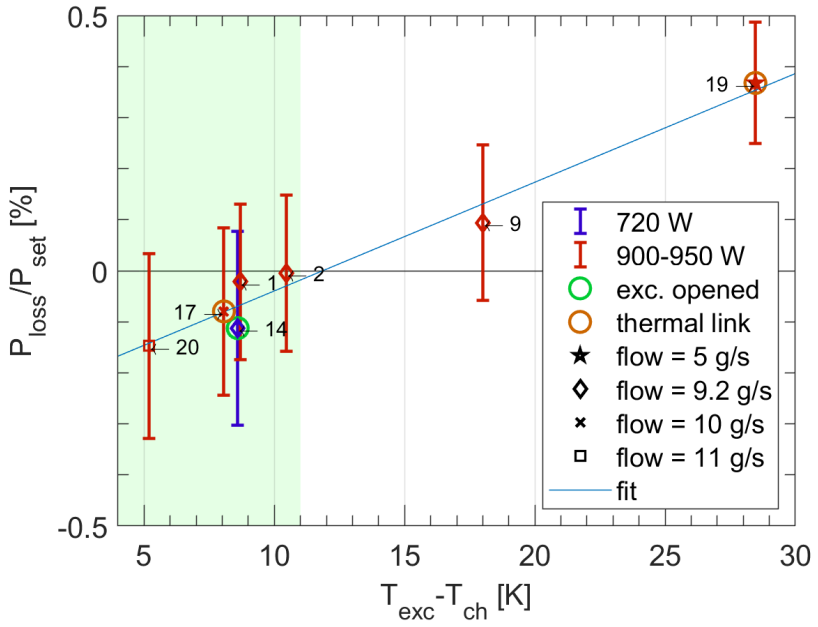

Figure 5.11: Steady state measurements with the tungsten shield: as for the measurements with the aluminum shield a linear dependence of the heat losses on the temperature difference between the heat exchanger and the vacuum chamber $T_{\mathrm{exc}} - T_{\mathrm{ch}}$ is observed. The green area marks the region, where heat losses are negligible that was found with the aluminum shield measurements. Here we see that also for the tungsten shield losses in this region are negligible and that the condition $0°\mathrm{C} < T_{\mathrm{exc}} - T_{\mathrm{ch}} < 11°\mathrm{C}$ holds true.

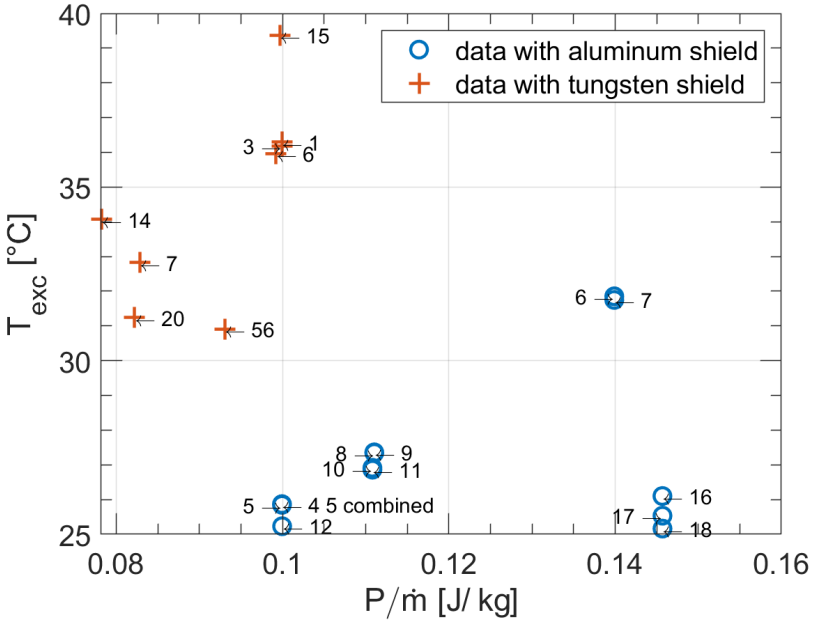

Figure 5.12: The heat exchanger temperature T_{exc} as a function of $P/\dot{m}$ compared for measurements with the aluminum and tungsten shields. One can see that the heat exchanger temperature is much higher for measurements with the tungsten shield. The condition $T_{\mathrm{exc}} < 11°\mathrm{C}$ for the heat loss minimization imposes a limit of $\sim 40°\mathrm{C}$ on T_{exc}, that is fulfilled with the tungsten when $P/\dot{m} < 0.11\,\mathrm{J/kg}$.

Run №	comment	P_{set} [W] at t_0	$\dot{m}$ [g/s]	T_{in} [°C]	T_{exc} [°C]	T_{ch} [°C]	P_{meas} [W] at t_0
4 3		920.0	9.2	15.5	36.2	25.9	919.7 ± 1.4
4 5		920.0	9.2	15.5	36.0	25.7	919.9 ± 1.4
4 6		913.6	9.2	15.5	36.0	25.7	913.4 ± 1.4
4 7		911.4	11	15.5	32.8	25.6	911.9 ± 1.6
4 15	exc. opened	917.8	9.2	15.5	39.4	25.6	918.3 ± 1.4
4 18	thermal link	960.0	5	16.0	54.7	25.8	956.4 ± 0.9
4 56	blind meas.	1117.0	12	15.5	30.9	29.2	1116.9 ± 1.8

Table 5.6: List of measurements with a decaying source in the tungsten shield. The power difference in the last column was corrected by a factor 0.9989 according to the time delay. A few measurements were conducted with a non-standard configuration, as noted in the comment column.

one can see that the temperature of the heat exchanger is higher with the tungsten shield, and second, that indeed T_{exc} is smaller than 41°C, since all measurements with the tungsten had a mass flow that kept $P/\dot{m}$ below 0.11 J/kg.

Finally the calorimeter was calibrated for transient measurements with a decaying source by letting the electrical power decline following an exponential function with the lifetime of ^{144}Ce, $\tau = 411$ d. As explained in section 5.2, due to the heat propagation through the shield the measured power follows the source decay with a delay of 0.45 d. This delay can be compensated by multiplying the measured power by a factor $e^{-0.45/411} = 0.9989$. The results of the transient measurements are listed in table 5.6 and plotted in figure 5.13. The uncorrected values are displayed with gray markers. As it can be seen, the correction moves the heat losses closer to zero. Also with a decaying source, measurements with a thermal link and a not fully closed copper shell of the heat exchanger were performed. While the measurement with the thermal link shows significant heat losses due to the large difference of chamber and heat exchanger temperature, the measurement with the copper shells opened shows negligible heat losses.

5.4.1 Final tests: blind measurement with the tungsten alloy shield and ISPRA test

The calibration campaign was concluded with another blind measurement, this time with the tungsten shield and a decaying source power. The power value was set on 25th of September 2017 at 08:40:00 without being known to the analysis team, and was from then decaying with a life time of 411 days (known to the analysis team). Since a power between 1000 and 1200 W was expected (as with the final source) a mass flow of 12 g/s was chosen to satisfy the condition $P/\dot{m} \sim 100$ J/g and T_{ch} was set to 31°C.
The blind measurement was simulated as the measurement with the radioactive source, i.e. a first measurement was done with the CEA calorimeter, and directly afterwards the measurement presented in the following was performed. In the CEA calorimeter the shield is in direct contact with water, as a consequence it had to be cleaned before the insertion into the TUM-Genova calorimeter. Still, stable conditions were not reached for several days due to outgassing from the shield. The trend of the pressure is shown in figure 5.14 together with the outlet water temperature. One can see that even small fluctuations in the pressure on 1st and 2nd of October disrupted the stability. Only 5 days after the insertion of the source into the TUM-Genova calorimeter the

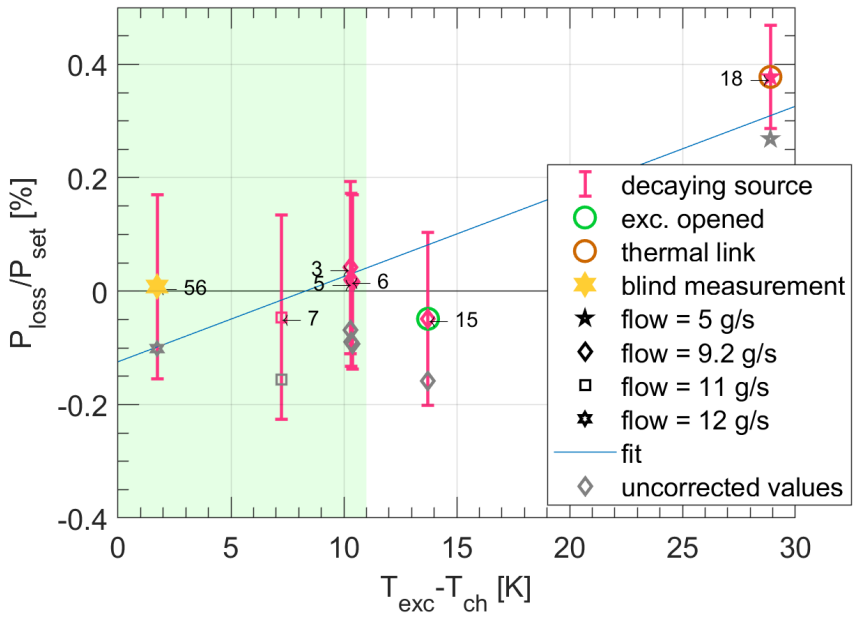

Figure 5.13: Heat losses for measurements with a decaying source in the tungsten shield as a function of $T_{\mathrm{exc}} - T_{\mathrm{ch}}$. The colored data shows the measured power with a correction for the time delay, the uncorrected data is shown in gray. The green area marks again the region, where heat losses are negligible, as it was derived from the measurements with the aluminum shield. Also here the heat losses are in agreement with zero. Some data was taken in non-standard configuration with a thermal link or an only partially closed heat exchanger. However, this did not significantly affect the heat losses and the temperature distribution.

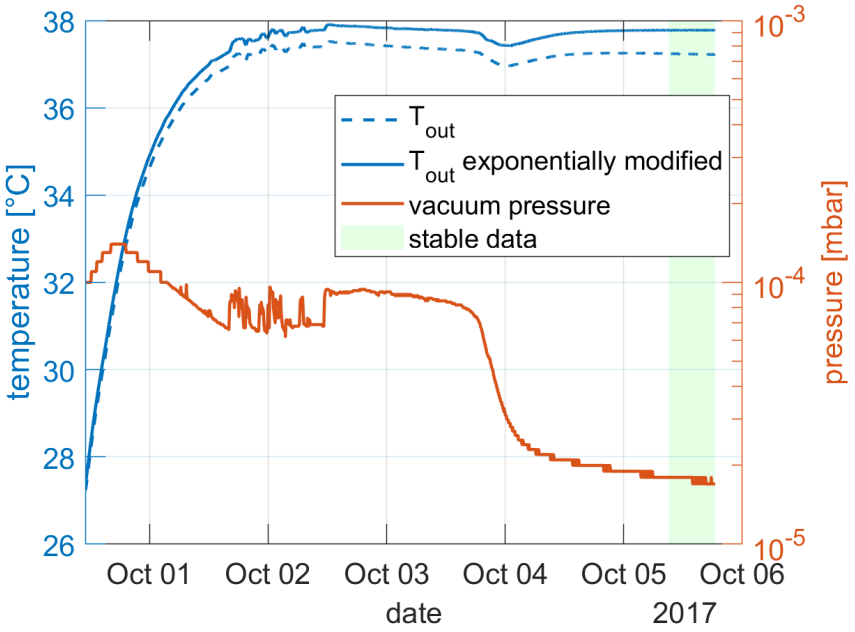

Figure 5.14: Blind measurement: on the left axis the outlet temperature of the water is plotted (dashed line). The solid line shows the exponentially modified temperature (with respect to t_0 = Sept. 25, 2017, 08:40:00) that becomes constant when the system is stable. On the right axis the residual air pressure within the calorimeter is shown. One can see that stability is only reached, after the pressure is stable (green area). Even small pressure changes on 1st and 2nd of October disrupt the stability. In the end the measurement lasted more than five days.

stability condition is fulfilled (green area) and the measured power evaluated. The data were stable enough to allow a 6 h time window for the stability condition (see chapter 4).

To present this measurement with greater detail, also plots of the power (figure 5.15) and the temperature distribution (figure 5.16) are shown here. For the remaining data as the mass flow and inlet water temperature no plots are shown, since both were constant without any unusual features.
In the power plot of figure 5.15 the measured and input power are shown. The exponentially modified power is colored, the original measured data is gray. Since it was a blind measurement the value of the set power was not acquired and just added to the plot after its revelation. The power is fluctuating as the outlet water temperature plot. The measured power is a bit higher than the input power due to the time delay described in section 5.2. The measured power corresponds to the set power 0.45 days earlier, which makes a difference of 0.11%, i.e. ~ 1 W.
In figure 5.16 the temperatures measured by the RTDs at several positions are plotted. The temperature of the top flange on the shield is out of the plot boundaries at ~ 120°C. One can see that there was a problem with the actively controlled chamber temperature when its average value was dropping by 1°C. The oscillations of the chamber temperature are normal and are caused by the temperature control. In addition, also here fluctuations are visible in the temperatures of the internal components. However, when the stability condition is fulfilled, also the temperature distribution is not changing anymore.

To estimate the source power which was set at 25th of September 2017 at 08:40, de-

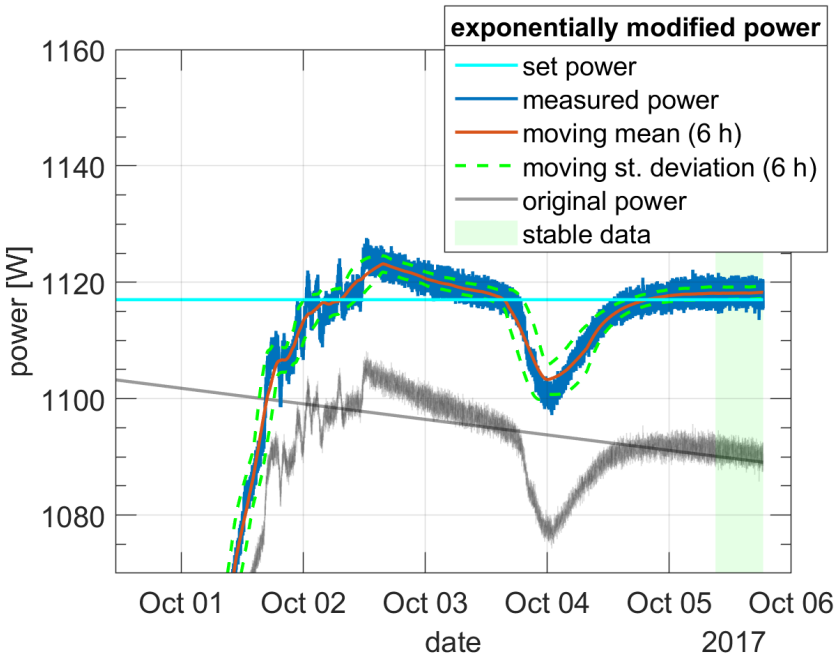

Figure 5.15: The measured power with the exponential modification (in color) and without any modification as measured (gray). The measured power is a bit higher than the input power due to the time delay described in section 5.2. The measured power corresponds to the set power 0.45 days earlier, which makes a difference of 0.11%, i.e. $\sim 1\,\mathrm{W}$. As in figure 5.14 one can see that the power is fluctuating as the outlet temperature. The region where the stability condition was fulfilled is marked in green. The measured power in this region was then averaged to obtain the final value.

fined as t_0, the measured power was first multiplied with the exponential correction $\exp(t - t_0/\tau)$, and then its value was averaged over the period when the stability condition was fulfilled, which is the green area in the plot of figure 5.15. It was found that $P_{\mathrm{meas}}|_{t_0} = (1118.1 \pm 1.8)\,\mathrm{W}$. This value was shared with the collaboration, and, considering the error, is in agreement with the set power of 1117 W at t_0. However, the measured value has to be corrected for the time delay, i.e. to be multiplied by a factor 0.9989[2]. Doing so results in

$$P_{\mathrm{meas}}\Big|_{t_0} = (1116.9 \pm 1.8)\,\mathrm{W},$$

which is exceptionally close to the actual source power. The uncertainty of the measurement is 0.16%.
In summary the capability of the calorimeter to measure the heat of the antineutrino source for SOX with an error of a few per-mill for SOX was proven.

In addition the source operations including the handling tasks for the calorimetric measurements were demonstrated to the Italian Institute for Environmental Protection and Research of the Italian government (ISPRA, Istituto Superiore per la Protezione e la Ricerca Ambientale) to obtain the permission to proceed with SOX. This test included the unloading of the source from the truck, the casket, transportation to the

[2]The time response was not completely analyzed when the blind measurement was done, so that the correction was added later. However, it was already known that the delay causes an error which is in the order of the heat losses and is covered by the measurement error, as verified by the calibration measurements before.

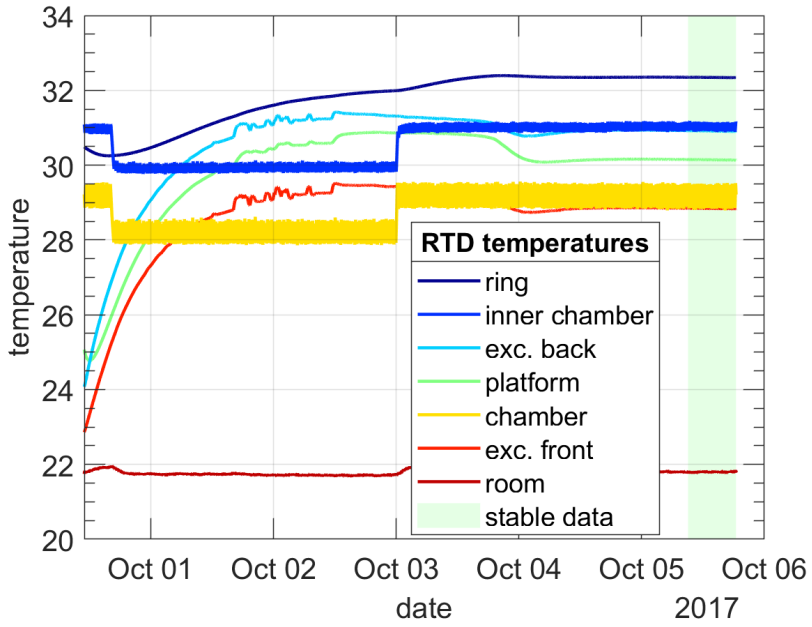

Figure 5.16: The temperature distribution as measured from the RTDs within the calorimeter. The temperature at the top flange of the shield is out of the plot borders at 120°C. Also these temperature sensors detected instabilities due to the pressure fluctuation as shown in figure 5.14. In addition, there was a problem with the chamber thermalization, as there is a drop of one degree. The oscillation in the chamber temperature are caused by the active temperature control and are normal. In the green area - the region of stability - the temperatures are not changing anymore.

clean room, insertion into and extraction from the CEA calorimeter, insertion into the TUM-Genova calorimeter and finally the relocation into the pit. The operations with the calorimeter were performed according to a procedure where the task of every involved person was clearly defined and exposure times were assigned such that the radiation doses could be calculated. The tasks were distributed such that the radiation doses were shared equally among the crew. However, no significant doses were expected and the legal limits for non-exposed workers should not have been exceeded. The safety of the operations was convincingly demonstrated such that approval by ISPRA was granted. The photograph of the source extraction from the casket can be found in figure 5.17. Another picture from the ISPRA test where the source is moved into the pit can be seen in the next chapter in figure 6.1.

5.5 Summary and impact on sensitivity

The TUM-Genova calorimeter was designed with the goal to determine the activity of the ^{144}Ce-^{144}Pr source with an accuracy of 1% or better by measuring the decay heat. The calorimeter allowed a high precision heat measurement thanks to the sophisticated design, where heat losses are minimized by suspending the source with Kevlar ropes in an evacuated chamber, the use of radiation shields and an active temperature control of the vacuum chamber. In this chapter it was presented how the measurement conditions were optimized for minimal heat losses. In general, the optimum condition is attained when the temperature difference between the vacuum chamber and the heat exchanger is small. In addition it was verified that problems as they could occur during the final

Figure 5.17: The extraction of the tungsten shield from the casket to demonstrate the safe handling of a radioactive source during the ISPRA test. The floor is covered with plastic to contain possible radioactive contaminations. During these tests no actual radioactive material was used, in contrary to local news reports.

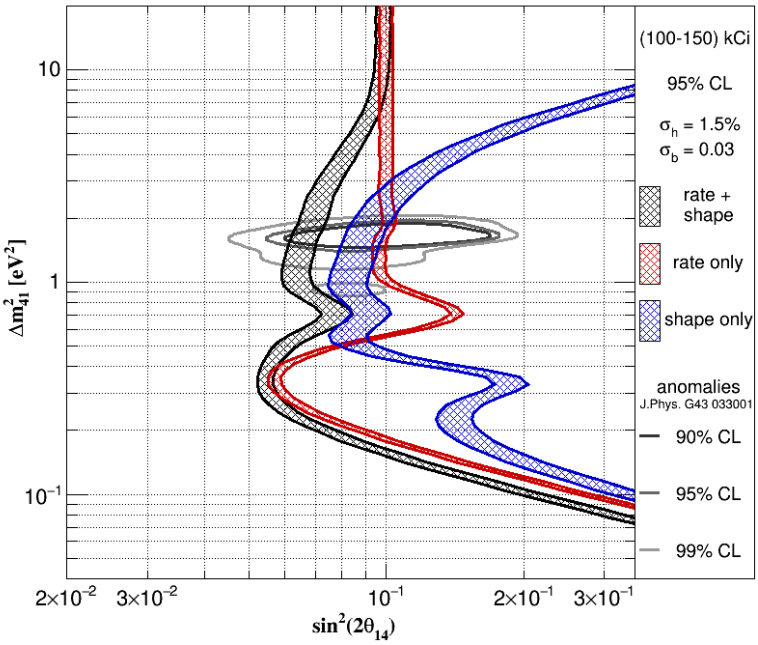

Figure 5.18: The sensitivity of SOX for a source with an activity between 100 and 150 kCi [Neu16]. This plot was already shown in chapter 2.5 in figure 2.7. The uncertainties used in this plot ($\sigma_b = 0.03$ for the spectrum shape factor, $\sigma_h = 1.5\%$ for the activity) can be achieved, also thanks to the calorimeter, and thus almost the complete parameter space where the existence of a sterile neutrino is motivated by the anomalies, can be ruled out.

measurement, as a poor vacuum, a thermal link or a not entirely closed heat exchanger, do not interfere significantly with the result. In a blind measurement it was proven that the heat released by the radioactive decay can be measured with an uncertainty of 0.2%.
For the activity determination one has to consider also the error from the mean energy per decay, which goes into the heat-to-activity conversion. With the proposed PERKEO III spectrometer, it would have been possible to determine the heat per decay with an uncertainty of 0.3% (see table 2.3 in section 2.5). In summary the 1% accuracy goal of the activity determination is achieved.
The sensitivity of SOX was already shown in section 2.2, but the plot is shown again here in figure 5.18. The heat uncertainty σ_h is here assumed to be 1.5%, because it contains additional systematics like the error of the fiducial volume size of the Borexino detector. The error on the spectrum shape factor parameter b is 0.03, which is propagated into heat and interaction rate uncertainties. In conclusion, thanks to the excellent calorimeter performance and the PERKEO III measurement, the parameter space, where the existence of a sterile neutrino is motivated by the anomalies, can be almost completely ruled out with a 150 kCi source.

Chapter 6

Thermal impact from the calorimeter operation on Borexino

After the initial calorimetric measurements the source was planned to be moved into the pit directly beneath the center of Borexino. The vacuum chamber and the super-insulator stages are removed and replaced by a cover to protect the apparatus (see figure 6.1). The system continues to be operated in order to cool the source and to resume the measurement with a reduced accuracy. In principle the pit is a moist environment, as water from the rock enters it. To prevent damage to the system and corrosion from the humidity dried air is pumped into the pit. This operation can affect the temperature of Borexino. A lot of effort was put into the thermal stability of Borexino, since convective currents can compromise the stability of the background rate in the detector's fiducial volume. While this is no problem for SOX itself, which will detect the anti-neutrinos from the source via the inverse beta decay with its unambiguous signature, the cleanness of the active volume is of utmost importance for the solar neutrino program, which continues in parallel to SOX, and especially for the efforts to measure or further constrain the CNO-neutrino rate. For SOX convective currents could be a problem if they result in a change of the inner vessels shape, which is made of a nylon balloon. To estimate the thermal impact from the calorimeter activities on Borexino simple finite element simulations were carried out with Comsol Multiphysics.

6.1 The simulation Model

The model was realized in 3D, since the pit has a T-shape and cannot be described by axial symmetry. The model is shown in figure 6.2. It consists of the following components:

- a large volume of stone, on which Borexino is sitting. The stone has a density ρ of $2\,600\,\mathrm{kg/m^3}$, a thermal conductivity λ of $3\,\mathrm{W/m\cdot K}$ and a heat capacity c_P of $910\,\mathrm{J/kg\cdot K}$ at constant pressure. While ρ and c_P are textbook values for limestone, λ was found by reproducing the measured Borexino temperatures[1]. Typical thermal conductivities for limestone are $1.3\,\mathrm{W/m\cdot K}$, but since the Gran Sasso rock is very porous and contains a lot of water, one can assume that the real thermal conductivity is indeed larger;

[1]The temperature of Borexino is monitored at multiple points at the external surface below the thermal insulation and on the inner side of the steel sphere.

Figure 6.1: The calorimeter is moved into the pit without the vacuum chamber lid, but a protective cover during the ISPRA test (see section 5.4.1). To ensure that the source and the calorimeter are not damaged by the humidity in the pit, dried air is pumped in.

- the pit is an open space within the rock that is not filled by any material, but treated as outer surface of the model. It has a cross-section of $1 \times 1\,\mathrm{m}^2$, and consists of two 10 m long tunnels, arranged as a "T";
- the Borexino water tank is modeled as thin layer (a COMSOL feature for implementing 3D structures as 2D surfaces) with 0.2 m thickness, made of glass fiber blankets[2] to simulate the thermal insulation of the detector. Its thermal conductivity is $0.033\,\mathrm{W/m \cdot K}$. The tank is filled with water;
- the 10 cm thick stainless steel sphere is also modeled as a thin layer. The inner vessel is filled with Pseudocumene;
- two structural steel plates between the bottom of the water tank and the pit, according to the actual design;
- several highly conductive layers are placed as disks within the simulated Borexino. These layers ensure that the temperatures on horizontal surfaces are equal, such that one can avoid to include natural convection into the simulation. The 3-dimensional solution for convection at small temperature gradients requires a lot of computing power and regularly returns obviously wrong results.

The system is then simulated in the following: the rock acts as a thermal sink. The air in Hall C of LNGS, where Borexino is located, is pumped in from the external environment and has a temperature higher than the rock. Borexino is heated through free convection by the air, the heat is then flowing through the detector into the rock. In the case without the SOX project, the pit is filled with air, but sealed. After the

[2] Isover Ultimate Tech Roll 2.0, www.isover.com

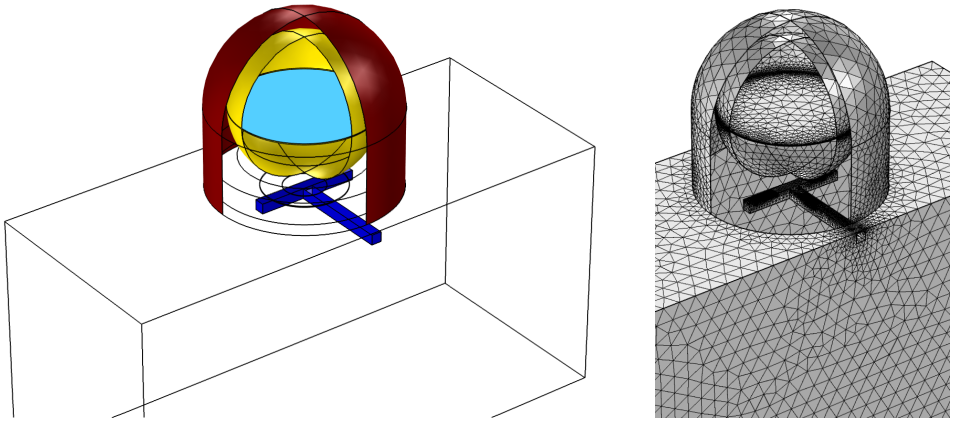

Figure 6.2: The simulated model (left) and the mesh (right). Borexino is sitting on a large volume of rock, whose borders are kept at a fixed low temperature (5.5°C) to simulate a heat sink. The top surface of the rock and Borexino are subjected to free external convection at 16°C. One can see the stainless steel sphere for the inner detector as yellow surface. Some horizontal highly conducting layers were added to emulate free convection in the fluid volumes. One of them is here shown in cyan. The blue T-shaped volume is the pit.

source is inserted in the pit, the air in the pit is heated. However, since the source is cooled by the water circuit, it will only have a small impact on the thermal environment. The dominating factor is the dried air that will be blown into the pit to dehumidify it. The air will come from Hall C and thus have a larger temperature than the rock. In the end this will heat up the region beneath Borexino and reduce the heat flux from Borexino into the rock, resulting in a temperature increase of the detector. To simulate this behavior, following physical effects were included in the model:

heat transfer: solution of the heat equation in solids and fluids;

heat sink: the temperature at the outer surfaces (lateral and bottom) of the rock is fixed at 5.5°C;

convection in Hall C: the upper surface of the rock and the outer surface of the Borexino water tank are subjected to free external convection at 16°C;

convection in fluids: as mentioned before, no natural convection within the fluid domains was simulated, but approximated by including highly conducting layers;

operation in the pit: to simulate the calorimeter operation in the pit, the surface of the rock in the pit is simulated with internal forced convection. Air with a temperature of 16°C is moving with a speed of 0.05 m/s, which corresponds to the maximum mass flow of the dehumidifier $\dot{m} = 190\,\mathrm{kg/s}$, which was planned to be used[3].

[3]Seibu Giken DST, RECUSORB DR-010B

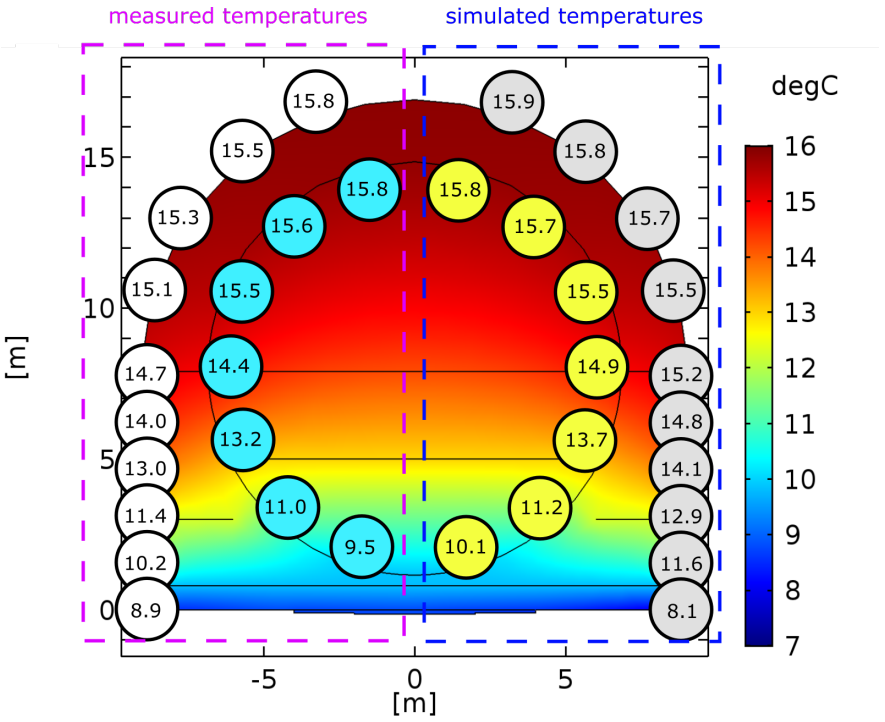

Figure 6.3: A comparison of the measured (left) with the simulated temperature (right) at several points throughout Borexino. The outer temperatures were measured on the external surface of the water tank below the thermal insulation. The corresponding simulated temperatures were read out close to the model border. The inner data points are the temperatures within the inner Pseudocumene filled volume close to the stainless steel sphere. The measured and simulated temperatures are in agreement within 0.5 °C for most data points.

6.2 Simulation results

In a first step some of the parameters were optimized to reproduce the actual temperature measured in Borexino. These parameters were the thermal conductivity of the rock and the temperature of the rock. The simulated temperature distribution with a sealed pit is shown in figure 6.4. A zoom onto Borexino is shown in figure 6.3, where also the measured and simulated temperatures at several points are compared. The outer temperatures were measured on the outer surface of Borexino below the thermal insulation. The simulated points were read out close to the model border. The inner data are the temperatures of the buffer close to the stainless steel sphere. One can see that simulated and measured data are in agreement with less than 0.5°C deviation for almost all points, which is satisfying for such a simplified model.

Some important parameters that can be compared between different simulations are the average temperature of Borexino (as a whole, or only the water or the inner detector temperature), the heat flux through the bottom of Borexino and the heat flux into the pit. These parameters are listed in table 6.1.
After reproducing the Borexino temperature distribution, in the next step the forced internal convection in the pipe was turned on and the model was solved for thermal equilibrium. As a result, the average temperature of Borexino increased by 0.3°C as it can be seen in table 6.1. The temperature of the inner vessel, which is important for the solar neutrino program, is 0.2°C higher. When the heat flux into the rock is compared,

simulation	$\overline{T}$ [°C]	$\overline{T}$ water tank [°C]	$\overline{T}$ inner det. [°C]	heat flux to the rock [W]	convective heat flux to pit [W]
A	13.7	13.4	14.2	-214	0
B (thermal equilibrium)	14.0	13.7	14.4	-190	-183
B ($t = 200$ d)	13.7	13.5	14.2	-164	-193
B ($t = 600$ d)	13.8	13.6	14.2	-177	-187

Table 6.1: Comparison of output parameters from different simulated scenarios: **simulation A:** sealed pit, no source operation; **simulation B:** operations in pit, forced internal convection turned on as described in section 6.1. This case was solved for thermal equilibrium, and also as a time dependent simulation. The output at two times, 200 and 600 days, is listed here as well. The most important parameter for the radio-purity of Borexino is the temperature of the inner vessel. In the 600 days of expected SOX activities, the change is smaller than 0.1°C.

its absolute value is reduced by 24 W. Thus by heating up the region beneath Borexino, indeed the heat flux through the detector is lowered such that it is heated up by the environment. However, the reduction of 24 W is quite small, considering the huge heat capacity of Borexino. The question is then, when the thermal equilibrium is reached. It can be assumed that it is reached only after a period longer than the SOX project. To answer this, time-dependent simulations were conducted, where the evolution of the temperature distribution is studied. In 6.1, the parameters evaluated at 200 and 600 days after starting forced convection in the pit are shown. 600 days is roughly the expected duration of the SOX project, taking into account 1.5 y of measurement time and a start of the pit dehumidification about one month before the source insertion. As one can see, the inner vessel temperature rises by less than 0.1 °C after 600 days. The complete evolution of the total Borexino average temperature up to 1000 days is plotted in figure 6.5. Even after 1000 d the thermal equilibrium is not yet reached.
In conclusion it can be said that the SOX operations in the pit have only a small impact on the temperature distribution of Borexino. Considering the limited accuracy of these simple simulations, one could expect an increase of a few tenth degrees of the detector. However, this change would happen on a time scale of several hundred days, and the temperature gradient within the detector is at no point inverted, such that no convective circulations are expected.
Of course these study is obsolete after the cancellation of SOX. In the meantime, more work was put into the thermal stabilization of Borexino in order to reach extremely stable background levels.

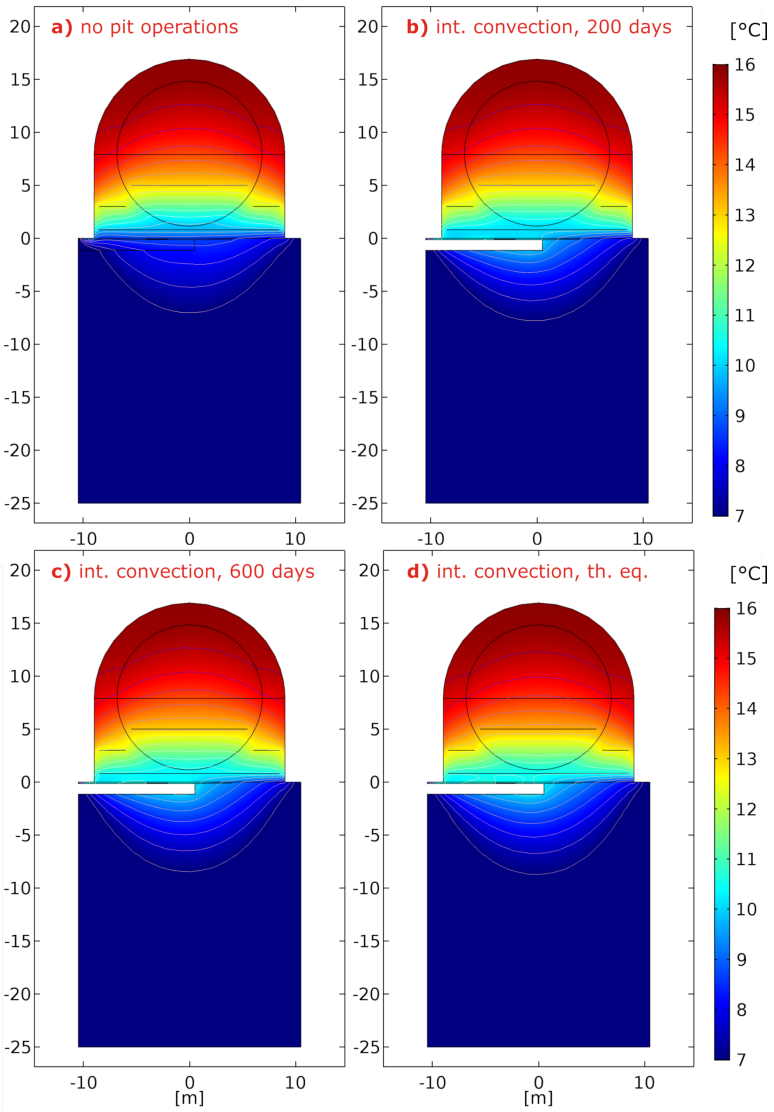

Figure 6.4: The evolution of the heat distribution. Here one sees a vertical cut plane through Borexino, the pit and the rock volume beneath it. The inner detector of Borexino is visible as circle. The horizontal lines in the detector are highly conductive layers, a work-around to avoid the simulation of free convection in the fluid volumes. The four plots show the temperature distribution with and without source operation in the pit: **a)** the pit is sealed and filled with air, the standard case for Borexino without SOX; **b)** the source operations are running since 200 days, simulated by internal forced convection in the pit; **c)** the heat distribution after 600 days of source activities in the pit; **d)** thermal equilibrium with a pit heated by internal forced convection. The differences of simulated scenarios are very small (see table 6.1), but a small shift of the isothermal lines (1 K spacing) is visible.

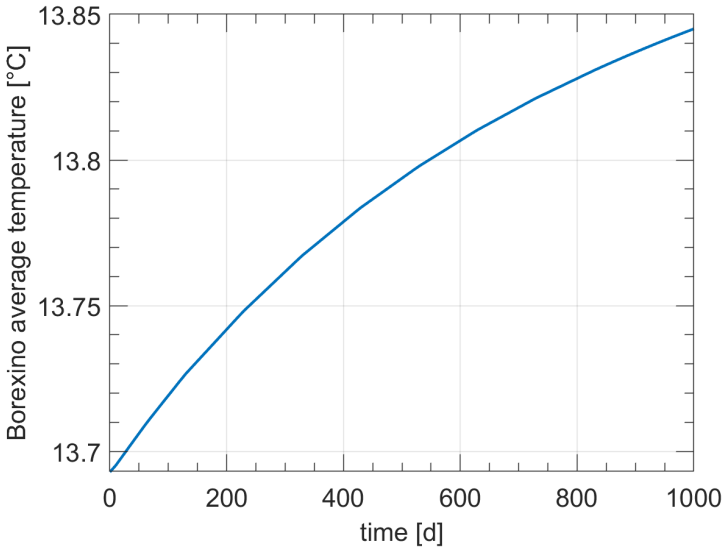

Figure 6.5: Evolution of the average Borexino temperature over time, derived from time dependent simulations. One can see that the change of temperature on the time scale of the SOX activities ($\sim 600\,\mathrm{d}$) is only around 0.1°C.

Chapter 7

SOX summary

The SOX (**S**hort distance neutrino **O**scillations at Bore**X**ino) project was a neutrino oscillation experiment that was designed to discover or refute the existence of a eV-scale sterile neutrino, which could be responsible for several anomalous observations in previous experiments. It was planned to study neutrino oscillations within the active volume of the Borexino detector by installing a 5.5 PBq $\overline{\nu}_e$-source, made of the isotopes ^{144}Ce and ^{144}Pr, in 8.5 m distance from the detector center. For the experiment it was crucial to know the number of neutrinos emitted from the source and their energy spectrum. Concerning the number of neutrinos, a thermal calorimeter was developed to measure the decay heat, from which the source activity can be calculated. To determine the spectral shape, a measurement with a magnetic spectrometer was in preparation. Unfortunately, a technical problem during the production of the $\overline{\nu}_e$-source in the Mayak nuclear factory occurred that made the delivery of a source with the requested characteristics (activity and purity) impossible, resulting in the cancellation of SOX and related sub-projects as the spectral measurement. However, the calorimeter was developed to completion and its excellent performance was demonstrated in a series of tests.

The principle of the calorimeter is that the source is completely encased in a heat exchanger, in which the generated heat is transferred to a water flow. The activity is then calculated from the temperature increase and water mass flow, which are both measured with high precision. To prevent an undetected heat transfer, the system is placed in a sophisticated thermal insulation: the source with the heat exchanger is suspended by Kevlar ropes with a poor thermal conductivity to prevent conductive heat losses, a multi-layer radiation shield prevents radiative heat transfer, and convection is minimized by operating the system in a vacuum. In addition, the temperature of the vacuum chamber can be adjusted to further reduce heat losses by minimizing temperature gradients. Within this thesis, following results were achieved:

- the calorimeter was commissioned and its setup optimized with respect to the thermal insulation;
- the calorimeter data analysis was developed, including the selection of the region of thermal equilibrium, the calculation of the emitted power and the uncertainty calculation;
- calibration measurements, where the radioactive source was simulated by an electrical heater, were performed to identify heat losses, and study the performance under different conditions, e.g. at an increased residual air pressure. It was shown that the calorimeter is still fully functional even in case of a poor vacuum or a not

fully closed heat exchanger, which are typical problems that could occur during the final measurement with the radioactive source;

- the measurement conditions were optimized by adjusting the internal temperature distribution via the mass flow value and the chamber temperature, such that measurements with negligible heat losses became possible;
- the time response of the calorimeter was studied with dedicated measurements. As a result the delay time between a transient source heat and the measured heat could be modeled and taken into account to correct measurements with a decaying heat source;
- the analysis of two blind measurements – one with a constant source power, one with a decaying power – proved that the emitted heat can be determined in a single measurement with an accuracy of 0.2%.

In addition, it was studied with finite element simulations whether the operation of the $\overline{\nu}_e$-source beneath Borexino has an effect on the detector temperature. It was shown that the average temperature changes by less than 0.1°C within the duration of the project.
Furthermore, a measurement of the ^{144}Ce-^{144}Pr β-spectrum with the PERKEO III spectrometer was prepared by calculating the expected uncertainties on the inverse-β-decay interaction rate in Borexino and on the heat-activity conversion for the calorimetric measurement. Preparatory measurements showed that a CsI detector-array can be used to distinguish the different decay branches by γ-tagging.
In summary, the excellent performance of the calorimeter together with the spectral measurement ensures that the SOX experiment would be sensitive for the entire sterile neutrino parameter space of interest. The description of the calorimeter and the results of its characterization were published in [ADN+18].

The calorimeter was a joint project of TUM and INFN Genoa, lead by Stefan Schönert (TUM) and Marco Pallavicini (INFN). The measurement program, data analysis and system optimization was performed by the author together with Lea Di Noto of INFN, while most of the technical work on the hardware was conducted by the engineers Laszlo Papp (TUM) and Roberto Cereseto (INFN). Many other people were involved at various stages and contributed to the success.

Part III

TRISTAN

Chapter 8

Troitsk ν-mass, KATRIN and the TRISTAN project

The second part of this thesis is about the search for sterile neutrinos with masses of a few keV in the tritium β-decay with the TRISTAN project. This first chapter gives an introduction to this project and associated experiments.
KATRIN is attempting to measure the absolute neutrino mass by searching for a shift of the endpoint of the tritium β-spectrum. Within the collaboration, a project called TRISTAN is planned to scan the entire tritium spectrum with the KATRIN setup to search for the signature of a sterile neutrino. It is thus dealing with much higher counting rates than the original KATRIN, such that a new detector array is necessary. The work in this part of the thesis revolves around first 7-pixel silicon drift detectors that were produced as prototypes to test and develop the technology for the final array.
The concept and technology of a direct neutrino mass measurements with MAC-E type tritium spectrometers is shortly discussed in section 8.1. The detector prototypes developed for TRISTAN were tested at the Troitsk ν-mass spectrometer, which is introduced in section 8.2, followed by a description of the KATRIN experiment in section 8.3. The TRISTAN project itself is then explained in section 8.4.
The actual TRISTAN-related work presented in this thesis is focused on the characterization of a novel semiconductor detector system and the analysis of first data taken with it. This detector system is introduced in chapter 9 alongside with an overview on the principles of semiconductor detectors. The results of the detector characterization with X-ray sources are presented in chapter 10. Chapter 11 contains the results from a measurement campaign at Troitsk ν-mass including the analysis of first tritium data.

8.1 MAC-E type tritium spectrometers

This section introduces the concept of the direct neutrino mass measurement by analyzing the tritium β-spectrum, and the MAC-E type spectrometer technology. A tritium source in combination with such a MAC-E filter was used by three experiments, which are related to the TRISTAN project: Troitsk ν-mass, the Mainz neutrino mass experiment and KATRIN. Troitsk ν-mass and KATRIN are introduced in detail later.

8.1.1 The neutrino mass signature in the β-decay electron spectrum

When modeling the β-spectrum according to the Fermi theory one obtains:

$$\frac{\mathrm{d}\Gamma}{\mathrm{d}E} = C \cdot F(Z,E) \cdot p(E + m_\mathrm{e}c^2)(E_0 - E)\sqrt{(E_0 - E)^2 - m_\nu^2 c^4}, \tag{8.1}$$

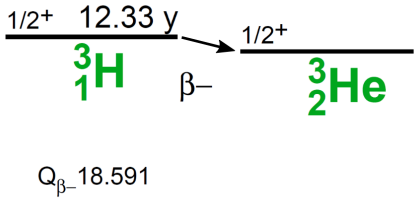

Figure 8.1: The tritium decay scheme [Fir96]: tritium β-decays with a half-life of 12 years and a maximum decay energy of 18.6 keV to helium, where an electron and an $\overline{\nu}_e$ are emitted. The transition is super-allowed.

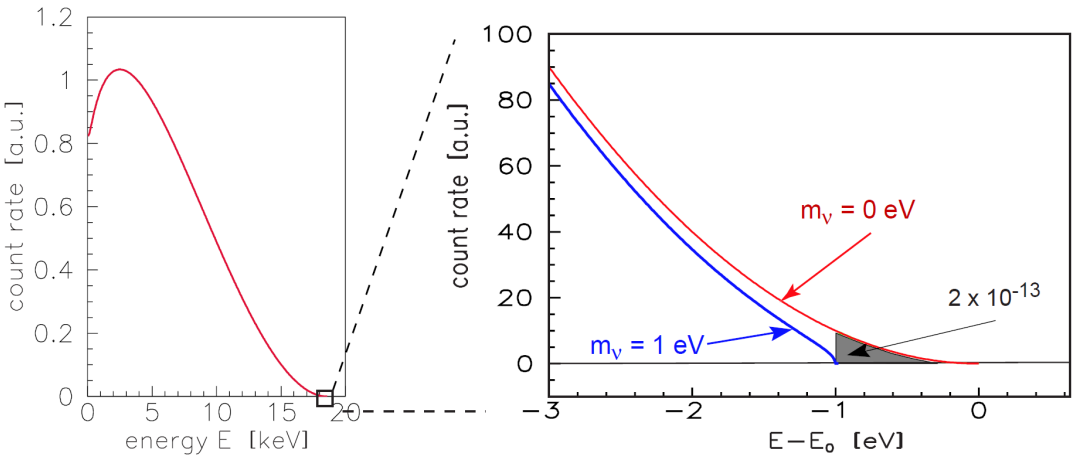

Figure 8.2: The effect of a massive neutrino on the β-decay spectrum, as illustrated in [KAT05]. **Left:** the entire tritium spectrum. **Right:** a zoom into the region close to the endpoint. Compared to a spectrum with massless neutrinos (red), the neutrino mass (here $m_\nu = 1\,\text{eV}$) shift the maximum electron energy towards lower values. The fraction of events in the last 1 eV-bin (gray area) is very small, such that a very strong source with a low endpoint is necessary.

where E is the electron kinetic energy, p the electron momentum and m_e and m_ν electron and neutrino mass. E_0 is the maximum electron energy, which is the Q-value corrected by the nuclear recoil and molecular excitations. C is a shape factor that is independent of E for allowed transitions and $F(Z, E)$ is the Fermi function that accounts for the interaction of the emitted electron with the electron cloud of the daughter atom. From this equation one can see that the endpoint of the spectrum is shifted to a lower value by the massive neutrino and that this effect is more pronounced for a low Q-value.
The β-decaying isotopes with the lowest endpoints are ^{187}Re ($E_0 \approx 2.6\,\mathrm{keV}$, $T_{1/2} = 4.3 \cdot 10^{10}\,\mathrm{y}$) and tritium ($E_0 \approx 18.6\,\mathrm{keV}$, $T_{1/2} = 13.6\,\mathrm{y}$). Tritium is favored, because due to its short half life a high activity is already achieved with a small amount of the isotope. In addition, thanks to the super-allowed transition the spectrum can be modeled with high accuracy since the nuclear matrix element is independent of the electron energy. The decay scheme of tritium is shown in figure 8.1.
While the Mainz experiment used a condensed tritium source, for Troitsk ν-mass and KATRIN a gaseous tritium source was implemented [WDB+99, ABB+11, KAT05]. In case of KATRIN the source is made predominantly of the molecule T_2, which has the additional advantage that the final state spectrum can be quantitatively calculated [OW08].

In equation 8.1 one has to consider that there are three different neutrino mass eigenstates (if we assume that there are no sterile neutrinos), which are generated with certain admixtures in the β-decay. The total observed spectrum is actually a superposition of three individual spectra, each one with a differently reduced endpoint and normalized with respect to the eigenstate's admixture. As the separation of the neutrino masses is very small ($\Delta m \approx 0.05\,\mathrm{eV}$ between lightest and heaviest [Par18]), one can approximate the observed spectrum according to equation 8.1 with a single neutrino with the effective mass

$$m_\nu^2 = \sum_{i=1}^{3} |U_{ei}|^2 m_i^2. \tag{8.2}$$

This effective electron neutrino mass is the quantity, which the experiments attempt to measure or constrain. An illustration of how the neutrino mass affects the neutrino spectrum is shown in figure 8.2 for $m_\nu = 1\,\mathrm{eV}$. Only a tiny fraction of events falls into the last 1 eV-bin below the endpoint, thus it becomes clear that only a high precision experiment with a highly active source made from an isotope with a low Q-value can probe this effect in a reasonable time.

8.1.2 MAC-E filter

A MAC-E filter (**M**agnetic **A**diabatic **C**ollimation combined with an **E**lectrostatic Filter) was first proposed by Beamson, Porter and Turner in [BPT80], and later reinvented specifically for the Troitsk and Mainz neutrino mass experiments [LS85, PBB+92]. In a spectrometer with a MAC-E filter the magnetic field expands from a very strong field of a few Tesla at the entrance to less than a millitesla in the center, called the analysis plane, and then increases again to a strong value at the exit. When electrons move adiabatically (the change of magnetic field is small within one gyration) through the spectrometer, the circular motion of the electrons around the field lines with a large perpendicular component in the region of a strong magnetic field is changed at the analysis plane – where the magnetic field reaches its minimum value – into a motion predominantly parallel to the field lines. With an electrical field in parallel to the mag-

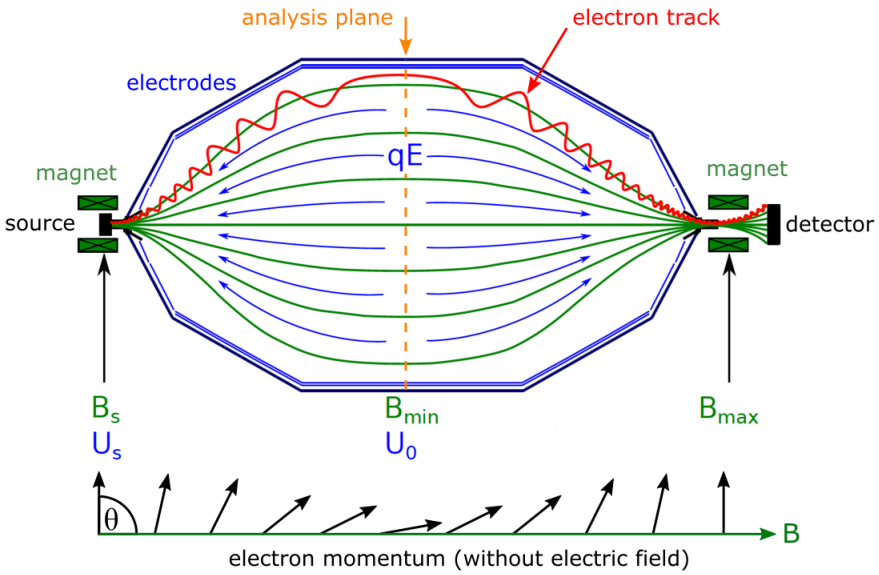

Figure 8.3: A scheme of the MAC-E filter. The electron is moving adiabatically from a strong magnetic field ($B_s = 4.5\,\mathrm{T}$) into the center of the spectrometer, where the field reaches a minimum of 0.3 mT. Since the orbital magnetic moment is conserved, the perpendicular component of the momentum is transferred into a parallel motion (see also the momentum vectors at the bottom), such that one can sharply set and energy threshold for the electrons through an electric field.

netic field one can then select the electrons by their parallel kinetic energy, which is in the analysis plane almost equal to the total kinetic energy. The electric field is called retarding potential.
The concept of the MAC-E filter is illustrated in figure 8.3. The transformation of perpendicular into parallel motion can be explained via the orbital magnetic moment of a gyrating particle (the first adiabatic invariant in plasma physics)

$$\mu = \frac{E_\perp}{B}, \tag{8.3}$$

where $E_\perp$ is the perpendicular component of the electron kinetic energy with respect to the magnetic field lines with the field strength B. This magnetic moment is conserved in case the change of the magnetic field strength is small within one cyclotron period ($\nabla B/B \ll 1$), i.e. the change is adiabatic. From the equation above it becomes clear that $E_\perp$ is decreasing with B such that its fraction of the whole kinetic energy is reduced to $B_{\mathrm{min}}/B_{\mathrm{max}}$. Consequently, the MAC-E filter achieves an energy resolution

$$\Delta E = E \cdot \frac{B_{\mathrm{min}}}{B_{\mathrm{max}}}. \tag{8.4}$$

Another important concept in this context is the acceptance angle: the electrons are guided through the entire beam line adiabatically and since the magnetic field at the source is typically not the strongest in the entire beam line, electrons that were emitted at large angles with respect to the field lines are reflected by a magnetic mirror when the field is increasing. The maximum angle of electrons that are not reflected, called the acceptance angle, can be calculated through

$$\sin\theta_{\mathrm{max}} = \sqrt{\frac{B_{\mathrm{source}}}{B_{\mathrm{max}}}}. \tag{8.5}$$

Now, to calculate the energy resolution of the spectrometer according to equation 8.4, one could assume that $B_{\max}$ is the field strength at the entrance of the spectrometer as frequently stated in the literature. However, one has to insert the field strength at the spectrometer exit into this equation if the field there is stronger than at the spectrometer entrance, as it is the case for KATRIN. This becomes clear with the magnetic mirror effect: the magnet at the exit with 6 T (KATRIN) sets the acceptance angle, since it is the maximum in the entire beam line. Thus, electrons that pass to the detector cannot have the maximum angle (90°) at the spectrometer entrance, because they would be reflected at the exit. As a consequence, the angles have to be smaller at the entrance, resulting also in a smaller $E_\perp$ in the analysis plane and thus a better energy resolution.

8.2 Troitsk ν-mass

The Troitsk ν-mass experiment can be considered as a technological predecessor of KATRIN, as both have a similar layout with a gaseous tritium source, transport section, pre- and main spectrometer and silicon detector, where Troitsk ν-mass is much smaller and of course older. Another predecessor of KATRIN is the Mainz neutrino mass experiment, which also is a MAC-E-type spectrometer, but uses a condensed tritium source. The Mainz spectrometer started first measurements in the 90s, final results were published in 2005 [K$^+$05], where a limit $m(\nu_e) < 2.3\,\mathrm{eV/c^2}$ (95% C.L.) was derived. It now serves as monitor spectrometer for KATRIN.
Troitsk ν-mass was taking data from the late 80s and published final results in 2011 by setting a limit of $m(\nu_e) < 2.05\,\mathrm{eV/c^2}$ (95% C.L.) [ABB$^+$11]. The setup is still in use with an upgraded (larger) vacuum tank and currently searching for sterile neutrinos [A$^+$17a].

A photo of the setup is shown in figure 8.4 and a detailed drawing in figure 8.5. The tritium is injected into a cryogenic pipe with a magnetic field of about 0.8 T. Since the gas is not separated from the beam line, this type of source is called windowless gaseous tritium source (WGTS). At both ends fields of 5 T serve as magnetic mirrors. They are intended to prevent the acceptance of electrons, which stem from tritium that sticks to the walls of the source. At both ends of the source section the tritium is removed by mercury diffusion pumps and then recycled.
The electrons from the tritium decay are guided from the source along the magnetic field towards the spectrometer through a transport section with zigzag-chicanes. This way the tritium molecules have no direct line-of-sight towards the detector and no molecular beam can form, as it can occur when gas is expanding through a small opening into a volume of lower pressure. The tritium is removed in this section by three mercury diffusion pumps and a titanium beam pump that together guarantee a pressure $< 10^{-9}$ mbar in the spectrometer. Another diffusion pump is installed at the rear side of the source.

The source has no long-term stability but is filled periodically. To minimize the systematic impact of the steadily decreasing activity, the scanning process to measure the integral spectrum involves a quick alternation of the retarding potential (each voltage value is kept for only a few minutes), where every fifth measurement point is taken as a reference value at a fixed voltage.
Another important systematic effect is scattering in the source, for which to estimate the source density has to be known. The density is measured with the help of an elec-

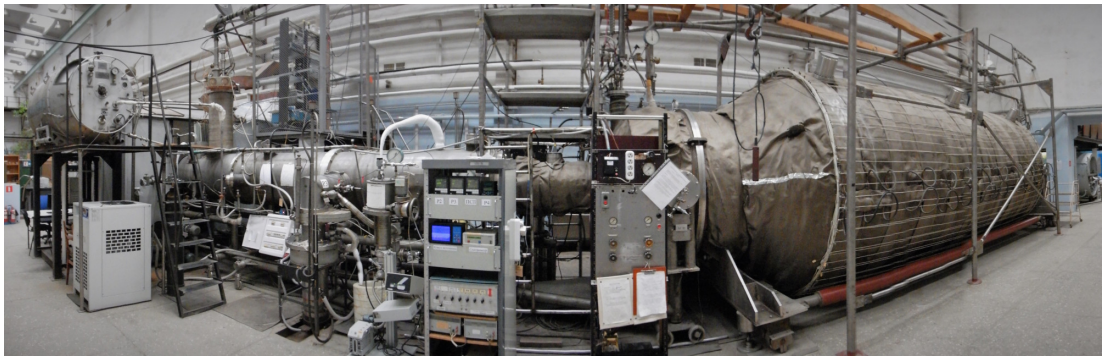

Figure 8.4: A photo of the Troitsk ν-mass experiment. The tritium source is housed in the gray shed on the far left. The huge vacuum tank with the MAC-E filter is dominating the right side of the picture. It is covered by an insulation such that it can be heated to improve the vacuum. The white wires on top of the insulation are the warm coils that allow to compensate for the earth magnetic field. The pipe in the middle and on the left side is the transport and pumping section.

tron gun that is installed at the rear end of the setup. It shoots a narrow beam of 19 keV-electrons through the source. At a retarding potential slightly below the e-gun energy the count rate corresponds to electrons that did not lose any energy, thus did not scatter. At lower retarding potentials (200 eV below e-gun energy) one observes an increased flux, because now also electrons that scattered can pass the filter. The ratio of both rates is depending on the source density. In addition a mass analyzer is measuring the partial concentrations of the T_2, TH, DT and H_2 molecules. From these measured quantities one can determine the amount of tritium compared to other hydrogen isotopes in the source. The gun also serves to measure the transmission function or energy resolution of the spectrometer.

Due to the layout of the source as magnetic bottle one has also to consider the impact of trapped electrons on the spectrum. These trapped electrons lose energy due to multiple scatterings. Eventually their angle changes such that they can leave the source and pass to the spectrometer. The resulting flux can be regarded as an additional spectrum superimposed on the unchanged tritium spectrum. More details are given in [ABB+11].

The spectrometer with the MAC-E filter is housed in a vacuum chamber with ~ 3 m diameter and a length of ~ 10 m. The magnet at the entrance – the **pinch magnet** – generates a maximum field of 8 T, while the magnet at the exit – the **detector magnet** – has a strength of 3 T. These names will be used in chapter 11, but one has to be careful to not confuse this nomenclature with KATRIN, where the pinch magnet is at the exit of the spectrometer. In the analysis plane, the field strength drops down to 3 mT. The spectrometer can achieve a resolution of 3-4 eV.
The entire spectrometer chamber can be heated to improve the vacuum. On the outer surface a coil is mounted that allows to fine-tune the magnetic field and compensate for the earth magnetic field. This system is called **correction coil**, or warm coil.

The detector, a single Si(Li) pin-diode with 17 mm diameter, is mounted at the front of the spectrometer, and can be moved into the center of the detector magnet. This detector can be removed easily by retracting it into a pipe that can be separated from the spectrometer with a gate valve and is closed with a detachable flange on the front.

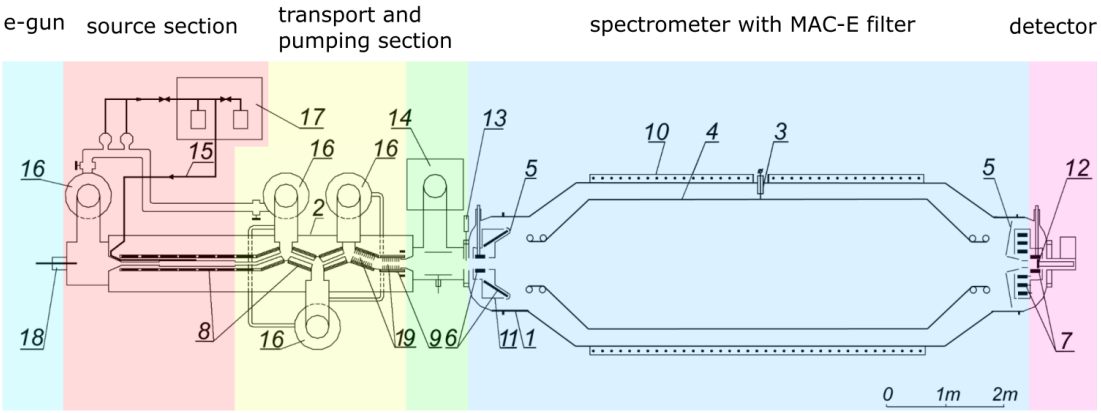

Figure 8.5: A detailed sketch of the Troitsk ν-mass setup: **1)** spectrometer vacuum tank; **2)** source vacuum tank; **3)** high voltage feed-through; **4)** spectrometer electrode; **5)** ground electrodes; **6),7),8),9)** superconducting magnets; **10)** warm coil; **11)** liquid nitrogen jacket; **12)** silicon detector with cooling system; **13)** gate valve; **14)** titanium sublimation pump; **15)** tritium loop; **16)** mercury diffusion pumps; **17)** tritium storage and purification system; **18)** electron gun; **19)** cryo argon pump. Sketch adapted from [A$^+$15a].

The detector has a fixed dead time of 7.2 µs. From this alone one can see that a scan of the entire tritium spectrum with high statistics is challenging, since the detector can handle only a limited count rate. The sterile neutrino scan presented in [A$^+$17a] was performed only down to 16 keV.

As reported in chapter 11, TRISTAN prototype detectors were installed at Troitsk ν-mass for testing purposes and to take physics data. Especially future measurement campaigns with the 166 pixel prototype detector can extend the range of Troitsk ν-mass in the sterile neutrino parameter space. As of early 2019, three collaborative measurements were performed at Troitsk with TRISTAN prototypes:

1) May / June 2017: three day measurement with a 7-pixel array with 1 mm pixel diameter and the IDeF-X BD ASIC. The response of electrons from different sources was studied. An analysis of the differential (ordinary) tritium spectrum was performed. The results from this campaign are presented in chapter 11;

2) November 2017: measurements with a 7-pixel array with 2 mm pixel diameter equipped with the ASIC by XGLab. Compared to the first measurement much more data from tritium were taken during two weeks. The data analysis is still in progress;

3) April / May 2018: after the first two measurement campaigns mostly served as detector testing and characterization, here the 7-pixel 2 mm-detector was integrated into the Troitsk experiment for three weeks with a synchronized DAQ that allowed to take an integral spectrum. The data is currently being analyzed;

8.3 The KATRIN experiment

KATRIN is a MAC-E type spectrometer that intends to further constrain or determine the effective neutrino mass by doing a high precision measurement of the tritium electron spectrum. It can be considered as a joint continuation of both the Mainz and

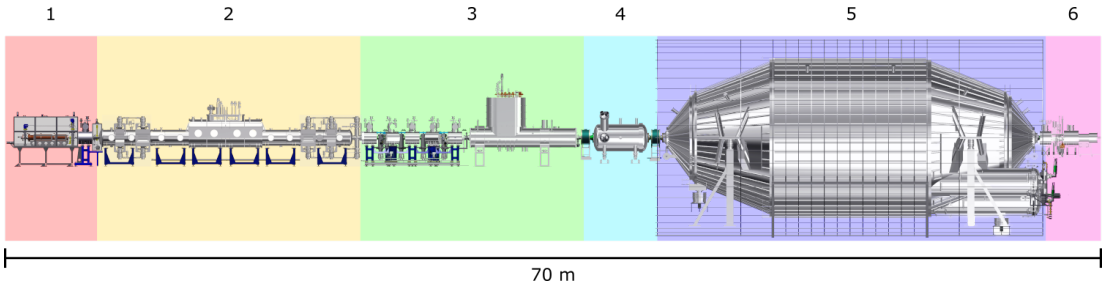

Figure 8.6: The KATRIN beam line: **1)** rear section with calibration devices; **2)** windowless gaseous tritium source; **3)** transport section with differential and cryogenic pumps; **4)** pre-spectrometer; **5)** main spectrometer with MAC-E filter; **6)** detector section.

Troitsk neutrino mass experiments. The expected sensitivity for the effective electron neutrino mass is 0.2 eV (90% C.L.). An initial outline of KATRIN was presented in 2001 in a Letter of Intent [O+01], while an advanced design study was published in 2004 in [KAT05]. The construction started shortly after and the installation of the main components was finished in July 2015 with the delivery of the cryogenic pump section. The entire vacuum system was commissioned in early 2016 [KAT16], followed by "first light" in October 2016, when a beam from the electron gun in the rear section reached the detector. A first run with tritium was performed in June 2018. The main measurement campaign started in March 2019.

8.3.1 Technical description

The KATRIN experiment was built to measure the endpoint of the tritium spectrum with unprecedented accuracy. Since the expected effect of the neutrino mass is a shift of the endpoint by an energy in a sub-eV range, the energy resolution of the setup has to be in a similar range. An ordinary semiconductor or scintillator particle detector alone cannot achieve such a resolution. The most important part of KATRIN is thus the MAC-E filter, which allows to set an energy threshold with a resolution of ≈ 1 eV. The detector itself is a segmented silicon pin-diode that counts the electrons reaching the detector at a certain filter threshold. As a result an integral spectrum is obtained. The other key component of the experiment is a gaseous source that has a very stable activity, from which the electrons are moving along magnetic field lines through the filter towards the detector. The advantage of a gaseous source over a condensed source is that the electrons are subjected to less scattering. Also, a low background is crucial. A detailed overview of KATRIN's design and physics goals can be found in the design report [KAT05]. Further information that were used for this introduction were published in [KAT16] (the vacuum system) and [KAT18a] (magnets). If not stated otherwise, the information in the following was taken from these three sources. It should be mentioned that the commissioning phase of KATRIN is still ongoing and many parameters are not fixed yet and may be changed.

A sketch of the entire KATRIN beam line is shown in figure 8.6. The individual sections and components are described in the following. We are starting from the rear (source side, on the left in the drawing) and end at the detector section. The numbers refer to the figure:

- **Rear section (1):** the rear section contains the rear wall that marks the end of the beam line. The tritium gas is here in contact with a gold plate that aims at defining the electric potential of the source. Else an uncontrolled space charge

could build up in the source, since the tritium decay produces positive helium ions.
In addition some diagnostic systems and an electron gun for calibration measurements are installed in the rear section.

- **WGTS (windowless gaseous tritium source) (2):** a loop system of tritium ensures that a constant stream of ultra-cold (27 K) molecular tritium is diffusing at a pressure in the order of 10^{-3} mbar through the source. It is injected in the middle of the 10 m long section and pumped out at both ends. At any time there are 30 µg of tritium in the source, resulting in an activity of about 10^{11} Bq with a very high stability. The isotopic composition is monitored with the LARA system (Laser Raman spectroscopy) [SRS+13]. The electrons are guided by superconducting magnets along the beam line. By adjusting the magnetic field strength in the source with respect to the magnets at the entrance and exit of the spectrometer one can control the acceptance angle of electrons in a way that electrons that were emitted at large angles from the beam axis are rejected through backreflection at the point where the field is increasing. This allows to exclude electrons which were moving for a long time through the gas and probably lost energy due to scattering. The maximum acceptance angle is fixed to 51°.

- **Transport section (3):** in this section the tritium is removed from the beamline with the help of several turbomolecular pumps and by a cryogenic pump, where the inner walls of the volume are covered with argon snow that creates a large surface on which tritium is adsorbed. The frost layer is regenerated every 60 days before its activity reaches 1 Ci (37 GBq). The cryogenic pump reduces the residual pressure in the beam line by a factor 10^6 down to 10^{-14} mbar. In addition the electrons are guided along a zigzag course as in the Troitsk ν-mass setup.

- **Pre-spectrometer (4):** the pre-spectrometer is a small MAC-E filter that can reject already all electrons with low energies that cannot be used to study the neutrino mass ($E < E_0 - 300$ eV). This reduces the flux into the main spectrometer and thus minimizes the background from ionization of residual gas molecules.

- **Main spectrometer (5):** the main spectrometer contains the MAC-E filter to measure the integral tritium spectrum. In the KATRIN main spectrometer the magnetic field expands from 4.5 T at the entrance to 0.3 mT in the center, called the analysis plane, and then increases again to 6 T at the exit. As a result, the energy resolution of the filter is 0.93 eV at 18.6 keV (see equation 8.4). The field strength at the source is 3.6 T, resulting in an acceptance angle of 51°. To house the magnetic field necessary for the MAC-E filter a huge 1240 m^3-vacuum tank (length: 23.2 m, max. diameter: 9.8 m; weight: 200 t) was constructed. It keeps a vacuum of $\sim 10^{-11}$ mbar. The electric field is generated by conical electrodes within the chamber and fine-tuned by a system of wire electrodes. The entire vacuum chamber is surrounded by a coil system ("air coils") to compensate for the earth magnetic field.

- **detector section (6):** the last component of the beam line is the focal plane detector, which counts the number of electrons that passed the filter. This detector is a 148-pixel pin-diode array on a monolithic silicon wafer. The segmentation of the detector allows to study electrons separately depending on the region where they crossed the analysis plane. The detector has an energy resolution of 1.5 keV

at 18.6 keV and can handle rates up to a few thousand counts per second in total [A$^+$15b].

Another important component that is not shown in the drawing is the old setup of the Mainz neutrino mass experiment, which now acts as a monitor spectrometer. It is located in an adjacent building next no the main spectrometer, but is connected to the same voltage supply as KATRIN. It monitors the voltage stability of KATRIN's electrode system by observing the position of the monoenergetic conversion electron line from a ^{83m}Kr-source. More information can be found in [SBD$^+$13].

8.3.2 Sensitivity, systematic effects and background

KATRIN's expected sensitivity for the effective electron neutrino mass after 5 years of data taking (3 beam years) is 0.2 eV (90% C.L. upper limit if the neutrino mass is zero). Concerning the discovery potential, a neutrino mass of 0.4 eV could be observed with 6.5 σ significance, while a mass of 0.3 eV would be seen with 3 σ.
After 3 years of beam time, systematic and statistic errors are about the same size. Systematic errors are due to several reasons. Some of them are related to the source and caused by density instabilities, the space charging, the determination of electron scattering probabilities (related to the uncertainty of the density) and the description of the final state distribution of ^{3}He$^+$T molecules after the tritium decay. Other systematic effects are due to voltage fluctuations of the retarding potential and the limited uniformity of the magnetic and electrostatic fields in the spectrometer analyzing plane.

Since the count rate of tritium electrons close to the endpoint is very small and only a few thousand electrons will be collected per 0.1 eV bin (retarding potential scanning point), the background has to be minimized to < 0.01 cps (counts per second) to achieve the projected sensitivity. The following background sources are relevant for KATRIN [KAT17]:

- **muon induced background:** cosmic muons produce secondary electrons at the inner surface of the spectrometer. These electrons are magnetically shielded by the guiding magnetic field for the electrons from the tritium. Indeed, measurements showed no correlation of the muon rate with the observed background rate;

- **radon induced background:** radon that emanates from some components, especially in the getter pumps, decays within the vacuum chamber and produces electrons, which are magnetically trapped in the spectrometer. Secondary electrons produced in collisions of trapped electrons with residual air can reach the detector. Liquid nitrogen baffles in front of the pump ports prevent radon from entering the main volume of the chamber with an efficiency of 97 % [GBB$^+$18]. In addition, magnetic pulses generated with the air coil system can periodically remove stored electrons from the spectrometer, such that they no longer produce secondary electrons [KAT18b];

- **natural radioactivity:** direct radiation from radioactive elements in the setup and environment is shielded by the main spectrometer vessel. However, Rydberg atoms can be produced that posses an electron in a highly excited state. These atoms can be ionized by thermal radiation and produce background. This and radon are suspected to be the dominant background sources in KATRIN.

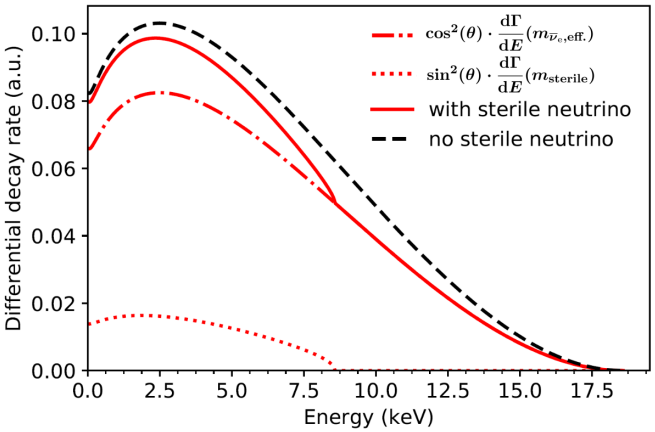

Figure 8.7: The signature of a sterile neutrino in the tritium spectrum [M+19]. One can regard the spectrum according to equation 8.6 as a superposition of two spectra, an "ordinary one" (red dash-dotted line) and another one, where the endpoint is reduced by the mass of the heavy (sterile) eigenstate, and which is normalized by the eigenstate's admixture (red dashed line). The resulting spectrum shows a kink-like signature (solid red line). The sterile neutrino mass for this plot was set to 10 keV. The mixing angle is expected to be very small, the signature here is greatly exaggerated.

It should be noted that the 0.2 eV sensitivity was published in the design report in 2004 and should be seen as preliminary value. Only after the commissioning of KATRIN detailed estimations of the systematic errors and background rates were possible. Currently new sensitivity studies are performed by the collaboration. More details about the updated KATRIN systematics and sensitivity can be found for example in [Sch19]. Also, the background sources are not fully understood yet and subject of current studies.

8.4 The TRISTAN project

TRISTAN is an extension of the KATRIN project to search for the signature of keV-scale sterile neutrinos in the tritium spectrum [MLG+15, M+19]. Already in section 8.1.1 the impact of the neutrino mass on the electron spectrum was explained: in case of three different neutrino mass eigenstates, the observed spectrum is a superposition of three different spectra, where each spectrum has an endpoint shifted by the corresponding mass and a normalization similar to the eigenstate's admixture in the electron antineutrino, which is produced in the β-decay of tritium. Since the differences between the masses are too small to be resolved, the spectrum can be regarded as a single spectrum, where the endpoint is shifted by the effective electron neutrino mass.
In case of a sterile neutrino with a mass in the keV range, one could observe a clear separation of the superimposed spectra, resulting in a kink in the combined spectrum. Referring to equation 8.1, one can write

$$\frac{d\Gamma}{dE} = \cos^2(\theta) \cdot \frac{d\Gamma}{dE}(m_{\bar{\nu}_e,\text{eff.}}) + \sin^2(\theta) \cdot \frac{d\Gamma}{dE}(m_{\text{sterile}}), \tag{8.6}$$

where θ is the active-sterile mixing angle and m_{sterile} the mass of the sterile neutrino. An exaggerated illustration of the signature of a 10 keV sterile neutrino is shown in figure 8.7. The mixing angle is expected to be very small (see section 1.6 in the introduction), such that statistical uncertainties alone demand an extremely high count rate, if one wants to probe the parameter space of cosmological interest in a reasonable

measurement time. Hence it is an natural choice to use the tritium source of KATRIN with its unmatched activity of 10^{11} counts per second.

KATRIN, which searches for a shift of the spectral endpoint to measure the absolute neutrino mass, scans the tritium spectrum only in a small interval down to a few tens of eV below the maximum decay energy. Since the signature of a sterile neutrino could occur at any point of the tritium spectrum, for TRISTAN a scan of the entire spectrum is necessary, resulting in an electron rate at the detector a few orders of magnitude larger than in normal KATRIN operation mode. During the main measurement phase with 10^{11} decays in the source, turning off the retarding potential would result in a rate of 10^{10} counts per second, when a small acceptance angle is chosen. With the original KATRIN detector of 148-pixels a measurement at such a high rate is not possible, as events would pile-up constantly. The TRISTAN project thus focuses on the development of a novel semiconductor detector array with much more pixels.

As a matter of fact a limited keV-scale sterile neutrino search is already possible with the KATRIN hardware as-is, but under non-standard measurement conditions. For the first KATRIN physics run in June 2018, only a small amount of tritium ($\sim 500\,\mathrm{MBq}$, $< 1\%$ of nominal activity) was in injected into the source that allowed to scan the spectrum down to 4 keV below the endpoint. This data is currently being analyzed and a publication is in preparation.
The tritium scan at full source strength will be performed after the neutrino mass program is finished by installing the new detector array at KATRIN. Actually the tritium density in the source will be reduced by a factor 100 compared to KATRIN to reduce scattering in the source, which has a strong impact at lower energies. As a result the detector has to deal with a maximum rate of 10^8 counts per second, taking into account also the acceptance angle.
To achieve a sensitivity at which one starts to probe the sterile neutrino parameter space of cosmological interest, apart from performing a high statistics measurement it is necessary to understand the spectrum at a parts-per-million level. It is planned to combine an integral and a differential measurement. The integral measurement is the standard KATRIN operation mode, where a threshold is applied to the MAC-E filter and the detector counts the transmitted electrons. In this mode one makes use of the high energy resolution of the filter, but is suffering from systematics as source stability. In the differential measurement the spectrometer is operated at a low retarding potential and the electron energy is determined by the detector. In this mode a full understanding of the energy response is necessary. By combining both measurement modes, improved results compared to a single mode are expected, as both have different systematic effects and thus can be cross checked against each other.

Concerning the analysis there are two different approaches: the classical χ^2-minimization and the wavelet approach, where wavelet transforms are used to search for an distortion in an otherwise smooth spectrum [MDK$^+$15]. The latter is almost independent from the general spectral shape but could lead to false detection in case of uncorrelated systematics (non-smooth functions). In the end, a combination of both techniques will result in the best sensitivity. A plot of a sensitivity study from [M$^+$19] is shown in figure 8.8. As one can see, previous laboratory limits would already be surpassed by a measurement with the unchanged KATRIN spectrometer (dashed line). With the TRISTAN setup including the new detector array and taking systematic effects into account the parameter space could be probed down to $\sin^2(\theta) \approx 10^{-6}$ after three years

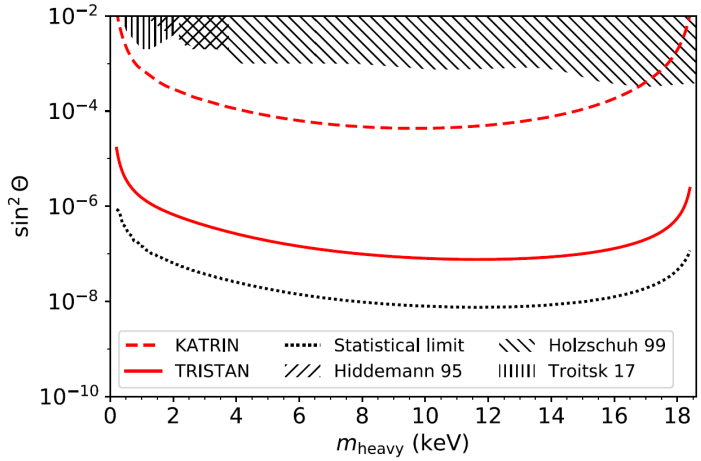

Figure 8.8: A plot of a TRISTAN sensitivity study from [M+19]. The sterile neutrino parameters here are the mixing angle ($\sin^2\Theta$) and the sterile neutrino mass (m_{heavy}). Even with the unchanged KATRIN setup (red dashed line) one could improve current laboratory limits by about one order of magnitude. The laboratory limits were published in [A+17a] (Troitsk ν-mass MAC-E type tritium spectrometer), [HKP+99] (measurement of ^{63}Ni-spectrum with a magnetic spectrometer) and [HDS95] (measurement with tritium embedded in a metal lattice and a magnetic spectrometer, interestingly performed at TUM). The statistical sensitivity of TRISTAN reaches an admixture of $\sim 10^{-8}$ after a 3 year measurement with $\sim 10^{16}$ events. Considering also systematical uncertainties a sensitivity down to $\sin^2(\Theta) = 10^{-6}$ is anticipated.

of measurement and about 10^{16} events. More detail about TRISTAN sensitivity studies can be found in [MLG+15].
In addition to the new detector, it is planned to adjust the setup in other ways for TRISTAN: to reduce backscattering from the rear wall it is planned to replace the gold rear wall with one made from Beryllium and change the magnetic field. Also the magnetic field in the main spectrometer might be changed to ensure the adiabatic transport also for electrons with large surplus energies. As mentioned above, also the source density will be reduced. This is not as trivial as it sounds because the source was designed for a certain gas composition and pressure. Since the TRISTAN project is still in active development, many of these aspects are subject to change. However, the main focus of the R&D effort is on the detector system. It has following requirements, as presented in [M+19]:

- **number of pixels:** the expected rate of $\sim 10^8$ counts per second (source strength reduced by factor 100 compared to KATRIN and $\sim 10\%$ acceptance) demands a detector with at least 1000 pixels, if the rate is constrained to 100 000 cps for each pixel. This upper rate is necessary to limit pile-up. On the other hand, the number of pixels should not be too high to keep the cost and complexity at manageable level;

- **resolution:** to observe the kink-like signature of a sterile neutrino in the differential measurement, one wishes the resolution to be as high as possible. A specific requirement is set by the wavelet analysis approach, which demands a resolution of a 100-200 eV in the energy region of interest [MDK+15];

- **size:** the pixel size has a lower limit to prevent the charge from splitting between adjacent pixels (charge sharing), and an upper limit by the fluxtube size (size of

the electron beam) and the necessary number of pixels, which have to fit into the constrained space. In addition it is desired that backscattered electrons, if they are reflected back onto the detector from a magnetic mirror, return to the same or a neighboring pixel. The pixel size is thus linked to the gyro-radius, which again is controlled by the magnetic field strength. The magnetic field on the other hand defines also the size of the fluxtube. A detailed optimization of the detector layout was performed with the help of Monte-Carlo simulations [Kor16, M$^+$19]. Considering also other aspects like the angle dependent (magnetic field-dependent) backscattering probability and fixing the pixel number to 3500, the optimum pixel diameter was found to be 3 mm and a total detector radius of 10 cm;

- **dead layer:** electrons have generally a short interaction length compared to X-rays or γ-radiation and thus are very prone to backscattering, resulting in a reduced energy resolution. To minimize backscattering the detector should have a very thin dead layer with a thickness of a few tens of nm. In addition a thin dead layer allows to set low energy thresholds such that coincident events due to charge sharing or backscattering with subsequent backreflection can be tagged also in cases when one of both events is very small.

The requirement of a high counting rate demands a very fast read-out system. As it will be shown in section 9.1.2, the electronic noise that dominates the energy resolution in a detector front-end with a fast signal shaping is scaling linearly with the system's (including the detector's) capacitance. The projected resolution can be achieved if silicon drift detectors (SDDs) are used, which generally have a very small capacitance compared to other semiconductor detectors thanks to their small electrodes. This technology is discussed in detail in section 9.1, where also more information about the planned final detector and its read-out system is given (section 9.4). Additional details about the TRISTAN detector developments were published in [M$^+$19].

The TRISTAN measurement with the changed KATRIN setup is planned to be launched after the neutrino mass program is finished in 2025. TRISTAN will then take data for 3 years beam time (5 calendar years) and probe the parameter space for masses up to 18 keV down to a mixing of 10^{-6}. Before this measurement, first sterile neutrino searches are performed during the commissioning of KATRIN with an unaltered setup, which can already deliver results that surpass previous limits set by laboratory measurements.

In the next chapter an introduction to semiconductor detectors is given and prototype detectors produced for TRISTAN are presented. In chapters 10 and 11 results from the characterization of these prototypes and the analysis of tritium spectra taken at Troitsk ν-mass are reported.

Chapter 9

TRISTAN detector prototypes

In this chapter an introduction to semiconductor detectors and particularly to the silicon drift detectors developed for TRISTAN is given. A comprehensive introduction to the physics of semiconductor detectors, the electronic systems, electronic noise and silicon drift detectors is given in section 9.1. The prototype detectors produced for TRISTAN are presented in section 9.2. The detectors which were used in the framework of this thesis are equipped with a specific read-out system – the IDeF-X BD ASIC –, which is described in section 9.3. An outlook on future developments for TRISTAN and the final detector system is given in section 9.4.

9.1 Semiconductor detectors and silicon drift detectors

The electron detector for TRISTAN is a silicon drift detector (SDD), a special type of semiconductor detector. A semiconductor detector works like an ionization chamber: ionizing radiation, for example X-rays or electrons, produce a cloud of mobile charge carriers in the detector – electrons and holes. Under the influence of an electric field applied to the sensor the charge carriers move to electrodes, where they induce a current pulse. The number of produced charges is proportional to the deposited energy, and can be determined by integrating over the induced current, obtaining the signal charge. In the following, the basic working principle of a semiconductor detector is recapitulated. A comprehensive overview on semiconductor detector systems, the underlying physics and read-out electronics can be found for example in [Spi05], which also served as a reference for this introduction.

9.1.1 Basic principles of semiconductor detectors

A classical silicon detector is a p-n-junction: a silicon bulk that is (typically) n-doped, i.e. "contaminated" with small donor-impurities that give extra electrons, with a p-doped surface on one side, where the doping consists of acceptors that supply extra holes. Silicon is a crystalline semiconductor. Within the crystals one cannot consider the discrete energy levels of electrons for each atom individually, but can describe them globally for the material. As a result one obtains the electronic band structure that describes the range of energies an electron may have, and the energies that are forbidden. In a semiconductor the Fermi level, which is the maximum energy of electrons at a certain temperature, lies within a forbidden region – the band gap – while the allowed band below – the valence band – is completely populated. Thus a movement of the charges is not possible and the material is not conducting. However, another

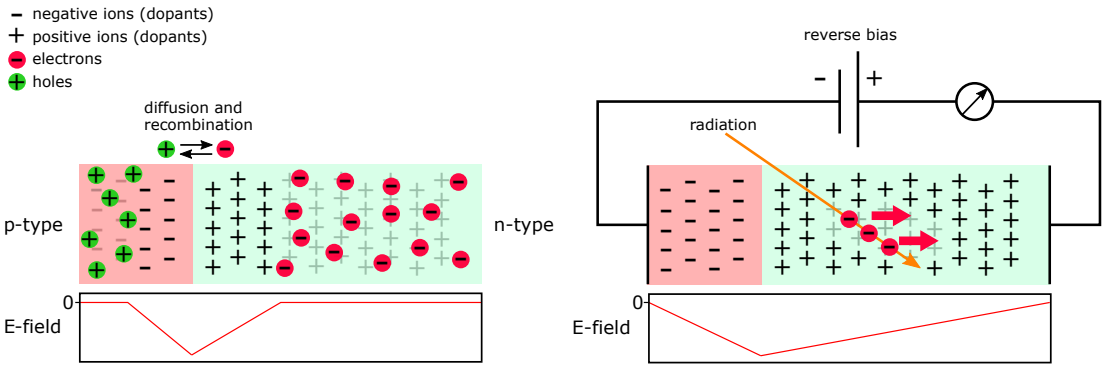

Figure 9.1: Left: a p-n-junction. In the depletion region electrons diffuse into the p-doped silicon, while holes diffuse into the n-type bulk. Electrons and holes then recombine such that the ionized dopants, which are immobile, remain and create an E-field. **Right:** when a reverse bias is applied to the junction, a detector is created. The depletion region is widened until it ideally extends through the entire silicon, ridding it of free charge carriers. Radiation can promote electrons into the conduction band, where they are moved by the E-field towards the anode. The movement of the electrons creates a current pulse in the external circuit that can be measured.

band – the conduction band – lies only slightly above the Fermi energy (for silicon the band gap has a width of 1.12 eV). Due to the small band gap some electrons are thermally excited into this band, granting the material a small electrical conductivity. By doping a semiconductor, one can move the position of the bands with respect to the Fermi level: in case of n-doping, the Fermi level is close to the conduction band, which then easily receives electrons from the donors. For p-doping the Fermi level is close to the valence band and the acceptor can remove electrons from it, such that a hole can move through the material in the valence band. In summary, the doping increases the conductivity of the semiconductor.
A doped semiconductor is neutrally charged, since for each charge carrier a doping atom (dopant) with its local space charge exists. However, at the boundary between p- and n-doped silicon the charges diffuse from one side to the other, i.e. holes from the p-doped silicon combine with free electrons in the n-doped material and vice-versa. As a result the boundary is depleted from free charge carriers and, since the dopants are not mobile, the p-doped side has a negative charge and the n-doped side a positive one. This potential difference creates an E-field that is directed against the diffusion of charges such that an equilibrium is attained. A semiconductor with a p-n junction is a diode: if a voltage is applied as a forward bias by connecting the p-type semiconductor with the positive terminal and the n-type with the negative terminal, the width of the depletion region is reduced because holes and electrons are pushed into the zone against the zone's electric field and neutralize it, and, if the bias voltage is sufficient, reverse its polarity. Then a current can flow.
For a voltage applied in the opposite way – reverse bias – the charge carriers are pulled away from the junction and the width of the depletion region increases. To create a detector the voltage is chosen such that the entire bulk is depleted. If now ionizing radiation creates free charges in the n-doped volume, they move in the electric field towards the electrodes, where they create a current pulse in the external circuit – voilà, we have a detector! The electrons and holes move non-ballistically, i.e. their speed is determined by their scattering and depends thus only on the electrical field, not on the time of acceleration. A scheme of a p-n-junction and a detector is shown in figure 9.1. One often speaks about "the charge being collected" and could thus think that the

signal is generated when the charge reaches the electrodes. But as a matter of fact the current flow begins instantaneously when the charge starts to move, according to the Shockley-Ramo theorem [He01].

A reverse biased detector is not completely free of mobile charges since thermal excitation can promote electrons across the band gap such that a current flows even when the detector is not exposed to radiation. This current is called leakage current or dark current. It depends exponentially on the temperature T:

$$I_{\text{leak}} \propto T^2 \cdot \exp\left(-\frac{E_g}{2k_{\text{B}}T}\right), \tag{9.1}$$

where E_g is the width of the band gap (1.12 eV for silicon). The leakage current is not constant but fluctuating due to electron emission statistics and is thus a source of electronic noise (see section 9.1.2). From the equation above one can derive that by lowering the temperature by 14°C, the leakage current is reduced by a factor of 10. This is the reason why a semiconductor detector shows optimum performance below room temperature, where the leakage current becomes negligible compared to other sources of noise.

To have a working detector system, some electronics are necessary. The essential components of a basic system are a preamplifier, a pulse shaper and a digitizer:

- **preamplifier:** the charge generated in the detector by an event is very small, so the signal has to be amplified. The average charge signal Q_s created by an event with energy E is

  $$Q_s = \frac{E}{E_i} \cdot e, \tag{9.2}$$

  where E_i is the energy required to form an electron-hole pair (3.6 eV for silicon), and e the electron charge. For 10 keV deposited energy, which is a typical energy for the TRISTAN project, a charge signal of 0.4 fC is generated. The gain of the amplifier in the IDeF-X BD ASIC (see section 9.3) is ~ 180 mV per fC;

- **pulse shaper:** the pulse shaper improves the signal to noise ratio by applying a frequency filter to the incoming signals. This is possible since noise spectra extend over a greater frequency band than the signal. In principle the pulse shaper consists of a high- and low-pass filter. This filter also changes the shape of the pulse from a delta-like function to a smooth peak (e.g. a Gaussian). The height of the peak is proportional to the signal strength, i.e. the energy of the detected event. An important parameter, associated with the pulse shaping, is the shaping time t_s that is the time difference between the charge injection (by the detector) and the maximum of the shaped pulse. The peaking time t_{peak} is the time from 5% of the maximum to the maximum;

- **digitizer:** an analog-to-digital converter (ADC) translates the continuously varying pulse heights to discrete digital values that in the end make up a measured histogram. A digitizer can also be placed earlier in the read-out chain.

9.1.2 Energy resolution and electronic noise

The amount of charge carriers $N = E/E_i$, generated by events with similar energies E, is statistically fluctuating. The relative resolution, according to Poissonian statistics,

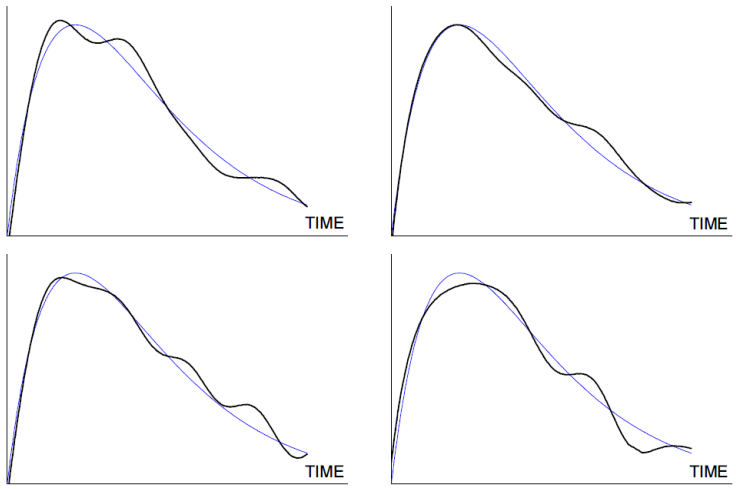

Figure 9.2: An illustration of electronic noise from [Spi05]: four different pulses (the shaped signal) are superimposed with fluctuations due to noise (signal to noise ratio 20). As a result, each pulse has a different amplitude. For many events with similar energy, one obtains a Gaussian amplitude distribution, i.e. instead of a delta-like spectral line a Gaussian peak is observed.

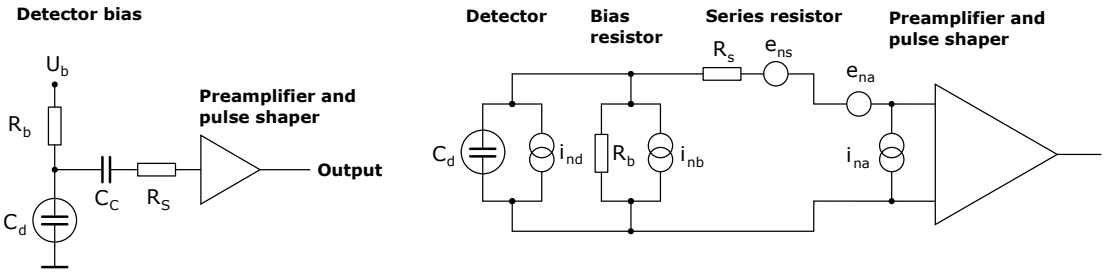

Figure 9.3: A scheme of a detector read out circuit and its equivalent circuit for noise calculation, adapted from [Spi05]. **Left:** a scheme of a simple front-end circuit. The detector is represented by the capacitance C_d and bias voltage is applied through the resistor R_b. The coupling capacitor C_c blocks the sensor bias voltage from the amplifier input. The series resistance R_s represents any resistance present in the input signal input path. **Right:** the equivalent circuit for the noise calculation. It includes both current (i) and voltage (e) noise sources. The detector leakage current is represented by a current noise generator i_{nd} in parallel with the sensor capacitance. Resistors can be modeled either as voltage or current generators. Here, the bias resistor acts as a current generator i_{nb} and its noise current has the same effect as the shot noise current from the detector. The series resistor R_s acts as a voltage generator. The electronic noise of the amplifier is described fully by the voltage and current sources e_{na} and i_{na}.

is described by following equation:

$$\frac{\Delta E}{E} = \sqrt{\frac{F \cdot E_i}{E}}, \tag{9.3}$$

where E_i is the energy necessary to create an electron-hole pair (3.6 eV). The statistical fluctuations are reduced by the Fano factor F, which takes into account that the energy in the crystal is also absorbed by lattice vibrations that have much lower excitation energies than the formation of electron hole pairs. Thus, many more excitations are involved than apparent from the charge signal alone and this reduces the statistical fluctuations of the signal. For example, in silicon the Fano factor is $F \approx 0.12$ (depending on energy and temperature [PF99]). Due to these fluctuations monoenergetic signals result in a spread of the signal charge with a Lorentzian shape. However, for the work presented in this thesis the Gaussian electronic noise is the dominating factor for the energy resolution.

Electronic noise, which is a fluctuation of the signal current, originates from variations in the velocity and number of charges. The velocity and number fluctuations themselves are caused dominantly by the thermal motions of the conductive material, leakage current and the stochastic nature of trapping and detrapping of charge carriers. The amplitude distribution of these fluctuations is a Gaussian, so if the noise is added onto a constant signal (i.e. a line in an energy spectrum), one obtains a Gaussian around the signal amplitude, whose width equals the noise level. An illustration how the noise affects the signal pulses is shown in figure 9.2. The noise level not only determines the resolution of the system, but also the detection threshold, as for an increased noise a higher signal amplitude is necessary to rise clearly above the level of fluctuations.
As the pulse shaper is in principle a high / low-pass filter, one is interested in the frequency distribution of the noise. There are two different noise behaviors:

white noise: thermionic emission of charges, e.g. detector leakage current, causes number fluctuations and has a "white" frequency spectrum, i.e. the spectral density is independent of frequency. This is also called shot noise. Also thermal motion that results in velocity variations causes fluctuations with a white spectrum;

$1/f$-noise: trapping and detrapping of charges in resistors, dielectrics and semiconductors introduces noise with a $1/f$-spectrum, where the amplitude is decreasing with increasing frequency. It is also called "pink noise", or, if occurring in electronic devices, "flicker noise".

A typical detector front-end circuit and its equivalent for noise calculations are shown in figure 9.3, following [Spi05]. The front-end circuit consists of a capacitance C_d that represents the detector. Bias voltage is applied via a resistor R_b. A blocking capacitor C_c couples the signal to the preamplifier, while disconnecting it from the bias voltage. The series resistance R_s represents the sum of all resistances present in the connection from the sensor to the amplifier input. In addition, a bypass capacitor C_b stabilizes the bias voltage and shunts any external interference coming through the bias supply line to ground.
The equivalent circuit contains current and voltage noise sources. The fluctuating detector leakage current is modeled as a current source i_{nd} in parallel to the sensor. Resistors act as a source of noise due to thermal velocity fluctuations of the charge

carriers. They can be modeled either as voltage or as current generators. Choosing the appropriate model merely simplifies the calculation. Generally, resistors that shunt the input signal are modeled as noise current sources (called "parallel noise"), while resistors in series with the input are modeled as noise voltage sources ("series noise"). As a result the equivalent circuit contains the bias resistor's noise as current generator i_{nb} and the voltage source e_{ns} for the series resistance. The amplifier's noise is modeled by current and voltage generators i_{na} and e_{na}.
Since detectors usually measure charge, the noise level is commonly expressed as "equivalent noise charge" (*enc*) in units of elementary charge. It describes the number of electrons released in the detector that would create a signal, where the signal-to-noise ratio equals 1. The *enc* is depending on the pulse shaping, which acts as a frequency filter. Typically the characteristic time of the pulse shaper (for example the peaking time t_{peak} or shaping time) can be adjusted, such that the noise level can be minimized accordingly to the current status (e.g. temperature) of the system. White noise from current sources increases with t_{peak}. This becomes intuitively clear, when the pulse shaper is regarded as an integrator over time. Then the total current noise can be viewed as the result of "counting electrons". Keeping this notion, one can also conclude that current noise is independent of the detector capacitance. On the other hand, voltage noise is increasing with detector capacitance, because the latter reduces the signal voltage and thus the signal-to-noise ratio. In addition, voltage noise decreases with peaking time. One can imagine that with a longer peaking time fluctuations in the detected charge are averaged out. The total noise with $1/f$-spectrum depends on the ratio of upper and lower cutoff frequencies in the shaper (i.e. the pulse shape), and, if both are scaled by the same factor, is constant with peaking time.
Since the individual noise sources are random and uncorrelated, they have to be added in quadrature, such that one obtains for the noise level (after calculations that can be found for example in [Spi05])

$$enc^2 = i^2 \cdot F_1 \cdot t_{\text{peak}} + e^2 \cdot F_2 \cdot \frac{C^2}{t_{\text{peak}}} + F_3 \cdot A_f \cdot C^2, \tag{9.4}$$

where i is the sum of the current noise, e the white voltage noise, C the sum of capacities, F are shape factors that depend on the pulse shaper, and A_f is the noise coefficient for $1/f$-noise. Actually, i and e are spectral densities of the noise. Their individual contributions, according to the equivalent circuit in figure 9.3, are:

- **shot noise:** the shot noise spectral density (i.e. current variance per Hertz of bandwidth) for the detector current source in the equivalent circuit is

  $$i_{nd}^2 = 2 \cdot e \cdot I_{\text{leak}}, \tag{9.5}$$

  as it was originally derived by Schottky. A review of shot noise and the calculation of the spectral density can be found in [BB00];

- **thermal noise:** the spectral density of thermal noise, also called Johnson-Nyquist noise, for voltage and current sources (the bias and series resistors in the equivalent circuit), are

  $$i_{nb}^2 = 4 \cdot k_{\text{B}} \cdot T/R_b \quad \text{and} \quad e_{ns}^2 = 4 \cdot k_{\text{B}} \cdot T \cdot R_s, \tag{9.6}$$

  as derived by H. Nyquist in [Nyq28];

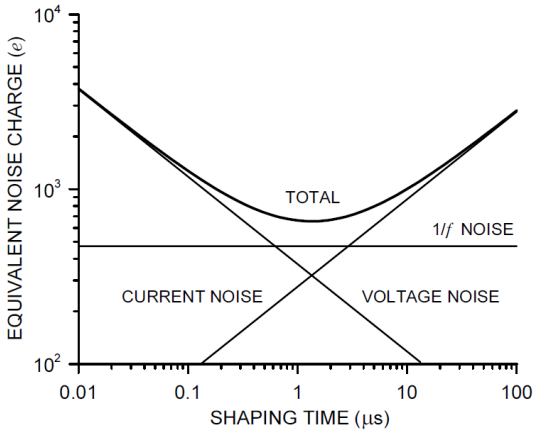

Figure 9.4: A sketch of the different noise contributions from [Spi05]: as one can see, the different time dependence of the voltage and current noise lead to an optimum peaking time (or shaping time), where the noise level is minimized. The noise level and the position of the minimum are depending on parameters of the read-out system, but also strongly on the detector capacitance and temperature.

- **$1/f$-noise:** The spectral density of $1/f$-noise is

$$e_{nf}^2 = \frac{A_f}{f}, \tag{9.7}$$

  where A_f is a noise coefficient specific for the detector.

The derivation of the spectral densities can be also found in [Spi05].

If we insert the spectral densities from above in the equation 9.4 for the *enc*, one obtains:

$$enc^2 = \left(2eI_{\text{leak}} + \frac{4k_{\text{B}}T}{R_b}\right) F_1 t_{\text{peak}} + (4k_{\text{B}}TR_s + e_{na})F_2\frac{C^2}{t_{\text{peak}}} + F_3 A_f C^2 \tag{9.8}$$

As one can see there is a peaking time, where the white noise current and voltage contributions are equal and the noise level thus minimal. The $1/f$ noise increases the noise level independently of time. A sketch of the different contributions is shown in figure 9.4. From the equation one can see that the capacitance of the system, including the detector, should be as small as possible if one wants to achieve a high energy resolution. A low capacitance also shifts the optimum shaping time to lower values and thus allows a faster read-out system. In addition, from equation 9.8 the temperature dependence of the noise level becomes clear. What is not clear from just the equation, is that the leakage current I_{leak} is strongly temperature dependent (as mentioned in section 9.1.1). Thereby, reducing the temperature not only lowers the general noise level, but also moves the optimum peaking time to shorter times. In conclusion, a lower temperature and a small capacitance both increase the energy resolution and the maximum rate the detector can handle, before pile-up becomes a problem.

The IDeF-X read-out circuit is more advanced than the simple front-end circuit for which the noise was derived here, but the basic dependence of the noise level on peaking time, temperature and capacitance is still valid. The important messages of this (a bit lengthy) introduction are: a low noise-level allows a high energy resolution, a low

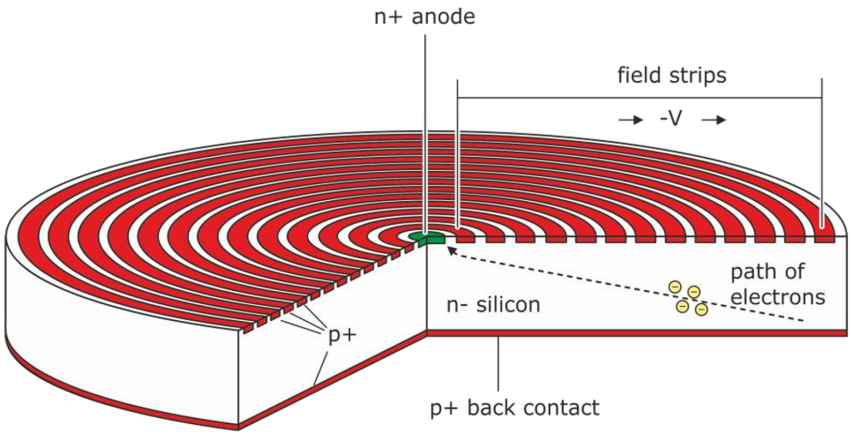

Figure 9.5: A scheme of a silicon drift detector [LFH+01]. The point-like anode is surrounded by drift rings, where a negative voltage that increases with radius is applied. Together with the bias voltage on the back side a static electric field is created, in which the electrons created by an event move towards the anode.

detection threshold and high counting rates, all important characteristics for the TRISTAN project. The noise can be minimized by cooling the sensor and by constructing a detector with a small capacitance. This leads to the next section, where silicon drift detectors are introduced.

9.1.3 Silicon drift detectors

A classical semiconductor detector consists of a large cathode and an equally large anode. In a silicon drift detector (SDD), the anode is reduced to a small dot, which results in a reduction of the detector capacitance. The cathode, i.e. the entrance window, is much larger. A detector that has such a configuration of small anode and large cathode alone would have a sensitive volume much smaller than the silicon bulk. To create a functional detector, several rings with a negative potential surround the anode. When proper ring voltages are applied that increase with radius (become more negative) the detector is depleted also from the sides and a static electric field is generated in the silicon that moves electrons towards the anode, wherever they are created [LFH+01]. This working principle is based on the semiconductor drift chamber introduced by Gatti and Rehak in 1984 [GR84]. A scheme of a silicon drift detector is shown in figure 9.5. The electric potential within a SDD is illustrated in figure 9.6. As one can see, the negative potential on the entrance window (back contact) and on the drift rings on the front form a funnel-like potential, in which the electrons are moving towards the anode at the front center.

There are many advantages of SDDs over conventional semiconductor detectors. As already mentioned the capacitance of the sensor is ultra low thanks to the tiny anode, resulting in a generally low noise, but also an optimum performance at short shaping times such that a high counting rate can be achieved. The capacitance can be further reduced by integrating the amplifier – a field effect transistor (FET) – directly onto the chip surface next to the anode. This was not realized for the detectors which were used in the work presented here, but the next TRISTAN prototypes will have integrated FETs, which bring additional advantages like the removal of electrical pick-up and microphony, i.e noise generated by mechanical vibrations [LFH+01].

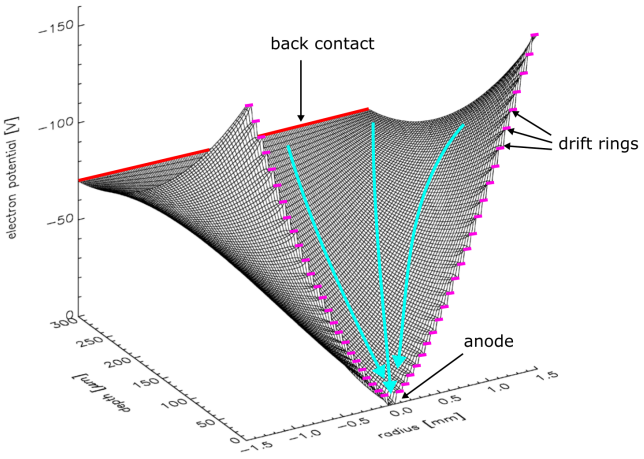

Figure 9.6: The electron potential in a silicon drift detector, adapted from [LFH+01]. The cyan arrows mark the path of electrons. The negative bias voltage is applied to the back contact (i.e. the radiation entrance window), the anode is at ground potential. The potential on the drift rings is increasing (negative) with radius, such that a funnel is formed, where the electrons (cyan arrows) move from the entrance window side towards the anode.

SDDs can be produced in various sizes and shapes. In addition, large monolithic arrays can be created by contouring a doped silicon wafer with anodes and drift rings on one side, while the other side is one large cathode. A separation and definition of pixels is then achieved alone by the electric field. There is no physical boundary between the pixels, such that a detector with 100% surface coverage can be produced. In case of charge sharing, i.e. when an event close to the border is split between two pixels, no charge is lost. The size of a monolithic array is only limited by the wafer production.
To reduce the amount of necessary cabling the drift rings are connected on the chip with integrated voltage dividers, such that in addition to the back contact bias only two voltages have to be applied, the voltage for the outermost ring and another one for the innermost ring.
The SDD prototypes produced for TRISTAN are presented in the following section.

9.2 Prototype-0: first detector developments for TRISTAN

Several silicon drift detector (SDD) prototypes with 7 hexagonal pixels each have been produced by the semiconductor lab of the Max-Planck-Society (HLL MPG), see for example [LFH+01]. As these are the first detectors produced for TRISTAN, we call them "prototype-0". The various detectors differ in size ($0.25 - 2\,\mathrm{mm}$ pixel diameter) and number of drift rings ($2 - 12$). As discussed in section 8.4, the scale of the pixels is determined by three factors: while the expected count rate sets a lower limit on the number of pixels, the fluxtube constrains the maximum detector radius. Both requirements together set an upper limit on the pixel size. In addition, the pixel size should be as large as possible to limit charge sharing. This results in an optimum pixel diameter in the order of $1 - 2\,\mathrm{mm}$.
One of these detectors is shown in figure 9.7. Here, one can see that there are actually three 7-pixel detectors on the silicon chip, which has an area of $1 \times 1\,\mathrm{cm}^2$ and a thickness of $450\,\mu\mathrm{m}$. However, only one detector (with $0.5\,\mathrm{mm}$ pixel diameter) is bonded to the

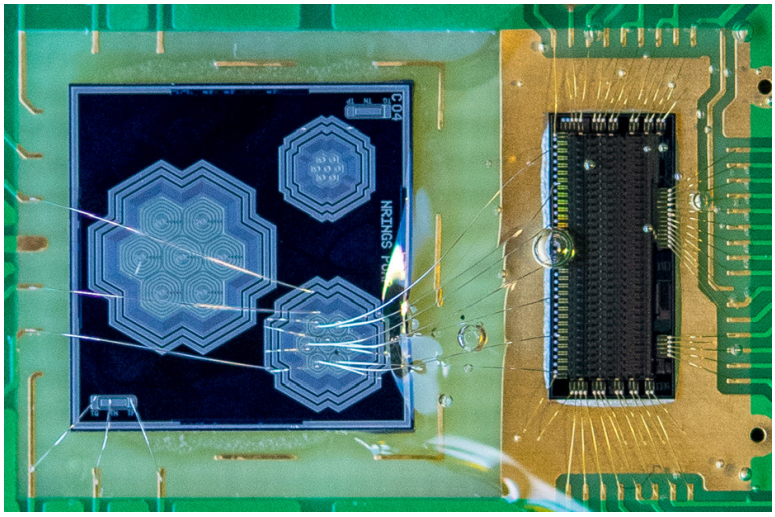

Figure 9.7: A prototype detector: this chip contains 3 individual 7-pixel detectors in different sizes, one is bonded to the IDef-X BD ASIC on the right. The chip with the detectors has the dimensions of 1x1 cm.

read-out chip. The read-out on the photograph is the IDeF-X BD ASIC[1] (see section 9.3), which was used for the first prototypes. It was developed at CEA Saclay in the electronics department of DRF/IRFU and is a proven and reliable system. Since the ASIC contains also the signal amplifier, the prototype-0 SDDs don't feature a state-of-the-art on-chip amplification (integrated FET).
The photo shows the contoured side of the detector, such that the anodes, which are bonded to the ASIC, are visible together with the surrounding drift rings. The entire 7-pixel array is surrounded by a guard ring and two voltage rings, from where the ring voltages are distributed to each pixel. The drift rings are interconnected on the chip with resistors such that only the inner and outer voltage have to be set. Since there is also a ground connection, in total three bond wires are visible in addition to the 7 anode bonds. The other side of the detector – the entrance window – is entirely covered by the cathode. There the bias voltage (back contact) and guard ring voltage (back frame) are set. Each detector chip is equipped in addition with two diodes for a temperature measurement. In the TRISTAN prototypes only one of these diodes is contacted with wire bonds, visible in the photo on the lower left of the chip. The diode is operated at a constant current in forward direction. The voltage drop then linearly changes with the temperature at about $\sim 3\,\mathrm{mV/K}$ [Lec].

As discussed in section 9.1, the SDDs have following features:

- no dead area due to monolithic design;
- efficient and fast charge collection by shaping the electric field with multiple drift rings;
- low capacitance $\sim$ fF, energy resolution of a few hundred eV;

and, not a general characteristic of SSDs:

- ultra-thin ($\sim 30\,\mathrm{nm}$) dead layer that allows a low threshold $\sim 1\,\mathrm{keV}$ and minimizes backscattering for electrons.

[1] ASIC: application specific integrated circuit. In this case an ASIC is a miniaturized detector front-end.

detector name	pixel diameter [mm]	number of drift rings
I-02	0.5	2
C-04	0.5	3
L-13	1	2
I-11	1	6
F-09	2	12

Table 9.1: Parameters of the prototype detectors that were tested with the IDeF-X BD ASIC.

Detectors with an ultra-thin dead layer are a specialty of HLL MPG. How they are produced is an in-house secret. The exact width of the dead layer has to be measured by comparing measurements with simulations (as for example done in section 11.4.4, where a good agreement was found for a 40 nm dead layer). First results of dedicated measurements show that the dead layer thickness of the tested detectors is between 50 and 100 nm [Sie19].
A list of the prototypes with the IDeF-X read out and their parameters can be found in table 9.1. These are the detectors that are relevant for the work presented in this thesis. Later, more prototype-0 detectors were produced with a different read-out (based on the CUBE by XGLab), as presented for example in [M$^+$19, BFF$^+$11].

9.3 The IDeF-X BD ASIC

The read-out system of the first prototypes is the IDeF-X BD ASIC, a well proven system that is optimized for low capacitance and low leakage current silicon detectors. It was originally developed for space applications by the electronics and detectors division of IRFU at CEA Saclay. IDeF-X stands for Imaging Detector Front-end. The noise floor of this ASIC is 44 electrons, which corresponds to a resolution ($fwhm$) of 400 eV at 17 keV. It has 32 channels, thus allowing us to read out all 7 pixels of one SDD prototype synchronously and to detect coincident events.
A special feature of this ASIC is that it has dual polarity, i.e. it can be connected to the detector anode or cathode[2]. A description of this system was published in [GDH$^+$15]. The first component of the ASIC in a signal channel is a charge sensitive amplifier (CSA) with a continuous reset system, i.e. after each pulse the voltage at the amplifiers output is decaying back to the baseline value. This is in contrast to a pulsed reset, where the charge signals are integrated over a certain time (that can contain multiple events) such that the voltage increases at the amplifier output until it is periodically reset, forming a characteristic sawtooth function. The next component in the read-out chain of this ASIC is a two stage pole-zero cancellation that prevents the decaying output of the amplifier from undershooting below the baseline. A fluctuating baseline would lead to a spread in the pulse heights, and thus have the same effect as noise. The pole-zero cancellation is followed by the pulse shaper with selectable shaping time, an polarity selector and a peak detector that memorizes the amplitude of the pulse. A discriminator checks whether the signal is rising above a programmable threshold to start the read-out chain. The last component in the ASIC is a multiplexer that can combine on demand the signals from all 32 channels and forward them through a single

[2]The dual-polarity version of the ASIC was chosen such that the same PCBs and test bench can be used for other TRISTAN prototype detectors produced at LBNL (USA), where holes instead of electrons are read out.

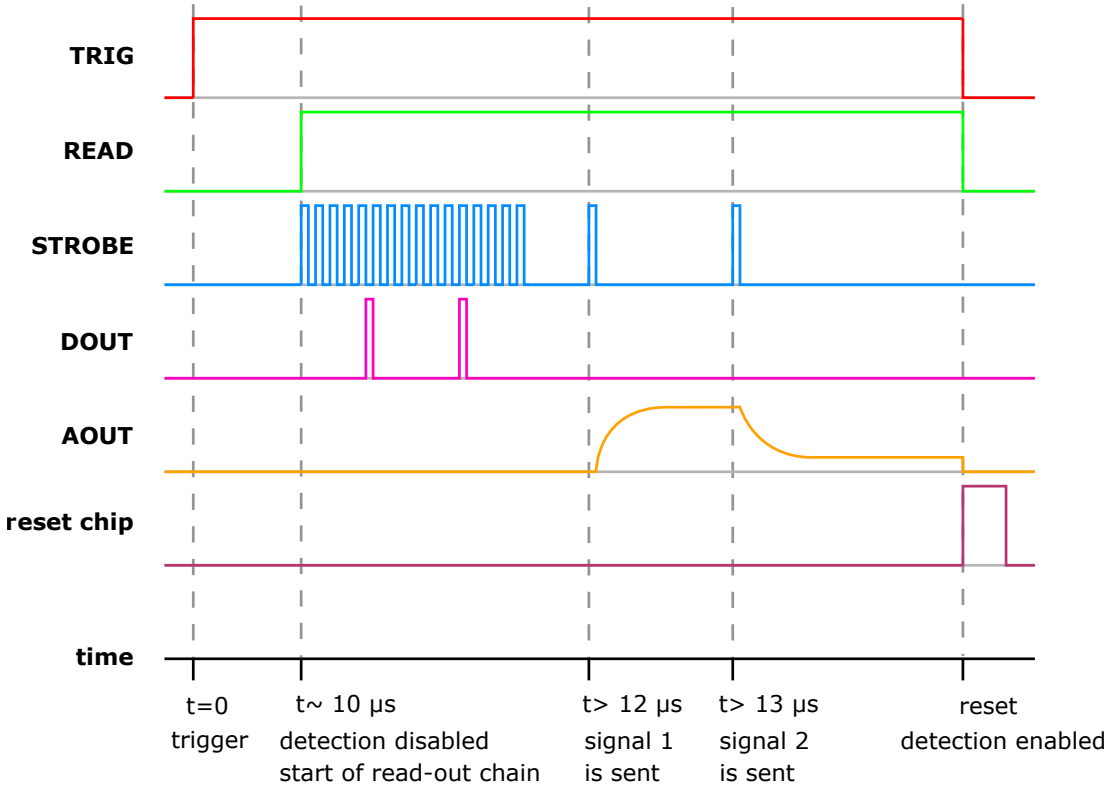

Figure 9.8: A simplified scheme of the signal chain that controls the read-out of the chip. In this example, two events are registered. See the text for explanations.

output line.
Several parameters of the ASIC can be set by the user. For this work the most important adjustable parameters are the energy threshold and the peaking time (or shaping time). The peaking time can be set to 0.58, 0.95, 1.77, 2.6, 3.4, 4.4, 5.2 or 6.8 µs (shaping time: 0.9, 1.6, 2.4, 3.6, 4.8, 6.0, 7.2 or 9.6 µs). The threshold can be chosen in 285 eV steps (in anode mode) from -0.6 keV to 17 keV.

The particle detection can be separated into two steps: the detection of a particle by the chip, and a sequence of digital communication that results in the data stored in the ASIC being sent to the user. The signal chain is illustrated in figure 9.8. As long as the signal "READ" equals 0, the ASIC is waiting for a particle. If an event occurs and the shaped signal rises above the set threshold, the discriminator sets a trigger signal "TRIG" to 1, which stays at this value until the read out sequence is finished. In addition the hit register in the channel is set to 1. After TRIG rises up, the controller waits a delay equal to the shaping time before it sets the READ signal to 1 that freezes the peak detectors and the hit register. That means events in multiple channels can still be detected in one read-out, if the subsequent events follow the first within the shaping time. As soon as READ is 1, no further detection can be made. Next, the controller sends out a STROBE signal, which consists of 32 pulses with 50 ns delay, corresponding to the 32 hit registers, to which IDeF-X reponses with a "1" on DOUT, if the register is 1. E.g. if channel 5 detected an event, IDeF-X will answer the falling edge of the 5th STROBE pulse with a "1". After the controller found out this way, which channel was hit, it sends for each hit channel another pulse on STROBE that commands the multiplexer to send the event energy (pulse height) on the analogous output. The system can be also set to read out all channels, if at least one was hit,

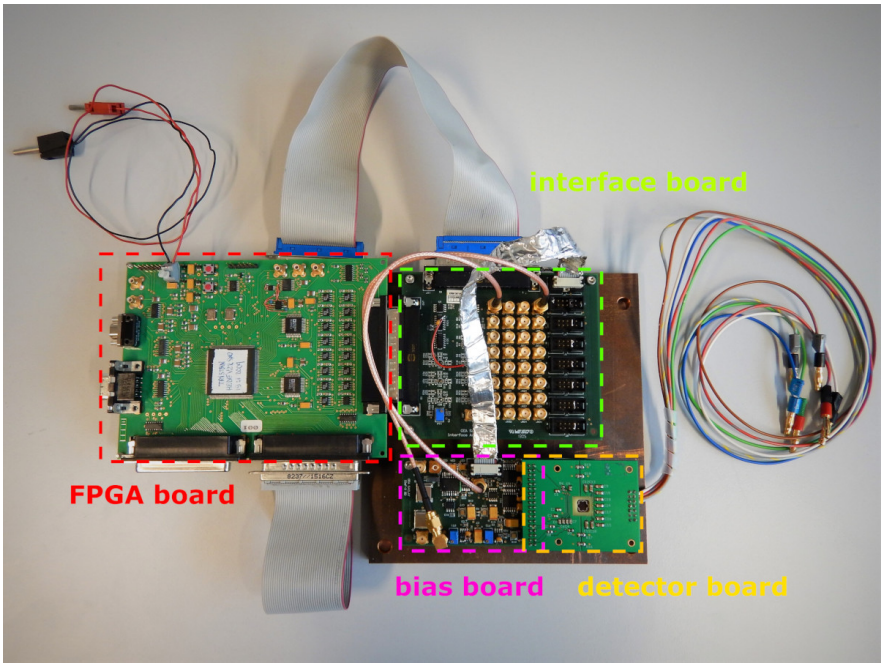

Figure 9.9: A detector with the IDeF-X read-out system, consisting of several boards. The disconnected cables on the top left are for the electronics power supply, the cables on the right for the detector voltages. The connectors on the left side of the FPGA board are for the communication with the computer. The interface board allows to connect 8 bias boards with detectors, thus there are many unused plugs.

or to read out the ASIC on demand. At least one µs after the last strobe pulse, i.e. the multiplexing of the last event, READ is set back to 0. This clears the hit register, and after a programmable delay also the peak detector is reset and the discriminator enabled again, ready to detect another particle. As one can see, for each hit the entire ASIC is stopped for several µs, even if only one channel detected an event. This read out results in a well defined dead time, but it also limits the maximum event rate.
Outside of the ASIC, the analogue output is processed by an ADC. Events that were detected in a single read-out sequence have the same time stamps.

The 7 pixels of the prototype-0 detectors are bonded to channel 1, 6, 11, 16, 21, 26 and 31, i.e. the separation was maximized and thus cross talk is minimized. The central pixel is connected to channel 16, except for the 2 mm-detector, where it is connected to channel 21.

The complete system consists of several boards (see figure 9.9):

- **detector board:** the detector PCB (printed circuit board) holds the detector and the ASIC (see figure 9.7) together with two plugs, one for the voltage supply of the detector and for the temperature diode (14 pins), the other for the ASIC power supply and communications (36 pins);
- **bias board:** this board has a 36 pin connector for the detector board on one side, on the other side a connector with 14 pins for the digital communication. The analog signal is here split into a differential signal (positive and negative voltage) to satisfy the redundancy required by space-born applications, and then transmitted through coaxial cables (SMA). In addition the board has a SMA connector for charge injection;

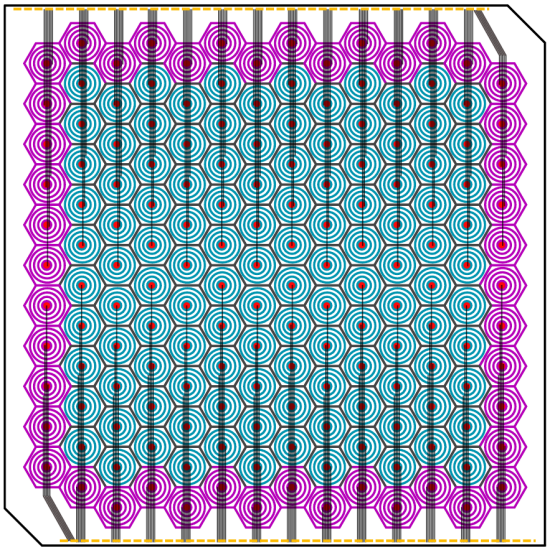

Figure 9.10: A sketch of the prototype-1 layout with 166 pixels. The red dots mark the anodes, which are contacted by long traces. The edge pixels are colored differently to make clear, that data from these cells cannot be fully used because charge sharing and other coincidences cannot be always vetoed. The size of the chip is $4 \times 3.8\,\mathrm{cm}^2$.

- **interface board:** This board allows to connect in total 8 bias boards. The communication is then continued via two 37 pins cables with DSUB connector, one for the digital and one for the analog signals, towards the controller;
- **FPGA board:** this board hosts the FPGA (Field Programmable Gate Array) and connects the ASIC finally with a computer via a space wire (a space-proof protocol). The FPGA is programmed by the user on the computer and controls the ASIC, the timing, and processes the received signals. Here also the ADC (analog-to-digital converter) is housed that converts the analog pulse height amplitudes into digital signals. The power supply of the entire read-out system is located on this board, too. It requires a 5 V voltage. The typical current is 0.3 A;
- **a computer with a special PCI card:** to operate the system a computer with a special PCI card is needed that has a space wire connector and the proper firmware. The card has four connectors, in theory it is thus possible to have a system with $4 \times 8 \times 32 = 1028$ pixels.

To start a measurement a file with the parameters as threshold, peaking time etc. is created and sent to the FPGA.

9.4 Prototype-1 and the final TRISTAN detector system

After the 7-pixel prototypes showed that the SDD technology is suitable for TRISTAN, the next stage of prototype detectors with 166 3 mm-pixels, called “prototype-1”, is in development. A sketch of the pixel layout can be found in figure 9.10. The chip will have a size of $4 \times 3.8\,\mathrm{cm}^2$. The layout of prototype-1 is also defined by the final TRISTAN array, as it will consist of multiple prototype-1 modules. On one hand the modules should be small such that the electron flux tube can be efficiently covered and that the length of the traces gets minimized. On the other hand the modules should be large to improve the ratio of pixels that are completely surrounded by other pixels to edge

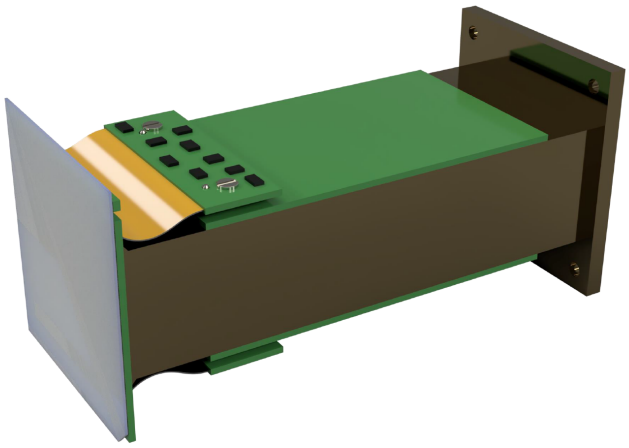

Figure 9.11: The mechanical layout of prototype-1. The detector is glued onto a copper cold finger that can be mounted on a cooling system. Two PCBs with the ASIC are fixed on the sides of the cold finger.

pixels. Another essential consideration is that the pixel size and position in the B-field (concerning the field strength) should be chosen in a way that backscattered electrons, which are back-reflected onto the detector, hit either the same pixel or a neighbor, i.e. the pixel size should be larger than the electrons cyclotron radius ($\lesssim 1\,\mathrm{mm}$). More detail about the layout optimization can be found in [M$^+$19, Kor16].
A draft of prototype-1's mechanical layout is pictured in figure 9.11. The silicon chip is attached by an adhesive foil onto a copper cold finger that can be mounted onto a cooled base plate. The ASICs are placed on PCBs on two sides of the cold finger, connected with a flex cable to another PCB below the silicon, which itself is linked to the detector through wire bonds.
Such a module is also planned to be used in the KATRIN monitor spectrometer that monitors the voltage stability of the KATRIN MAC-E filter by observing the decay of a $^{83\mathrm{m}}$Kr source.

The final TRISTAN detector will consist of several prototype-1 modules. A possible configuration with 21 modules is shown in figure 9.12 with in total 3486 pixels, of which 2520 are non-edge pixels. The circular flux tube is smaller than the entire array and covers 2460 non-edge pixels.
Prototype-1 and the final array have an integrated nJFET (n-channel junction field-effect transistor) as a first amplification stage. This transistor is coupled to the anode via a metal strip, which greatly reduces the input capacitance of the front-end and thus the noise.
The data acquisition system (DAQ) is currently in development at XGLab and Politecnico di Milano in Italy and at Max-Planck-Institute for Physics in Germany. It is derived from the CUBE ASIC [BFF$^+$11]. In measurements with 7-pixel prototypes equipped with this ASIC a resolution of $fwhm = 139\,\mathrm{eV}$ at $5.9\,\mathrm{keV}$ (^{55}Fe peak) was observed, corresponding to an *enc* smaller than $10\,\mathrm{e^-}$ [M$^+$19]. The DAQ will be divided into modules that match the detector segmentation, where each segment has 166 pixels. But also each module consists of 4 sub-modules with up to 48 channels to lower the complexity caused by the high number of channels and input count rate. The front-end is further segmented into 12-channel ASICS. The DAQ will provide three different read-out modes:

histogram mode: the spectra are produced inside the DAQ and no information

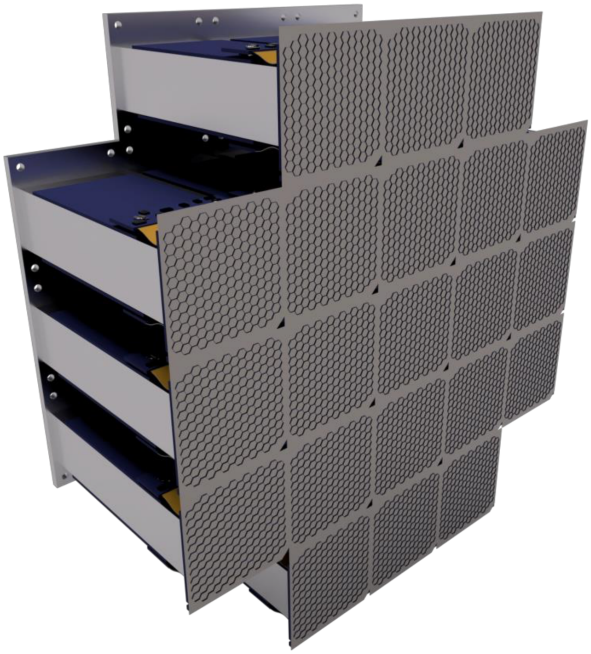

Figure 9.12: The final TRISTAN detector as array of 21 prototype-1 modules.

about the individual events is stored;

list mode: each event with energy, time stamp and several flags (pile-up, multiplicity) is provided;

waveform mode: the sampled analogue output of the signal is provided, which is helpful for testing purposes and diagnostics.

The DAQ will also recognize if an event is shared between pixels (due to charge sharing or magnetic backreflection) within one detector module and then flag the event by either searching for coincident events of neighboring pixels in a defined time window or triggering for each event also all neighbors. To achieve this every sub-module of the DAQ has to communicate with its neighboring sub-modules. Another feature of the DAQ will be the pile-up flagging.

In summary, the TRISTAN detector system with 3500 pixels is still in early development, where the current step is the production of a 166-pixel prototype. The SDD technology has been tested with 7-pixel prototypes, as presented in the following chapters.

Chapter 10

Characterization of the 7-pixel prototype detectors with X-rays

In this chapter the characterization of the TRISTAN 7-pixel prototype detectors with X-ray and γ calibration sources is presented. The goal of these measurements was to test the novel detectors together with the IDeF-X BD read-out and to verify that this technology is suitable for the TRISTAN project. These measurements were the first with TRISTAN silicon drift detectors. The IDeF-X BD ASIC was chosen for these early prototypes as it was a proven system and provides a synchronized read-out of all 7 pixels, even though the noise floor is rather high with an equivalent noise charge of $44\,\mathrm{e^-}$. However, reaching the noise floor with the detectors shows that the resolution is limited by the electronics and gives a good indication that the detectors work as intended.
In section 10.1 the setup is described. In section 10.2 the analysis of the data and results regarding the detector performance are presented. In section 10.3 charge sharing is studied. The work presented in this chapter was partially published in [ABB+18].

10.1 The experimental setup

For the characterization the detectors were operated in a vacuum chamber and actively cooled with a combination of a Peltier cooling device and an ethanol-based liquid cooling. A picture of the setup is shown in figure 10.1. In addition to the detector board, also the bias board (where the detector board is directly attached to, see section 9.3) and the interface board are placed in the vacuum chamber. All components are mounted on a copper plate. This plate is connected to a circuit of ethanol that is pumped and cooled down to $-40\,^\circ\mathrm{C}$ by an external chiller. The Peltier device is attached to the detector board, and its warm side is connected through a cold finger to the copper plate (see figure 10.2). Resistance temperature detectors are placed on the copper plate and close to the cold side of the Peltier device. For the analysis of the detector performance as a function of temperature, it is important to know the temperature of the silicon chip, which can deviate a lot from the temperatures measured elsewhere in the setup. It is thus necessary to read out the temperature diode on the chip. The circuit for this diode is shown in figure 10.3: a voltage of $1\,\mathrm{V}$ and a large resistor of $1\,\mathrm{M\Omega}$ create a constant current. One then observes the voltage drop over the diode, which is changing approximately linearly with temperature. As a reference thermometer for the diode calibration the temperature sensor at the Peltier device, which is close to the detector, was used. To ensure that the temperature of the sensor matches the detector temperature the calibration was performed at atmospheric pressure and with the detector

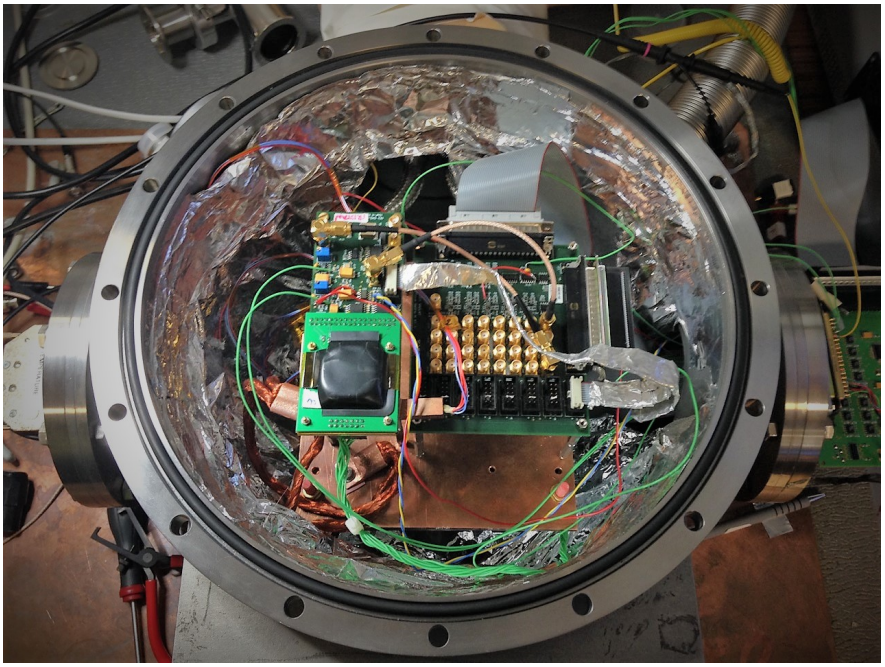

Figure 10.1: The best bench with the detector system installed. The detector is under the black plastic cover on the top PCB. This picture was taken when many cables were placed as probes at different points of the system to observe the data- and communication signals during operation at cold temperatures and in vacuum with an oscilloscope.

disconnected from its power supply. As soon as the detector was turned on, a fast increase of the chip temperature could be seen from the diode measurement, while the temperatures measured by the other probes stayed constant.
The calibration source was placed outside the vacuum chamber behind a beryllium window. For the measurements presented here, a ^{241}Am source was used. It has several X-ray lines at 11, 14, 17 and 21 keV and Gamma lines at 26 and 59.5 keV [LPF08], thus a similar energy range as expected for tritium measurements is covered ($Q_\beta = 18.6\,\text{keV}$). For higher energies the detection efficiency of the 450 µm thin detector becomes too small, as the photons then only rarely interact in the silicon. Some of the X-ray lines are actually groups of lines. Especially the group at 17 keV that consists of three major peaks makes it possible to estimate the noise level with a quick glance, seeing if the individual lines are resolved or not, which is quite helpful for quick comparisons of measurements without a real analysis. A spectrum that shows the different lines, taken with the I-11 detector (see table 9.1), is shown in figure 10.5.

Special attention was given to the optimization of the setup in order to minimize noise:

- the detector voltage was supplied by multiple in series connected 9-V batteries to ensure a high stability;
- all cables were shielded;
- all components were properly grounded;
- the non-grounded metal protective cover of the detector bond wires was removed. This greatly improved the detector resolution by removing capacitance. For the first measurements the entrance-window side of the detector board was covered by a metal shield, which was intended to help reducing the chip's temperature. However, the performance was improved by removing also this cover.

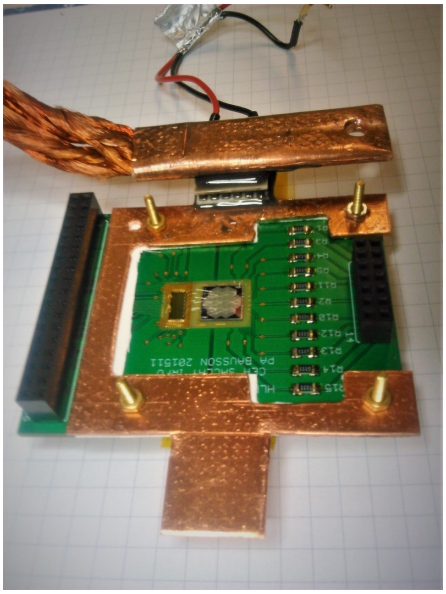

Figure 10.2: The underside of the detector board with the ASIC. Here, the cooling with a Peltier device is displayed. A copper mask is screwed on the board, separated by a thermal pad. On the top side the Peltier device is fixed to the mask with an epoxy glue. The warm side of the device is connect via a copper cold finger to a ethanol-cooled plate in the vacuum chamber. The woven copper cold finger, visible on the top left, was later replaced with a solid rod that had a higher thermal conductivity.

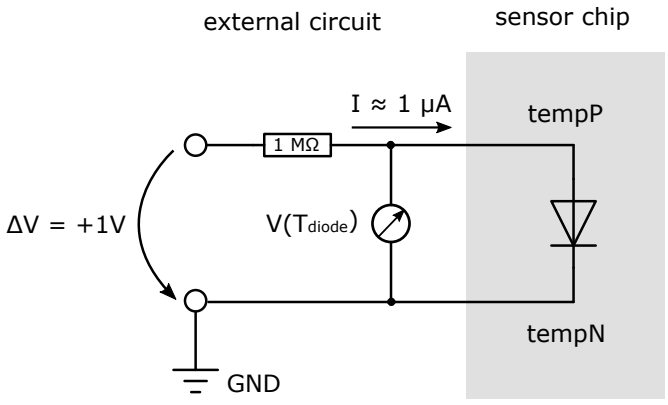

Figure 10.3: A simple circuit to read out the temperature diode. With a voltage of 1 V and a large resistor a constant current is generated. The voltage drop $V(T_{diode})$ is linearly changing with temperature.

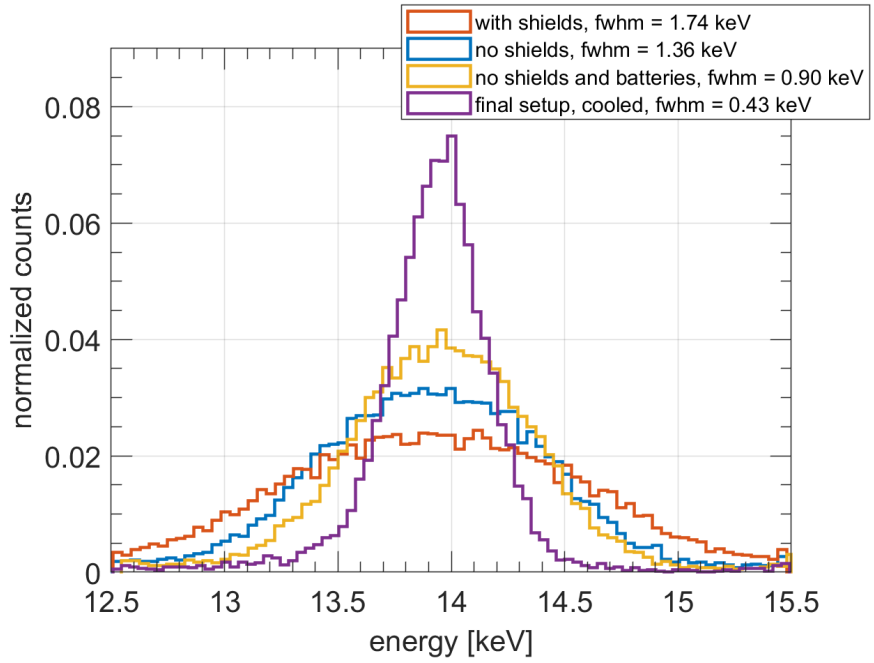

Figure 10.4: The evolution of the detector performance while optimizing the setup by measuring the full width at half maximum of the 14 keV peak in the americium spectrum. The data here was taken with the central pixel of the 2 mm-detector. The first three data sets (red, blue and yellow data) were taken at room temperature. For the first spectrum (red) the voltage was provided by ordinary laboratory power supplies. To improve the cooling of the detector and to protect the bond wires, both sides of the detector were covered by metal shields. At a resolution of 1.7 keV the noise is way above the intrinsic ASIC noise level. The performance improved after the shields were removed (blue spectrum). Also increasing the voltage stability by switching to a battery power supply reduced the noise (yellow spectrum). The violet data was taken at low temperatures with the final setup after some more improvements and shows the best achieved resolution of 0.4 keV, which corresponds to an equivalent noise charge of 44 electrons. This is the minimum noise level of the ASIC [GDH+15].

detector	∅ pixel [mm]	drift rings	U_{R_1} [V]	U_{R_X} [V]	U_{Bc} [V]	U_{Bf} [V]
I-02	0.5	2	-18	-36	-85	-90
C-04	0.5	3	-18	-36	-85	-90
L-13	1	2	-18	-34	-85	-90
I-11	1	6	-18	-63	-85	-90
F-09	2	12	-18	-110	-90	-93

Table 10.1: The optimum voltages for the different detectors. Due to the battery-pack power supply the voltage could only be set in discrete steps, where the exact values depend on the state of charge of the batteries. However, a few Volts difference do not change the detector performance, as long as the bias voltage is sufficient to deplete the detector.

The noise is further reduced by cooling the detector. Figure 10.4 highlights the importance of these optimization efforts, showing how the resolution improved after several changes to the setup. While the full width at half maximum ($fwhm$) of the 14 keV peak in the unoptimized setup was 1.7 keV, it was lowered to 0.4 keV in the final setup.

In addition to optimizing the setup from a hardware side, also the best voltages for the detector bias and ring potentials have to be found. Following voltages can be set:

- **back contact voltage (U_{Bc}):** the bias voltage that depletes the detector;
- **back frame voltage (U_{Bf}):** this voltage is applied to a guard ring that surrounds the entrance window. Its value has to be set slightly higher than the bias voltage to remove free charges and create a well defined separation between the detector and the non-active substrate;
- **ring X voltage (U_{R_X}):** the voltage of the outermost drift ring. Together with other rings it shapes the electric field within the detector and steers the charges towards the anode;
- **ring 1 voltage (U_{R_1}):** the voltage of the innermost drift ring. If there are rings in between R_X and R_1, they are connected on the detector with resistors such that their voltages are declining from outside to inside.

In the optimization process the voltages were varied until the detector resolution was maximized. The optimum voltages are tabulated in table 10.1. Since the voltages come from a series of 9 V-batteries, their values are multiples of ~ 9 V, where the exact value depends on the charging state of the batteries. However, a few Volts difference does not change the performance of the detector. In fact, the most important voltage are the back contact voltage that has to exceed a minimum value for the detector to be fully depleted, and the difference between U_{R_1} and U_{R_X} that shapes the electric field and thus controls the speed and efficiency of the charge collection. The back frame and back contact voltage values are very close, due to some connection on the detector.
All detector voltages have to be seen in reference to the anode voltage, which is at ground potential. The anode is connected to the ASIC, thus it is absolutely mandatory that detector and ASIC power supply have a common grounding.

10.2 Detector performance and electronic noise

The detectors were characterized with a ^{241}Am-source. The spectra were measured usually with a threshold between 1 and 3 keV. A full spectrum at minimum noise level

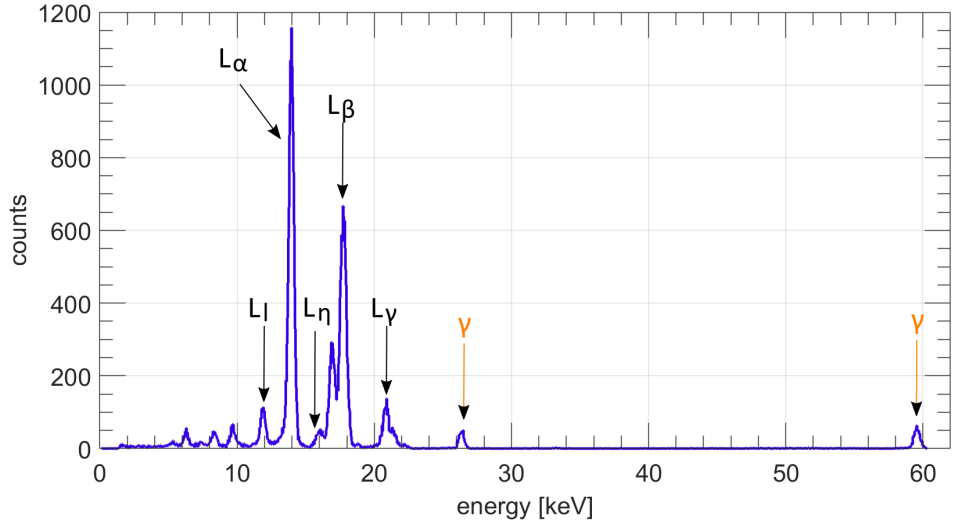

Figure 10.5: A ^{241}Am-spectrum with the different X-ray and γ-lines. This spectrum was taken with the I-11 detector (1 mm diameter, 6 drift drings) at a minimized noise level.

(best possible resolution) is shown in figure 10.5. To study the detector performance and to estimate noise parameters it is necessary to do scans over the pulse shaper's peaking time and the chip temperature (see section 9.1.2). To facilitate the analysis of the resulting high number of spectra, a program for an automatic calibration was written, based on the ECC (energy calibration via correlation) method [ML16]. With this method a synthetic spectrum is used, and a correlation factor between the observed spectrum and the synthetic spectrum is maximized with respect to the calibration parameters. The advantage of this method over least-squares fitting is that the systematic calibration error is decreasing faster with increasing statistics, i.e. especially measurements with low event numbers have a comparably small calibration error. The calibration model includes a non-linearity c that can add a curvature to the linear calibration:

$$E = (gain \cdot ADU + offset)^c, \tag{10.1}$$

where the parameter ADU are the ADC channels. When looking at the low energy peaks of the spectrum between 0 and 26 keV, the non-linearity is not apparent and can be neglected. However, it improves the overall calibration when the 60 keV peak is included. The linearity of the energy calibration is further discussed in section 11.1.1 for electron data taken at Troitsk ν-mass.
The performance of the detectors was studied and noise parameters were obtained by measuring the full width at half maximum ($fwhm$) as a function of the peaking time, i.e. measuring the noise curve. The peaking time is defined as the time from 5% of the maximum pulse height to the maximum of the shaped signal. From the measured $fwhm$ the equivalent noise charge (enc) can be calculated according to the relation

$$enc\,[\mathrm{e^-}] = \sqrt{\left(\frac{fwhm}{E_i \cdot 2.35}\right)^2 - \frac{F \cdot E}{E_i}}, \tag{10.2}$$

where E is the line energy, $F = 0.12$ is the Fano factor and $E_i = 3.65$ eV is the energy required to create an electron-hole pair in silicon. The equivalent noise charge is a measure to characterize the detector noise, as explained in section 9.1.2. The enc is the charge of a signal that corresponds to a signal-to-noise ration of one. It is

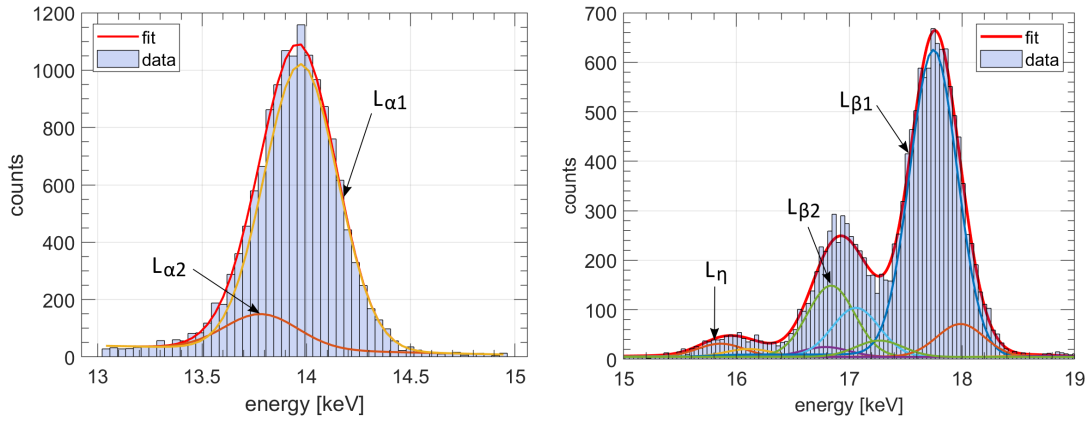

Figure 10.6: The detectors were characterized with a ^{241}Am-source. **Left:** the 14 keV peak group. **Right:** the 17 keV peak group. The peaks in the spectrum were fitted with Gaussians to obtain the $fwhm$ and the enc. The plot shows the neptunium L X-ray lines at a resolution of 400 eV and an enc of 44 e$^-$, which is the noise floor of the ASIC. The most intense lines are marked with arrows and labels.

measured in units of the electron charge [e$^-$]. The equation above can be understood intuitively, when rearranged to calculate the energy resolution in terms of standard deviation ($\sigma = fwhm/2.35$): the total energy resolution is then the one generated by noise (enc) plus the resolution from charge statistics ($\sqrt{F \cdot E/E_i}$, see equation 9.3), where both are multiplied by E_i to transform the electron number fluctuation into a variation of energy and then added quadratically, since both are not correlated.

The $fwhm$, i.e. the energy resolution, was obtained by fitting the measured ^{241}Am-spectrum via the minimization of a chi-squared function. As mentioned before, many "lines" of the americium-spectrum are in fact groups of lines that are not resolved. Thus these peaks were fitted as groups of Gaussians, where the energy and intensity of each line was taken from the measurements reported in [LPF08]. The assumption of a Gaussian peak shape instead of e.g. a Voigt profile is justified, because the observed width of a few hundred eV is much larger than the Lorentzian natural line width, i.e. the Gaussian detector resolution is dominating the shape. Also, since dead layer effects are negligible for measurements with X-rays, a peak-asymmetry doesn't have to be taken into account. The line intensities were then modified with the transmission probability of an X-ray in the 0.5 mm thick beryllium window and the photo-absorption probability in a 450 µm silicon volume, which are energy dependent and were calculated with an online tool from the GSI [GSI]. An energy offset was included as free parameter in the fit to correct for small deviations of the calibration. A background following a linear function was included in the fit as well. A resulting fit of the 17 keV peak group is shown in figure 10.6 on the right. Now, in principle one could expect best results by using all fitted peaks to estimate the equivalent noise charge. However, results obtained this way resulted in strongly fluctuating noise curves, caused probably by an error in the peak positions and intensities. More consistent results, where the noise curve is following the theoretical shape, where obtained by fitting only the 14 keV peak, which is the most intense peak and consists of two lines, see figure 10.6 on the left.

The first measurements showed a poor detector resolution (see figure 10.4), but after optimizing the setup and the parameters of detector operation as described in section 10.1, a resolution ($fwhm$) of $\sim$ 430 eV at 17 keV was reached with all detectors. This

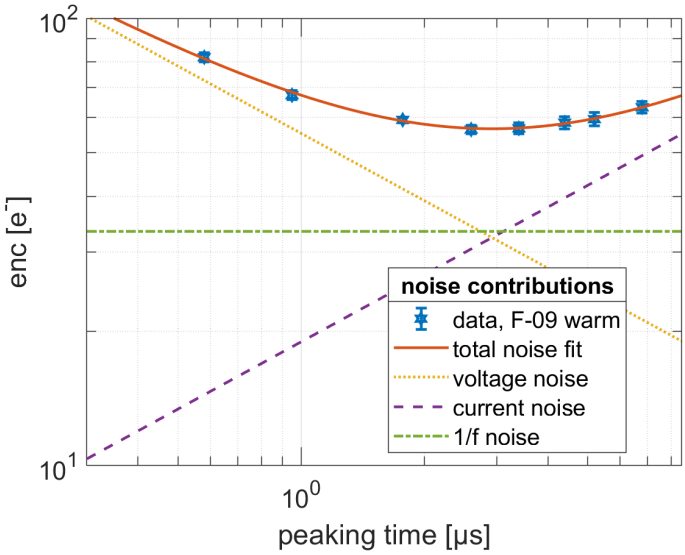

Figure 10.7: The *enc* at different shaping times: a fit of equation (10.3) to data obtained with the 2 mm-detector at room temperature shows the three noise contributions.

resolution corresponds to an equivalent noise charge of 44 e^-, which is the noise floor of the IDeF-X BD ASIC. The minimum *enc* achieved with each detector is listed in table 10.2. This means that the detector performance is limited only by the electronics, thus the SDD prototypes are fully functional and could deliver an even better performance with a tailored front-end.

The *enc* is a function of the peaking time t_{peak}, as already discussed in section 9.1.2. The exact noise function for the IDeF-X front-end was published in [GBC+09]:

$$enc^2 = \left(\frac{\alpha_{\mathrm{d}}}{t_{\mathrm{peak}}} + \alpha_{1/\mathrm{f}}\right) C_{\mathrm{tot}}^2 + \alpha_{\parallel} \cdot I_{\mathrm{leak}} \cdot t_{\mathrm{peak}} + const. \tag{10.3}$$

The ASIC noise parameters α_{d}, $\alpha_{1/\mathrm{f}}$ and $\alpha_{\parallel}$ were measured and reported in [GBC+09] and [MGO+10]. C_{tot}^2 is the total input capacitance of the ASIC's charge amplifier, plus the additional soldered capacitance and the detector capacitance, I_{leak} is the leakage current and *const.* describes the $1/f$-noise that is depending on the capacitance and the dielectric constant of the detector. To determine the leakage current I_{leak} and capacitance C_{tot}, noise curves were taken, i.e. the *enc* was measured at different peaking times. The function in equation (10.3) was then fitted to the noise curves and values for C_{tot} and I_{leak} were obtained. The different noise contributions for a measurement with the 2 mm-detector F-09 can be seen clearly in figure 10.7. In figure 10.8 a few noise curves with the 2 mm- and a 1 mm-detector are shown to illustrate that cooling down the sensor reduces the *enc* at large peaking times. One can see that the 1 mm detector achieves even lower noise levels as the 2 mm detector, since it has a lower power consumption and thus gets even cooler. In the end, both detectors are performing very well close to the noise floor of the ASIC at an *enc* of 44 electrons.

The noise curves for each detector at two temperatures are shown in figures 10.9 to 10.13. Here the spread of the performance across the pixels can be seen. The error bars of the data for each pixel results from the peak fitting. The noise curve is then fitted to the averaged *enc* over all pixels. For the average *enc* the standard deviation is taken as an error, however with only 7 pixels one cannot say if the performance spread

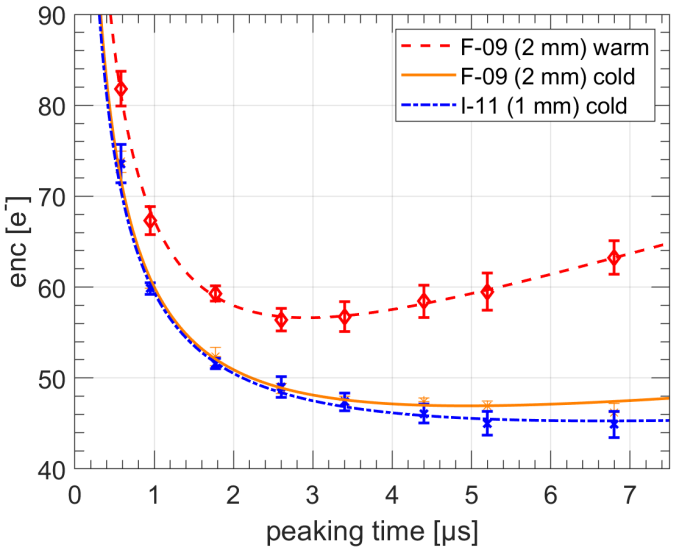

Figure 10.8: Noise curves: detector parameters can be obtained by measuring the equivalent noise charge (enc) as a function of peaking time. It is clearly visible how the noise decreases with temperature. With a cooled setup the 2 mm-detector (orange curve) has a higher *enc* at long peaking times than the 1 mm-detector (blue), because more heat and thus more leakage current is produced. Also at the same temperature a higher leakage current is expected for the 2 mm-detector due to its bigger surface. However, both detectors achieve a noise level close to the intrinsic ASIC noise of 44 e^-.

is following a normal distribution. The 0.5 mm-detectors I-02 (figure 10.9) and C-04 (10.10) show larger error bars than the other detectors, because due to the small sensitive surface and time constraints less data was collected with these sensors. Some data that showed clearly anomalous noise was excluded from the fit, e.g. the data of channel 16 in the measurements with F-09 at room temperature (figure 10.13) and the data for all pixels at 4.4 µs peaking time for the measurements with a cooled down C-04 (figure 10.10). These anomalies are not reproducible and are due to external disturbances like a poor connection of a cable etc. In channel 21 of detector C-04 at room temperature the noise is significantly larger than for the other pixels at large peaking times, but follows the typical shape of a noise curve with increased leakage current. This data is not excluded from the fit since the observation here is probably due to a real difference in the pixels of the detector. It also should be mentioned that only for the 2 mm detector a large difference between the noise during warm and cold measurements is visible. As leakage currents are scaling with the detector surface, it is clear that larger detectors are more sensitive to temperature. For the smaller prototypes, the leakage current does not seem to be a dominant source of noise.

From the fit the parameters leakage current I_{leak} and total capacity C_{tot} were obtained. The average total capacity was found to be $C_{\text{tot}} = (3.45 \pm 0.15)$ pF. This agrees with measurements of the capacitance of ASICs in the IDeF-X family (e.g. 3.9 pF for IDeF-X HD [MGO+10]). The direct comparison is possible because the contribution of the detector capacitance to the total capacitance is negligible for the case of the TRISTAN SDDs. The fitted leakage current values are tabulated in 10.2 and they scale as expected with detector surface area and temperature. The leakage currents for each detector were measured by HLL MPG to be 180 pA/cm^2 for the 2 mm-detector and $\sim$ 400 pA/cm^2 for the 1 mm and 0.5 mm-detectors [Lec], resulting in leakage currents

Detector	∅ pixel [mm]	drift rings	min. *enc* [e^-]	I_{leak} [pA], room temp.	I_{leak} [pA], cooled
F-09	2	12	44 ± 1	21.4 ± 3.4 (35 °C)	5.4 ± 1.5 (−2 °C)
I-11	1	6	40 ± 2	4.2 ± 2.0 (25 °C)	2.8 ± 2.1 (−22 °C)
L-13	1	2	41 ± 1	0.7 ± 5.1 (22 °C)	0.2 ± 3.5 (−15 °C)
C-04	0.5	3	44 ± 3	9.5 ± 5.8 (21 °C)	4.3 ± 3.5 (−16 °C)
I-02	0.5	2	46 ± 4	18.0 ± 6.0 (24 °C)	7.4 ± 4.9 (−13 °C)

Table 10.2: Detector characteristics: the noise floor of 44 e^- was reached with all detectors at peaking times $t_{peak} > 4\,\mu s$ in a cooled setup. Leakage currents were obtained from the noise curves at room temperature and in a cooled setup. The errors are quite big due to taking an average over all 7 pixels and in case for the 0.5 mm-detectors also due to low statistics for the $fwhm$ measurement. The temperatures were measured in a simple way via the voltage drop of a diode on the detector chip and have a non-negligible uncertainty.

of 6 pA (2 mm), 3 pA (1 mm) and 1 pA(0.5 mm). The fitted currents are in agreement with the HLL measurements for the cooled 2 mm detector and the 1 mm detectors. On the other hand the fitted currents of the 0.5 mm-detectors are too large, even though they were operated at low temperatures $< -10\,°C$. Also, the leakage current was not reduced as expected by theory (ten-fold reduction when temperature is lowered by 14 °C from room temperature [Spi05], see section 9.1.1). However, since some of the values have large errors it is hard to tell how the leakage current scales in reality. The large errors of the fitted parameters are also due to the large errors of the pixel-averaged *enc*, and indeed a chi-squared goodness-of-fit test on most of the data reveals that the errors are overestimated. However, since it is not clear if the large spread in the noise curves for each pixel is caused by low statistics or if the channels have large differences in their noise behavior, the error cannot be arbitrarily reduced. Either way it should be mentioned that the leakage currents were measured by HLL and no abnormalities were found. The goal of the measurements presented here was to test if the detectors work properly, which was achieved since the ASIC noise floor was reached when cooling down the detectors. In table 10.2, in addition to the leakage currents the minimum achieved equivalent noise charge is listed for each detector. Note that the values are not always similar to the measured *enc* in the noise curve plots, because here also other measurements apart from the peaking time scan were taken into account. However, also in the noise curves it can be seen that an *enc* of 50 is surpassed by all detectors.

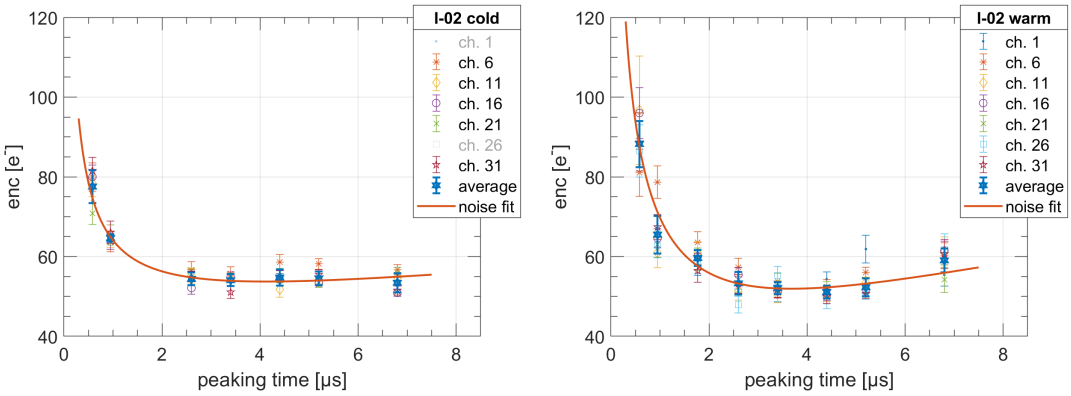

Figure 10.9: Noise curves for the I-02 detector (0.5 mm, 2 rings) at different temperatures. **Left**: cold, −13 °C. Unusual noise in channel 1 and 26 distorted the spectra such that this data was excluded. Also there were not enough statistics for peaking time = 1.77 µs to fit the peaks. **Right**: warm, 24 °C.

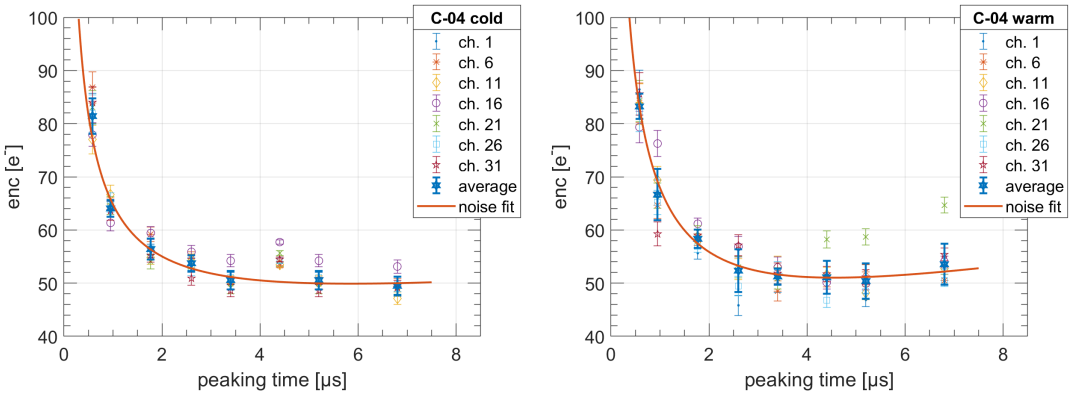

Figure 10.10: Noise curves for the C-04 detector (0.5 mm, 3 rings) at different temperatures. **Left**: cold, −16 °C. the data at peaking time = 4.4 µs shows an anomalous increase in noise and was not included in the fit. At this peaking time the energy threshold was changed, but this should not be the reason for the noise. **Right**: warm, 21 °C. Channel 21 shows an increased leakage current. However, this channel was not excluded from the fit because the shape of the noise curve is smooth and thus consistent with the theoretical function.

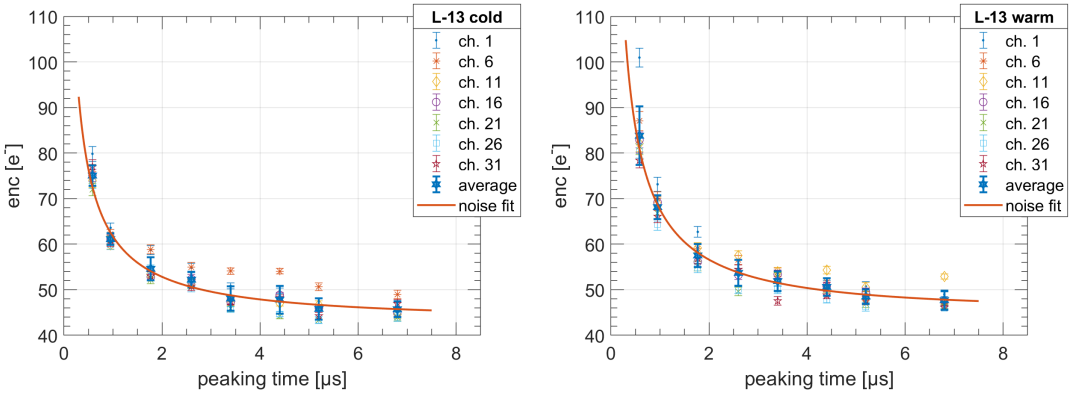

Figure 10.11: Noise curves for the L-13 detector (1 mm, 2 rings) at different temperatures. **Left**: cold, −15 °C. **Right**: warm, 22 °C.

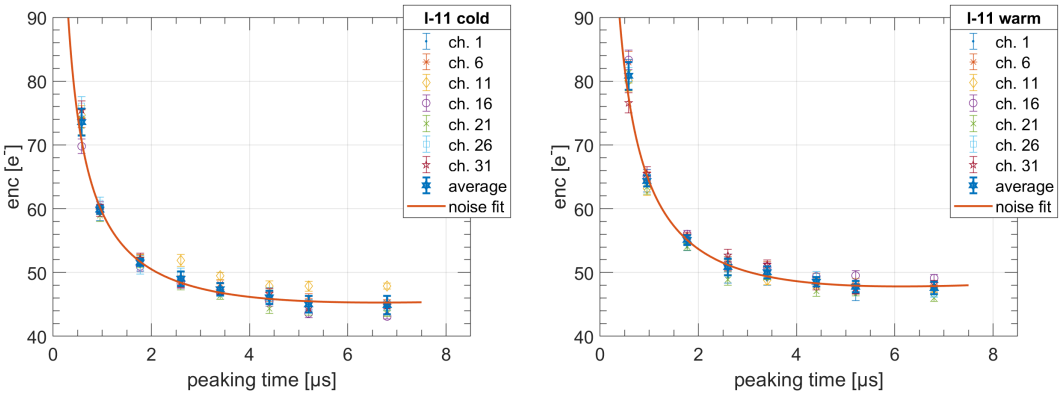

Figure 10.12: Noise curves for the I-11 detector (1 mm, 6 rings) at different temperatures. **Left**: cold, −22 °C. **Right**: warm, 25 °C.

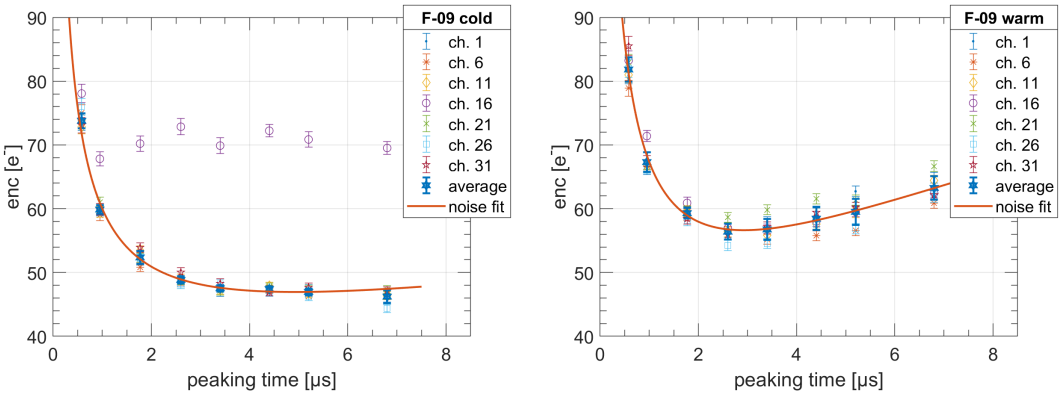

Figure 10.13: Noise curves for the F-09 detector (2 mm, 12 rings) at different temperatures. **Left**: cold, −2 °C. Channel 16 shows anomalous noise and was excluded from the fit. **Right**: warm, 35 °C. The leakage current is larger due to the higher temperature such that the noise increases with the peaking time.

10.3 Charge sharing

In case of an event localization close to the border between adjacent pixels, the signal charge is split between those pixels due to the extension of the charge cloud. As the charge drifts along the electric field lines towards the detector anode, the charge cloud is growing in size due to transverse diffusion, leading, in addition, to charge sharing also for those events, which have an initial charge cloud that is not extending into a neighboring pixel. This phenomenon results in the observation of coincident events, where the sum of the measured energies in both events matches the energy of the detected particle, assuming that no charge is lost between the pixels. The concept of charge sharing is illustrated in figure 10.14. For an event in the center region of the pixel, no charge is diffusing into the neighbors and thus no coincidence is detected, i.e. the multpilicity of the event equals 1. If the event creates a charge cloud close to the border between two pixels, the charge is split. In some cases the charge is even shared between three pixels, such that the resulting detection has a multiplicity of three. If the pixel size is small compared to the charge cloud, events with even higher multiplicities can be observed.

A plot of the energies of coincident events (multiplicity = 2) in the central and neighboring pixels is shown in figure 10.15 for the detector I-02. Shared events are visible as diagonal lines, where the sum of energies matches the spectral lines of the ^{241}Am source. These events can be used in principle for the data analysis by summing up the energies of coincident events, but the $fwhm$ of the reconstructed peaks is by a factor $\sqrt{2}$ larger than for single events. The 60 keV peak of the americium spectrum reconstructed from shared events is shown in figure 10.16 in comparison with the peak that contains no coincident events. The broadening of the reconstructed peak is clearly visible. In addition the reconstructed peak is shifted from the line energy about 0.5 keV to lower energies. This shift is caused by integral cross talk and one could correct the data for it in principle. The strongest impact of cross talk was observed for the 2 mm-detector F-09, where the coincident events were shifted by about 4 keV to lower energies, as evident in figure 10.17. Since the 2 mm detector has the longest wire bonds, cross talk has a larger impact than for the other detectors. Additionally, in this data also pile-up is clearly visible as horizontal and vertical bands and cumulations of events, where in each pixel an X-ray from one of the peaks was detected.
Instead of cross talk one could assume that the aforementioned shift of the diagonal lines is caused by a loss of charge. However, this is not true, because if charge would be lost between the pixels, one would observe a curvature of the diagonal line instead of a constant shift[1]. No such curvature was observed, see e.g. figure 10.15.

Shared events can be removed from the data by applying a multiplicity cut, i.e. removing all coincident events. This is trivial for the IDeF-X readout, since it provides the multiplicity of each event in the output. The time window in which subsequent events are detected coincidentally is the shaping time of the setup, which is related to the adjustable parameter peaking time, which was mentioned in the previous section 10.2 (also see section 9.3 for the discussion of the IDeF-X BD ASIC). The shaping time is the difference between the time at the charge injection by the detector and the time at the maximum of the shaped signal. For example a peaking time of 6.8 µs corresponds to a shaping time of 9.6 µs. If both hits within this window were detected in the same

[1] Charge loss between the detectors is common for many pixelated detectors, where the pixels are structurally separated. In the TRISTAN SDDs the segmentation of the detector is entirely achieved by the electric field configuration, a charge loss is thus very unlikely.

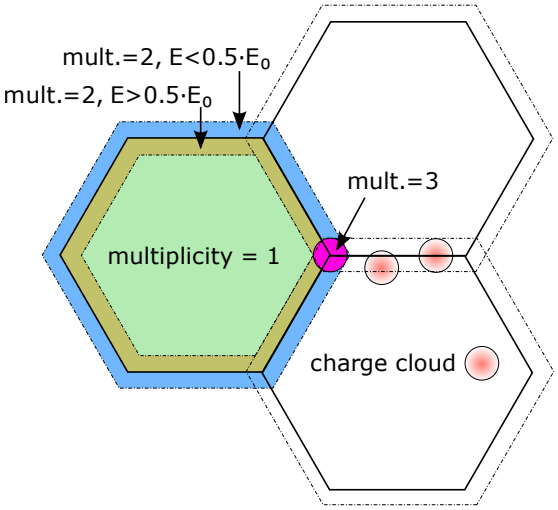

Figure 10.14: A sketch to illustrate the concept of charge sharing. For an event in the center region of a pixel, no charge is diffusing into the neighbors and no coincidence is detected, i.e. the multiplicity of the event equals 1. If radiation creates a charge cloud close to the border between two pixels, the charge is split and the event has multiplicity 2. In some cases the charge is even shared between three pixels, such that the event has a multiplicity of 3.

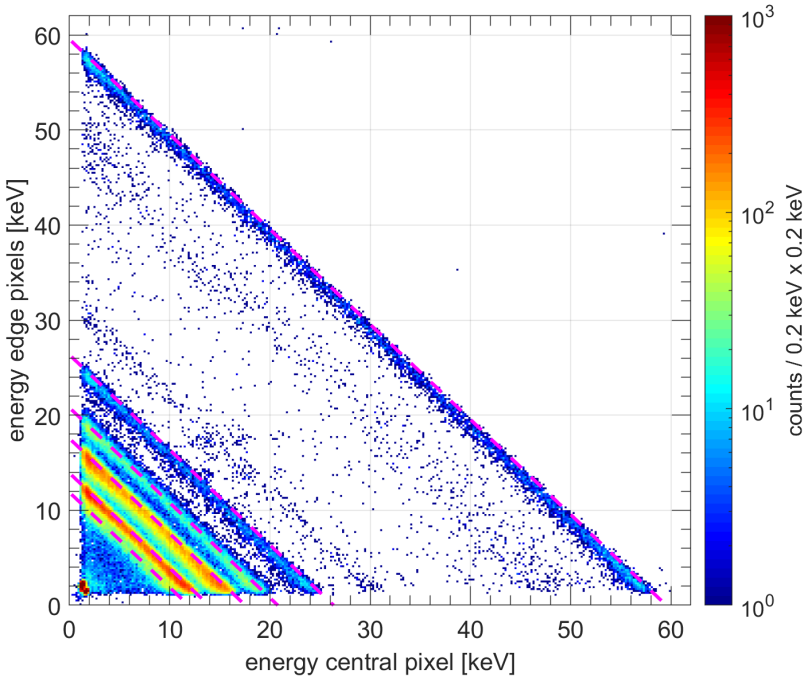

Figure 10.15: Charge sharing: when plotting coincident events with the energies in one pixel (center) versus the energies measured by neighbors (edge pixels) a correlation caused by charge sharing becomes visible as diagonal lines, where the energies of both events sum up to the peaks of the ^{241}Am-spectrum. The magenta dashed lines mark the peak energies. A slight shift of the sum of the energies from the full energies of the peaks caused by integral cross talk is visible. The data shown here was taken with the 0.5 mm-detector I-02.

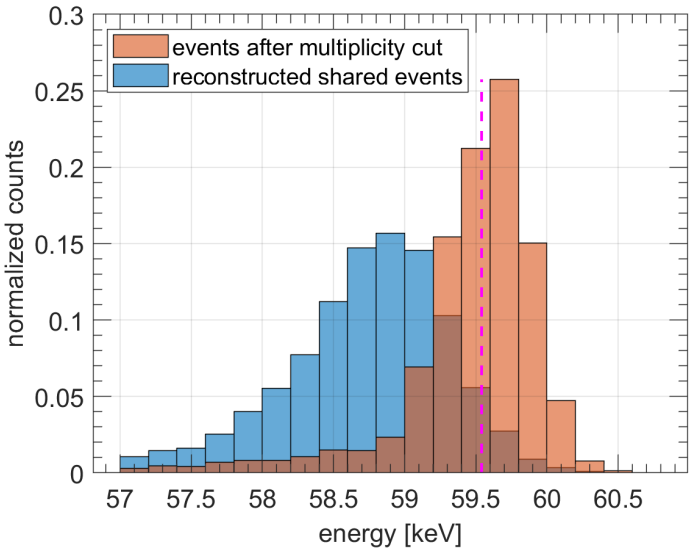

Figure 10.16: The comparison of the 60 keV americium peak as reconstructed from coincident events (blue) and as measured with singular events (red). The broadening of the reconstructed peak is evident. The actual energy of the γ-line in the ^{241}Am-spectrum at 59.5 keV is marked by the magenta dashed line. The peak without coincident events is aligned with this line except for a small calibration error, but one can see that the reconstructed peak is shifted to lower energies. This shift is caused by integral cross talk.

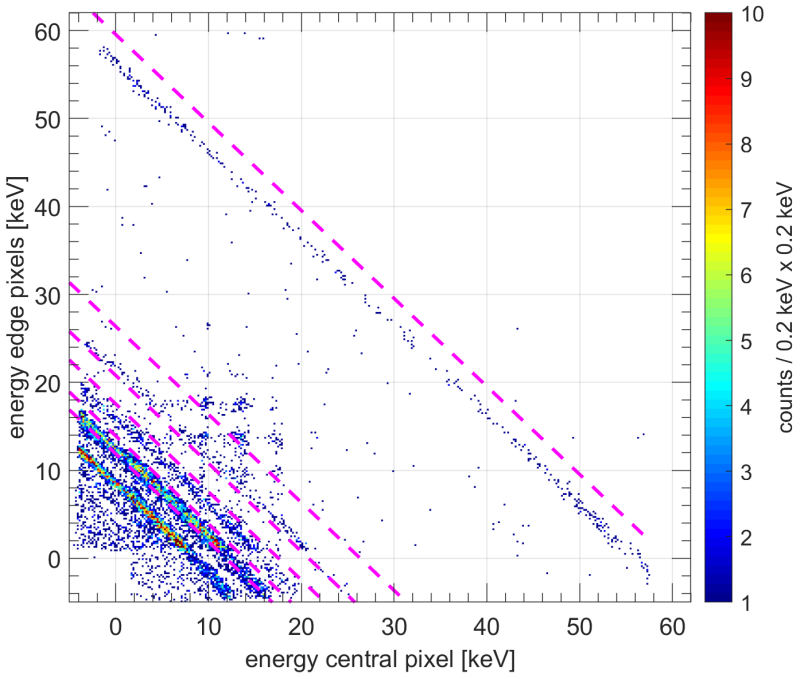

Figure 10.17: Most severe cross talk is observed in the F-09 detector (2 mm diameter). The signal in one of the pixels is moved by about 4 keV to lower energies with respect to the actual ^{241}Am-lines (magenta dashed lines), such that many coincident events are recorded with a negative energy. Also some pile-up (random coincidence) is visible in the region between 10 and 20 keV, which manifests itself in vertical and horizontal bands with strong cumulations of events at the peak energies in both participating pixels.

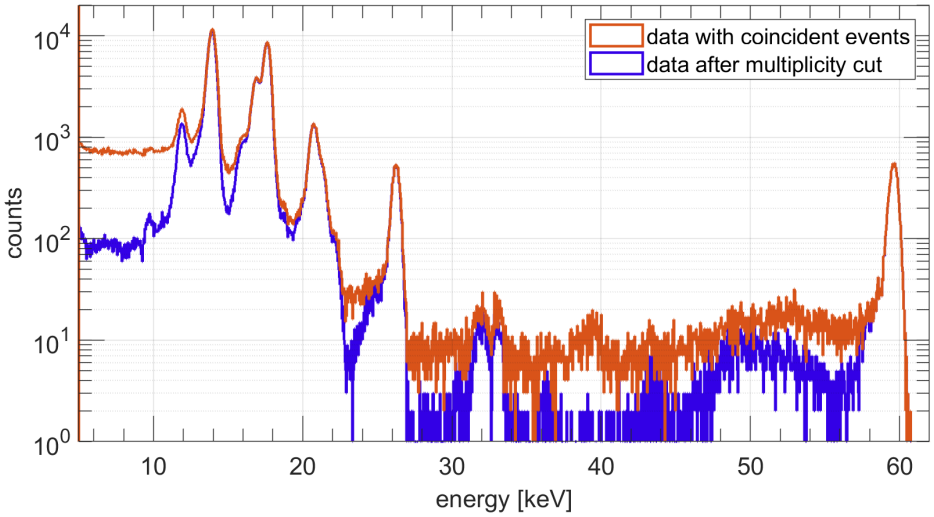

Figure 10.18: The ^{241}Am-spectrum of the central pixel with all events (orange), including events that were shared with a neighboring pixel (thus only a part of their energy is deposited in the central pixel), and after a multiplicity cut (blue) that removed all coincident events. The charge sharing adds a flat background that extends from a peak down to lowest energies. At low energies the background is at a maximum since here the charge sharing from all peaks is summed up. The data shown here was taken with a 0.5 mm-detector, where events are especially likely to be shared due to the small pixel diameter.

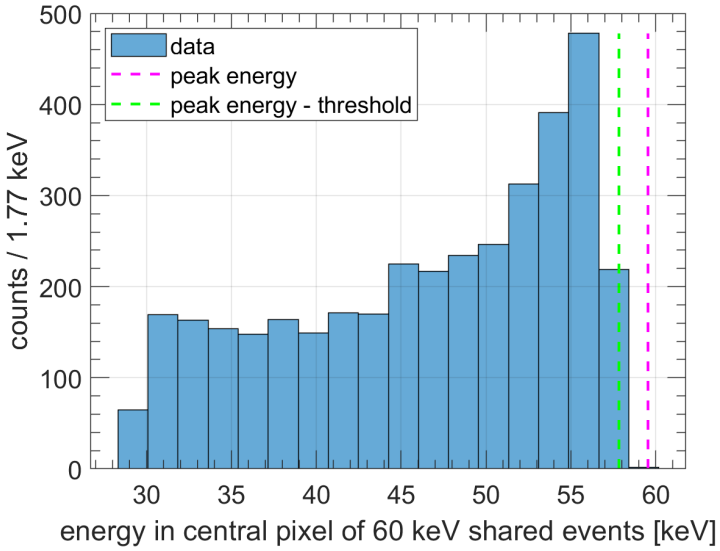

Figure 10.19: The energy distribution of events in the central pixel from 60 keV electrons that shared charge with a neighbor, i.e. a projection of the 60 keV diagonal line from figure 10.15. It can be seen that the charge sharing probability is not uniform with respect to the fraction of energy in one pixel. The event number is increasing towards high energies, thus the probability of charge sharing increases the less charge went to the neighbor. This can be explained by geometric effects. The data here was taken with a threshold of 1.77 keV. One can see that there are only a few events within 1.77 keV below the maximum energy (between the green and magenta lines), since the charge in the neighbor was below the threshold. However, from this distribution one can estimate the number of shared events below the threshold. Note that the threshold cut is washed out and the event number is already decreasing before, because the threshold is not an ideal step function.

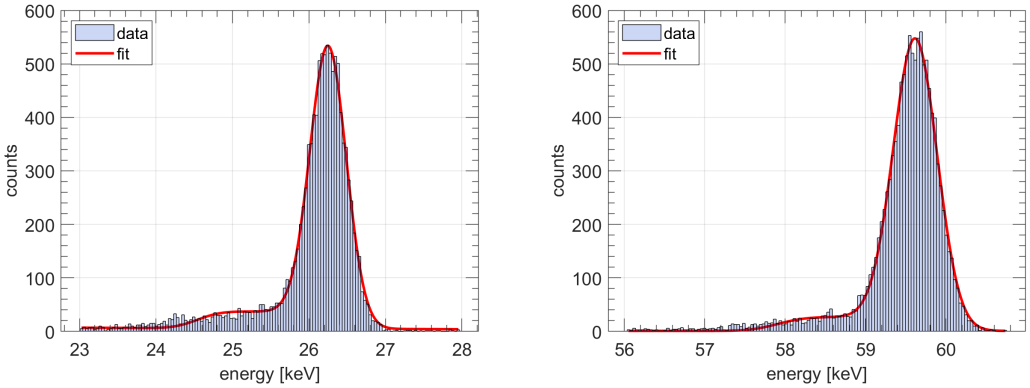

Figure 10.20: The energy response with charge sharing after the multiplicity cut. These plots show data from the detector I-02, for which charge sharing is most likely. The charge sharing effect modifies the Gaussian peaks (on the left: 26 keV; on the right: 60 keV) with a plateau that was modeled here with a cumulative distribution function (see equation 10.4). Due to the non-step-like shape of the threshold and a non-homogeneous distribution of shared events in the energy interval below the threshold the shapes are not in perfect agreement.

pixel, they are piled-up. For other setups with a pulsed reset as the XGLab system of the advanced TRISTAN prototype detectors, one could search after each event for subsequent events in a neighboring pixel within a time window of $\sim 100\,\text{ns}$ (> typical timescale of charge sharing as derived from simulations [Rad]) and then flag these events. The impact of a multiplicity cut is demonstrated in figure 10.18, where the spectrum of one dataset with and without multiplicity cut is plotted. The charge sharing results in a flat distribution of events that extend from each peak down to lowest energies. In the low-energy region of the ^{241}Am-spectrum the partial events of several peaks are summed up and result in a large background. Below 10 keV the number of events in the background is increased by a factor 10.

Even if the events with multiplicities other than 1 are removed, some effects of charge sharing are still present in the data: if only a small fraction of the charge cloud is diffusing into the neighboring sensor, such that it is below the detection threshold, no coincidence is detected, and the measured energy is slightly smaller than the initial energy. In principle one could set the IDeF-X ASIC to read out the entire array after each hit. But in practice the threshold is set to the lowest value as possible before triggering on noise, thus one could not distinguish a small shared charge from noise.
When we assume that the threshold is imposing a step-like cut onto the data, the remaining signature of the charge sharing in a multiplicity-1 spectrum would be a plateau that extends from a spectral line at the energy E_line down to $E_\text{line} - E_\text{th}$, where E_th is the energy threshold. Assuming that all combinations of the fractions of shared charges are equally likely within the interval of the threshold energy (i.e. the event distribution along the diagonal lines for example in figure 10.15 is flat), the plateau would have a rectangular shape that was smeared by the Gaussian resolution function. The edges of the plateau would then be described by cumulative distribution functions or error functions. The shape of the plateau can then be described by the formula:

$$N(E) = N \cdot 0.25 \cdot \left[1 + \text{erf}\left(\frac{E - E_\text{line} + E_\text{th}}{\sigma \cdot \sqrt{2}}\right)\right] \cdot \left[1 + \text{erf}\left(\frac{-E + E_\text{line}}{\sigma \cdot \sqrt{2}}\right)\right], \quad (10.4)$$

Detector	F-09	I-11	L-13	C-04	I-02
∅ pixel [mm]	2	1	1	0.5	0.5
№ drift rings	12	6	2	3	2

Table 10.3: The detector parameters.

where the factor 0.25 normalizes the cumulative distribution function to 1. An additional normalization factor N scales the plateau according to the number of shared events below the threshold. If the probability of charge sharing would not depend on the energy interval, one would normalize the spectrum with

$$N = 2 \cdot p_{\text{charge sharing}} \cdot \frac{E_{\text{th}}}{E_{\text{line}}}, \tag{10.5}$$

where $p_{\text{charge sharing}}$ is the general probability of an event being shared (depending on the initial energy and the detector) as tabulated in table 10.4. The factor 2 results from the fact that the charge sharing probability is taking only events into account where the larger part of the energy was deposited in the central pixel (half the diagonal line), as it will be explained later. The normalization of the plateau can be seen as projection of the entire diagonal line onto one pixel, where everything below $E_{\text{line}} - E_{\text{th}}$ is cut off, hence the factors 2 and $E_{\text{line}}/E_{\text{th}}$.
However, one can see in figure 10.19 that the probability of charge sharing is not uniform over energy, but more events lose only a small fraction of their charge to the neighbor than a large fraction. $p_{\text{charge sharing}}$ in the normalization factor thus has to be replaced by the charge sharing probability in the energy interval $(E_{\text{line}} - E_{\text{th}}, E_{\text{line}})$, called p_i, which itself is a function of energy and detector size. From the data in figure 10.19 one could extrapolate the charge sharing probability in the interval below the threshold. Here, for the sake of simplicity we assume that the number of events in the bin below the threshold is about twice the average bin count, resulting in $p_{\text{i}} = 2 \cdot p_{\text{charge sharing}}$.
With these parameters we add the plateau-function to the Gaussian peak and check if it models the 26 and 60 keV peaks of the americium spectrum (both peaks are single lines and are isolated in the spectrum such that the effect should be visible). Actually, the normalization parameter p_i is left free and fitted. Again we use data from the detector I-02, because here we have the highest probability of charge sharing (see table 10.4). The results are shown in figure 10.20. One can see that there is a plateau, but the agreement with the fitted cumulative distribution function is limited. From the fit it was found that the charge sharing probability p_{i} is 3 to 4 times larger than $p_{\text{charge sharing}}$. This value is plausible when looking at figure 10.19 that hints at a strong incline of the event distribution toward high energies (where the energy in the neighboring pixel then is below the threshold). Due to the non-step-like shape of the threshold and a non-flat event distribution, the fitted plateau-function is only an approximation. To calculate the energy distribution of the coincident events and thus derive the accurate normalization and shape of the plateau is not possible in an analytical way due to the complex geometry of the pixels and the unknown charge cloud shape. However, a simulation could deliver precise results.
Finally, it was not further pursued to find a more accurate model for the charge-sharing effects in the spectrum, because for the actual TRISTAN measurements with electrons this effect will be negligible compared to the backscattering-dominated response. In the end it is preferred to find an empirical model of the response including all effects.

In the following the absolute charge sharing probabilities $p_{\text{charge sharing}}$ are discussed.

Det.	E_{th} [keV]	14 keV [%]	17 keV [%]	21 keV [%]	26 keV [%]	60 keV [%]	$<$ 30 keV [%]
F-09	2	4.0 ± 0.1	4.7 ± 0.1	5.6 ± 0.3	8.4 ± 0.7	8.7 ± 0.7	4.5 ± 0.1
I-11	2	6.8 ± 0.2	7.1 ± 0.2	7.8 ± 0.6	10.1 ± 1.3	12.5 ± 1.3	7.0 ± 0.1
L-13	2	6.9 ± 0.2	7.3 ± 0.3	8.5 ± 0.7	9.0 ± 1.4	12.0 ± 1.5	7.1 ± 0.2
C-04	2.8	12.2 ± 0.2	13.4 ± 0.2	14.9 ± 0.5	16.6 ± 1.0	23.9 ± 1.1	12.8 ± 0.1
I-02	1.8	18.6 ± 0.1	20.1 ± 0.1	21.8 ± 0.3	23.6 ± 0.6	32.3 ± 0.7	19.5 ± 0.1

Table 10.4: Charge sharing characteristics of the five tested SDD prototypes. The amount of charge sharing for the different peaks is shown together with statistical errors. The rightmost column lists the averaged charge sharing probability for all ^{241}Am peaks from 11 to 26 keV, while the estimated number of random coincidence events was subtracted. The threshold is the one given to the ASIC and can vary from the nominal value. Note that the charge sharing probability is also a function of the energy threshold.

Det.	14 keV [%]	17 keV [%]	21 keV [%]	26 keV [%]	60 keV [%]	$<$ 30 keV [%]
F-09	3.2 ± 0.1	4.0 ± 0.1	4.9 ± 0.3	7.5 ± 0.7	8.2 ± 0.7	3.7 ± 0.1
I-11	5.5 ± 0.2	6.0 ± 0.2	6.7 ± 0.5	9.4 ± 1.2	12.0 ± 1.2	5.5 ± 0.1
L-13	5.7 ± 0.2	6.3 ± 0.2	7.5 ± 0.6	7.7 ± 1.2	11.0 ± 1.4	5.4 ± 0.1
C-04	10.0 ± 0.1	11.5 ± 0.2	13.1 ± 0.4	14.9 ± 0.8	23.5 ± 1.0	10.6 ± 0.1
I-02	10.6 ± 0.1	12.7 ± 0.1	17.0 ± 0.2	19.6 ± 0.5	29.5 ± 0.6	13.8 ± 0.1

Table 10.5: The charge sharing probabilities after applying a 3 keV software threshold to the data, allowing to compare the behavior of the detectors. As expected the charge sharing probability is decreasing with increasing detector size. Additionally, while both 1 mm-detectors have similar charge sharing probabilities independent of the number of drift-rings, the 0.5 mm-detector with 2 rings (I-02) has an increased charge sharing probability when compared to the 3 ring-detector C-04.

The charge sharing probability is the fraction of shared events, i.e. the number of events with multiplicity 2 (coincident event in central pixel and neighboring pixel) or higher divided by the number of events with multiplicity 1 (event only in central pixel). The probabilities are listed in tables 10.4 and 10.5 for the different detectors and different energies. As a reminder the sizes and number of drift rings of each detector are listed in table 10.3. To obtain the number of shared events the number of events between two values of the sum of energies, i.e. in a diagonal band across a histogram like in figure 10.15, were counted. Only events, where the energy in the central pixel was larger than the energy in the neighbor were taken into account (i.e. the diagonal line is cut in half), since other events are considered to be an event of the neighboring pixel that spread into the central pixel. The shift due to integral cross talk was compensated. The errors in the table are purely statistical. The charge sharing probabilities in table 10.4 cannot be compared a priori among the different detectors, because the data was not taken with similar threshold values and thus a varying amount of events was cut away. In order to compare the data a 3 keV software-threshold was applied. The resulting charge sharing probabilities are listed in table 10.5 in a similar fashion as before. With the increased threshold the number of shared events is strongly reduced. The reduction is more pronounced at low energies, because there a larger fraction of the diagonal line falls now below the threshold. Lowering the threshold could significantly increase the charge sharing probability, since the energy distribution of the fraction of charge sharing in one pixel increases strongly when approaching zero or the peak energy (see figure 10.19).
A systematic error on the charge sharing probabilities is imposed by random coincidence from the source or pile-up on the array. A separation of random coincidence and shared events is not possible as both effects overlap (see e.g. figure 10.17). To subtract this background the energy distribution of random coincidence would have to be known. However, from a simple calculation we can estimate the number of random coincident events and thus get an limit on the error. The rate of such events is:

$$\Gamma_{\mathrm{rc}} = \Gamma_{\mathrm{central}} \cdot \Gamma_{\mathrm{neighbor}} \cdot \Delta t, \tag{10.6}$$

where $\Gamma_{\mathrm{central}}$ and $\Gamma_{\mathrm{neighbor}}$ are the rates in the central pixel and in the neighbor pixels respectively. Δt is the time window of the read-out system, where multiple hits would be registered as coincident events. In the case of the IDeF-X ASIC, this time window is the shaping time. For the 14 keV and 60 keV lines the error from random coincidence is negligible, since, looking at figure 10.17, here both diagonal lines don't overlap with vertical or horizontal random-coincidence-lines. Also, for the 0.5 mm detectors random coincidence has a negligible impact due to the low rates. Most critical is this uncertainty for the 26 keV line, because here the random coincidence peaks of the 14 keV-line (which is the most intense) fall into the diagonal band. For the 1 mm detector, removing these events could reduce the measured charge sharing probabilities by up to 2 %. For the 2 mm detector the estimated number of random coincidence events is comparable with the number of shared events in the 26 keV peak. Of course not all random coincidence events fall into the diagonal band of this peak. An lower estimate of the charge sharing probability is given by the rightmost column in table 10.4 that lists the probabilities summed up over all peaks of the ^{241}Am-spectrum between 11 and 26 keV, where the estimated number of random coincidence events was subtracted.

The columns in the tables 10.4 and 10.5 show the charge sharing for different peaks in the spectrum, where most energies correspond to peak groups, e.g. the column "17 keV" covers the neptunium L_β and L_η line groups (see figure 10.5). As expected the charge

sharing probability is depending on the pixel size, i.e. a detector with bigger pixels has a smaller fraction of shared events. Also an increase of charge sharing with energy is evident. This is due to the energy dependency of the initial charge cloud size: simulations with the KESS software [Ren11] show that the standard deviation of the initial Gaussian-shaped electron distribution is 0.5 µm for $E = 10\,\mathrm{keV}$, 2 µm for $E = 26\,\mathrm{keV}$ and 9 µm for $E = 60\,\mathrm{keV}$ [Kor16, Kor]. In the data the fraction of shared events is not scaling as strongly with energy, because the additional transverse diffusion of the charge while it drifts through the detector adds typically a few µm to the charge cloud size. The size σ of the charge cloud after traveling the distance d and crossing the potential V_{bias} can be calculated, following [Spi05], through

$$\sigma = d\sqrt{\frac{\mathrm{k_B}T}{V_{\mathrm{bias}}\mathrm{e}}}. \tag{10.7}$$

For $d = 450\,\mu\mathrm{m}$ (thickness of the detector) and $V_{\mathrm{bias}} = 100\,\mathrm{V}$ a σ of 6.5 to 7.2 µm is obtained for temperatures between −30 and +20 °C. This is a simple approximation of the measured case because in a SDD due to the complex shape of the electric field the charge will not drift through the entire detector in parallel to the pixel border, but a rough estimate of the charge cloud size is obtained and it becomes clear that the increase of the charge cloud size by diffusion is in the same order as the initial size. The energy dependent absorption length has also a contribution to the energy dependency of charge sharing, because charge clouds will travel for a varying time through the detector (thus varying the amount of charge that diffuses into the neighboring pixel) depending on the depth of the vertex. It also should be mentioned that a small contribution for the increase of shared events with energy is caused by the rising Compton scattering probability (for the X-rays of interest here photoabsorption is the dominant interaction process).
Looking at the data from the 0.5 mm-detectors, we observe that the detector I-02 with 2 drift rings is subjected to more charge sharing than detector C-04 with 3 drift rings. This difference could mainly be due to the different speed of charge collection within the substrate, caused by differences in the E-field shape that affect the transverse diffusion. The weaker field gradient in the 2-ring detector grants the charge cloud more time to spread before being collected at the anode. Interestingly, the 1 mm-detectors I-11 (6 rings) and L 13 (2 rings) show the same charge sharing behavior. To study this behavior detailed simulations would be necessary.

In principle one has also to consider events with higher multiplicities, e.g. detections close to the intersection of three pixels, resulting in a multiplicity-3 event due to charge sharing. Figure 10.21 shows the normalized number of counts in each pixel of F-09 (2 mm, 12 rings) with respect to their multiplicity. Here it can be seen that multiplicity-3 events are one order of magnitude less likely than simple charge sharing with multiplicity 2 and thus can be neglected. In this plot one can also see that the central pixel has an increased number of coincident events. This is due to the geometry of the array. The central pixel has a larger effective surface, where hits result in charge sharing, because the pixel is entirely surrounded by 6 other detectors, while the edge pixels have only 3 neighbors. Figure 10.22 shows a similar plot for the detector I-02 (0.5 mm, 2 rings). In the central pixel only 70 % of all events have no coincidence in an adjacent pixel. In addition, events with multiplicity 7, i.e. all pixels were hit at once, occur and are more likely than events with multiplicities 4, 5 and 6. The counts for multiplicity 7 are not similar for all pixels because they are differently normalized and also noise events that might coincide with a real events were cut.

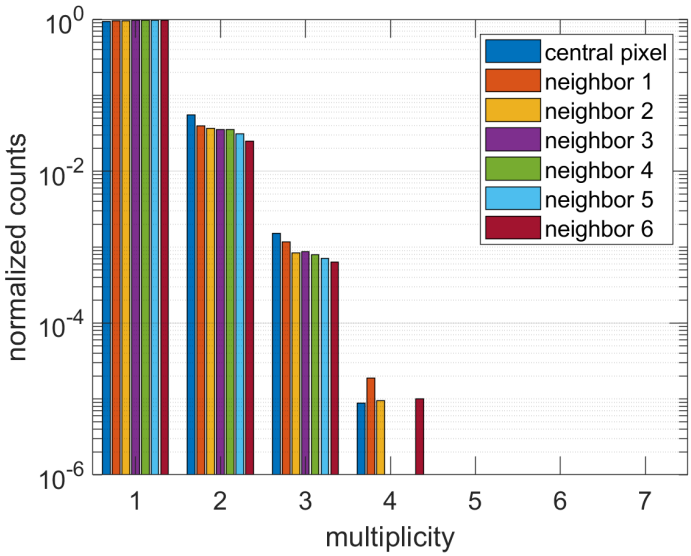

Figure 10.21: The multiplicity distribution of the different pixels of detector F-09 (2 mm, 12 rings). Most events are detected without any coincidence, a few percent with one coincident event (mostly charge sharing), i.e. multiplicity 2. In the central pixel more coincident events are observed than in the neighbors due to geometric effects. Events with multiplicity 3 are one order of magnitude less likely than multiplicity 2 events.

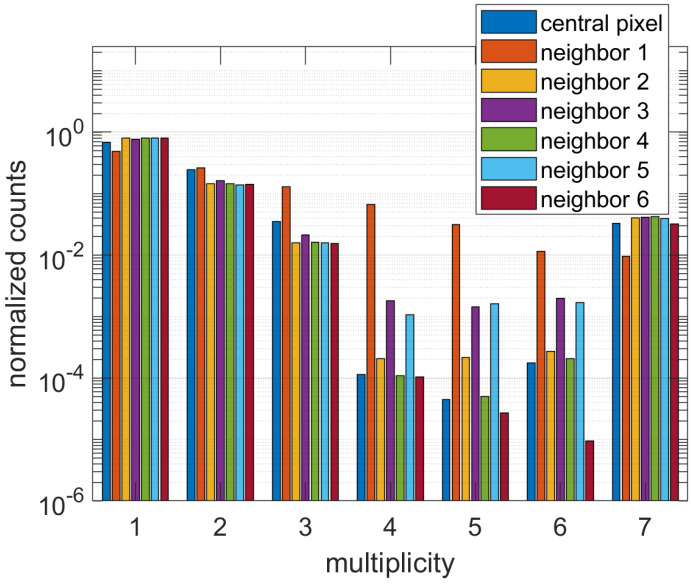

Figure 10.22: The multiplicity distribution of the different pixels of detector I-02 (0.5 mm, 2 rings). Due to the small size of the detector, also events with multiplicity 7 occur and are more likely than events with multiplicities 4, 5 and 6. In the central pixel, only about 70 % of all events have no coincidence in an adjacent pixel.

In conclusion, a large pixel diameter is preferred for TRISTAN not only to minimize the general charge sharing probability, but also to avoid events with high multiplicities. Reconstructing the energy of these events would further reduce the energy resolution. Also, if the coincident events are discarded from the analysis ($\approx 20\%$ for the 0.5 mm-detectors, see table 10.4), one would obtain an increased dead time.

It should be noted that the charge sharing behavior can be different for electron data (as from the tritium decay) due to the short interaction length in silicon. This was studied with measurements at the Troitsk ν-mass-spectrometer and is presented in section 11.2.

10.4 Summary

In this chapter results from the characterization of 7-pixel prototype-SDDs for the TRISTAN project with X-rays were presented. In an optimized setup the noise floor of the ASIC (44 e^-equivalent noise charge) was reached with all tested detectors. This means that the detector resolution is limited by the electronics and that the detectors are working properly and are suitable for the TRISTAN project. To achieve an even better performance, a different low-noise read-out is required, as it is already in development (see section 9.4).
In addition the effect of charge sharing was studied. As expected, charge sharing is minimized for large detector sizes. For the 2 mm detector, less then 5 % of the events in the energy region of interest are shared between two or more pixels. In principle these events can be reconstructed for an analysis, but result in a decreased energy resolution. In conclusion, and what concerns charge sharing only, the pixel size for the final TRISTAN array should be chosen as large as possible (an upper limit is given by the available space and the necessary number of pixels).
It was shown that even when removing shared events from the data, charge sharing has still an impact on the measured energy response. The shape of the additional contribution to the spectrum is determined by the energy threshold, the functional form of the threshold (e.g. if it is a step function or something else) and the energy distribution of coincident events, which is depending on geometry of the detector and the charge cloud. To model this effect on the response with a high accuracy, simulations of the charge transport within the detectors is necessary. In addition, measurements with high statistics could help to understand the effect, but one has to keep in mind that the shape of the response depends on the read-out system. In the end, it is not absolutely necessary to model this effect independently, since in measurements with electrons other effects are expected to dominate the response and it is considered to find a global empirical model.
The characterization of the TRISTAN detectors with CEA read-out was continued with electrons by installing the I-11 (1 mm diameter, 6 drift rings) detector at Troitsk ν-mass, which is presented in chapter 11.

Chapter 11

Measurements at Troitsk ν-mass: detector characterization with electrons and a pilot sterile neutrino search

One of the prototype detectors was installed at the Troitsk ν-mass experiment. As described in section 8.2, Troitsk ν-mass is a technological predecessor of KATRIN and the perfect testbed for the TRISTAN detector prototypes. It provides several electron sources that allow us to further characterize the detectors and to test hardware components. In addition, tritium data can be used to develop analysis techniques for TRISTAN. All of this is not possible directly at KATRIN: at the time of the measurements presented here KATRIN was not yet operational. In addition KATRIN does not allow the uncomplicated installation of a different detector for a short period. In section 11.1 the different measurements taken at Troitsk, the achieved detector performance and calibration are described. The analysis of coincident event and charge sharing is presented in section 11.2. In sections 11.3 to 11.3.8 the analysis of a tritium spectrum is presented including a sterile neutrino search. This was primarily not done in a serious attempt to scan the parameter space for a sterile neutrino, but rather to develop and test techniques for the analysis of a differential spectrum from a MAC-E type spectrometer. This was not done before and thus will be very useful for TRISTAN. In section 11.4 simulations to study the energy response of the system are presented. The tritium analysis is concluded with a sensitivity study and exclusion curves in section 11.5. A summary of this chapter can be found in section 11.6.

11.1 Setup and measurements

The Troitsk ν-mass setup itself was introduced in section 8.2. The TRISTAN prototype detector, which was installed in the Troitsk spectrometer, is designated I-11 (see table 9.1 in chapter 9). It has 7 pixels, each with a diameter of 1 mm and 6 drift rings. The original Troitsk ν-mass-detector is inserted in a 30 cm long pipe with 12 cm inner diameter at the end of the spectrometer that can be separated from the vacuum with a gate valve. When the flange at the rear end is closed and the pipe is evacuated, the gate valve is opened and the detector moved into the center of the detector magnet. This detector can be easily removed together with its liquid nitrogen cooling system. For the first TRISTAN measurement campaign at Troitsk, which is presented here,

Figure 11.1: The detector on its mounting structure. The detector board is screwed onto a plastic plate that is attached to two rods, which are fixed on the flange in the back. Between the detector board and the plastic is a thermally conductive pad to improve the passive cooling of the detector. Behind the detector board is the bias board. Both are connected with a shielded flat cable. The detector voltage, the ASIC voltage and the digital communication are sent through the two feedthroughs in the flange in the back. The analog pulse heights are sent through the two coaxial cables that connect to another feedthrough on the right (not pictured).

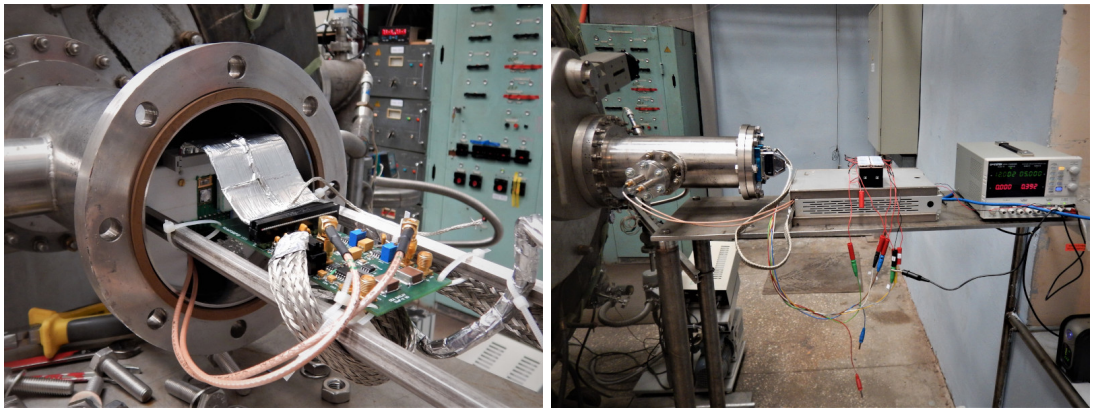

Figure 11.2: Left: the detector during its insertion into the pipe. The two coaxial cables are already connected to feedthroughs on another flange on the side (outside of the left border of the picture). **Right**: the setup during operation. The box in the middle houses the interface and FPGA boards. The blue space wire connects it to the computer. The battery-pack on the box powers the detector, the power supply on the right the read-out electronics.

only a fixed mount could be manufactured that places the detector in the pipe close to the gate valve, about 20 cm away from the detector magnet. The mounting structure together with the detector is shown in figure 11.1. The mount consists of two rods with a plastic plate to which the detector board is attached. The rods are fixed on the flange and also carry the bias board. There are two D-SUB feedthroughs with 37 pins each in the flange for the voltage supply of the detector and ASIC and for the digital communication. In addition there is a small flange at the side of the pipe with two SMA feedthroughs for the analog transmission of the pulse heights. Outside the vacuum the remaining components of the system, the interface board and FPGA board, are placed in a grounded case (see section 9.3 for a description of the detector system and its components). The read-out electronics are powered by a conventional 5 V power supply, while for the detector again batteries are used to ensure a highly stable voltage. The detector is not actively cooled, but is close to a superconducting (i.e. very cold) magnet. To improve the passive cooling a thermally conductive pad was put between the detector board and the plastic plate, as it can be seen in figure 11.1. Before installing the system in the spectrometer, the detector was calibrated and tested together with its mounting structure in a separate box on-site, which is also shown in the photograph. The insertion of the detector in the pipe and the complete setup are shown in figure 11.2.

Following settings were used for the detector:

- the **energy threshold** was set to 1.14 keV. This was possible because the system was carefully optimized to minimize noise by shielding the components and taking care of the proper grounding;
- the **peaking time** was set to 6.8 µs, which corresponds to a shaping time of 9.6 µs. This shaping time, which is similar to the signal integration time, ensures that electrons, which are back-scattered on the detector and subsequently reflected by the electric or magnetic field and hit the detector again are either detected as coincident events with a multiplicity $\neq 1$ on different pixels or as one event in a single pixel, where the individual charges are summed up. The maximum time between both hits was later simulated and is indeed within 9.6 µs, as shown in section 11.4.

There are three different electron sources at Troitsk ν-mass, which were used for the measurements presented here:

- **tritium electrons:** the gaseous tritium source is made of a mixture of isotopes, mostly ^{2}H, ^{3}H, ^{3}He, ^{4}He and some residual air. The gas pressure is not measured directly in the source, but can be assumed to be in the order of 10^{-4} mbar. The total amount of tritium in the source is a priori not known and difficult to measure.
- **wall electrons:** electrons are emitted from the spectrometer electrode. It is assumed that these electrons are created through impact ionization, when positive helium ions produced by the decay of residual tritium in the spectrometer are accelerated onto the electrode. These ions can produce secondary ions and electrons when colliding with air molecules, resulting in a pressure dependence of the flux. The produced electrons are then accelerated by the potential difference away from the electrodes and reach the detector with an energy similar to the retarding potential (e.g. 13 kV retarding potential $\rightarrow$ 13 keV electron energy at the detector). This measurement is possible without any magnetic field, but results in a low rate. The rate can be increased by configuring the magnetic field

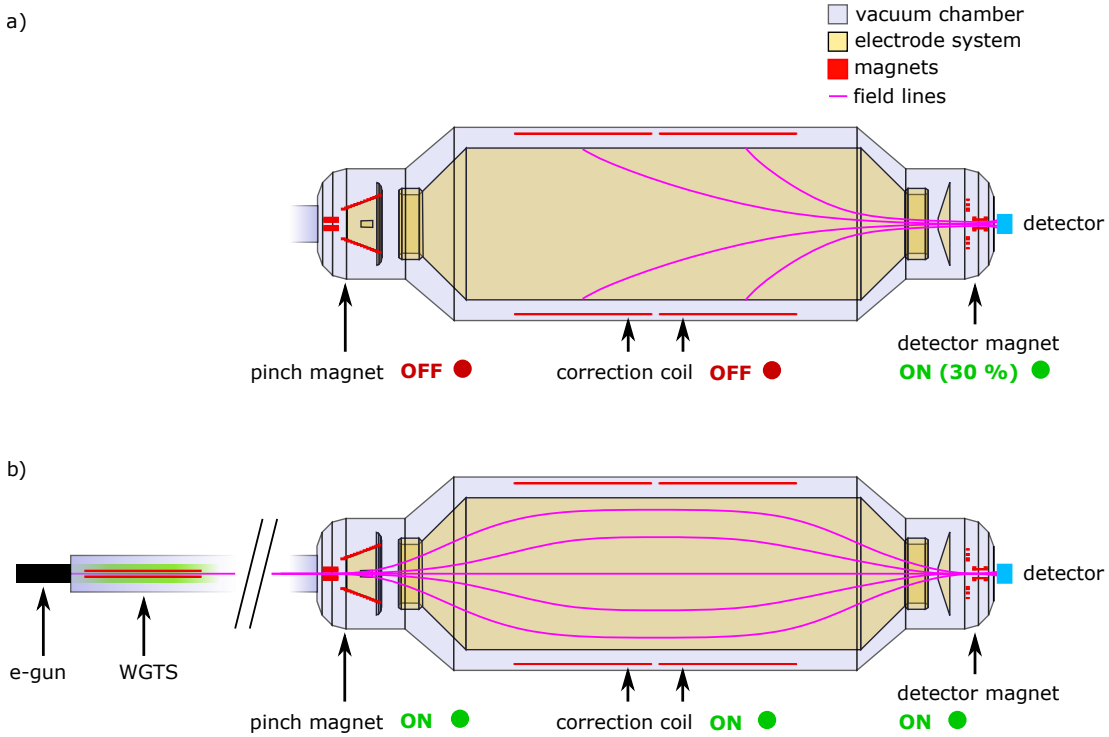

Figure 11.3: a) Configuration of the spectrometer to measure electrons emitted from the high voltage electrode. The pinch magnet is turned off, while the detector magnet is powered with a 50 A current, a third of the current in the standard configuration. As a result the magnet field lines connect the detector with the main electrode. To ensure that the small detector flux tube connects really to the electrode and not to the gate valve in front of the pre-spectrometer, the correction coils were turned off, allowing the earth magnetic field to break the symmetry of the field lines.
b) Configuration of the spectrometer to measure electrons from the tritium source (WGTS) and from the e-gun – the standard configuration. Here all magnets are operated at full power such that they create together with the electric field a MAC-E filter.

such that the field lines focus electrons from the wall onto the detector. This is achieved by turning off all magnets except the detector magnet, which is operated at a reduced current of 50 A (instead of 150 A as in normal operation mode). The correction coil that usually should cancel out the earth magnetic field within the spectrometer is turned off. This way the central field lines (that should connect to the detector, if it is centered) are not pointing to the valve that separates the pre-spectrometer from the source, but onto the high voltage electrode. The retarding potential is also called HV in the following.

- **e-gun electrons:** the e-gun emits a narrow beam of monoenergetic electrons. The e-gun is usually used to measure the density of the tritium source by shooting a beam of 19 keV-electrons through the source and measuring the energy loss of the electrons.

The spectrometer configuration for the different measurements is summarized in figure 11.3.
A list of all measurements conducted with TRISTAN-prototype at Troitsk can be found in tables 11.1 and 11.2, including which electron source was used, the spectrometer configuration and event rates. The results from these measurements are presented in the following sections of this chapter.

date	run №	HV [kV]	magnets	e-gun [kV]	tritium	corr. coil	Γ_{central} [cps]	N_{central}	comment
1.6.	1	0					0.22	104	
1.6.	2	20					0.10	112	1)
1.6.	3	20					0.10	2 235	2)
1.6.	4	15					0.10	1 673	2)
1.6.	5	ramp	ramp				3.59	588	2)
1.6.	6	15	Det. mag. 50 A				5.54	10 388	
1.6.	7	16	Det. mag. 50 A				5.61	13 856	
1.6.	8	17	Det. mag. 50 A				5.65	10 099	
1.6.	9	18	Det. mag. 50 A				5.85	10 740	
1.6.	10	14	Det. mag. 50 A				5.46	10 243	
1.6.	11	13	Det. mag. 50 A				5.35	4 044	
1.6.	12	0	ramp				138.44	224 927	
1.6.	13	0	full field				–	–	3), 4)
1.6.	14	ramp	full field				–	–	3)
1.6.	15	?	full field				–	–	3)
1.6.	16	ramp	full field				–	–	3), 5)
1.6.	17	18.7	full field	19			266.42	555 750	
1.6.	18	18.7	full field	19			345.28	339 795	
1.6.	19	18	full field	19			84.82	47 963	
1.6.	20	17	full field	19			3.43	1 578	
1.6.	21	16	full field	19			1.13	2 208	
1.6.	22	15	full field	19			1.03	141	
1.6.	23	18	full field	19			79.83	99 525	
1.6.	24	13	full field	19			2.44	3 377	
1.6.	25	13	full field	16			36.75	179 290	
1.6.	26	13	full field	14			151.84	184 436	
1.6.	27	13	full field	15			27.99	52 779	
1.6.	28	13	full field				0.79	285	
1.6.	29	13	full field				10.86	539 685	

Table 11.1: The measurements at Troitsk (part 1/2). The colors indicate if the component was active (green), partially active (orange), or off (red). Γ_{central} [cps] is the mean count rate in the central pixel, N_{central} the number of events in the central pixel. Comments: 1) short run; 2) 8 keV threshold; 3) no file; 4) correction coils turned on during run; 5) e-gun turned on during run.

date	run №	HV [kV]	magnets	e-gun [kV]	tritium	corr. coil	Γ_{central} [cps]	N_{central}	comment
2.6.	1	13.5	full field				8.14	14 155	
2.6.	2	14	full field				5.82	14 321	
2.6.	3	13.25	full field				9.43	16 382	
2.6.	4	13.75	full field				6.97	12 639	
2.6.	5	14.5	full field				4.24	10 883	
2.6.	6	15	full field				2.86	7 880	
2.6.	7	15.5	full field				1.85	7 532	
2.6.	8	16	full field				0.92	7 380	
2.6.	9	13	full field				4.61	176 929	
3.6.	10	13	full field	19			3.15	2 711	
3.6.	11	18	full field	19			167.00	97 011	
3.6.	12	1	full field				29.83	53 716	
3.6.	13	?	full field				4.28	502	
3.6.	14	13	ramp				6.12	5 229	
3.6.	15	20	Det. mag. 50 A				6.64	24 522	
3.6.	16	20					0.31	5 463	
3.6.	17	15					30.25	27 431	6)
3.6.	18	18					27.15	4 032	
3.6.	18b	19					18.89	6 553	
3.6.	19	15					17.38	17 417	
3.6.	20	15					0.15	3 038	

Table 11.2: The measurements at Troitsk (part 2/2). The colors indicate if the component was active (green), partially active (orange), or off (red). Γ_{central} [cps] is the mean count rate in the central pixel, N_{central} the number of events in the central pixel. Comments: 6) increased rate due to higher residual air pressure in spectrometer.

11.1.1 Calibration and performance

For the energy calibration all available data with mono-energetic electrons was used. Some of the e-gun data was not used for every pixel, because the peak is not visible in each pixel (each pixel was calibrated independently). Note that the calibration was done with respect to the peaks of electron data. As a consequence this calibration is not absolute, since the energy loss due to the dead layer is not taken into account. A calibration with X-rays that are not affected by the dead layer was not possible in situ, but was done before the installation of the detector in the spectrometer. However, the calibration can be different when the setup is changed.

The bin centers of the peaks in the monoenergetic data were fitted with a Gaussian distribution by the non-linear least squares method. At the low-energy side of the peaks the data was cut to prevent asymmetries from affecting the fit (see figure 11.4). To obtain the calibration function, the fitted mean ADU values (ADU $\hat{=}$ analog-digital unit, i.e. the channels of the ADC) were tabulated as a function of initial energy and then fitted with a linear model, where each data point was weighted with its error. The initial energy is either similar to the high voltage potential for wall electron measurements or the set value for the e-gun, both values can be considered to be accurate. The resulting calibration function for the central pixel is:

$$\text{E [keV]} = \{(-88090.9 \pm 392.5) + (34.127 \pm 0.127) \cdot \text{channel [ADU]}\}/1000,$$

where the errors (95% confidence bounds) are not important for the analysis of the data. In fact, when fitting the tritium spectrum the calibration was included as free parameter in order to adjust for uncertainties and possible drifts (see section 11.3). The fitted calibration function for the central pixel and the deviation of each data point from the linear function are shown in figure 11.5. The deviations are in the order of a few ADU ($\mathcal{O}(10\,\text{eV})$) and there is no indication for a strong nonlinearity. Even though the red data points (wall electrons with B-field) show a energy dependent structure, other data as for example the blue points (wall electrons) at 15 keV show a spread at constant energy. The observed structure could thus be due to changing environmental conditions (temperature, fluctuations of voltages etc.) and not necessarily caused by ADC non-linearities, which would have to be studied with dedicated measurements.
The calibration functions for all the pixels and information about the used data can be found in the annex B.

The fit of the peaks of the monoenergetic data returns also the resolution of the detector. The average equivalent noise charge (*enc*) in the central pixel was 47.7 electrons (458 eV fwhm). This is close to the minimum intrinsic noise of the ASIC ($enc = 44\,\text{e}^-$). A similar performance was achieved with the other pixels, as tabulated in table 11.3. Such a good resolution is surprising, since the detector is not actively cooled and due to the dead layer a broadened peak is expected for electrons when compared to X-ray data. This shows that the optimization of the setup (shielded cables, grounded box) was successful. Also, these results prove that the detector works as good for electrons as for X-rays.

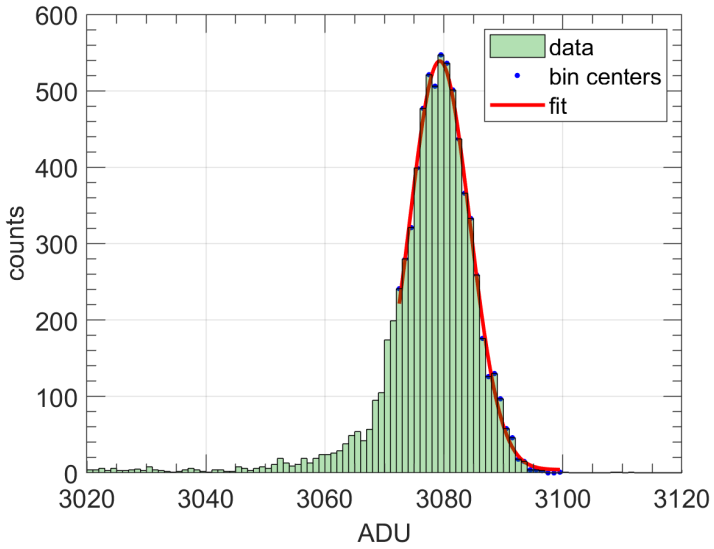

Figure 11.4: An exemplary fit to calibrate the data (17 keV wall electron data, run 8 from 01.06.2017, central pixel, multiplicity 1). The peak is fitted with a Gaussian, where the low energy side is not taken into account completely, because dead layer effects cause an asymmetry of the peak.

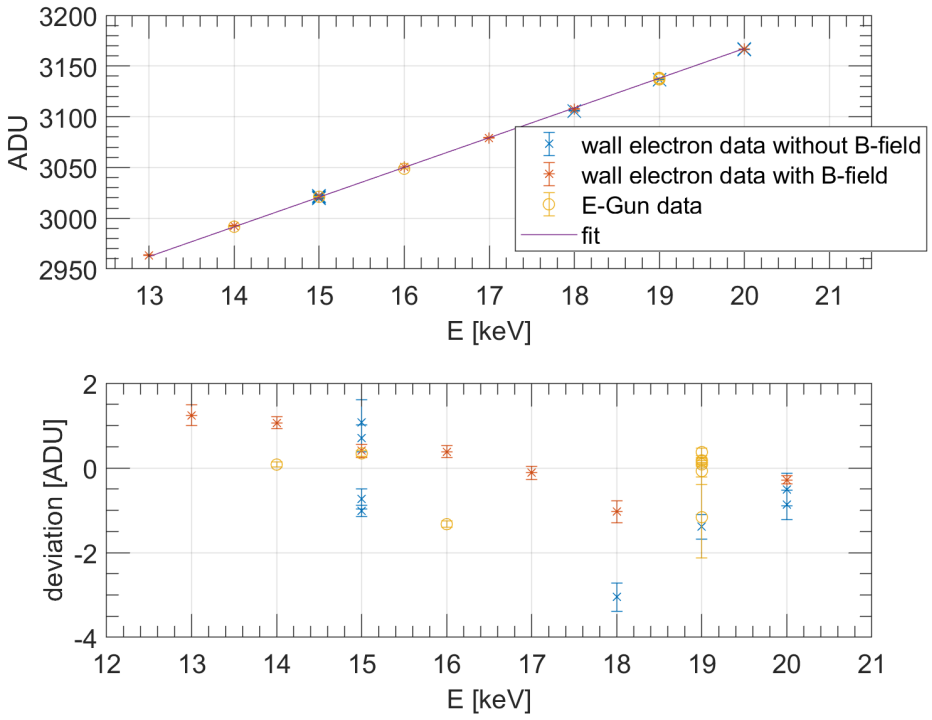

Figure 11.5: The calibration of the central pixel. In the top plot the mean ADU values of the fitted Gaussians are plotted as a function of initial energy together with the linear calibration fit. On the bottom plot the deviation of each data point from the fitted line is shown. The color code indicates the source of the data. The deviations are small and there is no strong indication of a non-linearity.

channel	mean *enc* [e$^-$]	mean $fwhm$ at 17 keV [eV]
1	45.7	443
6	44.6	434
11	45.8	442
16	47.7	458
21	44.7	435
26	45.3	438
31	44.5	433

Table 11.3: The resolution (*enc* and $fwhm$) of each pixel, averaged over all data sets with monoenergetic electrons. The noise level is close to the intrinsic ASIC noise of 44 electrons.

11.1.2 Measurements of electrons from the e-gun

Measurements with the e-gun are interesting for several reasons: the magnetic fields are in the same configuration as for measurements with the tritium source, such that the e-gun data can be used to model the energy response of tritium electrons. However, it has to be taken into account that the electrons from the e-gun have to cross the entire tritium source and thus experience more scattering than electrons emitted in the gas, and their angular distributions are different. The scattering can be studied with the e-gun by doing measurements with an empty source, and then comparing it to data, where the electrons were shot through the gas. Actually, the e-gun is used in the regular Troitsk ν-mass measurements to measure the column density of the source by observing the energy loss due to scattering. This procedure is described in [ABB$^+$11]. In addition, measurements with the e-gun at different retarding potentials allow to examine the adiabaticity of the electron transport through the spectrometer, which is depending on the surplus energy and the radial distance from the symmetry axis of the MAC-E filter.

The e-gun emits a narrow beam of monoenergetic-electrons. For the usual source density measurements electrons with an energy of 19 keV are used. A change of the e-gun energy is not trivial because also some magnet currents have to be adjusted. It was possible to do measurements also for 14, 15 and 16 keV. The correction coils are used to steer the beam onto the detector. The beam spot is in principle smaller than one detector pixel (<1 mm diameter), but is unfocused at the detector position behind the detector magnet and extends in a non-circular shape, such that several pixels can be hit.

Spectra taken with the e-gun are shown in figure 11.6. The spectrum consists of two distinct parts: a peak, where the electrons deposited their full energy (primary electrons), and a tail due to back-scattered and backreflected electrons. This tail is called the backscatter-tail. In the data shown, the fraction of events in the tail ($E < 18$ keV) is 14.4% for run 18 and 55.5% for run 24. The number of events in the backscatter tail is varying in the data because it depends on the position of the beam spot. While the beam spot from the e-gun itself has a diameter in the order of the detector diameter, the fluxtube of back-scattered and backreflected electrons seems to be larger, such that if a pixel is hit on the edge it detects less primary electrons from the e-gun, but the same flux of backscattered electrons as when the beam spot is centered. This can be explained by the primary electrons being emitted with a narrow forward angular distribution. Backscattered electrons can have large angles with respect to the field lines, such that the perpendicular velocity is larger than for primary electrons. Then the gyro-radius, which is proportional to the perpendicular velocity component of the

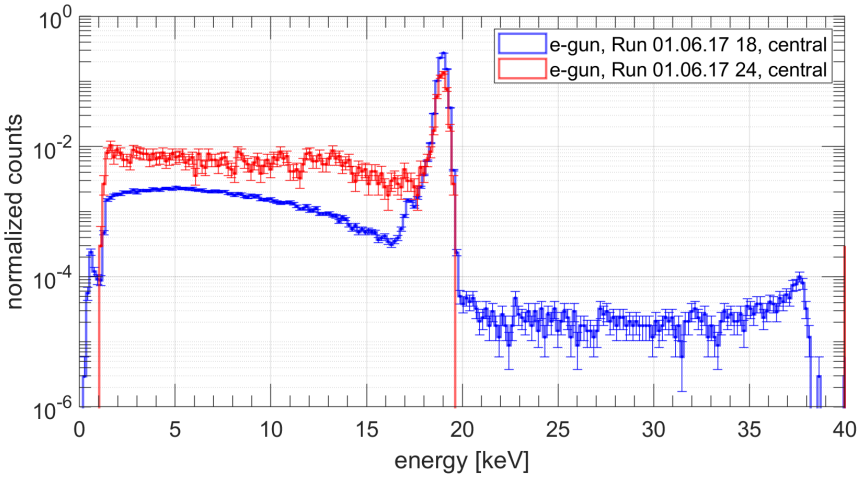

Figure 11.6: Two spectra taken with the e-gun at 19 kV. The energy response consists of a peak and a tail that contains events from backscattered and backreflected electrons. The fraction of events in the tail is different in both datasets due to a changed position of the beam spot on the detector. For Run 18 also pile up is visible.

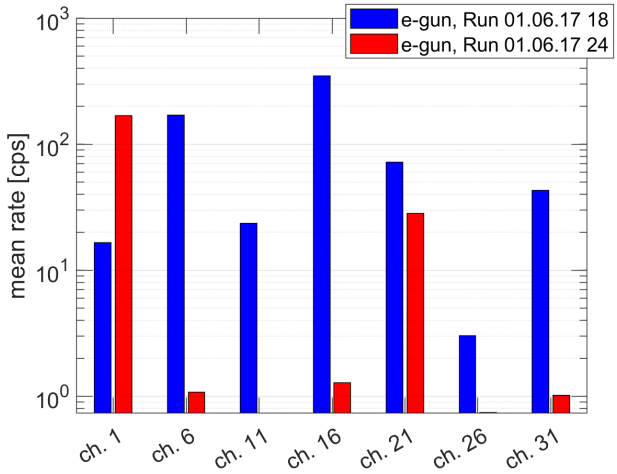

Figure 11.7: Here the rates for each pixel of the same data as in figure 11.6 (run 18 and 24 on 1.6.2017) are shown. It becomes clear that the e-gun is not homogeneously illuminating the detector (note the logarithmic y-scale). While the beam is centered on the central pixel (channel 16) for run 14, the highest rates are measured by the edge pixels channel 1 and 21 for run 24.

electrons, is also larger. In figure 11.7 the rates of each pixel for the two data sets, run 18 and 25 from 1.6.2017, are shown. Here it becomes clear that the e-gun does not create a homogeneous flux of electrons onto the detector (note the logarithmic y-scale). While for run 18 the beam spot seems to be centered, the edge pixels channel 1 and 21[1] measure the highest rates in run 24. The central pixel channel 16 receives 1-2 orders of magnitude less electrons. Due to the lack of a real time rate monitor in the used detector user interface, the centering of the beam by adjusting manually the correction coil currents was difficult and tedious.
The data in figure 11.6 was taken with different retarding potentials (run 18: 18.7 kV, run 24: 13 kV). This cannot explain the observed differences in the response, because other data taken with different retarding potentials don't show a changed fraction of events in the tail. Also, for data with higher retarding potentials an increase of events in the tail would be expected, since more back-scattered electrons are backreflected from the electric potential, but the two data sets in plot 11.6 show the contrary.

For run 18 also pile-up is visible. There are 977 events above 20 keV, which is 0.29% of all events. The pile-up rate is calculated according to:

$$\Gamma_{\text{pile-up}} = \Gamma_1 \cdot \Gamma_2 \cdot \Delta t, \tag{11.1}$$

where both Γ_1 and Γ_2 are the measured rate of 345 cps and Δt is the integration time, i.e. the shaping time of 9.6 µs. Thus in this measurement, which lasted 984 s, 1124 events of pile-up are expected in total, which is close to the measured value.

Data, where the e-gun was shot through the source gas are shown in figure 11.8, and the corresponding rates in figure 11.9. The measurement, where the retarding potential was set to 18 keV, is not distinguishable from the empty source measurement. However, electrons that lost more then 1 keV due to source scattering are filtered out by the retarding potential. In the run with 13 kV retarding potential the e-gun was poorly aligned, such that the rate was very low and too few events were collected.

In summary the e-gun measurements are not suitable for a detailed analysis due to the beam spot position dependency of the spectrum. This makes it not only hard to study the energy response, but also prevents us from examining source effects. In addition, to study the adiabaticity a more defined positioning of the beam is needed.

[1] The pixels are named by the ASIC channel they are connected to, see section 9.3

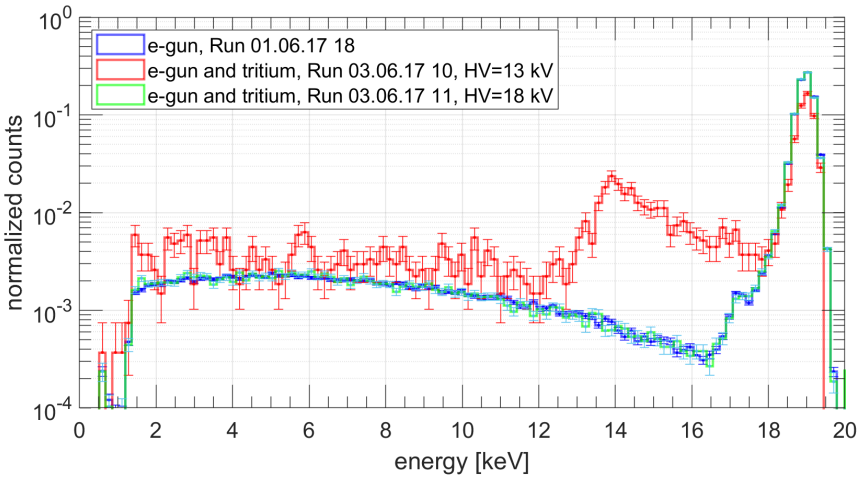

Figure 11.8: Spectra from the e-gun, where the electrons were shot through the source gas (run 10 (red) and run 11 (green) from 3.6.2017), compared to a run with an empty source (blue). The e-gun is set to 19 keV. For run 10 the retarding potential was set to 13 keV, for run 11 to 18 keV, i.e. there is almost no tritium in the spectrum. Run 11 and 18 are almost indistinguishable from each other. However, electrons that lost more than 1 keV due to source scattering are cut off by the retarding potential. Due to a poorly aligned e-gun the statistics in run 10 are too low to properly examine source effects.

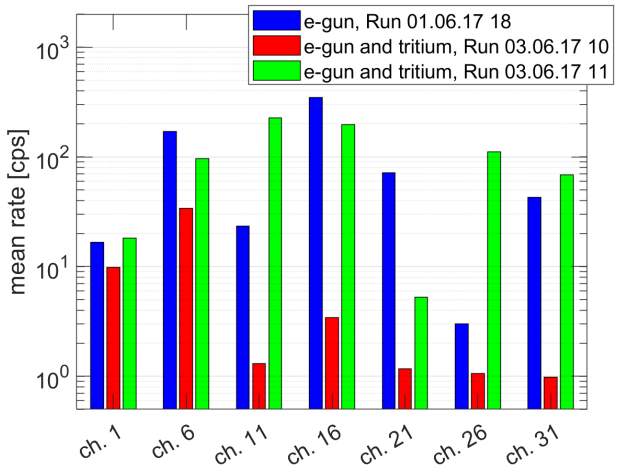

Figure 11.9: The rates in the measurements with e-gun and tritium (run 10 and 11) and for comparison a run with an empty source (run 18). In run 11 and 18 the e-gun beam is centered onto the detector, but for run 10 it is poorly aligned.

11.1.3 Measurements of electrons emitted from the electrodes (wall electrons)

Electrons emitted from the electrodes (called "wall electrons") illuminate the entire detector with a isotropic flux, such that position effects as during the e-gun measurements are not expected. Some measurements were done without any magnetic field, which resulted in very low rates (~ 0.1 cps in the central pixel, see run 2-4 on 1.6.2017 in table 11.1). At the end of the measurement campaign this was repeated, but much higher rates up to 30 cps were observed in run 17-19 from 3.6.2017 (see table 11.2) due to an increased pressure in the spectrometer after the pumps were turned off. Some of the spectra taken without any magnetic field are shown in figure 11.10. The energy response shows a peculiar shape: the general shape of peak and backscatter-tail is in principle still preserved, but an additional peak $\sim$2 keV below the main peak is present. The origin of this peak is not entirely clear, but it is related to an increased pressure in the spectrometer and might be caused by negative ions. The rates across the detector pixels are shown in figure 11.11. The rate is similar in all pixels, showing that the electron flux onto the detector is isotropic over the entire area. However, due to the peculiar shape of the spectra, these data cannot be used to study the energy response. Later (see section 11.2) this data will be used to study charge sharing. For measurements with magnetic field, charge sharing is indistinguishable from backscattered and backreflected electrons. In the measurements with the magnets turned off, there is no directed backreflection onto the detector.

The energy response of wall electrons with the detector magnet turned on has a more familiar and consistent shape, as shown in figure 11.12. For different energies, the spectra have a similar shape and a similar number of events in the backscatter tail. The fraction of events in the backscatter tail is on average $32.88 \pm 0.94\%$. The rate is also constant over the entire array (see figure 11.13). This data is suitable to study the response of the system. It is later used as a reference energy response for the analysis of the tritium spectrum in section 11.3. The description and fitting of the response

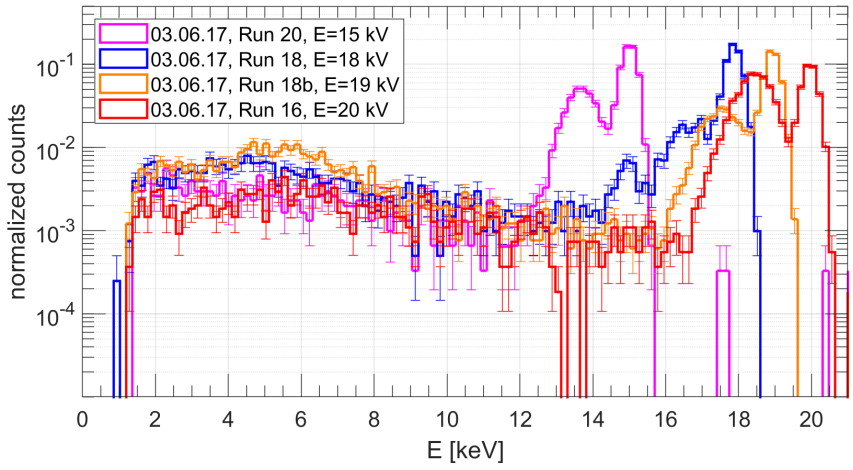

Figure 11.10: The spectra of wall electrons in the central pixel. The detector magnets are turned off. The energy response has a peculiar shape. In principle it consists still of the peak and the backscatter tail, but there is another prominent broad peak $\sim$2 keV below the main peak visible (the "bump"). Its origin is not clear, but it is related to the increased pressure in the vacuum tank.

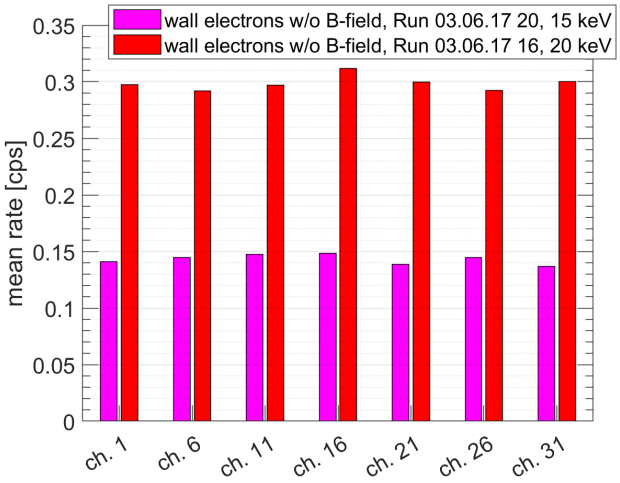

Figure 11.11: The rates in the individual pixels for two measurements of wall electrons. The rate is similar in all pixels, the electrons illuminate the entire detector isotropically. The rate in the central pixel (channel 16) is slightly increased, because this detector detects shared events from all neighbors.

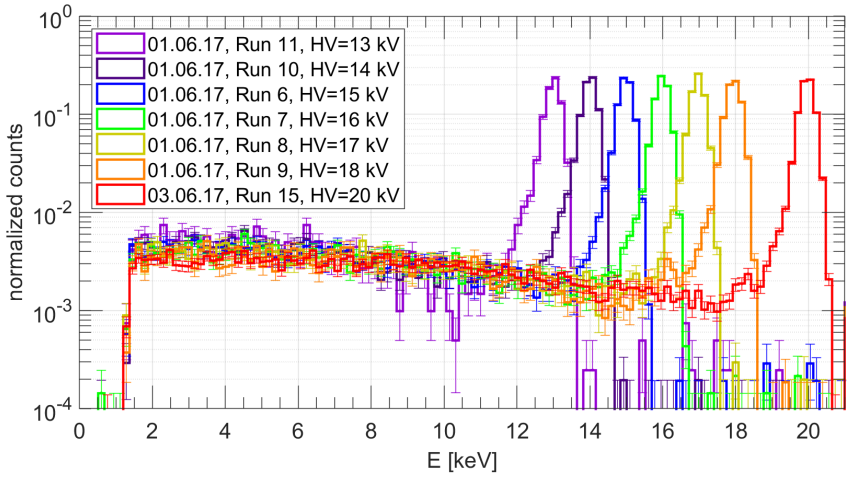

Figure 11.12: The spectra of wall electrons with the detector magnet activated to focus the electrons onto the detector, taken with the central pixel at different HV values, ranging from 13 to 20 keV. It can be seen that the spectra have similar shapes for different energies.

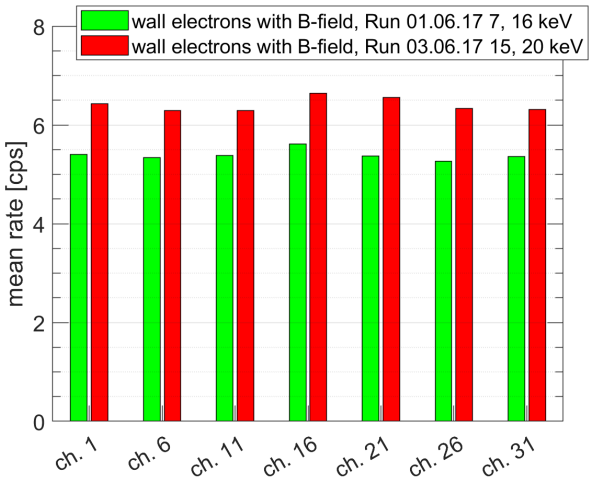

Figure 11.13: The rates in the individual pixels for two measurements of wall electrons with magnetic field. The observation is the same as for the measurements with the magnet turned off: the rate is similar in all pixels, the electrons illuminate the entire detector isotropically. The rate in the central pixel (channel 16) is slightly increased, because this detector detects shared events from all neighbors.

with an empirical model is presented in section 11.3.3.

The comparison of the measured spectrum in the central pixel with the response in the edge pixels in shown in figure 11.14 for 20 keV wall electrons. The shape of the backscatter tail in the edge pixels is changed and the tail contains more events. For this data a multiplicity cut was applied, which removes all events where two or more pixels were hit. Events, where the electron was backscattered on an edge pixel and then reflected onto the central pixel (or vice-versa) are effectively removed from the data of the central pixel, since it is completely surrounded by other pixels. The gyroradius of the electrons is ~ 1 mm, thus events that cannot be vetoed because they backscattered on the non-active silicon surface before they were reflected onto the central pixel, are unlikely. For the edge pixels the multiplicity cut is less effective, because only half of the surrounding area is covered with detectors, resulting in more events in the backscatter tail and a different shape. The spectrum in the central pixel shows a similar shape as in the edge pixels, when no multiplicity cut is done, as shown in figure 11.15.

The wall electron data with magnetic field and the e-gun data are compared in figures 11.16 (14 and 15 keV) and 11.17 (16 keV). The reduction of events in the backscatter tail of e-gun electrons is evident, which also has a different shape with a stronger curvature. As mentioned above, the mean fraction of events in the backscatter tail over all wall electron with B-field data is $32.88 \pm 0.94\%$. For the e-gun data the fraction is $22.53 \pm 11.79\%$. The large error in the latter is caused by the strong variation of the fraction due to the beam spot position dependency. In the 16 keV data (figure 11.17) the e-gun data additionally features a broader peak. At this point it is not clear, if these differences are due to the changed configuration of the magnetic and electric fields, or are related to effects from the beam spot size. The broadened peak in the 16 keV data could also be due to an increased noise level, reducing the resolution of the detector.

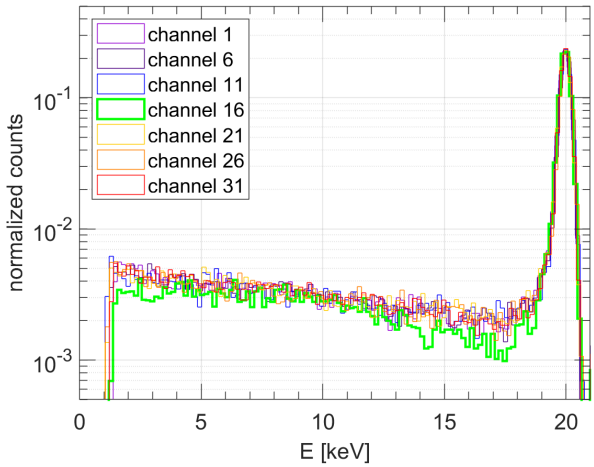

Figure 11.14: Here the response for 20 keV wall electrons with magnetic field in each pixel are shown. The green spectrum (channel 16) corresponds to the central pixel. The shape of the response of the central pixel deviates from the spectra measured in the edge pixels, which are all similar. The backscatter-tail in the central pixel is more curved and contains in total less events. Since it is completely surrounded by other pixels, backscattered and backreflected events are removed by the multiplicity cut, which is not possible for many events in the edge pixels. If no multiplicity cut is applied, the spectral shape of the central pixel is similar to the one in the edge pixels (see 11.15).

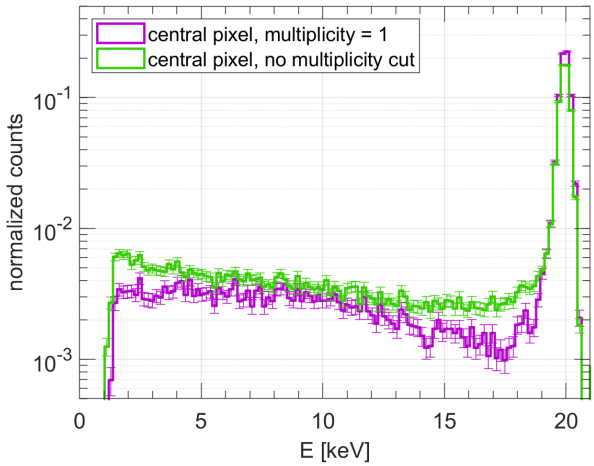

Figure 11.15: A comparison of the spectrum for 20 keV wall electrons with magnetic field in the central pixel with and without multiplicity cut. Without the cut, events that have a coincidence in one of the edge pixels are not removed. As expected the cut removes events that deposited not their full energy and changes the shape and height of the backscatter tail.

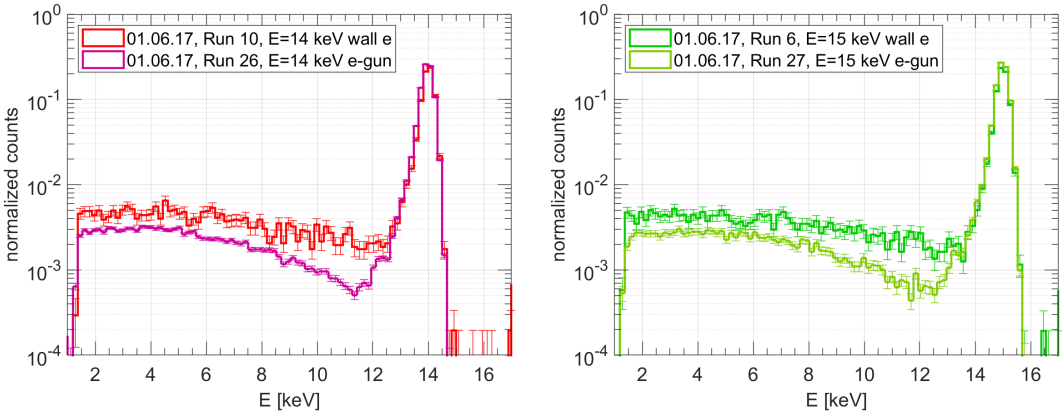

Figure 11.16: Comparison of e-gun data with wall electron measurements with active detector magnet for 14 and 15 keV electrons. In the e-gun response the back-scatter tail contains less events and its shape shows a stronger curvature.

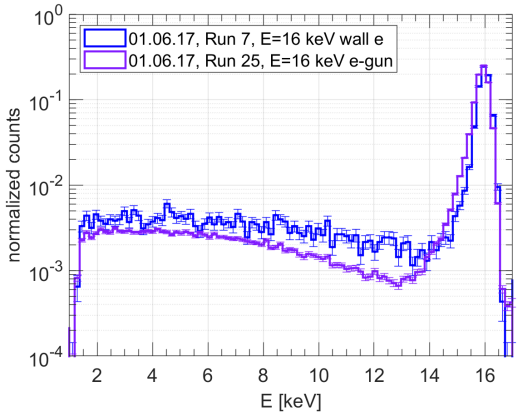

Figure 11.17: Comparison of e-gun data with wall electron measurements with active detector magnet for 16 keV. The backscatter tail in the e-gun response contains less events and the peak is broadened on the low energy side.

11.1.4 Measurements with the gaseous tritium source

In figure 11.18 the spectra taken from the gaseous tritium source are shown. Also here the two distinct parts of the response - the peak and the backscatter tail - are clearly visible, where the peak is replaced by a differential tritium spectrum above the high voltage threshold. The data at 13 kV retarding potential contains more than 700 000 events and is later analyzed for a pilot sterile neutrino search (see section 11.3). The data taken at other retarding potentials has much less statistics ($\sim$ 10 000 events). With a scan of the spectrum across different retarding potentials in principle an integral spectrum can be constructed, as it is done for the KATRIN and original Troitsk ν-mass measurements. However, this requires well defined times for each measurement, frequent measurements of the column density with the e-gun, and letting the high voltage alternate quickly ($\sim$ 2 minutes per high voltage value) to level out the effects of fluctuations of the source density and rate, and of course high statistics. None of these requirements were fulfilled for the high voltage scan shown here.
By subtracting two spectra that were taken at different retarding potentials that ideally are very close to each other, a quasi-monoenergetic response can be obtained. This is demonstrated in figure 11.19. Here both spectra were normalized such that the number of events between 16 and 16.3 keV match. This could be used to study the mono-energetic energy response of electrons form the tritium source, but fails here due to low statistics and the arbitrary normalization. To properly employ this technique, the same requirements as for the integral spectrum scan have to be fulfilled as mentioned above.

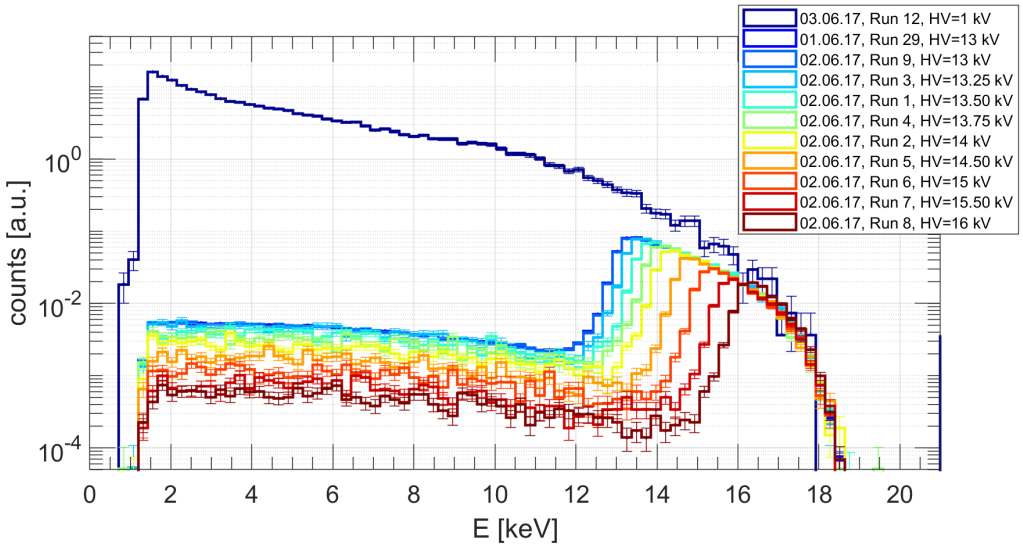

Figure 11.18: The spectra of the tritium measurements with different retarding potentials (HV). Each spectrum is made of two distinct parts: a differential tritium spectrum above the high voltage threshold, and a backscatter tail below the threshold. The histograms are scaled such that they match between 16 and 16.3 keV. The data at 13 kV has the most events ($>$ 700 000 events combined), other data much less ($\sim$ 10 000 events, see table 11.2). One dataset was taken with 1 kV retarding potential.

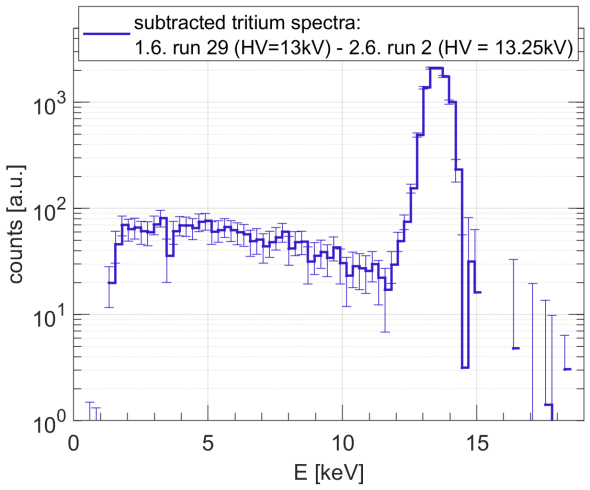

Figure 11.19: By subtracting two tritium spectra with different retarding potentials from each other, a mono-energetic energy response can be obtained. Here it is important that the spectra were taken for the same time to achieve a correct normalization. For this plot the spectra were just scaled such that they match between 16 and 16.3 keV and then subtracted. This approach fails already due to the low statistics in every dataset except for 13 kV-measurements. On the other hand, the resulting spectrum shows a similar shape as other monoenergetic data.

11.2 Coincident events and charge sharing

Charge sharing of the TRISTAN SSDs was studied already with X-rays (see section 10.3). Here the study is repeated with electron data from Troitsk. Electron data might show a different charge sharing probability than X-ray data, because electrons have much shorter interaction lengths in the silicon detector than X-rays (see section A in the annex) and thus the collection time of the charge can be different. This changes the spread of the charge cloud due to diffusion and affects the charge sharing probability. At Troitsk, charge sharing is not distinguishable from backscattering / backreflection when the magnets are turned on, since both effects produce coincident events, where the sum of both measured energies equals the initial energy. The only suitable data to estimate the charge sharing probability are then the wall electron measurements with turned off magnets. These measurements are runs 16 to 20 from 3.6.2017 (see table 11.2). Run 2 to 4 from 1.6.2017 can not be used because the threshold was set too high. Plots of the coincident events, where the x-axis marks the energy deposited in the central pixel and the y-axis the energy detected by the neighbors, are displayed in figure 11.20 for data with both the magnets turned off and on. In both measurements the retarding potential was set to 20 kV. The diagonal bands caused by charge sharing (and backscattering plus backreflection), where the sum of energies equals the full energy of the electrons, are clearly visible. The diagonal band in the left plot from the data without magnetic field is broadened due to the “bump” below the main peak (see figure 11.10). The data with the magnets turned on was taken at a much higher rate than the data without magnetic field (see again table 11.2), resulting in pile-up that is showing as vertical and horizontal bands in the plot.

The estimation of the charge sharing probability was done similarly as for the X-ray data. In table 11.4 the probabilities are listed for the electron data. In addition the probability of coincident events for data, where the B-field was turned on, are

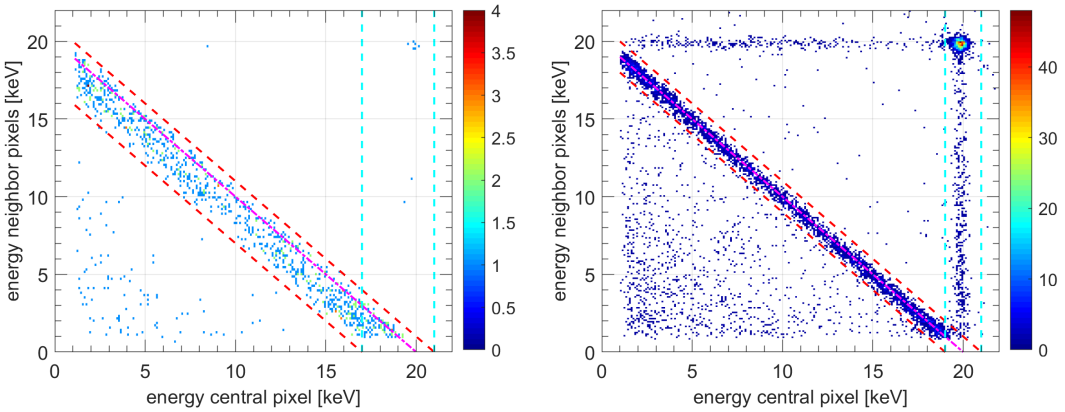

Figure 11.20: Left: The energy of coincident events in the central pixel (x-axis) and in the neighbors (y-axis) for wall electron data with the magnets turned off. **Right:** coincident events from wall electrons with the magnets turned on. The rate was much higher than for the data without magnetic field, resulting in horizontal and vertical lines and a spot at (20,20), where two full energy events were detected at the same time, all due to pile-up. The red dashed lines marks the interval, from which the events were taken for the analysis of the charge sharing probability. The cyan dashed lines mark the band, where pile-up is expected.

energy [keV]	threshold [keV]	charge sharing probability (data without B-field)	data with B-field
15	1.4	$(9.3 \pm 0.2)\%$	$(10.1 \pm 0.4)\%$
18	1.4	$(10.7 \pm 0.7)\%$	$(10.8 \pm 0.4)\%$
19	1.4	$(11.0 \pm 0.6)\%$	–
20	1.4	$(10.3 \pm 0.5)\%$	$(11.1 \pm 0.3)\%$

Table 11.4: The charge sharing probability of electron events for the 1 mm-detector I-11 with a threshold of 1.14 keV for different energies is listed in the second column. The third column shows the fraction of events in the diagonal band in data with turned on magnetic field. Thus here also backscattered and backreflected electrons are included. The increase of coincident event in the third column is small, the probability of a backscattered electron being detected on a neighboring pixel is low.

listed in the last column. The increase with respect to the charge sharing probability is low. From this we can conclude that a back-scattered electron is only rarely backreflected onto a neighboring pixel and charge sharing is the dominant reason for coincident events. While the charge sharing probability is around 10 %, the probability for a backreflection-coincidence is only $\sim 1\%$.
In table 11.5 the charge sharing probabilities of electron events is compared to the X-ray data. For this both data was processed with a 3 keV software threshold, thus the values are lower than in table 11.4. The electron data of each energy was matched with X-ray data from the closest peak of the americium spectrum. No significant difference was found. One can conclude that the behavior of charge sharing is not different for electrons and X-rays in the energy region of interest for TRISTAN.

electron energy [keV]	X-ray energy [keV]	electron charge sharing	X-ray charge sharing
15	14	$(5.4 \pm 0.2)\%$	$(5.5 \pm 0.2)\%$
18	17	$(6.5 \pm 0.5)\%$	$(6.0 \pm 0.2)\%$
19	–	$(6.9 \pm 0.4)\%$	–
20	21	$(6.9 \pm 0.4)\%$	$(6.7 \pm 0.5)\%$

Table 11.5: The charge sharing probability for electron data is compared with the X-ray data from detector I-11. Both data were processed with a 3 keV software threshold. Each electron energy was matched with the closest X-ray peak from the americium spectrum. There is no difference in the charge sharing probabilities for X-ray and electron data.

11.3 Pilot search for sterile neutrinos with the Troitsk Data

In the following section the analysis of a differential tritium spectrum to search for a sterile neutrino is described. The tritium spectrum to be analyzed was taken with a retarding potential of 13 kV. A histogram of this data is shown in figure 11.21. The data consists of two combined measurements (Run 010617 29 and 020617 9, see tables 11.1 and 11.2). In total there are 728 042 events in the central pixel. The first measurement was started at 1st of June 2017, running over night for 14.4 h. The average rate was 10.6 cps (see figure 11.22), 551 113 events were detected. The second measurement with 176 929 events was taken at 2nd of June for 10.7 h over night at a rate of 4.6 cps. Here the rate was strongly decreasing due to the tritium being removed from the source, as shown in figure 11.22. Only data of the central pixel was used and events with multiplicities > 1 were excluded.
The analysis was conducted not in a serious attempt for a sterile neutrino search, but rather as a study to develop and test analysis techniques, find out about difficulties in the analysis and how they can be avoided. In the end we can draw conclusion for future measurements, which are valuable information for the TRISTAN project, since a differential analysis of a spectrum taken with a MAC-E type spectrometer has not been done before.

11.3.1 Analysis approach for fitting the tritium spectrum

The observed tritium spectrum (figure 11.21) is a convolution of a theoretical tritium spectrum with the system's energy response. For an analysis of this spectrum and a sterile neutrino search it is therefore necessary to know the energy response. In principle it can be obtained through different ways:

1) measurement of the response of electrons from the tritium source by taking tritium spectra at different retarding potentials and subtracting them from each other. This will result in a quasi-monoenergetic response (see section 11.1.4). However, the subtracted spectra were taken at different retarding potentials, changing the contribution of many effects:
   - the spectra contain different amounts of electrons that lost energy in the source and still could pass the retarding potential;
   - for a certain energy, the electrons in the spectra that should be subtracted have different surplus energies. This changes the backreflection of electrons after they were backscattered on the detector and could also have an impact on the adiabatic transport, if the surplus energy is sufficiently high.

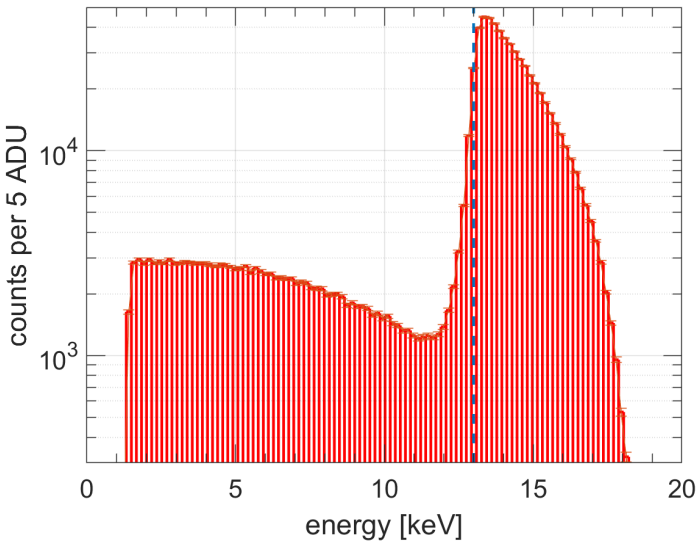

Figure 11.21: The observed tritium spectrum. The high voltage of the retarding potential was set to 13 kV (dashed line). Events below this threshold are due to partial energy deposition from backscattered and backreflected electrons. There are 728 042 events in the central pixel, the native bin-width is about ~ 30 eV, and 5 ADU are about 150 eV.

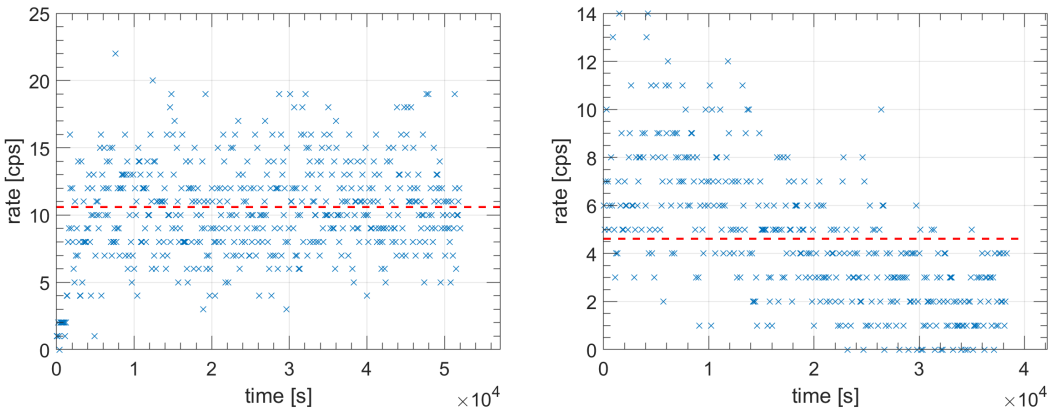

Figure 11.22: The rate during both analyzed tritium measurements: **Left:** run 29 on 01.06.2017. **Right:** run 9 on 02.06.2017. For better visibility the bin counts are converted into x-markers and only every 100th marker is shown. It is clearly visible that the rate during the second measurement is dropping due to the tritium getting removed from the source. The dashed line shows the average rate.

This approach requires a scan of the tritium spectrum in small high voltage steps and high statistics. During our measurement campaign we did not take enough data at retarding potentials other than 13 kV thus this approach was not used.

2) Measurement of the energy response of electrons from the e-gun. The response then includes source effects like scattering and trapping, however these electrons have to cross a larger source than the average tritium electron and also move with a different angular distribution. The analysis of the e-gun electrons was hindered by the beam-spot effects as mentioned in section 11.1.2. Depending on the position of the beam spot on the detector, a differently shaped spectrum was obtained.

3) Measurement of the response of electrons from the spectrometer walls. The wall electrons isotropically illuminate the detector and have a broad angular distribution (see section 11.1.3). In comparison to electrons emitted from the gaseous tritium source, following differences have to be taken into account:

   – WGTS effects (scattering and trapping of electrons in the source gas) are not included in the response;
   – backreflection: during the measurements with the wall electrons all backscattered electrons are subsequently reflected on the retarding potential (if they were not reflected before on the field of the detector magnet) and return to the detection plane. There they are either lost or hit the detector within the integration time of the first event. Further backscattering and backreflection can occur. Backscattered electrons during measurements with the tritium source could again pass the retarding potential, if they didn't lose too much energy and then get lost in the source, or get reflected by the pinch magnetic field. In conclusion, the shape of the response will be affected.
   – the magnetic field configuration is changed, leading to the aforementioned backreflection differences, but also changes the gyro-radius of the electrons at the detector, resulting in a different acceptance.

4) Simulation of the energy response. By simulations one can produce spectra of monoenergetic electrons that have the same conditions as the tritium electrons. However, many parameters needed as input for the simulations, for example the angular distribution of the electrons, the column density of the source or the detector dead layer thickness are not known to full extend and the simulation will have uncertainties.

Method 1) - the subtraction of tritium spectra - could not be used due to a lack of data with sufficient high statistics. Approach 2) - the e-gun measurement - was not pursued due to the beam spot effects. The most suitable analysis technique is using the energy response of wall electrons. Simulations are included to validate the results, but a full simulation of the system is not done as it would require a long computing time and still have many uncertainties. A list of the response data finally used is presented in table 11.6.

The starting assumption of the analysis is that the wall energy response and tritium energy response have the same general shape. Effects from the source, which are trapping and scattering of electrons and are not included in the measured response, can be added separately. How they change the observed spectrum can be simulated and then included in the model. As a consequence the only effects that are missing in the

response are related to the different field configuration, which affects the backreflection of backscattered electrons. The response function will be included with free parameters in the fit that can adjust the shape for these differences. The description of the energy response as a function with free parameters is achieved by parametrizing the measured wall electron data. Therefore a model for the response has to be found which is then fitted to the measured data. In the end a 2-dimensional function - the transfer function - is obtained. With this transfer function an energy response for any initial electron energy can be produced. How this parametrization is done is demonstrated in section 11.3.3.

A simple test before fitting the tritium spectrum is to convolve the measured wall energy response with a tritium model and then to see to which extent the result matches the observed spectrum. Since the response was measured only for 7 different energies, these data are interpolated to achieve a finer binning - a transfer matrix. This is described in section 11.3.2.

In summary, the general analysis approach for fitting the tritium spectrum is:

- obtain the energy response as a transfer function (2-dimensional function with the energy distribution for different initial energies). The shape of this function is described by parameters that are left free in the tritium fit;
- generate a theoretical tritium spectrum and modify it with WGTS effects;
- the function to describe the observed spectrum is the convolution of the transfer matrix with the spectrum model. This function is then fitted to the observed spectrum with following free parameters:
  - parameters from the transfer function. If a parameter was measured independently, it can be constrained with pull terms that also include the covariance of the parameters;
  - normalization and full-width-of-half-maximum (detector noise / resolution);
  - calibration parameters. The previous calibration of the data might not be accurate;
  - parameters that modify the shape of the source spectrum to account for uncertainties of the source effect simulations;
  - sterile neutrino parameters: by default these parameters are not included, but are necessary to conduct sensitivity studies;
- in a last step, the parameters found by fitting the observed spectrum have to be tested for plausibility and are cross-checked through simulations.

11.3.2 Interpolation of the response data

As a test the measured energy response of wall electrons is convolved with a theoretical tritium model. If the resulting spectrum matches the observed spectrum it can be concluded that the wall response is similar to the energy response of tritium electrons. Wall electron measurements were only done for 7 different energies. To improve the binning, these data were interpolated to obtain the transfer matrix.
The data were interpolated in a radial way: the interpolated number of electrons at

date	run №	retarding pot. voltage [kV]	fitted mean energy [keV]	fitted fwhm [keV]	enc [e$^-$]	# events
01.06.17	6	15	15.02±0.00	0.44±0.01	46.74	10 388
01.06.17	7	16	16.01±0.01	0.44±0.02	45.98	13 856
01.06.17	8	17	17.00±0.00	0.41±0.02	41.36	10 099
01.06.17	9	18	17.96±0.01	0.50±0.02	52.68	10 740
01.06.17	10	14	14.03±0.00	0.42±0.02	44.29	10 243
01.06.17	11	13	13.03±0.01	0.46±0.03	49.72	4 044
03.06.17	15	20	19.99±0.00	0.44±0.01	44.87	24 522

Table 11.6: Parameters of the wall electron data for the central pixel. These data are used to interpolate and parametrize the transfer matrix / function.

energy E_i for the response of electrons with an initial energy $E_{\mathrm{in},n}$ between two measured initial energies $E_{\mathrm{in},n-1}$ and $E_{\mathrm{in},n+1}$ - the neighboring data - was calculated from the weighted average of the neighboring data on a line that crosses the origin and E_i. Since this line usually doesn't pass through the bin centers in the neighboring data, a weighted average of the adjacent bins was taken. Instead of reading the following description of the interpolation process, the reader is advised to look at figure 11.23, where the interpolation is comprehensively illustrated. In summary, the interpolated number of events in bin E_i for energy $E_{\mathrm{in},n}$ is:

$$\begin{aligned} N(E_i, E_{\mathrm{in},n}) = 0.5 \cdot [&N(E_i + \tan\theta \cdot (E_{\mathrm{in},n} - E_{\mathrm{in},n-1}), E_{\mathrm{in},n-1}) + \\ &N(E_i + \tan\theta \cdot (E_{\mathrm{in},n} - E_{\mathrm{in},n+1}), E_{\mathrm{in},n+1})], \end{aligned} \tag{11.2}$$

where $\theta = \arctan(E_i/E_{\mathrm{in},n})$ is the angle of the radial interpolation line. As mentioned above, $E_i + \tan\theta \cdot (E_{\mathrm{in},n} - E_{\mathrm{in},n-1})$ is usually between two bins, such that here an average is taken. We assume here that the radial line passes somewhere through bin E_j for the data of $E_{\mathrm{in},n-1}$ and that the distance from the bin center to the next higher bin E_{j+1} is x bins ($0 < x < 1$), whilst the distance to the next lower bin E_{j-1} is $1 - x$ bins, and let $x < 0.5$. That means the line passes bin E_j closer to bin E_{j+1}, such that the desired number of counts we use for the calculation is not $N(E_j, E_{\mathrm{in},n-1})$, but an average of $N(E_j, E_{\mathrm{in},n-1})$ and $N(E_{j+1}, E_{\mathrm{in},n-1})$, weighted by the distance x:

$$\begin{aligned} N(E_i + \tan\theta \cdot (E_{\mathrm{in},n} - E_{\mathrm{in},n-1}), E_{\mathrm{in},n-1}) = &(0.5 + x) \cdot N(E_j, E_{\mathrm{in},n-1}) + \\ &(0.5 - x) \cdot N(E_{j+1}, E_{\mathrm{in},n-1}) \end{aligned} \tag{11.3}$$

If the line cuts through the bin closer to the next lower bin, the average can be calculated in a similar way. The error of the interpolated bin is also interpolated in the same way from the statistical error of the data. The interpolation can be iterated several times to achieve a finer binning of $E_{\mathrm{in},n}$. The original data and the result of the interpolation are shown in figure 11.24. Since there are no adjustable response parameters a fit to the tritium spectrum returns no good results. However, by simply constructing the spectrum by folding the interpolated matrix with a tritium model and comparing with the data, as shown in figure 11.25, we see that the general trend is accurately depicted, but there seem to be less events in the tail below the high voltage threshold in the observed spectrum (different backreflection) and above the threshold it has a different decline. This makes it clear that a fit has to take additional effects into account that are not included in the transfer matrix from the wall response.

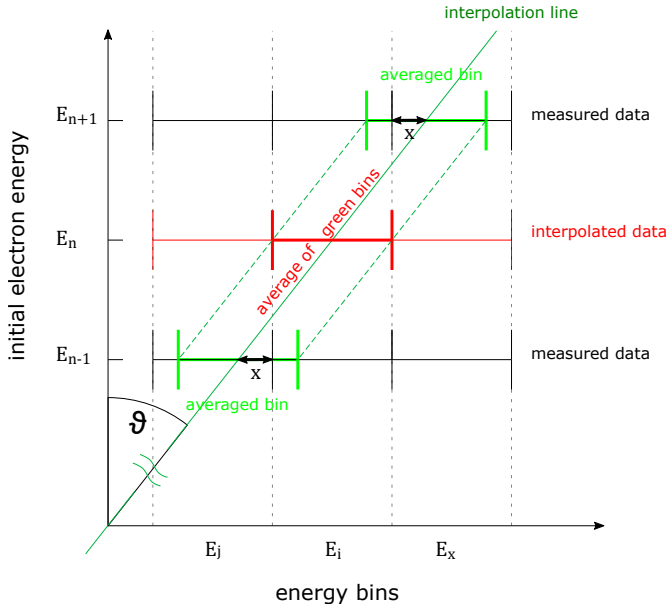

Figure 11.23: A visualization of the interpolation process. A line that crosses the energy bin which should be interpolated and the coordinate origin is drawn - the interpolation line. This radial interpolation is necessary to obtain an interpolated peak at the proper initial energy value. The interpolated bin (red bin) is an average of both green bins. These bins are generated as an weighted average of two adjacent bins in the measured data, since the interpolation line does not crosses the bin center.

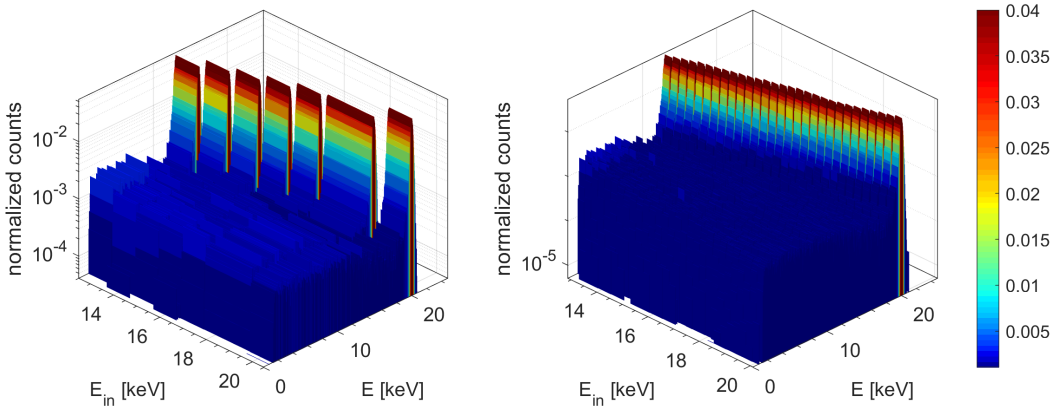

Figure 11.24: Left: the original data. Right: the interpolated transfer matrix after three iterations, resulting in a bin width for E_{in} of 0.25 keV.

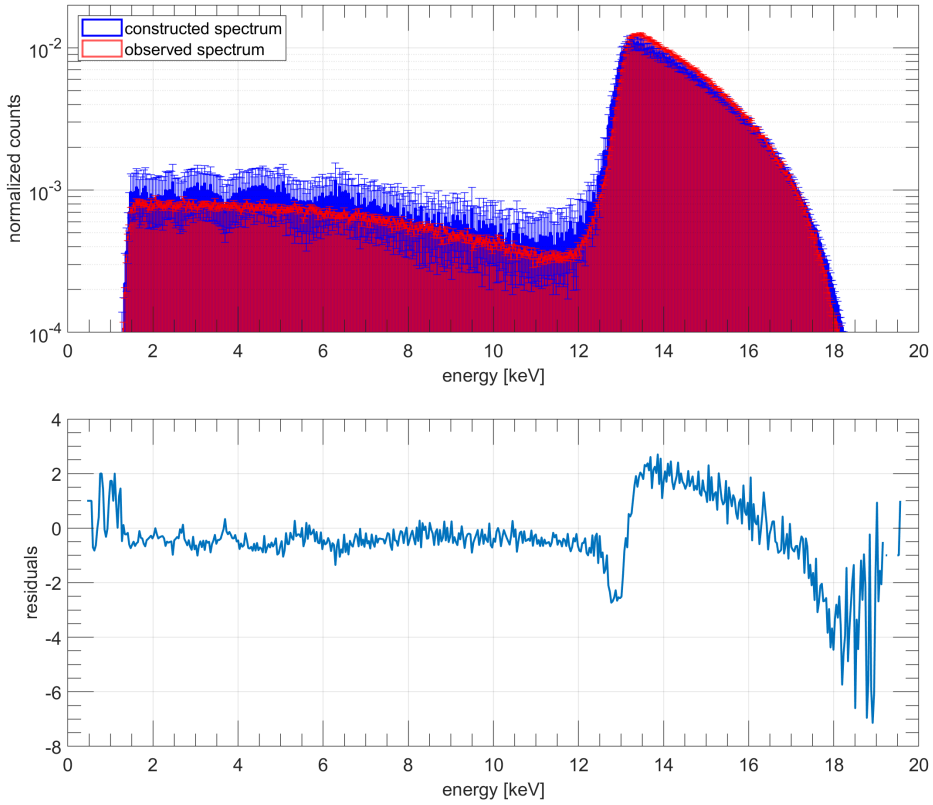

Figure 11.25: In the top plot the normalized observed spectrum and a spectrum constructed by folding the interpolated transfer matrix (3 iterations, 0.25 eV bin width for the initial energy) with a tritium model are shown in comparison. The residuals are shown in the bottom plot. A reduced number of events below the high voltage threshold in the data is visible as well as a different decline of the spectrum above the threshold.

11.3.3 Parametrization of the response data

In order to fit the tritium spectrum, the transfer function that describes the energy response for any initial electron energy has to be constructed. It is created by fitting a model to the measured spectra of monoenergetic wall electrons. Following function with 8 parameters (plus the energy dependence) describes the shape of the spectrum:

$$\begin{aligned} f_{\text{response}}(\sigma, n_1, n_2, n_3, \beta, b, c, E_{\text{in}}, E) = n_1 \cdot \exp\left(-0.5 \cdot \left(\frac{E - E_{\text{in}}}{\sigma}\right)^2\right) + \\ n_1 \cdot n_2 \cdot \exp\left(\frac{E - E_{\text{in}}}{\beta}\right) \cdot \operatorname{erfc}\left(\frac{E - E_{\text{in}}}{\sqrt{2} \cdot \sigma} + \frac{\sigma}{\sqrt{2} \cdot \beta}\right) + \\ \left| n_1 \cdot n_3 \cdot \left(\frac{E+1}{E_{\text{in}}}\right)^b \cdot \left(1 - \frac{E}{E_{\text{in}}}\right)^c \cdot \Theta(E_{\text{in}} - E) \right|. \end{aligned} \tag{11.4}$$

Here E is the energy of the response spectrum, E_{in} the initial energy of the electrons (i.e. the mean of the peak). The first term is a Gaussian peak with the standard deviation σ and with the normalization constant n_1. The second term is an exponential tail on the low-energy side of the Gaussian peak, defined by the parameters n_2 (height) and β (slope of the tail). The last term describes the so-called back-scatter tail, a plateau that extends to low energies. The height of this plateau is described by n_3 and the shape by b (increase at low energies) and c (decrease at high energies). One considers the absolute value of this term to keep it non-imaginary during the fitting. The Heaviside step function Θ sets the term for energies above E_{in} to be zero instead of negative.

All seven data sets were fitted simultaneously, while most parameters were treated as a linear function of the initial electron energy (e.g. $n_2 = n_{2,\text{offset}} + n_{2,\text{slope}} \cdot E_{\text{in}}$). The parameters not fitted in this way are:

- normalization: individual parameter for each data set. Adds 7 parameters;
- σ: individual parameter for each data set. Adds 7 parameters;
- E_{in} was not fitted since the set high voltage value is accurate.

In addition the calibration was left free, i.e. the variable E was modified with two parameters: $E' = \text{offset} + \text{gain} \cdot E$. The approach to recalibrate the response function instead of the data is valid, as long as the other parameters are fitted as a function of the real energy (there is no uncertainty assumed on the value of the high voltage) and is much more efficient than to recalibrate the data in the fit since this would require a dynamic binning. The calibration would add 14 parameters. However, best results were obtained when the calibration gain was fixed to 1 and only fitting an energy offset, thus only 7 more parameters need to be fitted. In total the fit contains 31 parameters: 10 parameters to describe the shape, and 7 each for the normalization, resolution and calibration.

In a previous fit the σ and shifts of the peak position (an inaccuracy of the calibration) were obtained (see table 11.6), serving as starting parameters for the fit. As several of the bins contain less than 5 events, a maximum-likelihood function χ^2_{p} that takes the poissonian distribution of the events in each bin into account was minimized (see for example [Cow98]):

$$\chi^2_{\text{p}} = -2 \cdot \sum_i \left(n_i - \nu_i + n_i \cdot \log\left(\frac{\nu_i}{n_i}\right)\right). \tag{11.5}$$

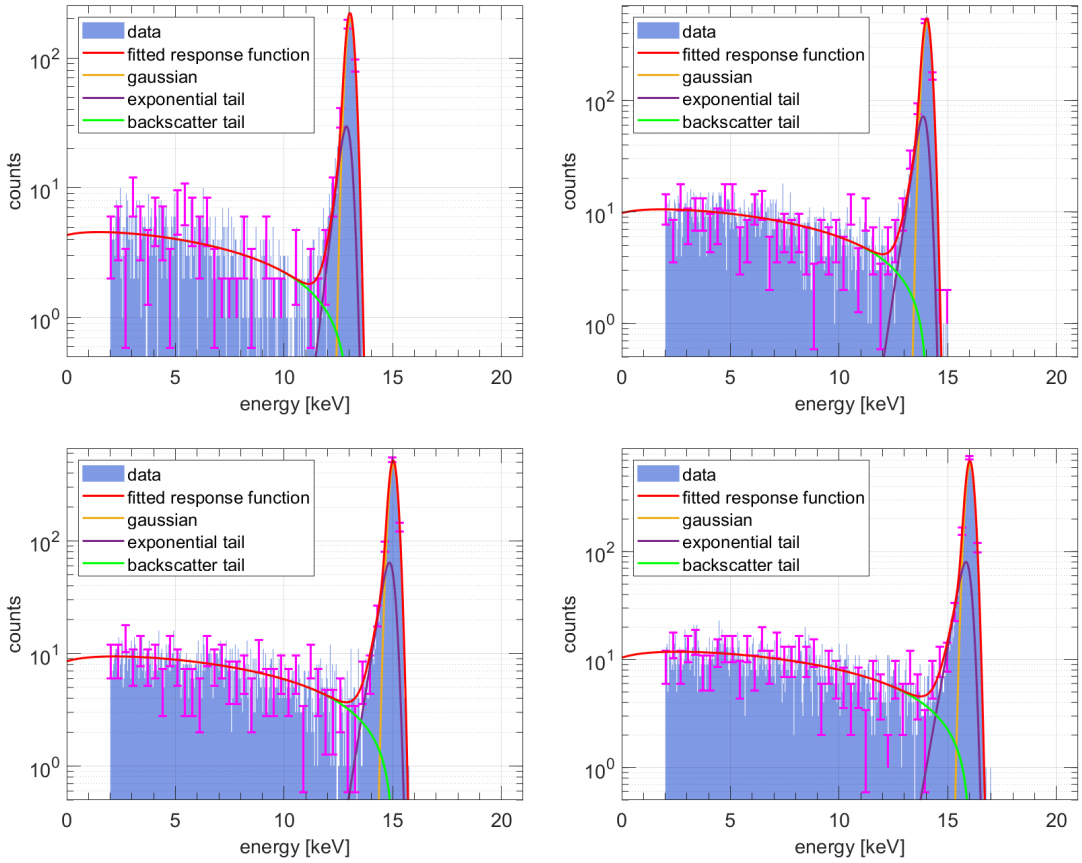

Figure 11.26: The fitted energy response for initial energies of 13, 14, 15 and 16 keV. The different components of the function are shown. All these data, including the data in figure 11.27, were fitted simultaneously.

Here n_i is the number of observed counts in bin i and ν_i the number of expected counts, i.e. $f_{\text{response}}(..., E_i)$, where i runs over non-empty bins. For the minimization an iterative approach was chosen to make the handling of this amount of parameters easier. In a first step the σ-parameters were fixed. The resulting best fit-parameters were used for a second step, where the calibration parameters were fixed. This was repeated 5 times. For more iterations an improvement of the χ^2_{p} was not observed. In a final fit all parameters were left free. The fit was executed with Minuit [Jam94]. The results of the fit are shown in figures 11.26 and 11.27. The resulting poissonian chi-squared is

$$\chi^2_{\text{p}}/\text{ndof} = 1.089 \ (\text{ndof} = 2969).$$

The correlation matrix of the fitted parameters is shown in figure 11.28. The correlation of the normalization-, σ- and calibration parameters are not included because they are all independent and also not relevant for the further analysis. The function with the best fit parameters, i.e. the transfer function, is shown in figure 11.29. The parameter values and their errors are tabulated in the appendix in table C.1.

11.3.4 Events below the threshold

In the figures 11.26 and 11.27 it can be seen that the fitted function extends down to 0 keV, while the data is cut at 2 keV. The actual threshold is below this value, but

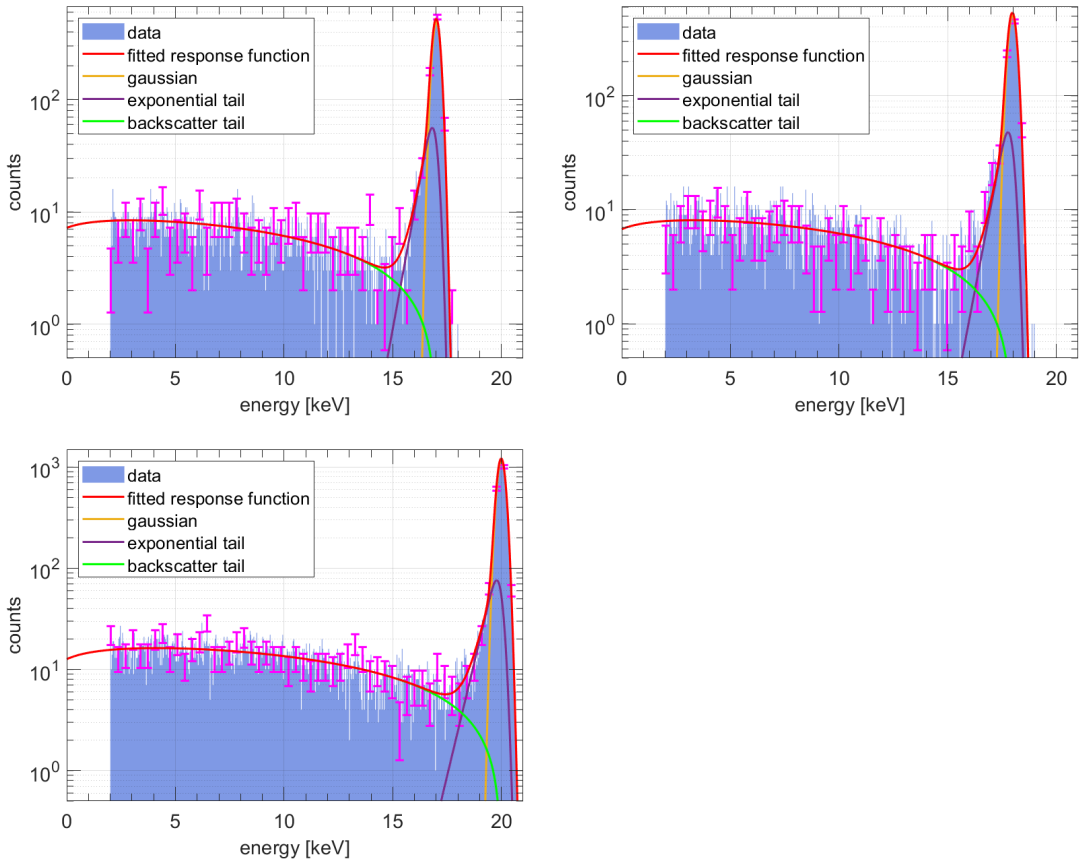

Figure 11.27: The fitted energy response for initial energies of 17, 18 and 20 keV.

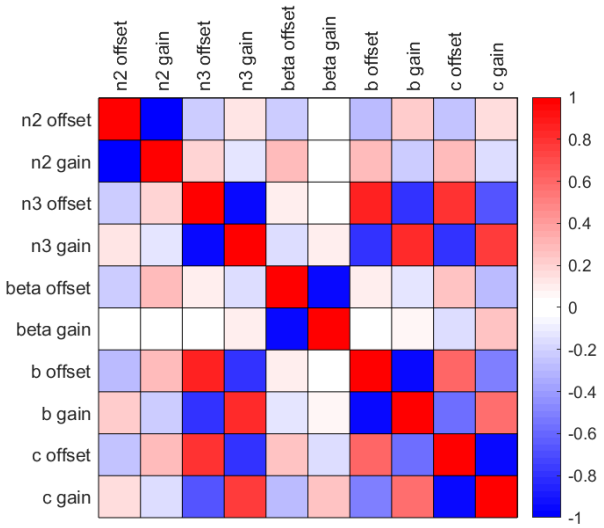

Figure 11.28: The correlation matrix of the fitted parameters. The uncorrelated normalization, resolution and calibration parameters are not included. The shape of the response is described by 5 parameters, which were fitted each as linear function of two parameters gain and offset. The two parameters in each of these pairs are as expected anti-correlated.

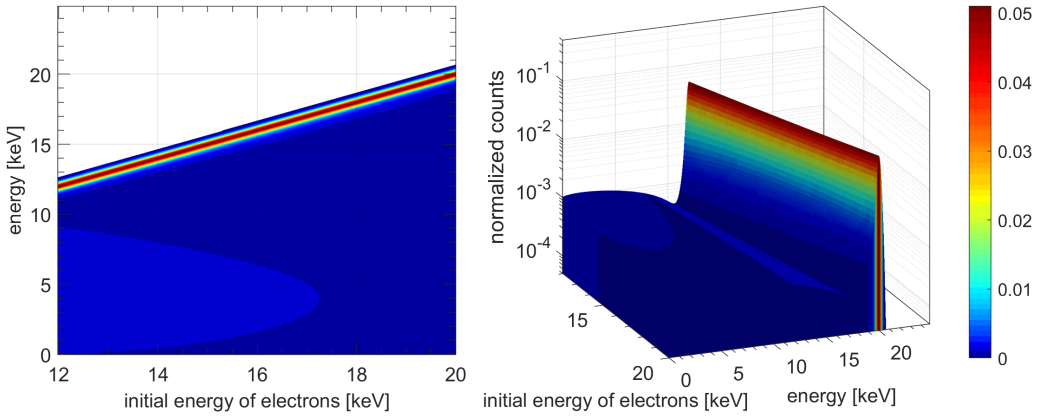

Figure 11.29: The transfer function in a 2-dimensional (left) and 3-dimensional view (right), i.e. the result of fitting the wall electrons response. This function describes the spectrum for any initial electron energy.

in order to achieve a clear cut a software threshold was set at 2 keV. The proper fit function for the tritium spectrum is a convolution of the normalized transfer matrix with the tritium matrix, where the normalization of the transfer matrix has to take into account events below the threshold. The chosen response function models the events below the threshold as a flat extension of the backscatter tail. Regarding the detector response this assumption can be justified through simulations as shown in section 11.4 and e.g. plot 11.41, where the flat plateau at low energies is visible. In addition to the detector response, it also has to be considered how effects from the tritium source as electron trapping and scattering affect the distribution below the threshold (see next section). These effects were simulated by the Troitsk-team and published in [ABB+11] as well as by the SSC-sterile group [Lok18]. Both simulations showed that the energy loss distribution is flat at high values (large losses) and thus justify the model.

11.3.5 The tritium spectrum model and parametrization of source effects

The model tritium spectrum $f_{\text{tritium model}}(m, \sin^2\theta, E)$ is a function of sterile neutrino mass m and mixing angle $\sin^2\theta$. The model used for this analysis was written by Thierry Lasserre [Las18]. It is calculated according to the Fermi theory (see for example [Kra87]) and then modified with the analytical non-relativistic Fermi function. Other corrections as excited states, radiative corrections, etc. are neglected since they are much smaller than other uncertainties of this analysis. However, the electron spectrum emitted from the Troitsk tritium source is not entirely described by the theoretical spectrum, because it is modified by additional source related effects that are not included in the transfer matrix and have to be added here. These effects are mainly scattering of electrons with molecules in the gaseous source and the trapping of electrons, both leading to an energy loss. In case of the trapping effect, electrons that move with certain angles with respect to the field lines are trapped within the source section, which is a magnetic bottle. As these trapped electrons remain a relatively long time in the source section, they can lose a large fraction of their energy through scattering. Eventually also their angle changes such that they can leave the source section. Instead of adding the trapping effect as an additional electron source, we can model the energy distribution of electrons which leave the source as a modified tritium spectrum, which takes both scattering and trapping into account. How the spectrum is

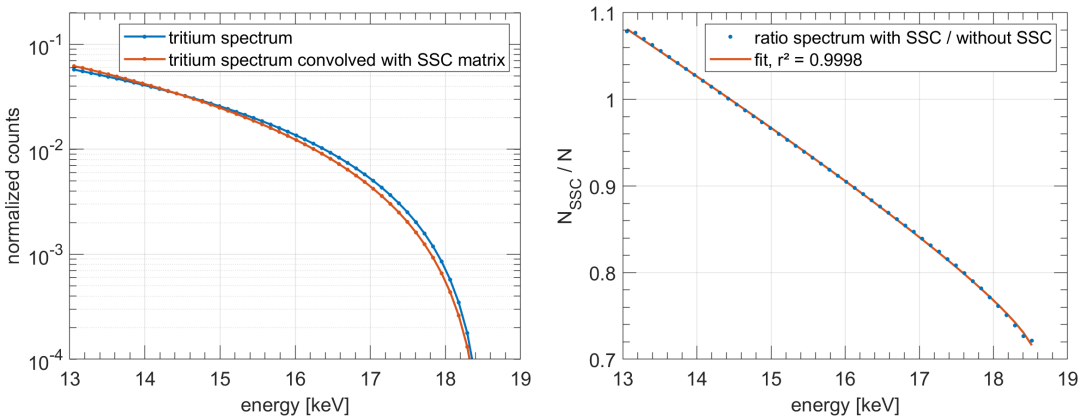

Figure 11.30: Left: the tritium spectrum without any modification (blue) and after the convolution with the SSC matrix (orange) that adds effects like scattering in the source and trapped electrons. **Right:** the ratio of both spectra and the fit, i.e. the SSC shape factor.

affected can be studied through simulations, as it was done by the SSC sterile project [Lok18]. The result of the SSC sterile simulations describes the distribution of lost energy for electrons with certain initial energies, expressed by a matrix (SSC matrix). The simulations produced data with 50×50 bins from 13 to 18.575 keV (the energy range of interest). There are several approaches as how to introduce the simulation results into the tritium model for the fit of the spectrum:

1) include the energy loss matrix as it is and conduct the fit in the same binning as the simulation;

2) parametrize the SSC matrix to obtain a continuous 2-dimensional function similar to the transfer function for energy response;

3) parametrize the effective shape factor, which is imposed on the tritium spectrum after convolving it with the SSC matrix.

Method 1) is not suitable because it results in large binning effects in the data and does not allow to vary parameters of the SSC response during the fit. The simulated energy loss is expected to have uncertainties, therefore we want to include free parameters. Method 2) is also not favorable since it requires a 2-dimensional distribution fit with a lot of free parameters similar to the energy response parameterization (see section 11.3.3). Approach 3) is the most feasible: the unmodified tritium spectrum and the spectrum after convolution with the SSC matrix are show in figure 11.30 on the left. Here it becomes clear that the scattering and trapping of electrons in the source effectively redistribute events from higher to lower energies, as expected. The ratio of both spectra, i.e. the shape factor resulting from the source effects, is shown in figure 11.30 on the right and can be described by a function with three parameters:

$$f_{\text{SSC shape factor}}(a, b, c, E) = a \cdot (Q - E) + b \cdot \sqrt{Q - E} + c, \tag{11.6}$$

where a, b, c are the free parameters and Q is the spectral endpoint (upper edge of last bin at 18.575 keV). This function describes accurately the simulated data with a coefficient of determination $R^2 = 0.9998$. The found parameters are:

parameter	value
a	0.0458 ± 0.0014
b	0.0545 ± 0.0040
c	0.7005 ± 0.0027

The fitted shape factor is also shown in figure 11.30 on the right. In summary, the source effects are included in the fit of the observed tritium spectrum by multiplying this shape factor with the theoretical tritium spectrum. The three parameters that describe the shape factor will be left free such that uncertainties of the SSC simulation can be compensated for. In the following the shape factor will be called "SSC shape factor".

11.3.6 Residual tritium from the rear wall

Background has to be subtracted from the observed spectrum. A measurement with the valve that separated the source section and the spectrometer closed showed a negligible background. A measurement with the source section opened, but not containing any gas, was at this time not possible. However, measurements from the third measurement campaign at Troitsk with a different TRISTAN prototype-detector ("Troitsk-III") with an empty source show clearly background electrons that have a distribution resembling a tritium spectrum. They originate from residual tritium that is stuck to the rear wall of the source section. The electrons lose energy while escaping from the wall, such that the observed spectrum is different from the one of the gaseous tritium. In principle such a background should be subtracted or included into the fit model. Since no empty-source measurement was performed during the measurement campaign presented here, we have to extrapolate the effect from the Troitsk-III data. According to the Russian research team, the residual tritium rate does not change much also on a time scale of a year [Pan].

The rates in Troitsk-I and Troitsk-III cannot be directly compared, as the detector that was used during Troitsk-III is larger (2 mm pixel diameter instead of 1 mm) and was located closer to the detector magnet (~ 1 T instead of ~ 0.2 T), resulting in an overall higher flux. Since the detector size is increased by a factor 4 and the magnetic field by a factor 5, we expect the rate in Troitsk-III to be 20 times higher than in Troitsk-I. Nonetheless, the assumed magnetic field strength might be inaccurate as the detector position is known only with limited accuracy. Also, the changed read-out system and detector could explain a small deviation from the expected rate differences. The rates for electrons of different sources are listed in table 11.7. Here we see that the rate of wall-electrons is increased by a factor of 55. It is a safe assumption that in both measurement campaigns the electron flux from the walls was the same. The tritium rate is increased by a factor > 100, but it is likely that during Troitsk-III there was more tritium in the source than during the first measurement campaign. If we now take the factor 55, the residual tritium rate in Troitsk-I was 0.4 cps. The contribution of the residual tritium is thus a priori not negligible, when compared to the total counting rate of $4 - 10$ cps4.

Figure 11.31 shows a comparison of the residual tritium spectrum and the total observed spectrum when the source was filled with tritium. Both data is from Troitsk-III, because a comparison with Troitsk-I would be misleading due to differences in the detector response. Both spectra are normalized. The residual spectrum has more events close to the HV-threshold, hinting at a much steeper spectrum than the observed tritium. This

	$\Gamma_{\text{T-I}}$ (Troitsk-I)	$\Gamma_{\text{T-III}}$ (Troitsk-III)	ratio $\Gamma_{\text{T-III}}/\Gamma_{\text{T-I}}$
residual tritium	-	22 cps	-
wall electrons @ 13 kV	∼5.5 cps	∼300 cps	∼55
tritium @ 13 kV	4.6 - 10.9 cps	∼1150 cps	∼106 - 250

Table 11.7: The rates of electrons from different sources, compared between Troitsk-I (CEA system) and Troitsk-III (XGLab system).

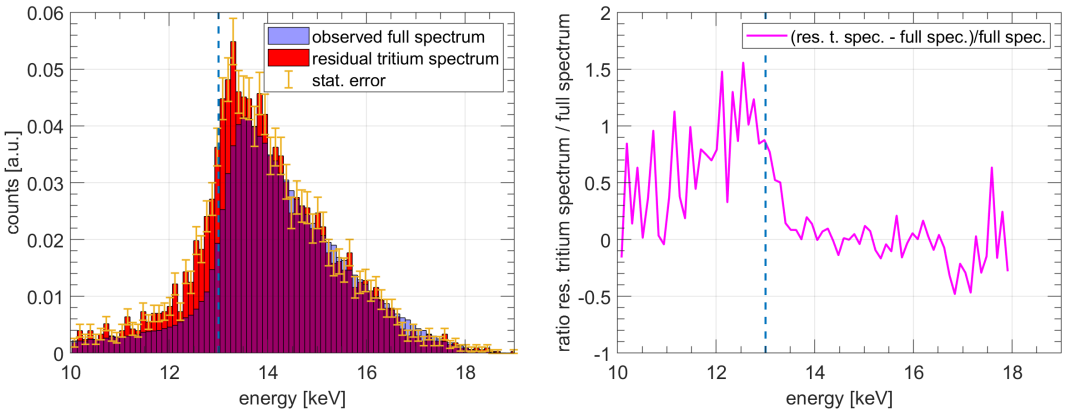

Figure 11.31: On the left: the residual tritium spectrum, measured with the XGLab system in comparison to the full spectrum observed during Troitsk-III. On the right the ratio of both spectra is shown.

is expected, since the electrons from the residual tritium lose energy when escaping from the rear wall. However, the difference could also be partially due to an inaccurate calibration of the data, which cannot be verified due to the lack of an in-situ calibration.

In summary, the contribution of residual tritium in the Troitsk-I spectrum is unclear. The fit of the tritium spectrum was thus executed without regarding it a priori. It can be assumed that the residual tritium spectrum is generally following the shape of the spectrum from the gaseous source with a few modifications that are accounted for by the many free parameters in the fit. In future measurements background-measurements with an empty source will always be done and the inclusion of radioactive sources close to the detector for a continuous calibration are planned in order to eliminate this uncertainty.

11.3.7 The tritium fit

The observed differential tritium spectrum N_{obs} was fitted with the following function that puts together all the components described in the preceding sections. The function is a convolution of the parametrized energy response with the tritium model, which was modified by the SSC shape factor. The functions f are evaluated for discrete energies (the binning of the data) such that matrices or vectors are obtained. The convolution becomes then a sum over N bins:

$$f_{\text{spectrum}}(p, p_{\text{calib}}, p_{\text{SSC}}, E) = n \cdot \sum_{j}^{N} f_{\text{response}}(p, E_{\text{in},j}, E \cdot p_{\text{calib}}[1] + p_{\text{calib}}[2]) \times \\ \times \left[f_{\text{SSC shape factor}}(p_{\text{SSC}}, E_{\text{in},j}) \cdot f_{\text{tritium model}}(\text{m}, \sin^2\theta, E_{\text{in},j}) \right] \tag{11.7}$$

It is ensured that f_{response} is normalized for each initial energy to 1. For each initial electron energy $E_{\text{in},j}$, i.e. a bin of the observed spectrum, f_{response} becomes a vector − the spectrum for mono-energetic electrons with the initial energy $E_{\text{in},j}$ − and $f_{\text{SSC shape factor}} \cdot f_{\text{tritium model}}$ becomes a number that scales this spectrum. All these spectra are then summed up. p, p_{calib} and p_{SSC} are vectors of parameters. p_{calib} allows to adjust the energy scale, since the calibration is known only with limited accuracy (it can change with external environmental parameters like temperature and grounding). However, this parameter is not recalibrating the data, but adjusting the model to fit the data, which is very efficient compared to re-calibrating the data since it doesn't make it necessary to have a dynamic binning and / or variable summation limits. A true recalibration can easily be calculated from the fitted parameters. The fitted function contains 17 parameters:

- p: 10 parameters from the response matrix (n_2, n_3, β, b and c each as a linear function of energy, see section 11.3.3) plus two parameters for the normalization and resolution;
- p_{SSC}: three parameters from the SSC shape factor;
- p_{calib}: two calibration parameters;

For the fit the chi-squared function was minimized:

$$\chi^2 = \sum_j \frac{[N_{\text{obs},j} - f_{\text{spectrum}}(p, p_{\text{calib}}, p_{\text{SSC}}, E_j)]^2}{f_{\text{spectrum}}(p, p_{\text{calib}}, p_{\text{SSC}}, E_j)} + f_{\text{pull terms}}(p, p_{\text{calib}}, p_{\text{SSC}}) \tag{11.8}$$

The pull term function is:

$$f_{\text{pull terms}}(p) = (p - \hat{p})^T \cdot Cov^{-1} \cdot (p - \hat{p}) \tag{11.9}$$

The covariance matrix Cov was obtained during the parametrization fit of the mono-energetic electrons data in section 11.3.3. If the parameters p would have been measured independently, such that an expected value $\hat{p}$ was obtained, these pull terms could prevent the parameters to venture into unphysical regions while respecting their covariances. Here, no such pull terms were used since no expectation values for the parameters exist. Pull terms are later used to generate an exclusion curve, as presented in section 11.5.

11.3.8 Tritium fit results

The resulting tritium fit is shown in figure 11.32. The obtained chi-squared is

$$\chi^2/\text{ndof} = 1.085 \text{ (ndof} = 467).$$

The p-value of this result is 0.0993. This means that given the model is correct, the probability to observe the present data is about 10%. By conventional criteria this is not a significant discrepancy and one can consider the fit to be good. The residuals, which are also shown in figure 11.32, do not display an irregular pattern, except for a small excess close to the endpoint (where the statistics are low) and at the "dip" just below the retarding potential threshold. The best fit values of the parameters and their errors are tabulated in the appendix in table C.2. The minimization was performed by a simplex algorithm, utilizing MATLAB®'s function "fminsearch". The result presented here is a local minimum of the chi-squared function. A global minimum was found

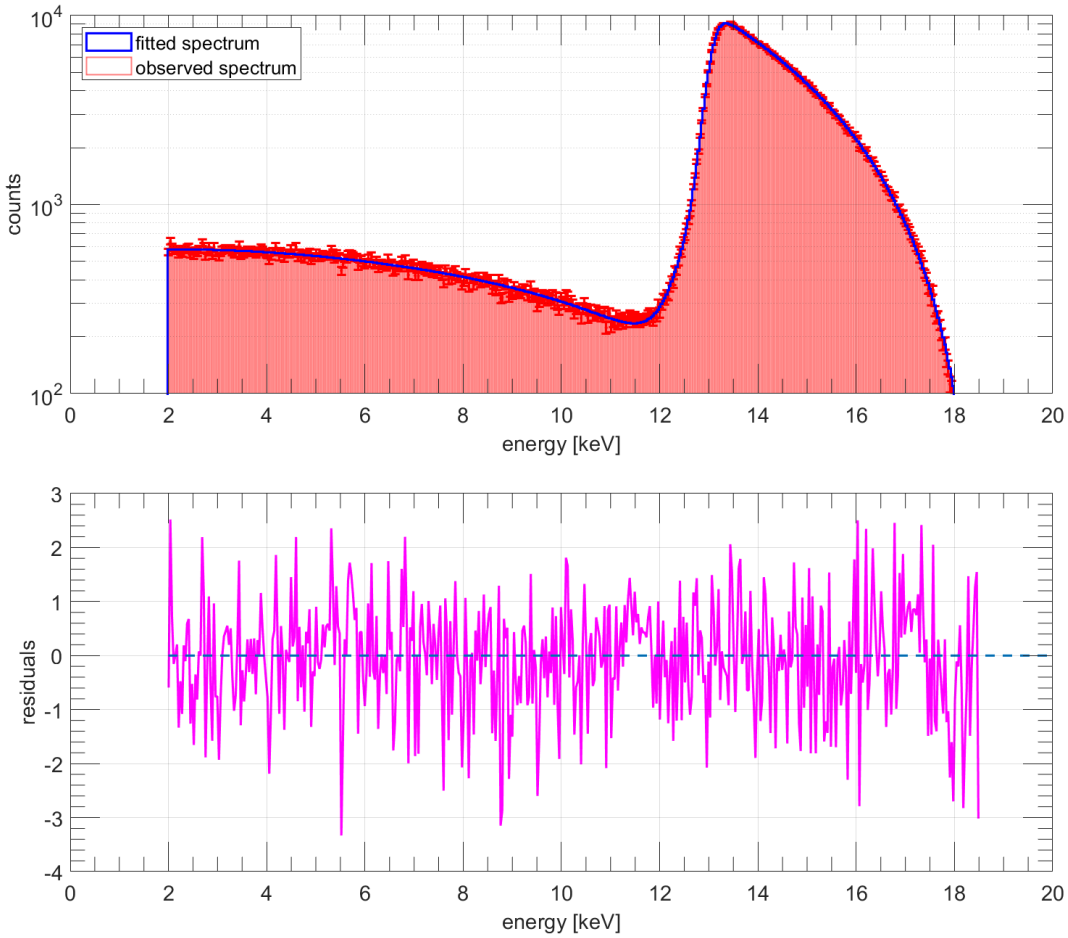

Figure 11.32: On the top: the fitted tritium spectrum (blue) compared to the observed spectrum with statistical error bars (red). On the bottom plot the residuals are shown. The reduced χ^2 is 1.085 at 467 degrees of freedom.

farther away from the starting parameters than the local minimum, however, it returned unrealistic parameters. "Realistic parameters" means that, if these parameters are put into the response function and SSC shape function, the basic shape of both functions is preserved, i.e. a peak, exponential tail and backscatter tail is observed for the response and the SSC shape function is still a redistribution of events from higher to lower energies. In detail, following tests are performed to check the plausibility of the fit results:

- we insert the fitted parameter values in the function for the mono-energetic energy response and compare it with the wall electron data. The corresponding plots are shown in figures 11.33 and 11.34. A reduced rate in the back-scattering tail of the response from the tritium fit is clearly visible. Also the exponential tail is higher and has a less steep slope, resulting overall in a slightly widened peak. The poissonian chi-squared of the fitted tritium response with respect to the wall electron data is calculated and yields

  $$\chi^2_{\mathrm{P}}/\mathrm{ndof} = 3.109 \ (\mathrm{ndof} = 2420).$$

  One can exclude the 20 keV data, because the tritium spectrum does not extend beyond 18.6 keV. It is thus not required to reproduce a realistic response at this energy. Excluding this data, one obtains $\chi^2_{\mathrm{P}}/\mathrm{ndof} = 2.605$.
  Anyways, we know that the response for wall electrons is different from the response for tritium electrons and a good agreement is not expected. Yet the response as extracted from the tritium fit shows all the characteristic elements: a Gaussian peak, a low energy exponential tail and a backscatter tail and can be considered to be realistic;

- the parameters of the SSC shape factor are compared to the original ones as retrieved from the simulation (see figure 11.35). The shape factor obtained from the tritium fit follows the original trend as it moves events from higher energies to lower energies, but with a noticeable different slope. It has to be discussed, if this could be allowed by uncertainties of the SSC simulations. In addition to uncertainties of the simulation / calculation itself, it also has to be noted that the source density was decreasing during the measurements and strongly reduced in the second data set, the source effects are thus changing during the measurement;

- the energy calibration is verified. In figure 11.36 one can see on the left side the first derivative of the data and the fitted tritium spectrum close to the high voltage threshold. The turning point of the function, i.e. the maximum of the first derivative is expected to be close to the high voltage value and, if the fitted function is reasonable, has to be at the same position for the data and for the fit. This is true as visible in the plot. The second test for the energy calibration is the end point of the spectrum. The data and the fit were converted into a Kurie plot to achieve a linear shape. The x-intercept of the fitted line is at the same position for both the data and the fit. The calibration parameters found in the fit are $E = 0.9989 \cdot E' - 0.0085$, where E' is the real physical energy. Correcting the obtained x-intercept with these parameters leads to an endpoint $Q = (18.538 \pm 0.145)\,\mathrm{keV}$, which is close to the expected endpoint of 18.575 keV.

It has to be noted that the response function can absorb uncertainties from the SSC shape function and vice versa, and that both functions compensate for the residual tritium background. Also, the response function assumes a linear energy dependence of the parameters which might be not true.

In addition to comparing the response found in the tritium fit with the wall electron data, it is also interesting to see the tritium response with respect to the e-gun data, although it was shown in section 11.1.2 that the e-gun measurements are not suitable to study the energy response due to an dependency of the number of events in the backscatter tail on the position of the beam spot. The comparison is shown in figures 11.37 and 11.38 for 14, 15 and 16 keV. The response of wall electrons is also included in the plots, and for 16 keV additionally the simulated response of electrons started in the pinch magnet (see next chapter). The overall shape of the responses is similar, except the number of events in the backscatter tail is smaller and the curvature of the tail is more pronounced for the e-gun data. Considering the different shapes of wall and e-gun response, one can say that the fitted tritium response is in between them. It should be mentioned that the e-gun data for 16 keV (figure 11.38) shows a broadened peak that is neither present in the fitted response nor in the wall electron data. Even though the e-gun data is not reliable, the general agreement of the data from all three sources proves that the response obtained from the fit is plausible.

To check if the large differences between the wall electrons response and the fitted monoenergetic tritium response like the reduced number of events in the backscatter tail, which cannot be simply explained by uncertainties, are due to the different magnetic field configurations in both measurements, simulations were done as it is presented in the next section.

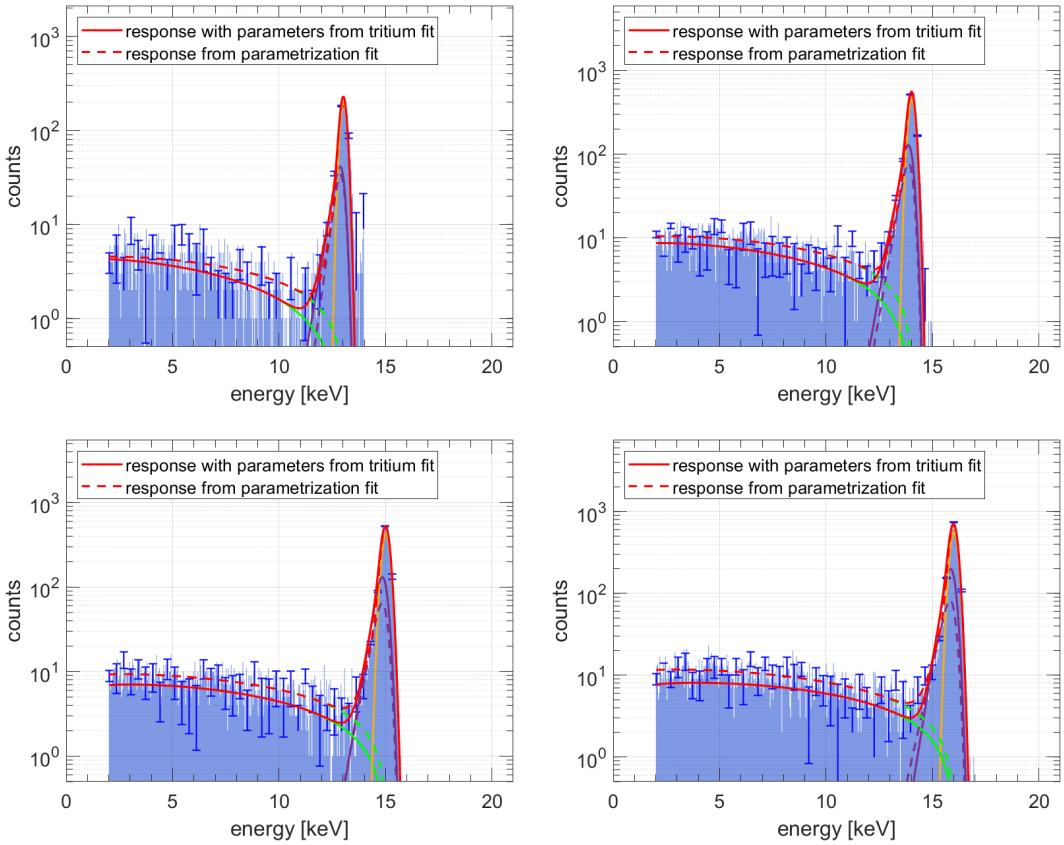

Figure 11.33: The energy response with the parameters obtained from the tritium fit (solid lines) compared to the wall response data (histogram) with the parametrization fit (dashed lines) for 13, 14, 15 and 16 keV. The tritium fit preserves the general shape of the response, but there are some differences in the shape: a reduced number of events in the backscatter tail and a larger exponential tail.

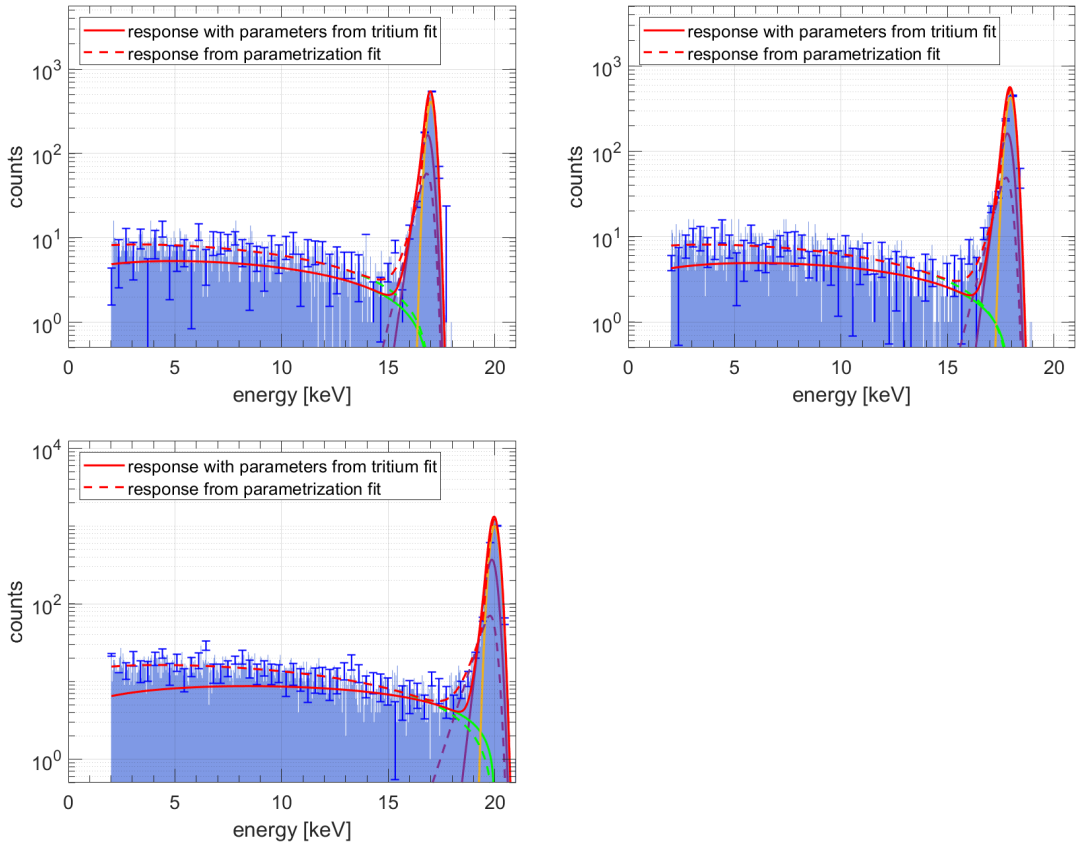

Figure 11.34: The energy response with the parameters obtained from the tritium fit (solid lines) compared to the wall response data (histogram) with the parametrization fit (dashed lines) for 17, 18 and 20 keV. The difference of the responses is largest for the 20 keV data. However, the fit is not required to return a good response for this energy since the tritium spectrum end point is below.

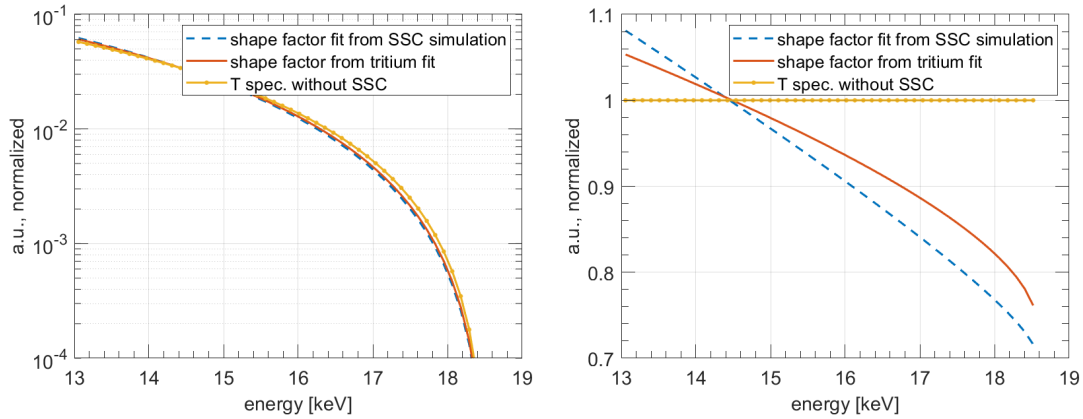

Figure 11.35: **Left**: The tritium spectrum with the SSC shape factor returned from the tritium fit (red) and with the "original" shape factor obtained from the simulations (blue) in comparison to the unmodified tritium spectrum (yellow). **Right**: the ratio of the different spectra. Even though the slope of the shape factors is different, both redistribute events from higher to lower energies as expected.

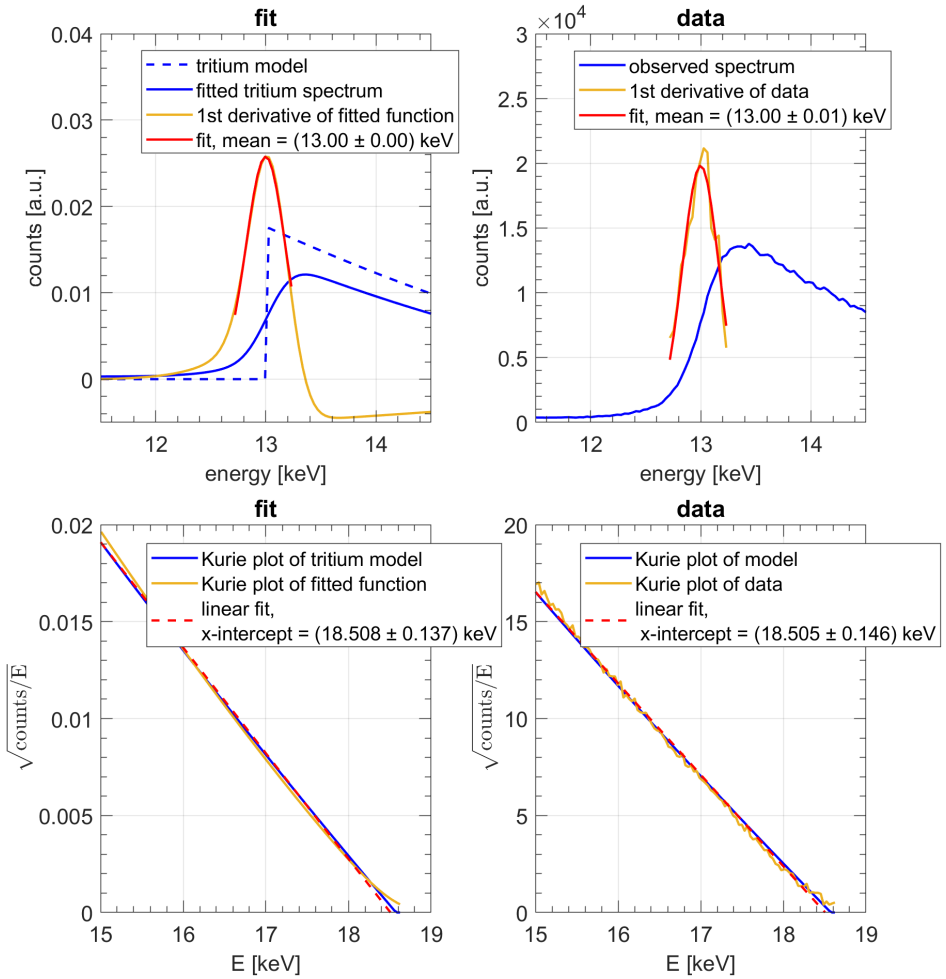

Figure 11.36: The test of the energy calibration of the fitted tritium spectrum. **Top:** the region around the retarding potential threshold is shown as well as the second derivative for the data and the fitted function. In both cases the peak of the second derivative is at the proper threshold value of 13 keV. **Bottom:** the Kurie plot of the data and fit. The x-intercept is in agreement for both data.

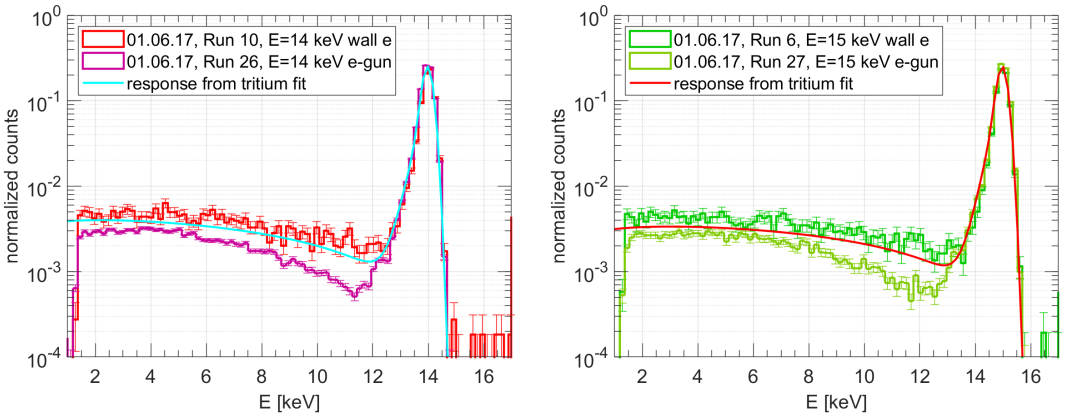

Figure 11.37: Comparison of the e-gun and wall electron data with the response obtained by fitting the tritium spectrum for 14 keV (left) and 16 keV (right). The overall shape of the tritium response is in agreement with the wall electron response, except for a varying number of events in the backscatter tail.

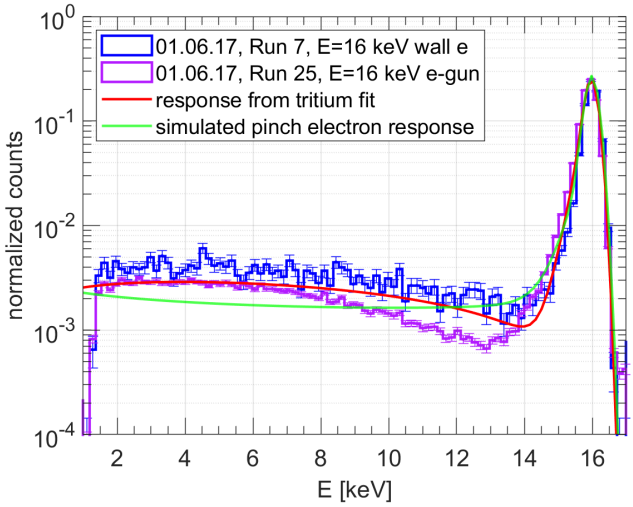

Figure 11.38: A comparison of the e-gun and wall electron data with the response obtained by fitting the tritium spectrum for 16 keV. The simulated response of electrons started in the pinch magnet is included as well (see chapter 11.4).

11.4 Simulations of the energy response

The energy response obtained through the tritium fit differs from the one measured with monoenergetic wall electrons. It features a different exponential tail and has less events in the backscatter tail. Montecarlo simulations were conducted to verify these differences. The goal of the simulations is to compare the response of electrons from the walls and electrons started at the pinch magnet. We will not take into account effects from the source itself, which are scattering and trapping of electrons, since this was included in the fit with the SSC shape factor. Differences in both responses can hence result only from the different settings of the electric and magnetic fields. If a simulation would show that there is no difference in the response of wall- and tritium-electrons, it would mean that systematic effects were not properly accounted for in the tritium fit.

While for tritium measurements both the pinch and detector magnet work at full strength, for measurements with wall electrons the pinch magnet was turned off and the detector magnet current was reduced to a 50 A, a third of the full strength. The field configuration affects the odds that an electron back-scattered from the detector is lost or hits the detector again. In general, for the wall electrons, all electrons, which are back-scattered will return to the detection plane, since the electrostatic potential will prevent them from crossing the spectrometer. However, electrons from the tritium have a surplus energy with respect to the retarding potential and can thus return to the source after being back-scattered. Also the magnetic field strength at the detector can influence how many backreflected electrons are detected by one pixel, because the gyro-radii of the electrons are changed. It is very hard to understand the impact of these effects on the spectrum analytically, but one can study them with simulations.

The simulations presented here were carried out with the Kasper software package, which was developed for KATRIN. This software contains the modules “Kassiopeia” to simulate the propagation of electrons in magnetic and electric fields [Gro15], and Kess, which simulates the interactions of electrons in the silicon detector [Ren11].

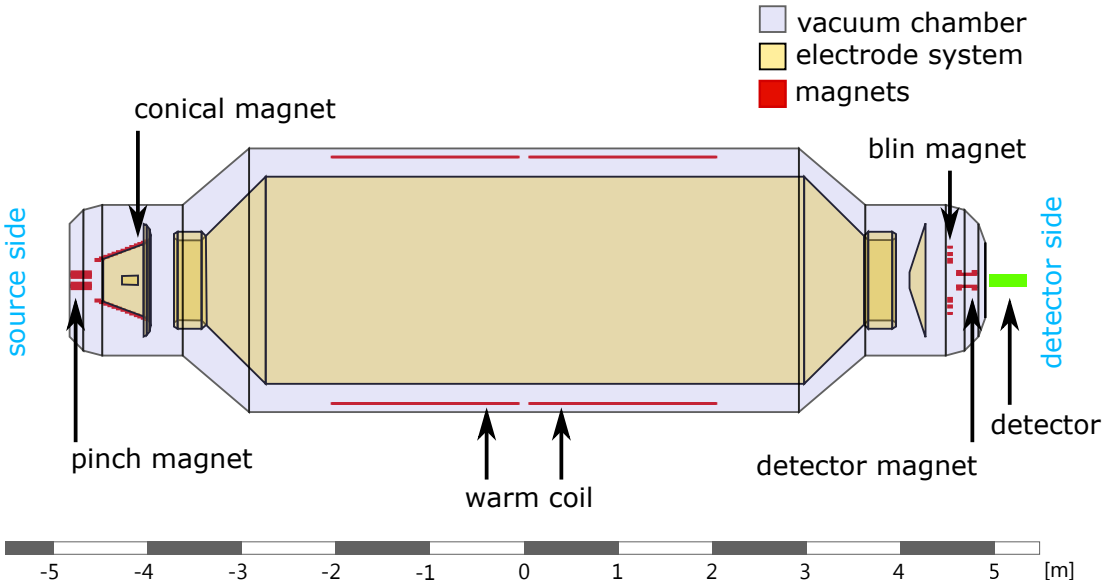

Figure 11.39: The simulated geometry. The source, the transport section and the pre-spectrometer are also modeled, but not of interest for these simulations and not shown in this sketch. The scale at the bottom is identical with the z-axis in the simulations.

11.4.1 Geometry and fields

The simulated geometry is shown in figure 11.39. The model was created by Anton Huber (KIT) and Aino Skasyrskaya (INR RAS). The z-axis is the symmetry axis of the spectrometer, while $z = 0$ marks the center (analysis plane of the MAC-E filter) and positive values move towards the detector. The radius r describes the distance from the z-axis. The source section is also included in the model, but not of interest for the simulations described here. In the simulation the fields are calculated from the given geometry, the electric potential of the electrodes and the currents and number of windings in the coils. Only the main electrode has a potential other than ground. The magnets of interest are the pinch and conical magnets on the source side, and the detector and "blin" (name of traditional Russian pancakes) magnets on the detector side, which are all superconducting. The detector and blin magnet are connected and have the same currents. In addition there is the "warm coil" over the length of the spectrometer that allows us to compensate for the earth magnetic field and to steer the beam from the e-gun.
For measurements in the standard configuration of the spectrometer the earth magnetic field can be neglected, since the warm coils were on and thus canceled the field. For the wall electrons these correction coils were turned off and thus a constant magnetic field was added. The vector of this field is ($x = 6.5445\,\mu\text{T}$, $y = 49.5655\,\mu\text{T}$, $z = 15.5447\,\mu\text{T}$) and was obtained from the NOA online calculator [fie] and transformed for the spectrometer coordinate system, taking into account that the z-axis of the spectrometer is pointing at 348° north. In principle this field does not affect the results of the simulation, but helps with the simulation of wall electrons, which sometimes encounters problems, when an electron propagates into a region with very weak fields (far away from the detector magnet, no earth magnetic field). The overall field strength can be extracted from the simulations and is plotted in figure 11.40.
The detector chip is placed at at $z = 4.945\,\text{m}$. It is modeled as a silicon disk with a radius of $r = 5\,\text{mm}$. The actual detector chip is rectangular, but the simulation software requires rotational symmetry of the geometry. It is covered by a 40 nm thick

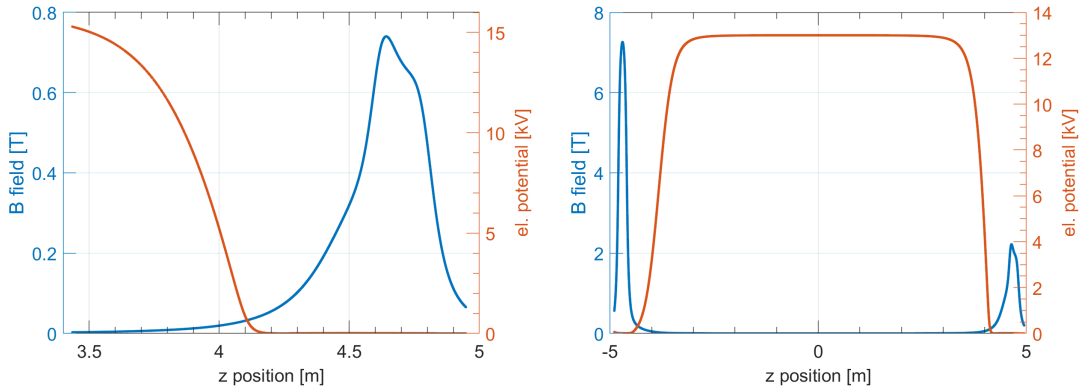

Figure 11.40: The absolute magnetic field strength (left y-axis) and the electric potential (right y-axis) along the simulated spectrometer. **Left:** the field strength for wall electrons with 15 kV retarding potential. As the electrons are started at the detector magnet and cannot cross the spectrometer towards the pinch magnet, only the fields close to the detector magnet are displayed. **Right:** the field strength for pinch electrons with 13 kV retarding potential throughout the entire spectrometer. Note that for pinch electrons the detector magnet was operating with a 3 times higher current than for the wall electrons, visible in the increased magnetic field.

dead layer, the rest is defined as sensitive volume. The detector itself (one pixel) has a diameter of 1 mm, but this will be taken care of in the analysis. It is important to include the complete silicon chip into the simulation, because electrons could backscatter somewhere on the non-sensitive surface of the chip and then return with a reduced energy to the defined pixel.

11.4.2 Simulation parameters for wall and pinch electrons

The electrons are generated with a fixed energy in a certain fluxtube with a specified angular distribution. Their propagation in a vacuum with electric and magnetic fields is calculated by Kassiopeia in 16 steps per full gyration (one complete circle around the field line). In the silicon volume the electron trajectory is calculated in 10 nm steps. Each event is terminated only after one of the following requirements is fulfilled:

- stopped in detector: energy of the electron is close to zero;
- transmission: the electron crosses $z = 4.946$, which is beyond the detector;
- electron is trapped: more than 100 turns in the spectrometer;
- too many steps: more than $1 \cdot 10^7$ calculation steps;
- backscattering: the electron crosses a plane behind the starting point. This is $z = 0$ for wall electrons (it is impossible for electrons to reach this plane because it is at the maximum of the retarding potential) or $z = -4.9$ m for pinch electrons (some electrons pass this plane and are assumed to be lost in the source section);
- radial escape: $r < 15$ m, the electron left the spectrometer. In the simulations presented here this termination criterion is not occurring;

To simulate the wall response only a 50 A current in the detector magnet is applied. The retarding potential is set to the desired potential. The electrons are started in the

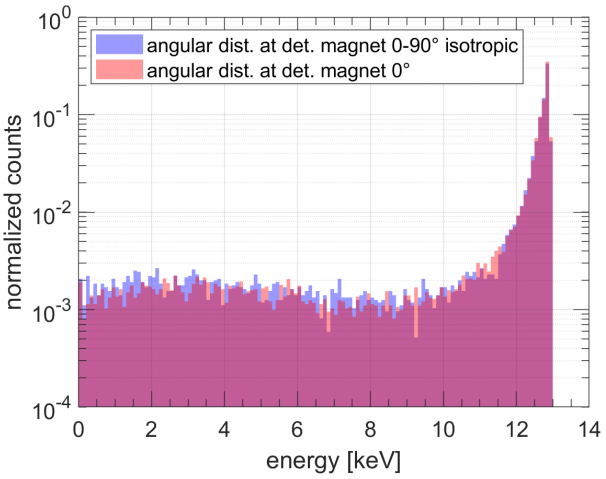

Figure 11.41: Comparison of two spectra, where the electrons were started with different angular distributions. The detector resolution was not included here. The blue histogram shows the simulated events from electrons that were started with an isotropic angular distribution between 0 and 90° in the forward direction. For the red histogram, all electrons were started in parallel to the symmetry axis. The difference is small.

middle of the detector magnet at $z = 4.65\,\mathrm{m}$ with a fixed energy, that matches the retarding potential. Indeed the electrons from the walls, which are in reality accelerated by the retarding potential, reach their maximum energy before crossing $z = 4.65\,\mathrm{m}$, where the potential is zero as it can be seen in figure 11.40. In the simulation the electrons are started within a fluxtube of 1.581 mm diameter. This fluxtube size ensures that the detector chip is illuminated completely (see figure 11.46). The real directional angular distribution of the wall electrons is not clear; we assume that they have an isotropic distribution on the forward-hemisphere at the detector magnet. In principle the angular distribution can affect the back-scattering from the detector. However, when the resulting spectra of a simulation with an isotropic angular distribution and another one, where the electrons are starting in parallel to the symmetry axis, are compared, the difference is small, as shown in figure 11.41. Thus we decide to stay with the assumption of an isotropic angular distribution of the electron directions at the starting point in the detector magnet.
The tracks of 100 simulated wall electrons are shown in figure 11.42. The colors show the time, which is normalized such that time 1 corresponds to the last step for each event. The gyration of the electrons is clearly visible. Three electrons were back-scattered and then subsequently reflected on the retarding potential.

For the pinch electron simulations all magnet currents are at full force. The events are started close to the maximum magnetic field in the center of the pinch magnet coil at $z = -4.8\,\mathrm{m}$ in a flux tube with 1.4 mm radius and angles homogeneously distributed between 0 and 52° with respect to the z-axis. Electrons with higher angles are reflected on the magnetic field. The tracks of 100 simulated pinch electrons are plotted in figure 11.43. One can see, how the gyration of the electrons close to the magnets transforms into a movement almost parallel to the field lines at the spectrometer center.

All important simulation parameters are listed in table 11.8 for the different simulations.

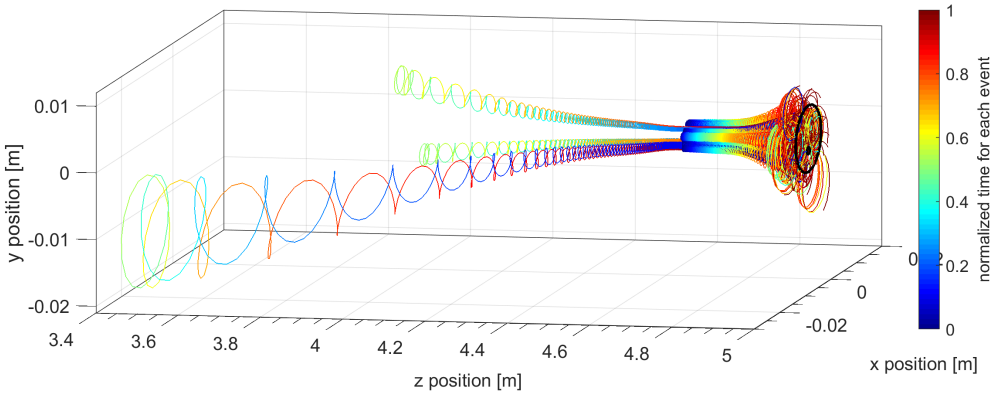

Figure 11.42: The tracks of 100 simulated wall electrons. The electrons are started at $z = 4.65\,\mathrm{m}$ and then gyrate around the field lines towards the detector. Three electrons are back-scattered, move then towards the spectrometer center, where they are reflected and return to the detector. The color code shows the normalized time of each simulation step, where the last step for each event is at time = 1. The detector chip is shown as black cylinder. The smaller black cylinder within is one pixel of the detector, as defined in the analysis.

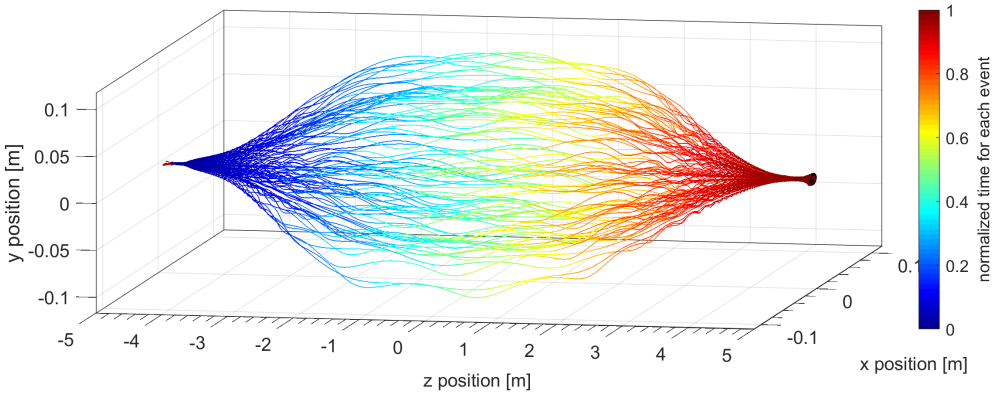

Figure 11.43: The tracks of 100 simulated pinch electrons. It is visible how the gyration of the electrons transforms into a movement parallel to the field lines in the center of the spectrometer. The color code shows the normalized time of each simulation step.

	wall electrons	**pinch electrons**
z start	$z = 4.65\,\mathrm{m}$	$z = -4.8\,\mathrm{m}$
angular distr. (w.r.t. z-axis)	0-90°	0-52°
fluxtube start radius	1.581 mm	1.4 mm
ret. potential	-13, -16, -18 kV	-13 kV
starting energy	13, 16, 18 keV	13, 16, 18 keV
warm coil current	0	19 A
pinch mag. current	0	150 A
conical mag. current	0	120 A
detector./blin mag current	50 A	150 A

Table 11.8: Simulation parameters.

11.4.3 Analysis of simulation output

The simulation has different levels of output – the event level, track level, and step level. Each event is the simulation of a single electron and consists of several tracks. A new track is started each time, when the electron crosses a defined surface, for example when it enters the silicon volume of the detector, crosses the boundary between the dead layer and the sensitive volume, or when it leaves the silicon volume after backscattering. Each track consists of many steps (see section 11.4.2 for details on the step calculation). The step output allows for example to plot the trajectory of the electron, because it contains the position of the electron for each calculation step (see figure 11.42 and 11.43). Due to the high memory demand, the step output was usually deactivated. For the analysis the track output is sufficient, which contains following important information: creator and terminator name (Is the track within the sensitive silicon volume? Was the simulated electron stopped, transmitted or back-scattered?), initial and final position (Did the electron hit a defined detector?), and lost energy (energy deposited in the detector). The simulation output was analyzed in the following steps:

- cut on creator name: only electrons that entered the sensitive volume of the detector chip are kept;
- cut on position: a pixel (the central pixel) with 0.5 mm radius is defined. Only energy deposited in this volume is added to the spectrum;
- multiplicity cut: in the measurement data we look only at singular events. Thus in the simulation we discard all events, where also an edge pixel was hit. This is achieved by defining a ring around the defined pixel with 0.5 mm inner radius and 1.5 mm outer radius that models the edge pixels. If there was a track in this ring, the event is excluded from the analysis, because it might contain another track in the central pixel, if it was backscattered and then backreflected.
- integrate multiple events in one pixel: if several tracks in the central pixel have the same event number, it means that the electron was back-scattered, backreflected and hit again the central pixel. The energies of these tracks are then summed up, because both events are within the 9.6 µs integration time and thus cannot be distinguished. This is also true for electrons that were backscattered more than 2 times, as shown in figure 11.44. Due to the generation of single electrons in the simulation there is no pile-up of independent electrons, which is not a problem because in the measurements pile-up is negligible.
- model the energy resolution of the detector: the simulation output does not take the energy resolution of the detector into account. The energy in the raw data is smeared by replacing every remaining event with a Gaussian random value, where the mean is the original energy and the spread the resolution of the detector. To compare the simulations with the measurements a resolution similar to the measured one was chosen.

The defined detector is not directly in the center of the chip, i.e. in the symmetry-axis of the spectrometer, but is offset by 1.8 mm as the central pixel was during the measurements. However, in these simulations a significant difference (beyond statistical effects) was not observed between detectors with or without offset. Anyways, to increase the efficiency of the analysis, detectors with an offset were used. We define in total 11 detector with 1 mm diameter each on a circle around the chip center with 1.8 mm radius. If one event was used for the analysis of one detector, it is not available anymore

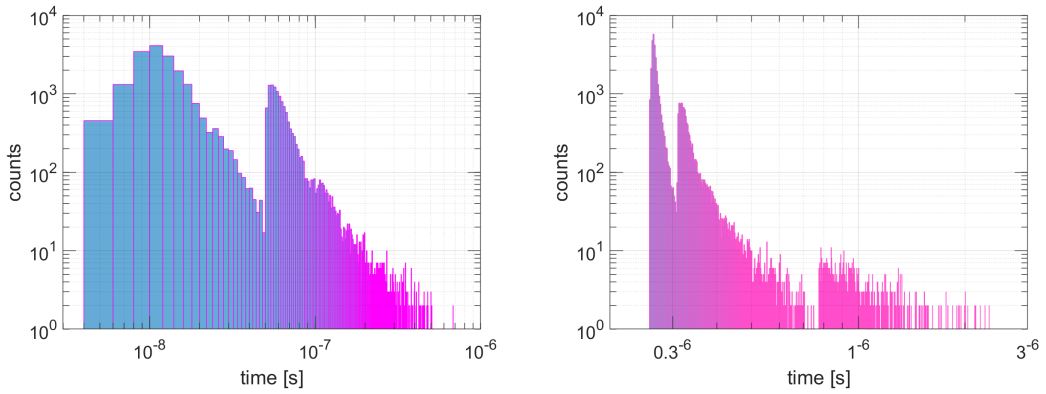

Figure 11.44: The time distribution of secondary hits, after the electron was backscattered on the detector. **Left:** the distribution of wall electrons. The electron is started at $t = 0$. Two populations of events are visible: at short times ($t = 10^{-8}$ s) electrons that were reflected on the field of the detector magnet. The second group of events at $t > 5 \cdot 10^{-8}$ s consists of electrons that were reflected from the retarding potential. The step-like feature at $t = 10^{-7}$ s is caused by events that were backscattered twice. **Right:** the distribution of pinch electrons. Similar features are visible as for the wall electrons, but in addition there is a third population of events at $t = 10^{-6}$ s, representing electrons that were reflected on the field at the pinch magnet. Due to the starting point at the entrance of the spectrometer, the time scale is here shifted to larger values. However, all events are within the system's shaping time of $9.6 \cdot 10^{-6}$ s, thus these events would pile up in one pixel (or be detected with a multiplicity > 1, when a detector array is considered).

for the other detectors. This way more events can be analyzed from each data set. To avoid a bias it has to be checked that the detectors are illuminated homogeneously. The distribution of electrons in the starting flux tube is shown in figure 11.45. Figure 11.46 shows the spatial distribution of electron that hit the detector. Hits of backreflected electrons are not included. The large cylindrical polygon marks the detector chip radius, the smaller cylinders are a pixel in the center and a second pixel with 1.8 mm offset. In both cases the central part of the detector with the defined detector pixels is illuminated homogeneously. For the electrons started in the pinch magnet the flux is homogeneous on the entire chip (right), while the wall electrons show a non-flat distribution (left), due to the reduced field of the detector magnet, causing the electrons to gyrate with larger radii. Starting the electrons in a larger flux tube would result in a homogeneous flux, but most events would be transmitted, reducing the efficiency of the simulation. Concerning the real world, from the measurement it is only known, that the flux is homogeneous on the scale of the 7-pixel array, there is no information on the spatial distribution of events on larger scales. Also in the simulation the flux is homogeneous in the center of the chip.
Finally, after following the steps listed above, the simulated spectra were fitted with the same model as for the response parametrization (equation 11.4). The results are presented in the next section.

11.4.4 Results

Simulations of wall and pinch electrons were done for three different energies: 13, 16 and 18 keV. For the wall electrons the retarding potential was set to the corresponding electron energy (e.g. 16 kV retarding potential for 16 keV electrons), and to always 13 kV for the pinch electrons to reproduce the tritium measurements. The number of simulated electrons are tabulated in table 11.9. An important detector parameter,

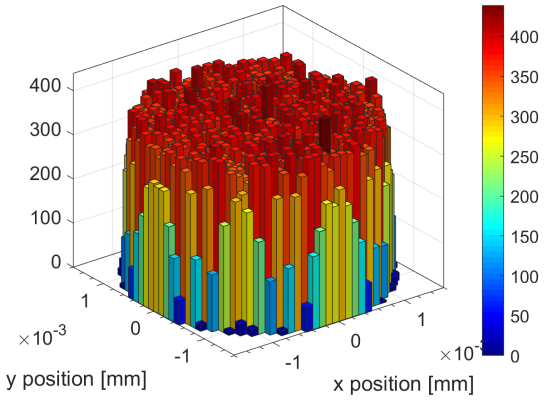

Figure 11.45: Start position of wall electrons. The electrons are started homogeneously distributed across the flux tube.

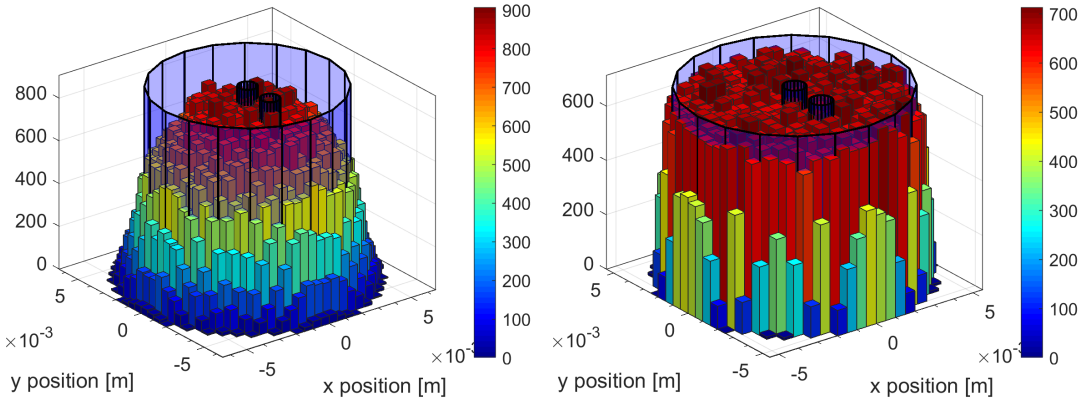

Figure 11.46: Hit position of simulated electrons on the detector chip. The polygons mark the detector chip (outer cylinder) and a defined pixel in the center and another one with an offset of 1.8 mm. **Left:** the hit distribution of wall electrons. Due to the reduced magnetic field, a complete homogeneous illumination of the chip is not achieved. **Right:** the hit distribution for pinch electrons.

	13 keV w.	13 keV p.	16 keV w.	16 keV p.	18 keV w.	18 keV p.
simulated ev.	240000	240000	282750	348750	237800	240000
hits chip	248558	187881	287179	272203	238286	187492
hits sens. vol.	224805	175476	255436	251386	209958	171767
analyzed hits	24767	14890	28683	21862	23961	15322

Table 11.9: The number of events in the different simulations of wall (w.) and pinch (p.) electrons. The number of hits on the chip can be higher than the number of simulated electrons, because one electron can reach the detector multiple times if it is backscattered and backreflected.

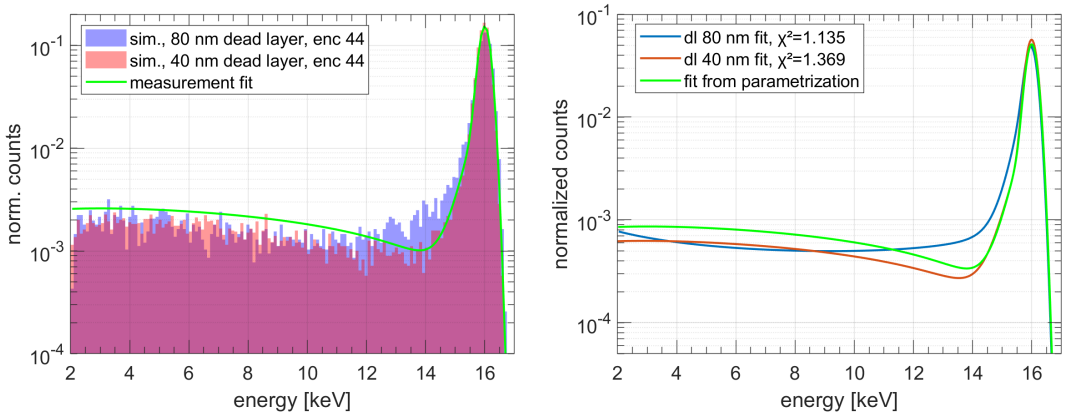

Figure 11.47: A comparison of simulated wall electrons with an energy of 16 keV and different dead layer thicknesses to the measured data. The parametrization fit of the corresponding wall electron measurement is shown in both plots in green. For comparison the simulated data was shifted such that the peak is at 16 keV. **Left:** the data and the wall response fit. The blue data represents the simulation with a dead layer thickness of 80 nm, the red data the simulation with a 40 nm dead layer. **Right:** The simulated data fitted with the same function as for the parametrization (equation 11.4).

which is yet unknown, is the dead layer thickness. Preliminary results of dedicated measurements and simulations hinted at a thickness of 80 nm[2]. However, when comparing a simulation of 16 keV wall-electrons and 80 nm dead layer with the corresponding measurement from Troitsk, the lower end of the exponential tail of the peaks are not in agreement. The simulated peak is too wide, even when the best possible resolution was used (40 enc, which is already slightly below the intrinsic ASIC noise level). A much better agreement is achieved when simulating a 40 nm dead layer. This is shown in figure 11.47. The overall shape of the 40 nm simulation and the measurement is similar, only the backscatter tail is scaled down in the simulation. This can be explained by differences in the real and simulated detector geometry (the actual pixel is not a circle, but hexagonal) and the position. A small uncertainty in the detector position can lead to a quite large uncertainty of the magnetic field strength at the detector. Depending on the field strength the gyroradius of the electrons that hit the detector will be different. Effectively this can change the detector's acceptance for backscattered and backreflected electrons. In these simulations we are interested in the relative difference of the response from wall- and pinch-electrons, so the simulations were continued without further adjustment of the detector position and with a dead layer of 40 nm. Note that the agreement of simulation and measurement does not necessarily mean that the detector really has a dead layer of 40 nm. As the exponential tail is overlapping with the backscatter tail, whose shape is given by the magnetic field (which affects e.g. the backreflection probability) and read-out parameters (e.g. the multiplicity cut), incorrect settings in the simulations could in principle compensate for a wrong dead layer thickness. In order to certainly find out the dead layer thickness a dedicated and sophisticated measurement is required, as prepared for example in [Sie19].

The comparison of measured and simulated spectra of wall electrons for all energies is shown in figure 11.48 (13 keV), 11.49 (16 keV) and 11.50 (18 keV) on the left. For all energies it can be seen that the simulated response agrees well with the measured one,

[2]Newer results show that the dead layer thickness is depending on the detector. Values between 50 and 100 nm were found [Sie19].

except for a slightly different height of the back-scatter tail, as mentioned above.
On the right panels of the plots, the comparison of simulated wall and pinch electrons is shown, together with the fitted response from the tritium fit. One can see that wall and pinch response are indeed different: for pinch electrons less events end up in the back-scatter tail, the shape of the backscatter tail is more flat, especially the dip below the peak is not present, and the low energy tail of the peak is slightly wider. However, the shape of the pinch response is not well in agreement with the response from the tritium fit. The disagreement could be attributed to the many uncertainties in the analysis. Also the accuracy of the simulations can be questioned since measurements with the e-gun (see figure 11.38 in section 11.3.8) show a shape of the back-scatter tail more similar to the measured / simulated wall response, where the number of events in the backscatter tail is declining towards higher energies instead of the constant plateau with a small incline as observed in the simulated pinch response.
One can compare the number of events in the backscatter tail for the different data by counting the electrons with energies below the initial energy minus 2 keV. In table 11.10 the relative differences of the event number in the tail between simulated wall and pinch electrons, and between measured wall electron spectra and the response obtained from the tritium fit are listed. For the simulations the reduction of events from wall to pinch electrons is the same for each initial energy, while in the comparison of measured wall electrons and the response obtained from the tritium fit the difference is increasing with energy. This is a hint that the initial assumption of the response parametrization in which the parameters of the transfer function are linearly dependent on the initial electron energy is not correct.
A summary plot of the different simulated spectra is shown in figure 11.51.

In summary the simulations show that wall- and pinch electrons indeed have different energy responses, justifying that the tritium fit returns a response different from the measured wall response. The simulations reproduce the trend observed in the result of the tritium fit that there are less events in the backscatter tail. However, the shape of the backscatter tail is not in good agreement. That the simulations do not exactly reproduce the observed shape might be due to uncertainties of the simulations itself and the many uncertainties in the tritium fit, which are the source effects calculated with the SSC code, the missing background subtraction and the assumed transfer function shape. In future measurements following actions would help to understand the response better with simulations by eliminating uncertain parameters:

- a very accurately defined detector position in order to determine the exact magnetic field at the detector;
- an independent dead layer measurement;
- accurate simulation of source effects and background measurement to include in the tritium fit, such that the fitted response really corresponds to the pinch electron response.

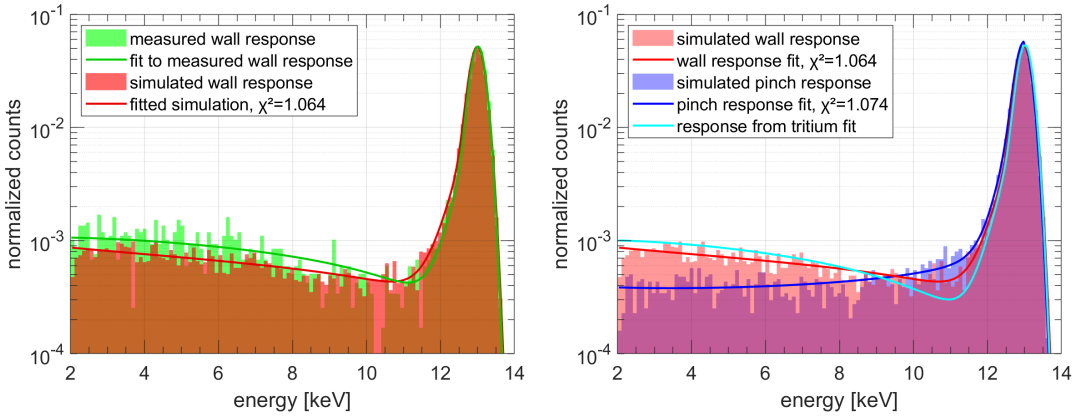

Figure 11.48: Simulation of 13 keV electrons. **Left:** comparison of measured (green) and simulated (red) wall electrons. The backscatter-tail contains slightly less events in the simulations, which can be explained by a not accurate simulation of the setup geometry. The width of the exponential tail is also slightly deviating. **Right:** comparison of the simulated wall response (red), pinch response (blue) and the response obtained from the tritium fit (cyan). The simulated pinch response has less events in the backscatter tail, and the shape of the exponential tail and the backscatter tail is different. Note that the response from the tritium has more events in the backscatter tail than the simulated wall response, but one has to keep in mind that the simulated wall response has also less events in the tail than the measured one.

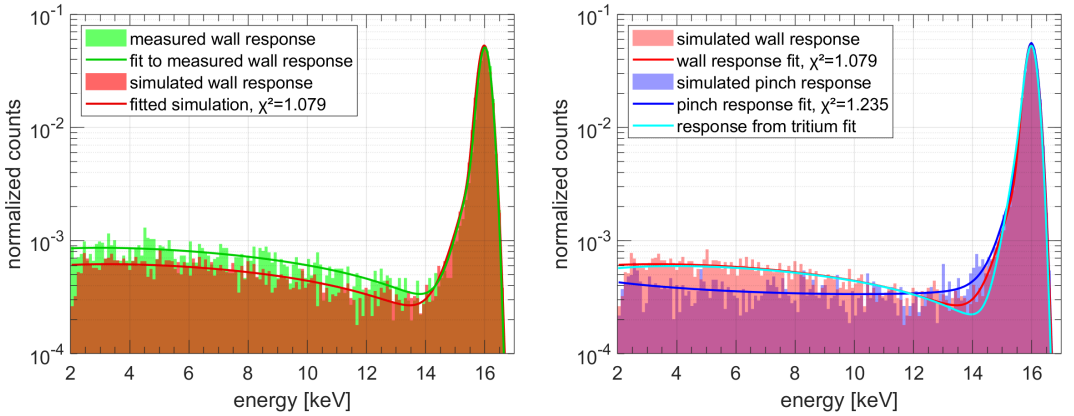

Figure 11.49: Simulation of 16 keV electrons. Similar observations as in figure 11.48 are made. **Left:** comparison of measured (green) and simulated (red) wall electrons. **Right:** comparison of simulated wall electrons (red), pinch electrons (blue) and the response obtained from the tritium fit (cyan). The rather large reduced chi-squared of the fitted pinch response model is due to the peak, which is at the very top a bit flatter than a Gaussian distribution.

	13 keV	16 keV	18 keV
tritium fit / measured wall response	86%	72%	67%
simulated pinch response / wall response	68%	65%	68%

Table 11.10: The number of events in the backscatter tail is reduced for simulated pinch electrons or the response obtained from the tritium fit when compared to measured wall electrons. The events where counted from 2 (threshold) to the initial energy minus 2 keV (e.g. 11 keV for 13 keV electrons).

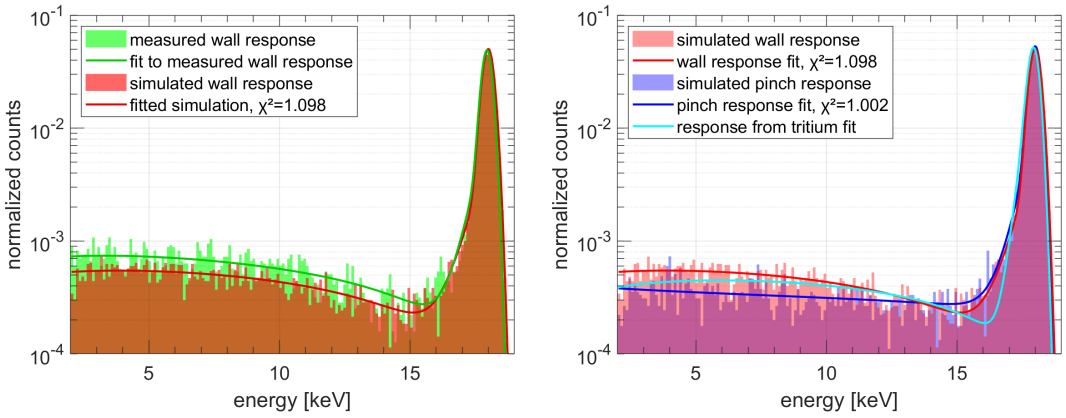

Figure 11.50: Simulation of 18 keV electrons. Similar observations as in figures 11.48 and 11.49 are made. **Left:** comparison of measured (green) and simulated (red) wall electrons. **Right:** comparison of simulated wall electrons (red), pinch electrons (blue) and the response obtained from the tritium fit (cyan).

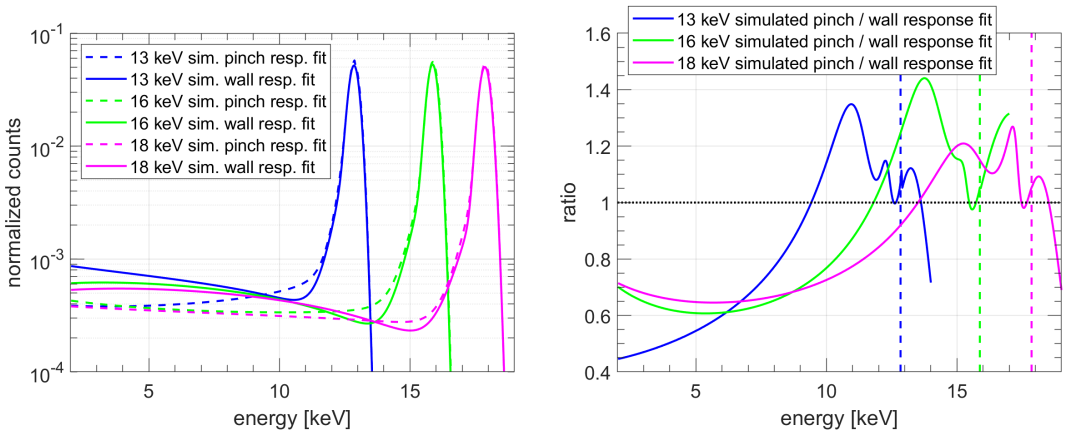

Figure 11.51: Left: a summary of the simulated wall (solid lines) and pinch energy response spectra (dashed lines) for the three energies 13, 16 and 18 keV. In all simulations there are less events in the backscatter tail for the pinch electrons. Also the shapes of the backscatter- and exponential tail are slightly different. This is not exactly reproducing the resulting response from the tritium fit, but shows that to use the wall response for the fit is not correct and that thus obtaining a different response from the tritium fit is in principle plausible. **Right:** the ratio of the spectra for each initial energy. The peak positions are marked by the dashed lines.

11.5 Sensitivity and exclusion curves

The tritium analysis is concluded with a sensitivity study and production of an exclusion curve for a sterile neutrino. The statistical sensitivity was determined with a toy-Monte Carlo simulation, where the null-hypothesis best fit was assumed to accurately depict the actual tritium spectrum and thus serves as a model of the observed spectrum. The model is then fitted to simulated data that contains statistical fluctuations. In this fit only the normalization and calibration (endpoint) are left free. The simulated data was generated from the model by replacing each bin with a Poissonian random number, where the expectation value is the model bin count. The fit was repeated over a grid of $\sin^2(\theta)$-m-parameters. The parameter-space scan was performed for in total 100 random spectra to see how the sensitivity is changing with statistical fluctuations.
Figure 11.52 shows the distribution of $\Delta\chi^2 = \chi^2_{0,0} - \chi^2_{\text{best fit}}$ over the 100 data sets, where $\chi^2_{0,0}$ is the minimized χ^2 for the $(m = 0, \sin^2\theta = 0)$ scanning point (i.e. the null hypothesis), and $\chi^2_{\text{best fit}}$ the minimum value in the entire parameter space scan. According to the Wilk's theorem one expects this histogram to follow a χ^2-distribution with n degrees of freedom, where the number of degrees of freedom is the number of scanned parameters, which are in this case m and $\sin^2\theta$ [CCGV11]. For $n = 2$, 90% of the values are expected to be below $\Delta\chi^2 = 4.6$. In figure 11.52 the χ^2 distribution with $n = 2$ is superimposed on the data. Due to the rather small sample size of 100 scans one can not conclusively say if the data follows the χ^2 distribution, but since there are no data above $\Delta\chi^2 = 4$, one can assume that the Wilk's theorem holds true and define the 90% confidence level (CL) bounds at $\Delta\chi^2 = 4.6$. The sensitivity curves derived from 100 datasets are shown in figure 11.54. Instead of showing each curve, only the maximum and minimum sensitivity are displayed. The gray-scale is proportional to the density of sensitivity curves: the black region is excluded by all curves, the white region by none. The gray area thus marks the parameter space where statistical fluctuation affect the sensitivity. The parameter space which could be excluded from the Troitsk measurement with 730 000 events, in case the spectrum is fully understood and thus no systematic effects are present, is then marked by the upper line.

An exclusion curve is created by performing a scan over the $\sin^2(\theta)$-m parameter space, where the model is fitted to the actual data with all 17 fit parameters left free (see section 11.3.7). In general, using pull terms to constrain the parameters is not justified, because there are no expectation values for the parameters. Nevertheless, for the scan the parameters of the SSC shape function were constrained by pull terms according to equation 11.8 with an error of 10% and no correlations, such that the function is forced to maintain its general shape of a redistribution of electrons from higher energies to lower energies. Otherwise, the fit would result in an unphysical shape function, as a redistribution of electrons from lower to higher energies can compensate for a kink induced by a sterile neutrino.
The $\Delta\chi^2 = \chi^2_{0,0} - \chi^2(m_i, \sin^2\theta_j)$ map is shown in figure 11.53. As one can see, there are neutrino parameters were the fit was better than for the null hypothesis, especially in the region of $m \sim 0.75\,\text{keV}$ and $\sin^2\theta = 0.2 - 0.5$. The best fit is achieved at $m = 0.75\,\text{keV}$ and $\sin^2\theta = 0.4$ with a reduced chi squared of 1.03 at 467 degrees of freedom. The plots of the corresponding spectrum and the energy response are shown in the appendix D. For sterile neutrino parameters in this region a response can be found that results in an improved fit. However, since the true response is unknown, one cannot determine if the resulting fit is correct. If one would draw an exclusion

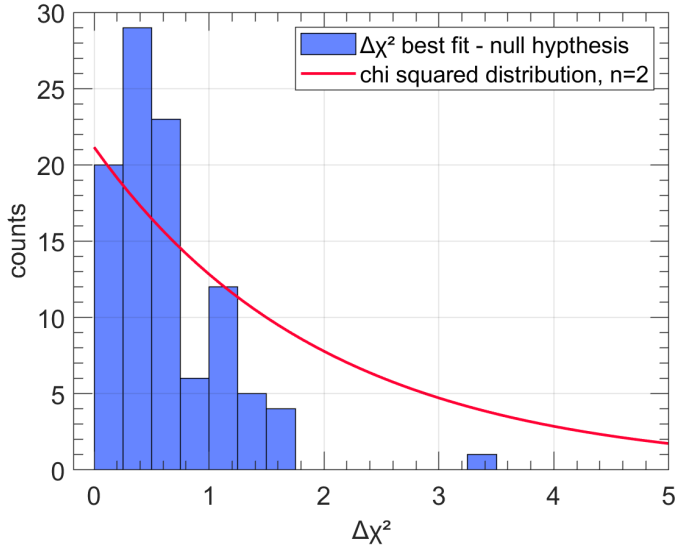

Figure 11.52: The distribution of $\Delta\chi^2 = \chi^2_{0,0} - \chi^2_{\text{best fit}}$ for 100 scans over the parameters space, where the model was fitted to random statistically fluctuated data with the normalization and calibration as free parameters. According to the Wilk's theorem the data should be χ^2-distributed, which is shown in red.

around this minimum the cyan 90% CL discovery island is obtained – which is contradictory to existing limits. The improved fit can be also attributed to systematic effects that are unaccounted for, as the missing background subtraction and a possible calibration drift between the two stacked spectra.
An 90% confidence level exclusion curve can still be generated by observing, for which parameters the χ^2 becomes by 4.6 larger than for the null hypothesis fit. In this region, despite the many free parameters, only a much worse fit can be found. The only assumption for this exclusion curve is that the functional form of the model is valid. The exclusion curve is drawn in yellow onto the map. Note that the color map is saturated for any values above 4.6. The exclusion reaches $\sin^2\theta = 0.02$ for masses between 2 and 3 keV. For larger masses only sterile neutrinos with mixing angles $\gtrsim 10\%$ can be excluded, as in this region the many free parameters allow a better compensation of the kink. The white region was not probed.
In addition, one can see in figure 11.53 that the χ^2 values are fluctuating. This is a problem of the model, as there are too many free parameters and it thus has multiple local minima. Different fits converge into different minima, despite a similar random seed, similar start parameters and fitting settings. This could be improved by reducing the number of fitted parameters and by the introduction of pull terms.

A summary of the exclusion and the sensitivity together is shown in figure 11.54. The sensitivity curves from the 100 scans are not plotted individually, but the region covered by them is marked by the red and blue lines. At low masses the exclusion curve reaches into the gray region. An exclusion in this region can be due to statistical fluctuations. In the end the existence of a sterile neutrino with a mixing down to a few percent is rejected.

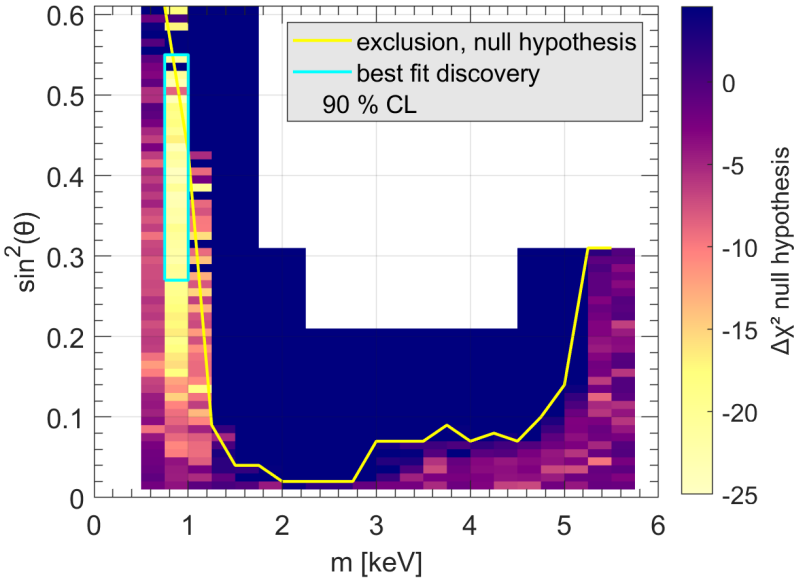

Figure 11.53: The $\Delta\chi^2 = \chi^2_{0,0} - \chi^2(m_i, \sin^2\theta_j)$ map from fitting the full 17 parameter model over a grid of sterile neutrino parameters to the data. As on can see, for some sterile neutrino parameters the resulting fit is better than for the null-hypothesis, resulting in a "discovery" at $m = 0.75\,\text{keV}$ and $\sin^2\theta = 0.27 - 0.55$. However, this can be rejected as the improved fit only means that a response function was found, which can compensate well for the kink signature. But it is not known at all, if the response is right. Also, a kink could be caused at low masses by systematic effects that were not accounted for. The 90% CL exclusion is marked by the saturated color and the yellow line. In this region, despite the many free parameters a good fit could not be found.

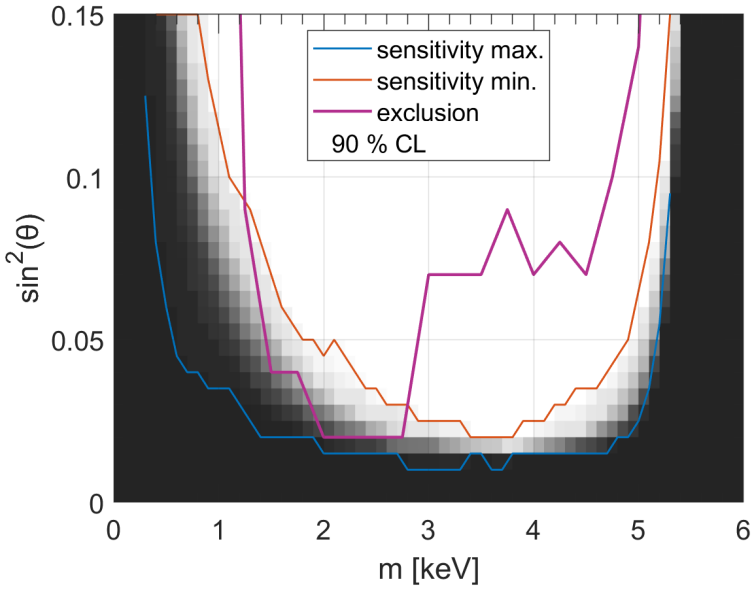

Figure 11.54: The 90% CL statistical sensitivity superimposed with the exclusion. The statistical sensitivity was obtained by performing a scan over the parameter space 100 times, where simulated data was fitted to the model with free normalization and calibration parameters. The white region is contained by all sensitivity curves, the black region by none. The exclusion curve is shown as solid magenta line.

11.6 Conclusions

In this chapter the results from a measurement campaign at the Troitsk ν-mass spectrometer with the first 7-pixel TRISTAN detector prototype were presented. The results from the previous X-ray characterization concerning the performance were confirmed also for electron data, as the noise floor of the ASIC was reached. Also a similar charge sharing behavior was observed.

A differential tritium spectrum with 730 000 events was analyzed in a proof-of-concept study. Previous studies of the tritium spectrum at MAC-E type spectrometers were based on integral measurements, which have to be treated in a different way and are prone to other systematic effects. For this study, the observed differential tritium spectrum was modeled as a convolution of the energy response and a model of the source spectrum, which is the tritium spectrum modified with scattering and trapping effects. The energy response was determined by measuring monoenergetic electrons emitted from the spectrometer walls. This data was taken for different energies and then fitted with an empirical function. Since it is not known, whether the measured response is similar to the one of tritium electrons, the parameters were left free in the final tritium fit. For the tritium spectrum an analytical model was used. The scattering and trapping effects were simulated, but then parametrized and added as a shape factor to the tritium spectrum. Also this function contained free parameters for the final fit, as the accuracy of the simulations is unknown. Finally, a fit of the spectrum was obtained with a reduced χ^2 of 1.09 at 456 degrees of freedom (p-value = 0.1). The best fit parameters show a different energy response, which is still reasonable, i.e. it maintains a general shape similar to spectra of monoenergetic data. Also the source effects shape function maintained its general shape.
The energy response was studied with simulations to verify the fit results. The observed feature that the tritium response has less events in the so-called backscatter tail than in the wall electron response could be reproduced, but not the exact shape. However, measurements with e-gun data are also not in agreement with the simulated shape, suggesting that the simulations have a limited accuracy.
The analysis of the tritium spectrum did not reveal any unexplainable features in the shape and thus strongly encourages to pursue the further development of the differential analysis. The analysis was concluded with a sensitivity study, showing that the sterile neutrino can be excluded in the mass range between 1.5 and 4.5 keV with mixing angles down to a few percent.
The analysis of future differential tritium measurements can be improved in several ways: a proper background measurement is absolutely necessary, as an advanced measurement of the energy response, e.g. with an improved and well characterized e-gun. If the parametrization approach of the response is continued, the model function should be improved. This has to be accompanied by more sophisticated simulations to study the detector response and source effects, such that in the end a fit with less and/or constrained parameters can be performed. Important for the simulations is also a well defined geometry and placement of the detector in the setup and an independent measurement of the dead layer thickness.

The measurements at Troitsk continued with two more measurement campaigns with 7-pixel prototypes. A continuation of the collaboration is planned also with the 166-pixel prototypes, as soon as it is available.

Chapter 12

TRISTAN summary

The TRISTAN project is an extension of the KATRIN experiment to scan the tritium β-decay spectrum for the signature of a sterile neutrino with a mass in the keV-range. KATRIN itself is attempting to measure the absolute neutrino mass by searching for a shift of the spectral endpoint in the order of a few hundred meV. To achieve this, the electron energy is selected with a high resolution with an electromagnetic filter. By varying the filter threshold and counting the number of passed electrons an integral spectrum is obtained. As TRISTAN is searching for a kink-like signature anywhere in the spectrum, the filter will be turned off or operate at very low thresholds. The resulting count rate of $\sim 10^8$ electrons per second cannot be handled by the current 148-pixel detector of KATRIN and thus demands a novel detector system. This detector should also have a very good energy resolution such that the spectrum can be additionally analyzed in a differential way, e.g. with a wavelet transform approach. Integral and differential measurements are both susceptible to different systematic effects, thus by combining both techniques the sensitivity can be enhanced. The high counting rate demands an highly segmented array with a fast read-out system. The final detector is planned to be made of 21 modules with each 166 silicon drift detectors (SDDs) with 3 mm diameter, resulting in a total of 3486 pixels. Due to their small capacitance, the SDDs achieve a low noise level also at short shaping times, granting thus a high energy resolution of a few hundred eV in the energy region of interest and allowing a fast read-out. In addition the detector chips feature an ultra-thin dead layer with a thickness of a few tens of nm, improving the energy resolution even more.
As a first stage in the detector development, several 7-pixel prototypes were produced with different pixel sizes and numbers of drift rings. These detectors were equipped with the IDeF-X BD ASIC readout system, which is a well proven device and allows to read out all pixels synchronously, although it is not optimized for SSDs and low noise applications. A dedicated ASIC for TRISTAN is still in development. The work that was presented in this thesis is about the characterization of the prototypes with the IDeF-X ASIC with X-rays and electrons and the analysis of a first tritium spectrum taken at Troitsk ν-mass. Following results were obtained:

- with all prototype detectors the noise floor of the ASIC was reached. That means the resolution is limited only by the electronics. The SDD detectors thus are working properly and a resolution of a few hundred eV can be reached with a dedicated read-out system. Additionally, the detector noise was studied at different temperatures;

- the amount of charge sharing was measured for the different detectors and found to be between 5 and 20% for energies below 30 keV and with a detection thresh-

old of $\sim 2\,\mathrm{keV}$, depending on the detector size. It was shown that, even when coincident events are removed from the data, charge sharing affects the energy response. In principle this effect is easy to control, but simulations and further measurements are required;

- the detectors were tested with electron sources at Troitsk ν-mass. The performance was similarly excellent as with X-ray sources and no significant differences in the charge sharing behavior were found;
- A differential tritium spectrum with $\sim 700\,000$ was analyzed in a proof-of-concept study. The analysis was challenging because a direct measurement of the energy response from tritium electrons was not possible. Instead the general shape of the energy response was determined through measurements of electrons emitted from the spectrometer electrode and then included in the tritium fit with free parameters. Finally, the spectrum could be fitted and the resulting energy response was validated by comparing it to e-gun measurements and simulations. The analysis was concluded with a sensitivity study, allowing to exclude the existence of a sterile neutrino in the range from 1.5 to 4.5 keV with a mixing larger than a few percent.

In summary, the results of the characterization of the SDD prototypes and the tritium analysis are very encouraging that the TRISTAN project will reach its design goals. Larger detector prototypes are already in production and a dedicated low-noise read-out system is in development (see chapter 13).

Part IV

Conclusions

Chapter 13

Conclusions and outlook

In this thesis the work within two different sterile neutrino experiments – SOX and TRISTAN – was presented: for the SOX project, which was designed to search for eV-scale sterile neutrinos at the Borexino detector, a thermal calorimeter was constructed, characterized and commissioned to determine the activity of a radioactive source, which serves as neutrino generator to study short baseline oscillations. A detailed summary of this work can be found in chapter 7. The final outcome was that the calorimeter is able to determine the heat released by the decaying source with 0.2%-accuracy in a single measurement of $\sim$ 5 days, and thus ensures that the projected sensitivity for sterile neutrinos can be achieved. Compared to previous source experiments as SAGE and GALLEX and calorimeters used in the industry, the accuracy of the heat measurement is unprecedented (see section 2.4). Unfortunately, SOX was canceled after the source production failed and the calorimeter could not be used for the actual measurement. However, a description of the device and the results of the calorimeter characterization, optimization and calibration were published in [ADN+18] and are available for future experiments.

Before the cancellation, the start of SOX was planned for May 2018. Since then several other experiments (as introduced in section 1.8.1) delivered results. At nuclear reactors following observations concerning short-baseline oscillations were made:

- NEOS (2017) excluded the best fit of the reactor antineutrino anomaly ($\Delta m^2_{41} = 2.3\text{eV}^2$, $\sin^2(2\theta_{41}) = 0.14$ [MFL+11]) at $> 90\%$ confidence level. In the analysis the best fit, yet not significantly better than the null-hypothesis, was obtained when a sterile neutrino with the parameters$\Delta m^2_{41} = 1.73\,\text{eV}^2$, $\sin^2(2\theta_{41}) = 0.05$ was added [Siy18, Col17];

- DANSS (2018) found no strong evidence of an oscillation and rejected the best fit of the reactor antineutrino anomaly at $> 5\,\sigma$ [A+18c];

- PROSPECT (2018) disfavors the best fit of the reactor antineutrino anomaly at 2.2 σ [A+18e];

- NEUTRINO-4 (2018) ruled out the reactor and gallium anomaly at $> 3\sigma$ for $\Delta m^2_{41} < 3\text{eV}^2$ and $\sin^2(2\theta_{41}) < 0.1$ (including the reactor anomaly best fit), but an oscillation at 2.8σ that corresponds to a sterile neutrino with $\Delta m^2_{41} = 7.34\text{eV}^2$ and $\sin^2(2\theta_{41}) = 0.39$ was observed. This is not in contradiction to the other experiments mentioned here, as this part of the parameter space is not excluded [S+19].

- STEREO (phase I and II combined, 2019) excluded the reactor anomaly best fit at $\sim 99.8\%$ confidence level ($\sim 3\sigma$) from the cell-to-cell analysis. A reduced overall flux is still observed. These results are preliminary [Ber19];

These results are model independent, as the fluxes at different distances (and energies) were compared. The published 90% confidence level exclusion curves do not cover the entire parameter space which is indicated by the anomaly global fits, but the best fit of the reactor anomaly is strongly disfavored. The origin of the reactor antineutrino anomaly however remains unclear.
Also in other oscillation channels new limits in the sterile neutrino parameter space were set. For example IceCube is sensitive to sterile neutrinos by observing the disappearance of atmospheric ν_μ that crossed earth on different lengths, as matter effects would be greatly enhanced by a sterile neutrino. No indications of an non-standard oscillations caused by an sterile neutrino with masses $\sim 0.1 - 1\,\text{eV}$ were found [Jon19]. This is in strong tension with the sterile neutrino explanation of the ν_e-appearance in the MiniBooNE and LSND experiments (see section 1.8.1). However, also the MINOS, MINOS+ and NOνA accelerator experiments reject the sterile neutrino hypothesis in the $\nu_\mu/\overline{\nu}_\mu$-disappearance channel [A$^+$19, EAS$^+$17].

In summary, one can say that the eV-scale sterile neutrino is not consistently ruled out as an explanation of the many observed anomalies. Many tensions between different experiments have yet prevented the emergence of a clear global picture. A rather recent global analysis from March 2018 that includes data from many more experiments than mentioned here can be found in [DHCK$^+$18], where the authors conclude that the sterile neutrino is still a possible explanation for the reactor and gallium anomaly. In the future, more data will be delivered by the short baseline reactor experiments, including SoLid [A$^+$17b], which has not published results yet. Concerning the gallium anomaly, the BEST experiment is in preparation with a segmented radiochemical detector which could solve this anomaly in 2020 [BCG$^+$18]. In the end, one can see that an experiment like SOX would still be very valuable and have the potential to finally resolve the long term question of the short-baseline neutrino oscillations.
It should be mentioned that eV-scale sterile neutrinos are strongly disfavored and not motivated by cosmology in contrast to keV-scale (and heavier) sterile neutrinos that serve as dark matter candidates. Still, conclusions on particle physics made from cosmic microwave background observations are model dependent and cannot replace laboratory measurements.

For the TRISTAN project, which plans to use the KATRIN tritium setup to search for keV-scale sterile neutrinos, a novel detector system is in development that can deal with rates up to 10^8 counts per second and has an energy resolution of a few hundred eV. In this thesis the characterization of prototypes – 7 pixel silicon drift detectors (SDDs) – was presented together with the first analysis of a differential tritium spectrum, taken with one of the prototypes at the Troitsk ν-mass spectrometer. Some of the results were published in [ABB$^+$18] and another paper with the Troitsk results is in preparation. A detailed summary of this work can be found in chapter 12. Through measurements with X-ray sources and electrons it was shown that the detectors are suitable for TRISTAN and the effect of charge sharing between the pixels was studied. To analyze the tritium spectrum a new analysis was developed. The work presented here was one of the first steps towards the final detector array and the full scale measurement, as it laid a foundation for the data analysis. The next development steps are a 166 pixel array, which is already in production together with a dedicated low-noise

read out system. As KATRIN itself is not available for about 5 years due to the ongoing neutrino mass program, this detector could be installed at Troitsk ν-mass, not only for testing but also for a serious sterile neutrino search that can set world-leading limits. For the differential spectrum analysis, further work is required:

- the energy response of electrons from the gaseous tritium source has to be determined. At Troitsk, this can be achieved through measurements for example with a gaseous ^{83m}Kr-source that emits mono-energetic electrons and with an improved e-gun, supported by detailed simulations of the entire setup;
- systematic effects have to be studied with more detail, as scattering and trapping of electrons in the source , the behavior of the read out (e.g. pile-up behavior, detection efficiencies and dead-time) and the adiabaticity of the electron transport through the spectrometer at high energies. These effects can be examined through measurements together with simulations;
- instead of measuring the entire response, also individual effects can be studied in more detail as charge sharing and dead layer effects. This can be done by separate laboratory measurements and detector simulations.

All of the above mentioned points can and will be realized in the continuing development. When TRISTAN enters the final phase at KATRIN by installing the new detector system, some aspects will change as for example the energy response has to be measured anew. In addition, systematic effects that are not important for KATRIN due to low surplus energies as multiple scatterings in the source or the adiabatic electron transport have to be studied. However, the tools and methods can be developed and tested at Troitsk. Also, TRISTAN will benefit from the KATRIN characterization, e.g. the background models etc.
Meanwhile, also KATRIN's neutrino mass program is profiting from the developments for TRISTAN: a 7-pixel SDD will be used for the forward beam monitor and a 166 pixel array (similar to a module of the final detector) will be installed in the monitor spectrometer.

On the frontier of keV-scale sterile neutrino searches TRISTAN is an one-of-a-kind experiment. Sterile neutrino runs are still performed also at Troitsk ν-mass, but the sensitivity is limited. Alone to reach a statistical sensitivity for the parameter space of cosmological interest in a reasonable time-frame, a spectrometer with a very strong radioactive source is necessary, which is and will be for a long time an unique feature of KATRIN. Other experiments to search for keV-scale sterile neutrinos are still in early stages.

The sterile neutrino, for which TRISTAN is searching, is a dark matter candidate. Several astrophysical observations at scales smaller than galaxies seem to favor warm dark matter, as which a keV-scale sterile neutrino would act, instead of cold dark matter. One has to keep in mind that many other experiments are searching for other dark matter particles, for example WIMPS, SIMPS and Axions. Most of these candidates would constitute cold dark matter (CDM). However, CDM plus baryonic feedback processes or self-interacting dark matter could resolve the small-scale anomalies in astrophysics.
If a different dark matter particle would be discovered, a sterile neutrino would not be ruled out, as it is anyways motivated by the seesaw mechanism, but on the other hand the keV-mass range would be not longer motivated.

The origin of the 3.5 keV X-ray line observed by some space telescopes, which could be caused by the decay of sterile neutrino dark matter, will be further investigated by the future satellites eROSITA, XRISM (a new version of Hitomi) and ATHENA/X-IFU. The combined high angular resolution, coverage and energy resolution of the experiments would not only lead to a clear detection of a possible 3.5 keV line above the background but also allow to scan the entire parameter space predicted by the νMSM (neutrino minimal standard model) [ZWA15, GT18, NM16]. XARM is planned to be launched in 2021, while ATHENA is scheduled for 2031.
Impetus on sterile neutrino search can also be given by searches for the $0\nu\beta\beta$-decay. One one hand a discovery of this decay would present a strong evidence for the seesaw mechanism and thus the existence of sterile neutrinos, on the other hand the decay rate is directly dependent on the parameters of sterile neutrinos [HZ19, AHCM19].

In conclusion, currently many experiments, including the work presented in this thesis, are searching for sterile neutrinos in an attempt to solve the questions of short-baseline oscillations and dark matter, trying to find missing parts of the standard model of particle physics for a more complete understanding of the universe. If a sterile neutrino is behind these phenomena is far from clear and demands many more complementary measurements. Whatever the result will be – the discovery or rejection of a sterile neutrino, the observation of a different dark matter particle or something else – its impact on fundamental physics will be tremendous, solving many issues and raising many more exiting questions.

Appendix A

Interaction of X-rays and electrons in matter

The absorption of X-rays within a silicon detector is dominated by photoabsorption for energies below $\sim 100\,\mathrm{keV}$. The attenuation is described by an exponential law:

$$I = I_0 e^{-\mu d}, \tag{A.1}$$

where I is the intensity at depth d, I_0 the initial intensity and μ the attenuation coefficient. The attenuation length λ is defined as the depth, where the intensity dropped to $1/e$ of its original intensity. The coefficients are tabulated in [BHS+10]. Following attenuation lengths are obtained:

$E = 5\,\mathrm{keV}$: $\lambda = 18\,\mu\mathrm{m}$;

$E = 10\,\mathrm{keV}$: $\lambda = 1.3\,\mathrm{mm}$;

$E = 20\,\mathrm{keV}$: $\lambda = 11\,\mathrm{mm}$.

The photoabsorption produces electrons, which lose their energy in a silicon detector due to subsequent inelastic scattering processes, that ionize the material and thus produce a charge cloud. Electron radiation is detected in the same way. The interaction length of electrons is defined via their stopping power. In contrast to X-rays, electrons continuously lose energy when traveling though the substrate. As they slow down, the number of scatterings and the energy loss per path length increase, resulting in the so-called Bragg peak. The ranges of the electrons are calculated within a continuous slowing down approximation and are tabulated in [BCZ+05]:

$E = 10\,\mathrm{keV}$: $\lambda = 1.5\,\mu\mathrm{m}$;

$E = 20\,\mathrm{keV}$: $\lambda = 4.9\,\mu\mathrm{m}$.

As one can see, in the energy region of interest electrons are stopped after a few μm, while X-rays can easily transmit the 450 μm thick detectors.

Appendix B

Troitsk calibration

B.1 Data

date	run №	initial energy [keV]	ch1: fitted mean energy [keV]	ch1: fitted fwhm [keV]	enc [e^-]	
01.06.17	3	20	(20.08±0.01)	(0.43±0.04)	42.57	HV without B-field
01.06.17	4	15	(15.11±0.01)	(0.40±0.03)	41.51	HV without B-field
01.06.17	6	15	(15.03±0.01)	(0.44±0.02)	45.66	HV with B-field
01.06.17	7	16	(16.03±0.00)	(0.42±0.02)	43.58	HV with B-field
01.06.17	8	17	(17.01±0.00)	(0.42±0.01)	42.10	HV with B-field
01.06.17	9	18	(17.98±0.01)	(0.50±0.02)	52.59	HV with B-field
01.06.17	10	14	(14.03±0.00)	(0.43±0.01)	44.86	HV with B-field
01.06.17	11	13	(13.04±0.01)	(0.43±0.02)	45.08	HV with B-field
01.06.17	17	19	(18.99±0.00)	(0.45±0.01)	46.38	E-Gun
01.06.17	18	19	(18.99±0.00)	(0.44±0.01)	44.71	E-Gun
01.06.17	19	19	(18.99±0.00)	(0.45±0.01)	46.13	E-Gun
01.06.17	20	19	(19.01±0.00)	(0.46±0.00)	46.73	E-Gun
01.06.17	21	19	(19.01±0.00)	(0.44±0.01)	44.54	E-Gun
01.06.17	22	19	(19.02±0.00)	(0.44±0.01)	44.48	E-Gun
01.06.17	23	19	(18.99±0.00)	(0.46±0.01)	47.07	E-Gun
01.06.17	24	19	(19.01±0.00)	(0.44±0.01)	45.03	E-Gun
01.06.17	25	16	(15.99±0.00)	(0.45±0.01)	46.71	E-Gun
01.06.17	26	14	(13.97±0.00)	(0.44±0.01)	47.02	E-Gun
01.06.17	27	15	(15.03±0.00)	(0.43±0.01)	45.05	E-Gun
03.06.17	15	20	(20.00±0.00)	(0.44±0.01)	43.96	HV with B-field
03.06.17	16	20	(19.99±0.01)	(0.47±0.05)	47.82	HV without B-field
03.06.17	17	15	(14.97±0.00)	(0.45±0.01)	47.05	HV without B-field
03.06.17	18	18	(17.91±0.01)	(0.51±0.03)	53.68	HV without B-field
03.06.17	18b	19	(18.97±0.01)	(0.41±0.04)	40.98	HV without B-field
03.06.17	19	15	(14.97±0.01)	(0.46±0.02)	49.25	HV without B-field
03.06.17	20	15	(15.02±0.01)	(0.44±0.04)	46.08	HV without B-field

Table B.1: Fitted means and fwhms of channel 1.

date	run №	initial energy [keV]	ch6: fitted mean energy [keV]	ch6: fitted fwhm [keV]	enc [e^-]	
01.06.17	3	20	(20.05±0.01)	(0.42±0.03)	41.41	HV without B-field
01.06.17	4	15	(15.06±0.01)	(0.43±0.04)	45.32	HV without B-field
01.06.17	6	15	(15.02±0.00)	(0.41±0.02)	42.80	HV with B-field
01.06.17	7	16	(16.02±0.01)	(0.43±0.01)	44.17	HV with B-field
01.06.17	8	17	(17.01±0.00)	(0.43±0.02)	43.51	HV with B-field
01.06.17	9	18	(17.97±0.01)	(0.44±0.02)	44.91	HV with B-field
01.06.17	10	14	(14.03±0.00)	(0.42±0.01)	43.69	HV with B-field
01.06.17	11	13	(13.02±0.01)	(0.42±0.02)	44.43	HV with B-field
01.06.17	17	19	(19.00±0.00)	(0.44±0.00)	45.20	E-Gun
01.06.17	18	19	(19.00±0.00)	(0.44±0.00)	44.90	E-Gun
01.06.17	19	19	(19.01±0.00)	(0.44±0.01)	45.05	E-Gun
01.06.17	20	19	(19.00±0.00)	(0.44±0.01)	44.61	E-Gun
01.06.17	21	19	(18.97±0.02)	(0.48±0.06)	49.35	E-Gun
01.06.17	22	19	(NaN±NaN)	(NaN±NaN)	NaN	E-Gun
01.06.17	23	19	(19.00±0.00)	(0.44±0.01)	44.39	E-Gun
01.06.17	24	19	(19.00±0.01)	(0.44±0.02)	44.40	E-Gun
01.06.17	25	16	(15.98±0.00)	(0.44±0.01)	46.17	E-Gun
01.06.17	26	14	(13.99±0.00)	(0.43±0.01)	45.23	E-Gun
01.06.17	27	15	(15.02±0.01)	(0.42±0.02)	43.51	E-Gun
03.06.17	15	20	(20.01±0.00)	(0.43±0.02)	42.66	HV with B-field
03.06.17	16	20	(19.98±0.01)	(0.43±0.03)	43.40	HV without B-field
03.06.17	17	15	(14.96±0.00)	(0.45±0.01)	46.89	HV without B-field
03.06.17	18	18	(17.91±0.01)	(0.43±0.05)	43.76	HV without B-field
03.06.17	18b	19	(18.96±0.01)	(0.43±0.03)	42.69	HV without B-field
03.06.17	19	15	(14.97±0.01)	(0.44±0.03)	45.79	HV without B-field
03.06.17	20	15	(15.02±0.01)	(0.45±0.04)	47.74	HV without B-field

Table B.2: Fitted means and fwhms of channel 6.

date	run №	initial energy [keV]	ch11: fitted mean energy [keV]	ch11: fitted fwhm [keV]	enc [e^-]	
01.06.17	3	20	(20.04±0.01)	(0.44±0.03)	44.43	HV without B-field
01.06.17	4	15	(15.04±0.01)	(0.46±0.04)	48.34	HV without B-field
01.06.17	6	15	(15.03±0.01)	(0.43±0.02)	44.95	HV with B-field
01.06.17	7	16	(16.03±0.00)	(0.42±0.01)	43.19	HV with B-field
01.06.17	8	17	(17.02±0.00)	(0.41±0.01)	41.74	HV with B-field
01.06.17	9	18	(17.99±0.01)	(0.47±0.02)	49.55	HV with B-field
01.06.17	10	14	(14.04±0.00)	(0.43±0.02)	44.55	HV with B-field
01.06.17	11	13	(13.03±0.01)	(0.43±0.03)	46.00	HV with B-field
01.06.17	17	19	(19.00±0.00)	(0.45±0.01)	45.58	E-Gun
01.06.17	18	19	(19.00±0.00)	(0.45±0.01)	45.44	E-Gun
01.06.17	19	19	(NaN±NaN)	(NaN±NaN)	NaN	E-Gun
01.06.17	20	19	(NaN±NaN)	(NaN±NaN)	NaN	E-Gun
01.06.17	21	19	(NaN±NaN)	(NaN±NaN)	NaN	E-Gun
01.06.17	22	19	(NaN±NaN)	(NaN±NaN)	NaN	E-Gun
01.06.17	23	19	(NaN±NaN)	(NaN±NaN)	NaN	E-Gun
01.06.17	24	19	(19.01±0.01)	(0.41±0.04)	40.12	E-Gun
01.06.17	25	16	(15.94±0.01)	(0.43±0.03)	45.12	E-Gun
01.06.17	26	14	(13.99±0.00)	(0.43±0.01)	45.83	E-Gun
01.06.17	27	15	(15.00±0.01)	(0.44±0.02)	46.76	E-Gun
03.06.17	15	20	(19.99±0.00)	(0.44±0.01)	43.70	HV with B-field
03.06.17	16	20	(19.96±0.01)	(0.47±0.04)	48.09	HV without B-field
03.06.17	17	15	(14.95±0.01)	(0.44±0.02)	46.77	HV without B-field
03.06.17	18	18	(17.89±0.02)	(0.51±0.06)	54.44	HV without B-field
03.06.17	18b	19	(18.95±0.01)	(0.45±0.03)	45.69	HV without B-field
03.06.17	19	15	(14.95±0.01)	(0.43±0.02)	45.25	HV without B-field
03.06.17	20	15	(15.00±0.01)	(0.44±0.04)	46.21	HV without B-field

Table B.3: Fitted means and fwhms of channel 11.

date	run №	initial energy [keV]	ch16: fitted mean energy [keV]	ch16: fitted fwhm [keV]	enc [e^-]	
01.06.17	3	20	(19.98±0.01)	(0.44±0.04)	44.88	HV without B-field
01.06.17	4	15	(15.04±0.01)	(0.43±0.05)	45.25	HV without B-field
01.06.17	6	15	(15.02±0.00)	(0.44±0.01)	46.74	HV with B-field
01.06.17	7	16	(16.01±0.01)	(0.44±0.02)	45.98	HV with B-field
01.06.17	8	17	(17.00±0.00)	(0.41±0.02)	41.36	HV with B-field
01.06.17	9	18	(17.96±0.01)	(0.50±0.02)	52.68	HV with B-field
01.06.17	10	14	(14.03±0.00)	(0.42±0.02)	44.29	HV with B-field
01.06.17	11	13	(13.03±0.01)	(0.46±0.03)	49.72	HV with B-field
01.06.17	17	19	(19.00±0.00)	(0.45±0.00)	46.27	E-Gun
01.06.17	18	19	(19.00±0.00)	(0.45±0.01)	46.51	E-Gun
01.06.17	19	19	(19.01±0.00)	(0.45±0.01)	45.96	E-Gun
01.06.17	20	19	(18.98±0.02)	(0.50±0.06)	53.17	E-Gun
01.06.17	21	19	(NaN±NaN)	(NaN±NaN)	NaN	E-Gun
01.06.17	22	19	(NaN±NaN)	(NaN±NaN)	NaN	E-Gun
01.06.17	23	19	(19.01±0.00)	(0.45±0.01)	46.57	E-Gun
01.06.17	24	19	(19.00±0.01)	(0.47±0.03)	48.08	E-Gun
01.06.17	25	16	(15.95±0.00)	(0.46±0.01)	48.53	E-Gun
01.06.17	26	14	(14.00±0.00)	(0.45±0.01)	47.30	E-Gun
01.06.17	27	15	(15.01±0.00)	(0.45±0.01)	46.82	E-Gun
03.06.17	15	20	(19.99±0.00)	(0.44±0.01)	44.87	HV with B-field
03.06.17	16	20	(19.97±0.01)	(0.47±0.04)	48.95	HV without B-field
03.06.17	17	15	(14.97±0.00)	(0.46±0.01)	48.79	HV without B-field
03.06.17	18	18	(17.90±0.01)	(0.51±0.04)	54.54	HV without B-field
03.06.17	18b	19	(18.96±0.01)	(0.44±0.03)	44.17	HV without B-field
03.06.17	19	15	(14.98±0.01)	(0.45±0.03)	47.12	HV without B-field
03.06.17	20	15	(15.02±0.01)	(0.46±0.04)	49.21	HV without B-field

Table B.4: Fitted means and fwhms of channel 16.

date	run №	initial energy [keV]	ch21: fitted mean energy [keV]	ch21: fitted fwhm [keV]	enc [e^-]	
01.06.17	3	20	(20.01±0.01)	(0.42±0.02)	41.22	HV without B-field
01.06.17	4	15	(15.06±0.01)	(0.44±0.04)	46.00	HV without B-field
01.06.17	6	15	(15.01±0.00)	(0.40±0.01)	41.10	HV with B-field
01.06.17	7	16	(16.00±0.00)	(0.42±0.01)	43.77	HV with B-field
01.06.17	8	17	(16.99±0.01)	(0.42±0.02)	42.71	HV with B-field
01.06.17	9	18	(17.97±0.01)	(0.47±0.02)	49.36	HV with B-field
01.06.17	10	14	(14.02±0.01)	(0.41±0.02)	42.91	HV with B-field
01.06.17	11	13	(13.03±0.01)	(0.44±0.03)	46.29	HV with B-field
01.06.17	17	19	(19.00±0.00)	(0.43±0.00)	43.98	E-Gun
01.06.17	18	19	(19.00±0.00)	(0.43±0.01)	43.72	E-Gun
01.06.17	19	19	(19.01±0.00)	(0.43±0.00)	43.68	E-Gun
01.06.17	20	19	(19.00±0.00)	(0.44±0.01)	44.07	E-Gun
01.06.17	21	19	(18.98±0.00)	(0.42±0.01)	42.29	E-Gun
01.06.17	22	19	(NaN±NaN)	(NaN±NaN)	NaN	E-Gun
01.06.17	23	19	(19.00±0.00)	(0.43±0.00)	43.96	E-Gun
01.06.17	24	19	(18.99±0.00)	(0.44±0.01)	44.16	E-Gun
01.06.17	25	16	(15.97±0.00)	(0.44±0.01)	46.27	E-Gun
01.06.17	26	14	(14.00±0.00)	(0.42±0.01)	44.03	E-Gun
01.06.17	27	15	(15.01±0.00)	(0.42±0.01)	43.99	E-Gun
03.06.17	15	20	(20.01±0.00)	(0.42±0.01)	42.20	HV with B-field
03.06.17	16	20	(19.98±0.02)	(0.45±0.05)	46.16	HV without B-field
03.06.17	17	15	(14.98±0.01)	(0.44±0.02)	46.27	HV without B-field
03.06.17	18	18	(17.92±0.01)	(0.50±0.04)	53.09	HV without B-field
03.06.17	18b	19	(18.96±0.01)	(0.46±0.03)	47.07	HV without B-field
03.06.17	19	15	(14.97±0.01)	(0.44±0.04)	45.91	HV without B-field
03.06.17	20	15	(15.03±0.01)	(0.44±0.04)	45.59	HV without B-field

Table B.5: Fitted means and fwhms of channel 21.

date	run №	initial energy [keV]	ch26: fitted mean energy [keV]	ch26: fitted fwhm [keV]	enc [e^-]	
01.06.17	3	20	(20.05±0.01)	(0.43±0.04)	43.52	HV without B-field
01.06.17	4	15	(15.06±0.01)	(0.44±0.05)	46.62	HV without B-field
01.06.17	6	15	(15.04±0.00)	(0.43±0.01)	45.34	HV with B-field
01.06.17	7	16	(16.05±0.00)	(0.43±0.01)	44.87	HV with B-field
01.06.17	8	17	(17.03±0.00)	(0.42±0.01)	42.10	HV with B-field
01.06.17	9	18	(17.99±0.01)	(0.45±0.03)	46.90	HV with B-field
01.06.17	10	14	(14.04±0.01)	(0.44±0.02)	46.20	HV with B-field
01.06.17	11	13	(13.03±0.01)	(0.43±0.02)	46.08	HV with B-field
01.06.17	17	19	(19.00±0.00)	(0.45±0.02)	46.55	E-Gun
01.06.17	18	19	(19.00±0.01)	(0.43±0.02)	43.87	E-Gun
01.06.17	19	19	(NaN±NaN)	(NaN±NaN)	NaN	E-Gun
01.06.17	20	19	(NaN±NaN)	(NaN±NaN)	NaN	E-Gun
01.06.17	21	19	(NaN±NaN)	(NaN±NaN)	NaN	E-Gun
01.06.17	22	19	(NaN±NaN)	(NaN±NaN)	NaN	E-Gun
01.06.17	23	19	(NaN±NaN)	(NaN±NaN)	NaN	E-Gun
01.06.17	24	19	(NaN±NaN)	(NaN±NaN)	NaN	E-Gun
01.06.17	25	16	(15.98±0.00)	(0.45±0.01)	46.59	E-Gun
01.06.17	26	14	(14.00±0.00)	(0.44±0.01)	45.96	E-Gun
01.06.17	27	15	(15.01±0.01)	(0.44±0.02)	45.50	E-Gun
03.06.17	15	20	(20.01±0.00)	(0.43±0.01)	43.39	HV with B-field
03.06.17	16	20	(20.01±0.01)	(0.44±0.03)	44.26	HV without B-field
03.06.17	17	15	(14.96±0.00)	(0.46±0.01)	48.28	HV without B-field
03.06.17	18	18	(17.92±0.01)	(0.43±0.03)	44.12	HV without B-field
03.06.17	18b	19	(18.98±0.01)	(0.42±0.03)	42.39	HV without B-field
03.06.17	19	15	(14.97±0.01)	(0.44±0.02)	46.15	HV without B-field
03.06.17	20	15	(15.02±0.01)	(0.43±0.03)	44.85	HV without B-field

Table B.6: Fitted means and fwhms of channel 26.

date	run №	initial energy [keV]	ch31: fitted mean energy [keV]	ch31: fitted fwhm [keV]	enc [e^-]	
01.06.17	3	20	(20.05±0.01)	(0.44±0.04)	43.73	HV without B-field
01.06.17	4	15	(15.07±0.01)	(0.39±0.03)	39.56	HV without B-field
01.06.17	6	15	(15.03±0.01)	(0.42±0.02)	43.40	HV with B-field
01.06.17	7	16	(16.02±0.00)	(0.43±0.01)	44.45	HV with B-field
01.06.17	8	17	(17.01±0.01)	(0.42±0.02)	42.53	HV with B-field
01.06.17	9	18	(17.97±0.01)	(0.46±0.02)	48.02	HV with B-field
01.06.17	10	14	(14.03±0.01)	(0.42±0.02)	44.20	HV with B-field
01.06.17	11	13	(13.04±0.01)	(0.41±0.02)	42.51	HV with B-field
01.06.17	17	19	(19.02±0.00)	(0.43±0.01)	43.15	E-Gun
01.06.17	18	19	(19.02±0.00)	(0.43±0.01)	43.20	E-Gun
01.06.17	19	19	(NaN±NaN)	(NaN±NaN)	NaN	E-Gun
01.06.17	20	19	(NaN±NaN)	(NaN±NaN)	NaN	E-Gun
01.06.17	21	19	(NaN±NaN)	(NaN±NaN)	NaN	E-Gun
01.06.17	22	19	(NaN±NaN)	(NaN±NaN)	NaN	E-Gun
01.06.17	23	19	(18.97±0.02)	(0.42±0.07)	42.64	E-Gun
01.06.17	24	19	(19.02±0.03)	(0.49±0.09)	50.63	E-Gun
01.06.17	25	16	(15.97±0.00)	(0.43±0.00)	44.38	E-Gun
01.06.17	26	14	(14.01±0.00)	(0.42±0.00)	44.18	E-Gun
01.06.17	27	15	(15.02±0.00)	(0.42±0.01)	43.61	E-Gun
03.06.17	15	20	(20.00±0.00)	(0.42±0.01)	41.79	HV with B-field
03.06.17	16	20	(19.96±0.02)	(0.45±0.05)	45.98	HV without B-field
03.06.17	17	15	(14.95±0.01)	(0.44±0.02)	46.60	HV without B-field
03.06.17	18	18	(17.88±0.01)	(0.49±0.05)	52.19	HV without B-field
03.06.17	18b	19	(18.94±0.01)	(0.43±0.02)	43.96	HV without B-field
03.06.17	19	15	(14.96±0.01)	(0.43±0.02)	44.34	HV without B-field
03.06.17	20	15	(15.00±0.01)	(0.42±0.02)	44.05	HV without B-field

Table B.7: Fitted means and fwhms of channel 31.

B.2 Calibration parameters

Channel 1:

$$\text{E [keV]} = \{(-84367.4 \pm 452.1) + (34.2741 \pm 0.1520) \cdot \text{channel [ADU]}\}/1000$$

Channel 6:

$$\text{E [keV]} = \{(-85685.7 \pm 376.1) + (34.8486 \pm 0.1264) \cdot \text{channel [ADU]}\}/1000$$

Channel 11:

$$\text{E [keV]} = \{(-86971.1 \pm 614.0) + (34.5980 \pm 0.2041) \cdot \text{channel [ADU]}\}/1000$$

Channel 16:

$$\text{E [keV]} = \{(-88090.9 \pm 392.5) + (34.1269 \pm 0.1270) \cdot \text{channel [ADU]}\}/1000$$

Channel 21:

$$\text{E [keV]} = \{(-90649.8 \pm 320.1) + (34.6371 \pm 0.1021) \cdot \text{channel [ADU]}\}/1000$$

Channel 26:

$$\text{E [keV]} = \{(-87904.2 \pm 662.2) + (35.1222 \pm 0.2245) \cdot \text{channel [ADU]}\}/1000$$

Channel 31:

$$\text{E [keV]} = \{(-91892.2 \pm 579.4) + (34.6279 \pm 0.1859) \cdot \text{channel [ADU]}\}/1000$$

Appendix C

Best fit values for tritium spectrum analysis parameters

parameter name	best fit value	error
normalization (13 keV)	199.8	4.1
normalization (14 keV)	494.7	7.2
normalization (15 keV)	473.2	6.7
normalization (16 keV)	636.3	8.0
normalization (17 keV)	486.7	6.5
normalization (18 keV)	502.6	6.3
normalization (20 keV)	1167.98	11.8
enc (13 keV)	45.65	1.00
enc (14 keV)	43.71	0.62
enc (15 keV)	44.41	0.63
enc (16 keV)	43.63	0.54
enc (17 keV)	42.26	0.60
enc (18 keV)	46.96	0.60
enc (20 keV)	44.37	0.43
calibration offset (13 keV)	-0.0437	0.0043
calibration offset (14 keV)	-0.0470	0.0028
calibration offset (15 keV)	-0.0315	0.0028
calibration offset (16 keV)	-0.0261	0.0025
calibration offset (17 keV)	-0.0092	0.0027
calibration offset (18 keV)	0.0181	0.0027
calibration offset (20 keV)	0.0025	0.0019
n_2 offset	0.4541	0.0533
n_2 gain	-0.0194	0.0027
n_3 offset	0.0451	0.0050
n_3 gain	-0.0010	0.0003
β offset	-0.0056	0.0542
β gain	0.0245	0.0035
b offset	-0.0903	0.1381
b gain	0.0183	0.0078
c offset	0.4168	0.1356
c gain	0.0217	0.0079

Table C.1: The best fit values and errors for the parametrization fit.

parameter name	best fit value	error
normalization	$4.6415 \cdot 10^{-13}$	$0.4786 \cdot 10^{-13}$
enc	42.9537	0.0819
calibration offset	-0.0842	0.0003
calibration gain	1.0046	0.0000
n_2 offset	-1.2041	0.0008
n_2 gain	0.1101	0.0001
n_3 offset	0.0661	0.0000
n_3 gain	-0.0024	0.0000
β offset	0.6000	0.0004
β gain	-0.0208	0.0000
b offset	-0.3150	0.0023
b gain	0.0405	0.0002
c offset	1.6762	0.0013
c gain	-0.0535	0.0001
a_{SSC}	0.0158	0.0010
b_{SSC}	0.1173	0.0021
c_{SSC}	0.8421	0.0043

Table C.2: The best fit values and errors for the tritium spectrum fit.

Appendix D

Best fit with a sterile neutrino: plots

Compared to the null-hypothesis an improved fit of the tritium spectrum is achieved when a sterile neutrino with the parameters $m = 0.75\,\mathrm{keV}$ and $\sin^2\theta = 0.4$ is included into the model function. The resulting reduced chi squared is 1.03 at 467 degrees of freedom. The fitted spectrum, energy response and SSC shape factor are shown in the following.

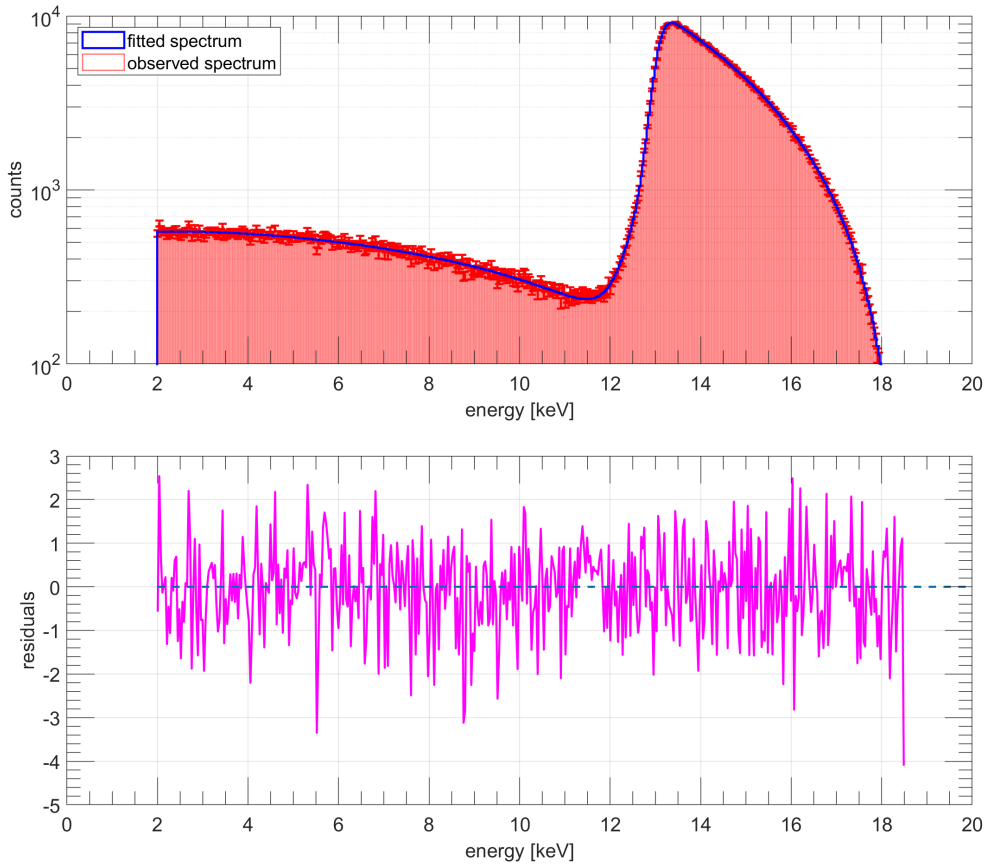

Figure D.1: On the top: the fitted tritium spectrum with a sterile neutrino (blue) compared to the observed spectrum with statistical error bars (red). On the bottom plot the residuals are shown. The reduced χ^2 is 1.03 at 467 degrees of freedom.

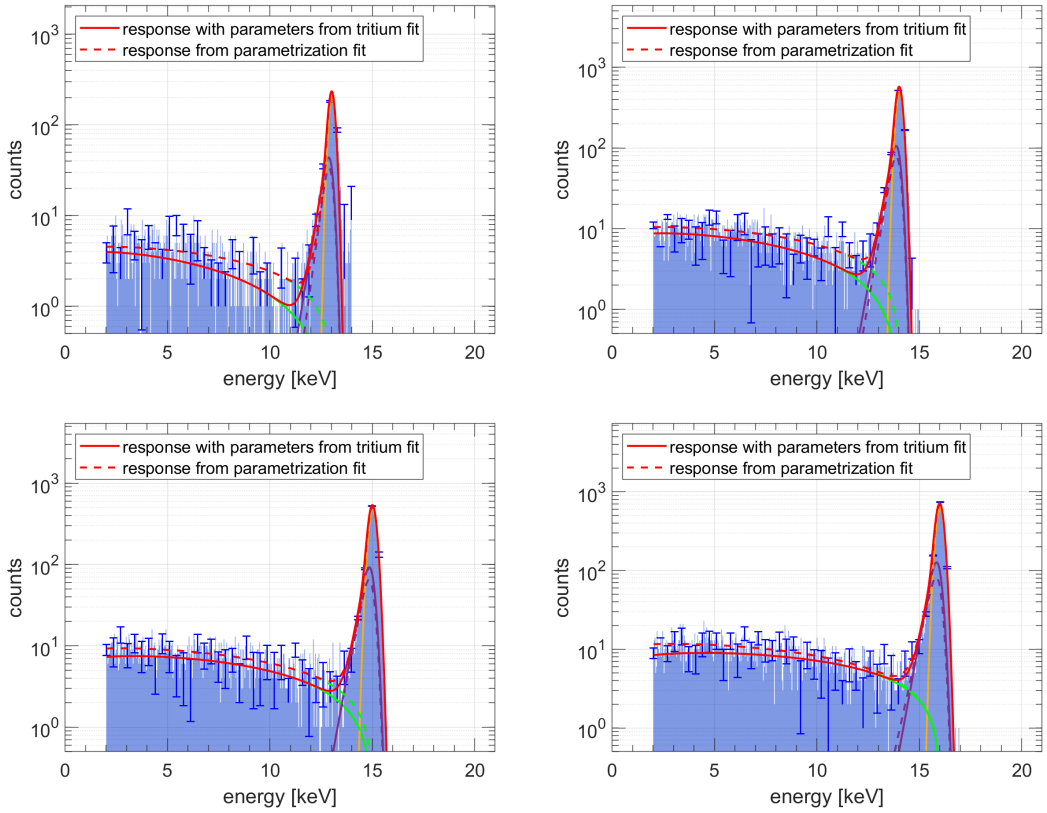

Figure D.2: The energy response with the parameters obtained from the tritium fit with a sterile neutrino (solid lines) compared to the wall response data (histogram) with the parametrization fit (dashed lines) for 13, 14, 15 and 16 keV.

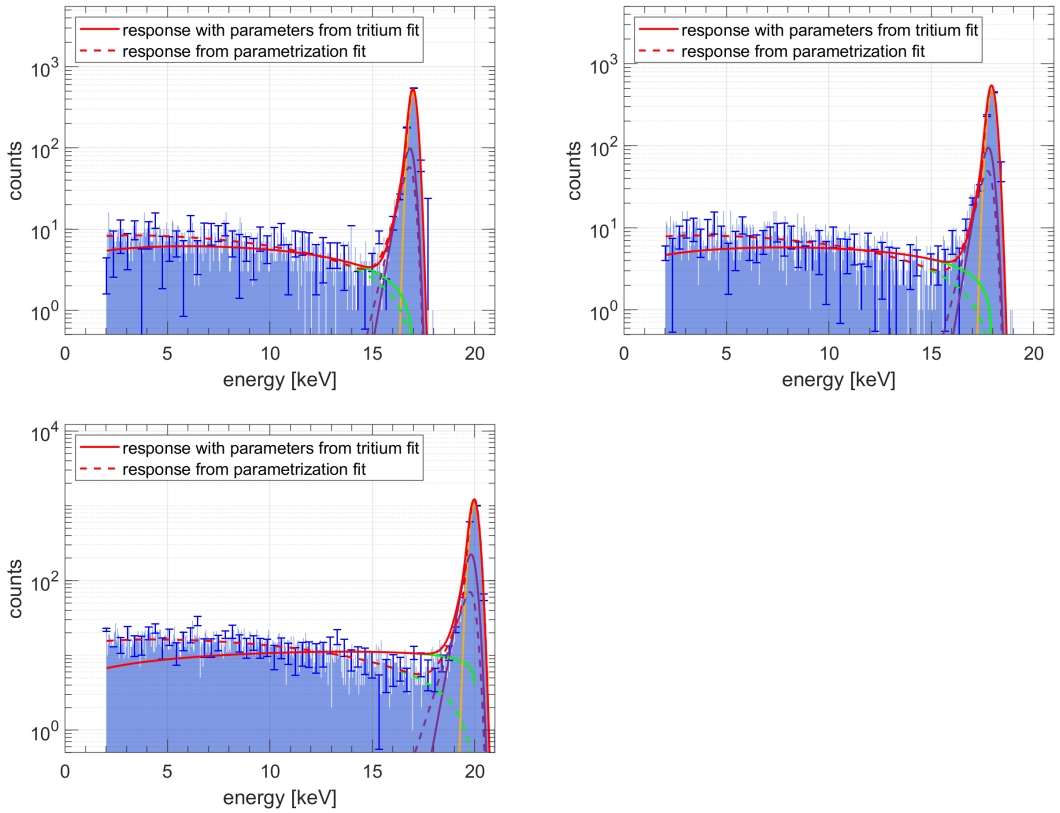

Figure D.3: The energy response with the parameters obtained from the tritium fit with a sterile neutrino (solid lines) compared to the wall response data (histogram) with the parametrization fit (dashed lines) for 17, 18 and 20 keV.

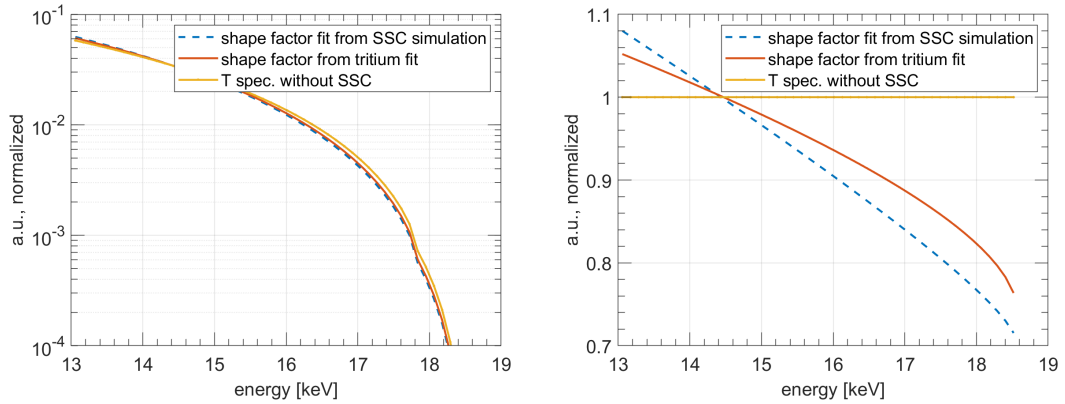

Figure D.4: **Left**: The tritium spectrum with the SSC shape factor returned from the tritium fit (red) and with the "original" shape factor obtained from the simulations (blue) in comparison to the unmodified tritium spectrum (yellow). The kink at 17.8 keV induced by the sterile neutrino is clearly visible. **Right**: the ratio of the different spectra, i.e. the SSC shape factor.

Appendix E

List of publications

Some results presented in this thesis were published by the author in

K. Altenmüller, L. Di Noto et al. A calorimeter for the precise determination of the activity of the ^{144}Ce-^{144}Pr anti-neutrino source in the SOX experiment. *JINST,* 13 (09): P09008 (2018). URL `http://dx.doi.org/10.1088/1748-0221/13/09/P09008`.

K. Altenmüller et al. Silicon drift detector prototypes for the keV-scale sterile neutrino search with TRISTAN. *Nuclear Instruments and Methods in Physics Research Section A: Accelerators, Spectrometers, Detectors and Associated Equipment*, 912: 333 – 337 (2018). ISSN 0168-9002. New Developments in Photodetection 2017, URL `http://dx.doi.org/10.1016/j.nima.2017.12.026`.

and

K. Altenmüller et al. Silicon drift detector prototypes for the keV-scale sterile neutrino search at KATRIN: detector characteristics and proof-of-concept analysis of a differential ^{3}H β-spectrum, *at the time of printing in the review process*

Bibliography

[A+65] C. V. Achar et al. Detection of muons produced by cosmic ray neutrinos deep underground. *Phys. Lett.*, 18: 196–199 (1965). URL http://dx.doi.org/10.1016/0031-9163(65)90712-2.

[A+95] P. Anselmann et al. First results from the ^{51}Cr neutrino source experiment with the GALLEX detector. *Physics Letters B*, 342(1): 440 – 450 (1995). ISSN 0370-2693. URL http://dx.doi.org/10.1016/0370-2693(94)01586-2.

[A+99] J. N. Abdurashitov et al. (SAGE). Measurement of the response of the Russian-American gallium experiment to neutrinos from a Cr-51 source. *Phys. Rev.*, C59: 2246–2263 (1999). arXiv:hep-ph/9803418, URL http://dx.doi.org/10.1103/PhysRevC.59.2246.

[A+02] Q. R. Ahmad et al. (SNO). Direct evidence for neutrino flavor transformation from neutral current interactions in the Sudbury Neutrino Observatory. *Phys. Rev. Lett.*, 89: 011301 (2002). arXiv:nucl-ex/0204008, URL http://dx.doi.org/10.1103/PhysRevLett.89.011301.

[A+06] J. Abdurashitov et al. Measurement of the response of a Ga solar neutrino experiment to neutrinos from an ^{37}Ar source. *Journal of Physics: Conference Series*, 39: 284–286 (May 2006). URL http://dx.doi.org/10.1088/1742-6596/39/1/070.

[A+14] Y. Abe et al. (Double Chooz). Improved measurements of the neutrino mixing angle θ_{13} with the Double Chooz detector. *JHEP*, 10: 086 (2014). [Erratum: JHEP02,074(2015)], arXiv:1406.7763, URL http://dx.doi.org/10.1007/JHEP02(2015)074,10.1007/JHEP10(2014)086.

[A+15a] D. N. Abdurashitov et al. The current status of "Troitsk nu-mass" experiment in search for sterile neutrino. *JINST*, 10(10): T10005 (2015). arXiv:1504.00544, URL http://dx.doi.org/10.1088/1748-0221/10/10/T10005.

[A+15b] J. Amsbaugh et al. Focal-plane detector system for the KATRIN experiment. *Nuclear Instruments and Methods in Physics Research Section A: Accelerators, Spectrometers, Detectors and Associated Equipment*, 778: 40 – 60 (2015). ISSN 0168-9002. URL http://dx.doi.org/10.1016/j.nima.2014.12.116.

[A+16] F. P. An et al. (Daya Bay). Measurement of the Reactor Antineutrino Flux and Spectrum at Daya Bay. *Phys. Rev. Lett.*, 116(6): 061801 (2016). [Erratum: Phys. Rev. Lett.118,no.9,099902(2017)], arXiv:1508.

04233, URL http://dx.doi.org/10.1103/PhysRevLett.116.061801, 10.1103/PhysRevLett.118.099902.

[A+17a] J. N. Abdurashitov et al. First measurements in search for keV-sterile neutrino in tritium beta-decay by Troitsk nu-mass experiment. *Pisma Zh. Eksp. Teor. Fiz.*, 105(12): 723–724 (2017). [JETP Lett. 105, no.12, 753 (2017)], arXiv:1703.10779, URL http://dx.doi.org/10.1134/S0021364017120013.

[A+17b] Y. Abreu et al. A novel segmented-scintillator antineutrino detector. *Journal of Instrumentation*, 12(04): P04024–P04024 (Apr 2017). URL http://dx.doi.org/10.1088/1748-0221/12/04/p04024.

[A+17c] R. Adhikari et al. A White Paper on keV sterile neutrino Dark Matter. *J. Cosmol. Astropart. Phys.*, 2017(01): 025 (2017).

[A+18a] M. G. Aartsen et al. (IceCube, Fermi-LAT, MAGIC, AGILE, ASAS-SN, HAWC, H.E.S.S., INTEGRAL, Kanata, Kiso, Kapteyn, Liverpool Telescope, Subaru, Swift NuSTAR, VERITAS, VLA/17B-403). Multimessenger observations of a flaring blazar coincident with high-energy neutrino IceCube-170922A. *Science*, 361(6398): eaat1378 (2018). arXiv:1807.08816, URL http://dx.doi.org/10.1126/science.aat1378.

[A+18b] C. Adams et al. (MicroBooNE). First Measurement of ν_μ Charged-Current π^0 Production on Argon with a LArTPC (2018). arXiv:1811.02700.

[A+18c] I. Alekseev et al. (DANSS). Search for sterile neutrinos at the DANSS experiment. *Phys. Lett.*, B787: 56–63 (2018). arXiv:1804.04046, URL http://dx.doi.org/10.1016/j.physletb.2018.10.038.

[A+18d] N. Allemandou et al. (STEREO). The STEREO Experiment. *JINST*, 13(07): P07009 (2018). arXiv:1804.09052, URL http://dx.doi.org/10.1088/1748-0221/13/07/P07009.

[A+18e] J. Ashenfelter et al. (PROSPECT). First search for short-baseline neutrino oscillations at HFIR with PROSPECT. *Phys. Rev. Lett.*, 121(25): 251802 (2018). arXiv:1806.02784, URL http://dx.doi.org/10.1103/PhysRevLett.121.251802.

[A+19] P. Adamson et al. (MINOS+). Search for sterile neutrinos in MINOS and MINOS+ using a two-detector fit. *Phys. Rev. Lett.*, 122(9): 091803 (2019). arXiv:1710.06488, URL http://dx.doi.org/10.1103/PhysRevLett.122.091803.

[AA+01] A. Aguilar-Arevalo et al. (LSND). Evidence for neutrino oscillations from the observation of anti-neutrino(electron) appearance in a anti-neutrino(muon) beam. *Phys. Rev.*, D64: 112007 (2001). arXiv:hep-ex/0104049, URL http://dx.doi.org/10.1103/PhysRevD.64.112007.

[AA+18] A. A. Aguilar-Arevalo et al. (MiniBooNE). Significant Excess of Electron Like Events in the MiniBooNE Short-Baseline Neutrino Experiment. *Phys. Rev. Lett.*, 121(22): 221801 (2018). arXiv:1805.12028, URL http://dx.doi.org/10.1103/PhysRevLett.121.221801.

[ABB+11] V. N. Aseev et al. Upper limit on the electron antineutrino mass from the Troitsk experiment. *Phys. Rev. D*, 84: 112003 (Dec 2011).

[ABB+18] K. Altenmüller et al. Silicon drift detector prototypes for the keV-scale sterile neutrino search with TRISTAN. *Nuclear Instruments and Methods in Physics Research Section A: Accelerators, Spectrometers, Detectors and Associated Equipment*, 912: 333 – 337 (2018). ISSN 0168-9002. New Developments In Photodetection 2017, URL http://dx.doi.org/10.1016/j.nima.2017.12.026.

[ADN+18] K. Altenmüller, L. Di Noto et al. A calorimeter for the precise determination of the activity of the ^{144}Ce-^{144}Pr anti-neutrino source in the SOX experiment. *JINST*, 13(09): P09008 (2018). URL http://dx.doi.org/10.1088/1748-0221/13/09/P09008.

[AE+17] A. Ashtari Esfahani et al. (Project 8). Determining the neutrino mass with cyclotron radiation emission spectroscopy - Project 8. *J. Phys.*, G44(5): 054004 (2017). arXiv:1703.02037, URL http://dx.doi.org/10.1088/1361-6471/aa5b4f.

[AGG+16] M. Archidiacono, S. Gariazzo, C. Giunti, S. Hannestad, R. Hansen, M. Laveder, and T. Tram. Pseudoscalar-sterile neutrino interactions: reconciling the cosmos with neutrino oscillations. *JCAP*, 1608(08): 067 (2016). arXiv:1606.07673, URL http://dx.doi.org/10.1088/1475-7516/2016/08/067.

[AHCM19] A. Abada, Á. Hernández-Cabezudo, and X. Marcano. Beta and Neutrinoless Double Beta Decays with KeV Sterile Fermions. *JHEP*, 01: 041 (2019). arXiv:1807.01331, URL http://dx.doi.org/10.1007/JHEP01(2019)041.

[AKL+17] V. Atroschenko, V. Kopeikin, E. Litvinovich, L. Lukyanchenko, I. Machulin, M. Skorokhvatov, and O. Titov. Calculation and measurement of ^{144}Ce-^{144}Pr β-spectrum. *Journal of Physics: Conference Series*, 934: 012012 (Dec 2017). URL http://dx.doi.org/10.1088/1742-6596/934/1/012012.

[Alt15] K. Altenmüller. *Search for sterile neutrino oscillations with SOX/Borexino: development and characterization of a thermal calorimeter for the precision measurement of the ^{144}Ce -^{144}Pr electron antineutrino source strength.* Master's thesis, Technical University of Munich (2015).

[ANS] ANSYS® Academic Research Mechanical. www.ansys.com.

[B+06] H. Back et al. (Borexino). CNO and pep neutrino spectroscopy in Borexino: Measurement of the deep underground production of cosmogenic 11C in organic liquid scintillator. *Phys. Rev.*, C74: 045805 (2006). arXiv:hep-ex/0601035, URL http://dx.doi.org/10.1103/PhysRevC.74.045805.

[B+12] K. Bays et al. (Super-Kamiokande). Supernova Relic Neutrino Search at Super-Kamiokande. *Phys. Rev.*, D85: 052007 (2012). arXiv:1111.5031, URL http://dx.doi.org/10.1103/PhysRevD.85.052007.

[B+19] M. G. Betti et al. (PTOLEMY). Neutrino Physics with the PTOLEMY project (2019). arXiv:1902.05508.

[BB00] Y. Blanter and M. Büttiker. Shot noise in mesoscopic conductors. *Physics Reports*, 336(1): 1 – 166 (2000). ISSN 0370-1573. URL http://dx.doi.org/10.1016/S0370-1573(99)00123-4.

[BBC+73] H. E. Bosch, M. Behar, M. C. Cambiaggio, G. Garcia Bermudez, and L. Szybisz. Investigation of the 0-→0+ and 0-→2+ Beta Transitions in the Decay of ^{144}Pr. *Canadian Journal of Physics*, 51(21): 2260–2269 (1973).

[BBG+14] A. I. Belesev, A. I. Berlev, E. V. Geraskin, A. A. Golubev, N. A. Likhovid, A. A. Nozik, V. S. Pantuev, V. I. Parfenov, and A. K. Skasyrskaya. The search for an additional neutrino mass eigenstate in the 2-100 eV region from 'Troitsk ν-mass' data: a detailed analysis. *J. Phys.*, G41: 015001 (2014). arXiv:1307.5687, URL http://dx.doi.org/10.1088/0954-3899/41/1/015001.

[BBK11] M. Boylan-Kolchin, J. S. Bullock, and M. Kaplinghat. Too big to fail? The puzzling darkness of massive Milky Way subhaloes. *MNRAS*, 415: L40–L44 (Jul 2011). arXiv:1103.0007, URL http://dx.doi.org/10.1111/j.1745-3933.2011.01074.x.

[BCG+18] V. Barinov, B. Cleveland, V. Gavrin, D. Gorbunov, and T. Ibragimova. Revised neutrino-gallium cross section and prospects of BEST in resolving the Gallium anomaly. *Phys. Rev.*, D97(7): 073001 (2018). arXiv:1710.06326, URL http://dx.doi.org/10.1103/PhysRevD.97.073001.

[BCZ+05] M. Berger, J. Coursey, M. Zucker, , and J. Chang. ESTAR, PSTAR, and ASTAR: Computer Programs for Calculating Stopping-Power and Range Tables for Electrons, Protons, and Helium Ions (version 1.2.3) (2005).

[Ber19] L. Bernard (STEREO). Results from the STEREO Experiment with 119 days of Reactor-on Data (2019). Contribution to the 2019 EW/QCD/Gravitation session of the 54th Rencontres de Moriond, arXiv:1905.11896.

[Bez08] F. L. Bezrukov. nuMSM and its experimental tests. *J. Phys. Conf. Ser.*, 110: 082002 (2008). arXiv:0710.2501, URL http://dx.doi.org/10.1088/1742-6596/110/8/082002.

[BFF+11] L. Bombelli, C. Fiorini, T. Frizzi, R. Alberti, and A. Longoni. "CUBE", A low-noise CMOS preamplifier as alternative to JFET front-end for high-count rate spectroscopy. In *2011 IEEE Nuclear Science Symposium Conference Record*, pages 1972–1975 (Oct 2011).

[BGW+15] M. Bendel et al. iPhos, a new technique for the CALIFA CsI(Tl) calorimeter. *Journal of Physics: Conference Series*, 587 (Feb 2015). URL http://dx.doi.org/10.1088/1742-6596/587/1/012049.

[BHS+10] M. Berger, J. Hubbell, S. Seltzer, J. Chang, J. Coursey, R. Sukumar, D. Zucker, and K. Olsen. XCOM: Photon Cross Section Database (version 1.5) (2010).

[BMF+14] E. Bulbul, M. Markevitch, A. Foster, R. K. Smith, M. Loewenstein, and S. W. Randall. Detection of an Unidentified Emission Line in the Stacked X-Ray Spectrum of Galaxy Clusters. *ApJ*, 789: 13 (Jul 2014). arXiv:1402.2301.

[BMS18] P. Boldrini, R. Mohayaee, and J. Silk. Does Fornax have a cored halo? Implications for the nature of dark matter (2018). arXiv:1806.09591.

[Bor09] Borexino Collaboration. The Borexino detector at the Laboratori Nazionali del Gran Sasso. *Nuclear Instruments and Methods in Physics Research Section A: Accelerators, Spectrometers, Detectors and Associated Equipment*, 600(3): 568 – 593 (2009). ISSN 0168-9002. URL http://dx.doi.org/10.1016/j.nima.2008.11.076.

[Bor14] Borexino Collaboration. Final results of Borexino Phase-I on low-energy solar neutrino spectroscopy. *Phys. Rev. D*, 89: 112007 (Jun 2014). URL http://dx.doi.org/10.1103/PhysRevD.89.112007.

[Bor15a] Borexino Collaboration. Spectroscopy of geoneutrinos from 2056 days of Borexino data. *Phys. Rev. D*, 92: 031101 (Aug 2015). URL http://dx.doi.org/10.1103/PhysRevD.92.031101.

[Bor15b] Borexino Collaboration. Test of Electric Charge Conservation with Borexino. *Phys. Rev. Lett.*, 115: 231802 (Dec 2015). URL http://dx.doi.org/10.1103/PhysRevLett.115.231802.

[Bor17a] Borexino Collaboration. A Search for Low-energy Neutrinos Correlated with Gravitational Wave Events GW 150914, GW 151226, and GW 170104 with the Borexino Detector. *The Astrophysical Journal*, 850(1): 21 (Nov 2017). URL http://dx.doi.org/10.3847/1538-4357/aa9521.

[Bor17b] Borexino Collaboration. Borexino's search for low-energy neutrino and antineutrino signals correlated with gamma-ray bursts. *Astroparticle Physics*, 86: 11 – 17 (2017). ISSN 0927-6505. URL http://dx.doi.org/10.1016/j.astropartphys.2016.10.004.

[Bor17c] Borexino Collaboration. Limiting neutrino magnetic moments with Borexino Phase-II solar neutrino data. *Phys. Rev. D*, 96: 091103 (Nov 2017). URL http://dx.doi.org/10.1103/PhysRevD.96.091103.

[Bor18] Borexino Collaboration. Comprehensive measurement of pp-chain solar neutrinos. *Nature*, 562: 505–510 (Oct 2018). URL http://dx.doi.org/10.1038/s41586-018-0624-y.

[Bor19] Borexino Collaboration. Modulations of the Cosmic Muon Signal in Ten Years of Borexino Data. *JCAP*, 1902: 046 (2019). arXiv:1808.04207, URL http://dx.doi.org/10.1088/1475-7516/2019/02/046.

[BPT80] G. Beamson, H. Q. Porter, and D. W. Turner. The collimating and magnifying properties of a superconducting field photoelectron spectrometer. *Journal of Physics E: Scientific Instruments*, 13(1): 64–66 (Jan 1980). URL http://dx.doi.org/10.1088/0022-3735/13/1/018.

[BRI09] A. Boyarsky, O. Ruchayskiy, and D. Iakubovskyi. A Lower bound on the mass of Dark Matter particles. *JCAP*, 0903: 005 (2009). arXiv:0808.3902, URL http://dx.doi.org/10.1088/1475-7516/2009/03/005.

[BRIF14] A. Boyarsky, O. Ruchayskiy, D. Iakubovskyi, and J. Franse. Unidentified Line in X-Ray Spectra of the Andromeda Galaxy and Perseus Galaxy Cluster. *Phys. Rev. Lett.*, 113: 251301 (Dec 2014).

[BRN+97] I. M. Balakin, A. N. Roshchin, S. L. Nikulin, V. T. Il'inykh, E. G. Dzekun, V. P. Ufimtsev, and P. P. Shevtsev. Filtrational and extractional equipment for reprocessing radioactive solutions. *Atomic Energy*, 83(6): 913–919 (Dec 1997). ISSN 1573-8205. URL http://dx.doi.org/10.1007/BF02418102.

[Bro02] G. Brown. The History of the Darcy-Weisbach Equation for Pipe Flow Resistance. *Proc. Environ. Water Resour. Hist.*, 38 (Oct 2002). URL http://dx.doi.org/10.1061/40650(2003)4.

[BRS09] A. Boyarsky, O. Ruchayskiy, and M. Shaposhnikov. The Role of sterile neutrinos in cosmology and astrophysics. *Ann. Rev. Nucl. Part. Sci.*, 59: 191–214 (2009). arXiv:0901.0011, URL http://dx.doi.org/10.1146/annurev.nucl.010909.083654.

[Buc14] W. Buchmüller. Leptogenesis. *Scholarpedia*, 9(3): 11471 (2014). Revision #144189, URL http://dx.doi.org/10.4249/scholarpedia.11471.

[BWGD10] O. Braissant, D. Wirz, B. Göpfert, and A. Daniels. Biomedical Use of Isothermal Microcalorimeters. *Sensors*, 10(10): 9369–9383 (2010). ISSN 1424-8220. URL http://dx.doi.org/10.3390/s101009369.

[C+16] J. H. Choi et al. (RENO). Observation of Energy and Baseline Dependent Reactor Antineutrino Disappearance in the RENO Experiment. *Phys. Rev. Lett.*, 116(21): 211801 (2016). arXiv:1511.05849, URL http://dx.doi.org/10.1103/PhysRevLett.116.211801.

[CBF+18] N. Cappelluti, E. Bulbul, A. Foster, P. Natarajan, M. C. Urry, M. W. Bautz, F. Civano, E. Miller, and R. K. Smith. Searching for the 3.5 keV Line in the Deep Fields with Chandra: the 10 Ms observations. *Astrophys. J.*, 854(2): 179 (2018). arXiv:1701.07932, URL http://dx.doi.org/10.3847/1538-4357/aaaa68.

[CCGV11] G. Cowan, K. Cranmer, E. Gross, and O. Vitells. Asymptotic formulae for likelihood-based tests of new physics. *Eur. Phys. J.*, C71: 1554 (2011). [Erratum: Eur. Phys. J.C73,2501(2013)], arXiv:1007.1727, URL http://dx.doi.org/10.1140/epjc/s10052-011-1554-0, 10.1140/epjc/s10052-013-2501-z.

[CDF+13] R. N. Cahn, D. A. Dwyer, S. J. Freedman, W. C. Haxton, R. W. Kadel, Yu. G. Kolomensky, K. B. Luk, P. McDonald, G. D. Orebi Gann, and A. W. P. Poon. White Paper: Measuring the Neutrino Mass Hierarchy. In *Proceedings, 2013 Community Summer Study on the Future of U.S. Particle Physics: Snowmass on the Mississippi (CSS2013): Minneapolis, MN, USA, July 29-August 6, 2013* (2013). arXiv:1307.5487, URL http://www.slac.stanford.edu/econf/C1307292/docs/submittedArxivFiles/1307.5487.pdf.

[CDJ+17] J. P. Conlon, F. Day, N. Jennings, S. Krippendorf, and M. Rummel. Consistency of Hitomi, XMM-Newton, and Chandra 3.5 keV data from Perseus. *Phys. Rev.*, D96(12): 123009 (2017). arXiv:1608.01684, URL http://dx.doi.org/10.1103/PhysRevD.96.123009.

[CFL+11] M. Cribier, M. Fechner, T. Lasserre, A. Letourneau, D. Lhuillier, G. Mention, D. Franco, V. Kornoukhov, and S. Schönert. Proposed Search for a Fourth Neutrino with a PBq Antineutrino Source. *Phys. Rev. Lett.*, 107: 201801 (Nov 2011). URL http://dx.doi.org/10.1103/PhysRevLett.107.201801.

[CGCM19] X. Chu, C. Garcia-Cely, and H. Murayama. Velocity Dependence from Resonant Self-Interacting Dark Matter. *Phys. Rev. Lett.*, 122: 071103 (Feb 2019). URL http://dx.doi.org/10.1103/PhysRevLett.122.071103.

[Col07] R. Collé. Classical radionuclidic calorimetry. *Metrologia*, 44(4): S118–S126 (Aug 2007). URL http://dx.doi.org/10.1088/0026-1394/44/4/s15.

[Col17] N. Collaboration (NEOS Collaboration). Sterile Neutrino Search at the NEOS Experiment. *Phys. Rev. Lett.*, 118: 121802 (Mar 2017). URL http://dx.doi.org/10.1103/PhysRevLett.118.121802.

[COM] COMSOL Multiphysics® v. 4.4. www.comsol.com.

[Coo97] N. Cooper. Celebrating the neutrino. *Los Alamos Science, Number 25* (1997). URL http://dx.doi.org/10.2172/569122.

[Cow98] G. Cowan. *Statistical Data Analysis*. Oxford Science Publication (1998).

[CRH+56] C. L. Cowan, F. Reines, F. B. Harrison, H. W. Kruse, and A. D. McGuire. Detection of the free neutrino: A Confirmation. *Science*, 124: 103–104 (1956). URL http://dx.doi.org/10.1126/science.124.3212.103.

[Csi57] J. Csikai. Photographic evidence for the existence of the neutrino. *Il Nuovo Cimento (1955-1965)*, 5(4): 1011–1012 (Apr 1957). ISSN 1827-6121. URL http://dx.doi.org/10.1007/BF02903226.

[Dan68] H. Daniel. Shapes of Beta-Ray Spectra. *Rev. Mod. Phys.*, 40: 659–672 (Jul 1968). URL http://dx.doi.org/10.1103/RevModPhys.40.659.

[Dan18] M. Danilov. Searches for sterile neutrinos at very short baseline reactor experiments. In *4th International Conference on Particle Physics and Astrophysics (ICPPA 2018) Moscow, Russia, October 22-26, 2018* (2018). arXiv:1812.04085.

[DDL+18] A. V. Derbin, I. S. Drachnev, I. S. Lomskaya, V. N. Muratova, N. V. Pilipenko, D. A. Semenov, L. M. Tukkhonen, E. V. Unzhakov, and A. K. Khusainov. Search for a Neutrino with a Mass of 0.01-1.0 MeV in Beta Decays of ^{144}Ce-^{144}Pr Nuclei. *JETP Lett.*, 108(8): 499–503 (2018). [Pisma Zh. Eksp. Teor. Fiz.108,no.8,531(2018)], URL http://dx.doi.org/10.1134/S0021364018200067.

[DGG+62] G. Danby, J.-M. Gaillard, K. Goulianos, L. M. Lederman, N. Mistry, M. Schwartz, and J. Steinberger. Observation of High-Energy Neutrino Reactions and the Existence of Two Kinds of Neutrinos. *Phys. Rev. Lett.*, 9: 36–44 (Jul 1962). URL http://dx.doi.org/10.1103/PhysRevLett.9.36.

[DHCK+18] M. Dentler, A. Hernández-Cabezudo, J. Kopp, P. A. N. Machado, M. Maltoni, I. Martinez-Soler, and T. Schwetz. Updated Global Analysis of Neutrino Oscillations in the Presence of eV-Scale Sterile Neutrinos. *JHEP*, 08: 010 (2018). arXiv:1803.10661, URL http://dx.doi.org/10.1007/JHEP08(2018)010.

[DHH68] R. Davis, D. S. Harmer, and K. C. Hoffman. Search for Neutrinos from the Sun. *Phys. Rev. Lett.*, 20: 1205–1209 (May 1968). URL http://dx.doi.org/10.1103/PhysRevLett.20.1205.

[DK66] H. Daniel and G. Kaschl. Spektralformen von (0→0)-β-Übergängen mit Paritätswechsel: ^{144}Ce, ^{144}Pr und ^{166}Ho. *Nuclear Physics*, 76(1): 97–117 (1966). ISSN 0029-5582. URL http://dx.doi.org/10.1016/0029-5582(66)90961-8.

[DLP90] J. Deutsch, M. Lebrun, and R. Prieels. Searches for admixture of massive neutrinos into the electron flavour. *Nuclear Physics A*, 518(1): 149 – 155 (1990). ISSN 0375-9474. URL http://dx.doi.org/10.1016/0375-9474(90)90541-S.

[Dre13] M. Drewes. The Phenomenology of Right Handed Neutrinos. *International Journal of Modern Physics E*, 22(8): 1330019-593 (Aug 2013). arXiv:1303.6912, URL http://dx.doi.org/10.1142/S0218301313300191.

[Dre19] M. Drewes. Auf dem Weg zu neuen Ufern. *Physik Journal 18*, 2 (2019).

[DV16] O. Dragoun and D. Vénos. Constraints on the Active and Sterile Neutrino Masses from Beta-Ray Spectra: Past, Present and Future. *J. Phys.*, 3: 77–113 (2016). arXiv:1504.07496, URL http://dx.doi.org/10.2174/1874843001603010073.

[EAS+17] S. Edayath, A. Aurisano, A. Sousa, G. Davies, L. Suter, and S. Yang. Sterile Neutrino Search in the NOvA Far Detector. In *Proceedings, Meeting of the APS Division of Particles and Fields (DPF 2017): Fermilab, Batavia, Illinois, USA, July 31 - August 4, 2017* (2017). arXiv:1710.01280, URL http://lss.fnal.gov/archive/2017/conf/fermilab-conf-17-516-nd.pdf.

[EGGHC+19] I. Esteban, M. C. Gonzalez-Garcia, A. Hernandez-Cabezudo, M. Maltoni, and T. Schwetz. Global analysis of three-flavour neutrino oscillations: synergies and tensions in the determination of θ_{23}, δ_{CP}, and the

mass ordering. *Journal of High Energy Physics*, 2019(1): 106 (Jan 2019). ISSN 1029-8479. URL http://dx.doi.org/10.1007/JHEP01(2019)106.

[Fer34] E. Fermi. Versuch einer Theorie der β-Strahlen. I. *Zeitschrift für Physik*, 88(3): 161–177 (Mar 1934). ISSN 0044-3328. URL http://dx.doi.org/10.1007/BF01351864.

[fie] Earth magnetic field caculator. www.ngdc.noaa.gov/geomag-web. Accessed: Oct. 2018.

[Fir90] Separation of californium and curium, americium, rare earths by means of chromatography with separating ions. *Radiochemistry*, 32: 79 (1990). ISSN 0033-8311.

[Fir96] R. B. Firestone. *Table of Isotopes*. Wiley-Interscience (1996).

[FKMP15] B. Follin, L. Knox, M. Millea, and Z. Pan. First Detection of the Acoustic Oscillation Phase Shift Expected from the Cosmic Neutrino Background. *Phys. Rev. Lett.*, 115: 091301 (Aug 2015). URL http://dx.doi.org/10.1103/PhysRevLett.115.091301.

[FMP+16] S. Farinon, R. Musenich, M. Pallavicini, F. Bragazzi, R. Cereseto, A. Caminata, L. D. Noto, G. Testera, and S. Zavatarelli. Thermal analysis of the anti-neutrino ^{144}Ce source calorimeter for the SOX experiment. *INFN-16-08/GE* (2016).

[FY86] M. Fukugita and T. Yanagida. Baryogenesis Without Grand Unification. *Phys. Lett.*, B174: 45–47 (1986). URL http://dx.doi.org/10.1016/0370-2693(86)91126-3.

[FY03] M. Fukugita and T. Yanagida. *Physics of Neutrinos and Applications to Astrophysics*. Springer (2003). ISBN 3-540-43800-9.

[G+13] A. Gando et al. CeLAND: search for a 4th light neutrino state with a 3 PBq ^{144}Ce-^{144}Pr electron antineutrino generator in KamLAND (2013). arXiv:1312.0896.

[GAB+01] V. Gavrin et al. Solar neutrino results from SAGE. *Nuclear Physics B - Proceedings Supplements*, 91(1): 36 – 43 (2001). ISSN 0920-5632. Neutrino 2000, URL http://dx.doi.org/10.1016/S0920-5632(00)00920-8.

[GBB+18] S. Görhardt et al. Impact of a cryogenic baffle system on the suppression of radon-induced background in the KATRIN Pre-Spectrometer. *Journal of Instrumentation*, 13(10): T10004–T10004 (Oct 2018). URL http://dx.doi.org/10.1088/1748-0221/13/10/t10004.

[GBC+09] O. Gevin, P. Baron, X. Coppolani, F. Daly, E. Delanges, O. Limousin, F. Lugiez, A. Meuris, F. Pinsard, and D. Renaud. IDeF-X ECLAIRs: A CMOS ASIC for the Readout of CdTe and CdZnTe Detectors for High Resolution Spectroscopy . *IEEE Trans. Nucl. Sci.*, 56 (Aug 2009).

[GBC+17] L. Gastaldo et al. The electron capture in 163Ho experiment – ECHo. *The European Physical Journal Special Topics*, 226(8): 1623–1694 (Jun

2017). ISSN 1951-6401. URL http://dx.doi.org/10.1140/epjst/e2017-70071-y.

[GBF+18] A. Genina, A. Benítez-Llambay, C. S. Frenk, S. Cole, A. Fattahi, J. F. Navarro, K. A. Oman, T. Sawala, and T. Theuns. The core-cusp problem: a matter of perspective. *MNRAS*, 474: 1398–1411 (Feb 2018). arXiv:1707.06303, URL http://dx.doi.org/10.1093/mnras/stx2855.

[GDH+15] O. Gevin, E. Delagnes, D. Huynh, O. Limousin, and F. Lugiez. IDeF-X BD: A low noise dual polarity ASIC for the readout of Silicon and CdTe detectors. In *2015 IEEE Nuclear Science Symposium and Medical Imaging Conference (NSS/MIC)*, pages 1–5 (Oct 2015).

[GDM+97] Y. V. Glagolenko, E. G. Dzekun, G. M. Medvedev, S. I. Povnyi, V. P. Ufimtsev, and B. S. Zakharkin. Reprocessing spent fuel from nuclear power stations and liquid radioactive waste at the Mayak processing center. *Atomic Energy*, 83(6): 904–909 (Dec 1997). ISSN 1573-8205. URL http://dx.doi.org/10.1007/BF02418100.

[GER18] GERDA Collaboration (GERDA Collaboration). Improved Limit on Neutrinoless Double-β Decay of ^{76}Ge from GERDA Phase II. *Phys. Rev. Lett.*, 120: 132503 (Mar 2018). URL http://dx.doi.org/10.1103/PhysRevLett.120.132503.

[GFGV01] M. Galeazzi, F. Fontanelli, F. Gatti, and S. Vitale. Limits on the Existence of Heavy Neutrinos in the Range 50–1000 eV from the Study of the ^{187}Re Beta Decay. *Phys. Rev. Lett.*, 86: 1978–1981 (Mar 2001). URL http://dx.doi.org/10.1103/PhysRevLett.86.1978.

[GGE58] R. L. Graham, J. S. Geiger, and T. A. Eastwood. Experimental Evidence for Axial Vector Interaction in the Disintegration of ^{144}Pr. *Canadian Journal of Physics*, 36(8): 1084–1111 (1958). URL http://dx.doi.org/10.1139/p58-115.

[GGH+16] A. Gando et al. (KamLAND-Zen Collaboration). Search for Majorana Neutrinos Near the Inverted Mass Hierarchy Region with KamLAND-Zen. *Phys. Rev. Lett.*, 117: 082503 (Aug 2016). URL http://dx.doi.org/10.1103/PhysRevLett.117.082503.

[GGL+16] S. Gariazzo, C. Giunti, M. Laveder, Y. F. Li, and E. M. Zavanin. Light sterile neutrinos. *J. Phys.*, G43: 033001 (2016). arXiv:1507.08204, URL http://dx.doi.org/10.1088/0954-3899/43/3/033001.

[GJGM18] K. Galliez, G. Jossens, A. Godot, and C. Mathonat. Characterization of Low Level Wastes: a new design for calorimetric measurement. *EPJ Web of Conferences*, 170: 07003 (Jan 2018). URL http://dx.doi.org/10.1051/epjconf/201817007003.

[GKST14] A. S. Gerasimov, V. N. Kornoukhov, I. S. Sal'dikov, and G. V. Tikhomirov. Production of High Specific Activity ^{144}Ce for Artificial Sources of Antineutrinos. *Atomic Energy*, 116(1): 54–59 (May 2014). ISSN 1573-8205. URL http://dx.doi.org/10.1007/s10512-014-9816-1.

[GL19] C. Giunti and T. Lasserre. eV-scale Sterile Neutrinos (2019). arXiv:1901.08330.

[GLL+12] C. Giunti, M. Laveder, Y. F. Li, Q. Y. Liu, and H. W. Long. Update of Short-Baseline Electron Neutrino and Antineutrino Disappearance. *Phys. Rev.*, D86: 113014 (2012). arXiv:1210.5715, URL http://dx.doi.org/10.1103/PhysRevD.86.113014.

[GMC98] V. Gelis, G. Maslova, and E. Chuveleva. Isolation of gram amounts of Pm-147. II. Preparation of high-quality promethium by displacement complexing chromatography. *Radiochemistry*, 40: 59–63 (Mar 1998).

[Gor16] D. Gorbunov. nuMSM: the model, its predictions and experimental tests. *Proceedings of Science*, 234: 092 (Mar 2016). EPS-HEP2015, URL http://dx.doi.org/10.22323/1.234.0092.

[GR84] E. Gatti and P. Rehak. Semiconductor drift chamber - An application of a novel charge transport scheme. *Nuclear Instruments and Methods in Physics Research*, 225(3): 608 – 614 (1984). ISSN 0167-5087. URL http://dx.doi.org/10.1016/0167-5087(84)90113-3.

[Gro15] S. Groh. *Modeling of the response function and measurement of transmission properties of the KATRIN experiment*. Ph.D. thesis, Karlsruher Institut für Technologie (2015).

[GSI] GSI X-ray absorption caculator. http://web-docs.gsi.de/~stoe_exp/web_programs/x_ray_absorption/index.php. Accessed: Dec. 2016, not accessible anymore as of 2019. See also reference [BHS+10].

[GT18] M. Guainazzi and M. S. Tashiro. The Hot Universe with XRISM and Athena. In *IAU Symposium 342: Perseus in Sicily: from black hole to cluster outskirts Noto, Italy, May 14-18, 2018* (2018). arXiv:1807.06903.

[Gun64] S. Gunn. Radiometric calorimetry: A review. *Nuclear Instruments and Methods*, 29(1): 1 – 24 (1964). ISSN 0029-554X. URL http://dx.doi.org/10.1016/0029-554X(64)90002-3.

[H+74] F. J. Hasert et al. (Gargamelle Neutrino). Observation of Neutrino Like Interactions without Muon or Electron in the Gargamelle Neutrino Experiment. *Nucl. Phys.*, B73: 1–22 (1974). URL http://dx.doi.org/10.1016/0550-3213(74)90038-8.

[HAF+95] C. Hagner, M. Altmann, F. v. Feilitzsch, L. Oberauer, Y. Declais, and E. Kajfasz. Experimental search for the neutrino decay $\nu_3 \to \nu_j + e^+ + e^-$ and limits on neutrino mixing. *Phys. Rev. D*, 52: 1343–1352 (Aug 1995). URL http://dx.doi.org/10.1103/PhysRevD.52.1343.

[Hay18] A. Hayes. Status of Reactor Antineutrino Flux Predictions (Jun 2018). XXVIII International Conference on Neutrino Physics and Astrophysics, URL http://dx.doi.org/10.5281/zenodo.1287950.

[HDS95] K. H. Hiddemann, H. Daniel, and O. Schwentker. Limits on neutrino masses from the tritium beta spectrum. *Journal of Physics G: Nuclear and Particle Physics*, 21(5): 639–650 (May 1995). URL http://dx.doi.org/10.1088/0954-3899/21/5/008.

[He01] Z. He. Review of the Shockley-Ramo theorem and its application in semiconductor gamma-ray detectors. *Nuclear Instruments and Methods in Physics Research Section A: Accelerators, Spectrometers, Detectors and Associated Equipment*, 463(1): 250 – 267 (2001). ISSN 0168-9002. URL http://dx.doi.org/10.1016/S0168-9002(01)00223-6.

[HHK+14] W. Hampel et al. Final results of the ^{51}Cr neutrino source experiments in GALLEX. *Physics Letters B*, 420: 114–126 (Jun 2014).

[HKK+87] K. Hirata et al. Observation of a neutrino burst from the supernova SN1987A. *Phys. Rev. Lett.*, 58: 1490–1493 (Apr 1987). URL http://dx.doi.org/10.1103/PhysRevLett.58.1490.

[HKP+99] E. Holzschuh, W. Kündig, L. Palermo, H. Stüssi, and P. Wenk. Search for heavy neutrinos in the β-spectrum of ^{63}Ni. *Physics Letters B*, 451(1): 247 – 255 (1999). ISSN 0370-2693. URL http://dx.doi.org/10.1016/S0370-2693(99)00200-2.

[HZ19] G.-Y. Huang and S. Zhou. Impact of an eV-mass sterile neutrino on the neutrinoless double-beta decays: a Bayesian analysis (2019). arXiv:1902.03839.

[Iak16] D. Iakubovskyi. Observation of the new emission line at 3.5 keV in X-ray spectra of galaxies and galaxy clusters. *Adv. Astron. Space Phys.*, 6(1): 3–15 (2016). arXiv:1510.00358, URL http://dx.doi.org/10.17721/2227-1481.6.3-15.

[IBF+15] D. Iakubovskyi, E. Bulbul, A. R. Foster, D. Savchenko, and V. Sadova. Testing the origin of 3.55 keV line in individual galaxy clusters observed with XMM-Newton (2015). arXiv:1508.05186.

[Ice14] IceCube Collaboration. Observation of High-Energy Astrophysical Neutrinos in Three Years of IceCube Data. *Phys. Rev. Lett.*, 113: 101101 (2014). arXiv:1405.5303, URL http://dx.doi.org/10.1103/PhysRevLett.113.101101.

[Ice18] IceCube Collaboration. Astrophysical neutrinos and cosmic rays observed by IceCube. *Advances in Space Research*, 62(10): 2902 – 2930 (2018). ISSN 0273-1177. Origins of Cosmic Rays, URL http://dx.doi.org/10.1016/j.asr.2017.05.030.

[Int03] International Association for the Properties of Water and Steam. Advisory Note No. 1: Uncertainties in Enthalpy for the IAPWS Formulation 1995 for the Thermodynamic Properties of Ordinary Water Substance for General and Scientific Use (IAPWS-95) and the IAPWS Industrial Formulation 1997 for the Thermodynamic Properties of Water and Steam (IAPWS-IF97). *IAPWS AN1-03* (2003). URL http://www.iapws.org/relguide/Advise1.pdf.

[Int18] International Association for the Properties of Water and Steam. Revised Release on the IAPWS Formulation 1995 for the Thermodynamic Properties of Ordinary Water Substance for General and Scientific Use. *IAPWS R6-95* (2018). URL http://www.iapws.org/relguide/IAPWS95-2018.pdf.

[Jam94] F. James. MINUIT Function Minimization and Error Analysis: Reference Manual Version 94.1 (1994).

[Jan11] H.-T. Janka. *Supernovae und kosmische Gammablitze*. Springer Spektrum (2011). ISBN 978-3-8274-2072-5.

[Jan17] H. T. Janka. Neutrino Emission from Supernovae (2017). arXiv:1702.08713, URL http://dx.doi.org/10.1007/978-3-319-21846-5_4.

[Jon19] B. J. P. Jones (IceCube). IceCube Sterile Neutrino Searches. In *8th Very Large Volume Neutrino Telescope Workshop (VLVnT-2018) Dubna, Russia, October 2-4, 2018* (2019). arXiv:1902.06185.

[Jun09] P. Junglas. WATER95 – A MATLAB® Implementation of the IAPWS-95 Standard for use in thermodynamics lectures. *International Journal of Engineering Education*, 25: 3–10 (Jan 2009).

[K+01] K. Kodama et al. (DONUT). Observation of tau neutrino interactions. *Phys. Lett.*, B504: 218–224 (2001). arXiv:hep-ex/0012035, URL http://dx.doi.org/10.1016/S0370-2693(01)00307-0.

[K+05] C. Kraus et al. Final results from phase II of the Mainz neutrino mass search in tritium beta decay. *Eur. Phys. J.*, C40: 447–468 (2005). arXiv:hep-ex/0412056, URL http://dx.doi.org/10.1140/epjc/s2005-02139-7.

[KAT05] KATRIN Collaboration. KATRIN design report 2004. Technical report, Forschungszentrum, Karlsruhe (2005). 51.54.01; LK 01.

[KAT16] KATRIN Collaboration. Commissioning of the vacuum system of the KATRIN Main Spectrometer. *JINST*, 11(04): P04011 (2016). arXiv:1603.01014.

[KAT17] KATRIN Collaboration. Background processes in the KATRIN main spectrometer. *Journal of Physics: Conference Series*, 888: 012070 (Sep 2017). URL http://dx.doi.org/10.1088/1742-6596/888/1/012070.

[KAT18a] KATRIN Collaboration. The KATRIN superconducting magnets: overview and first performance results. *Journal of Instrumentation*, 13(08): T08005–T08005 (Aug 2018). URL http://dx.doi.org/10.1088/1748-0221/13/08/t08005.

[KAT18b] KATRIN Collaboration. Reduction of stored-particle background by a magnetic pulse method at the KATRIN experiment. *The European Physical Journal C*, 78(9): 778 (Sep 2018). ISSN 1434-6052. URL http://dx.doi.org/10.1140/epjc/s10052-018-6244-8.

[Kay81] B. Kayser. On the quantum mechanics of neutrino oscillation. *Phys. Rev. D*, 24: 110–116 (Jul 1981). URL http://dx.doi.org/10.1103/PhysRevD.24.110.

[KCFP98] O. V. Kharitonov, E. A. Chuveleva, L. A. Firsova, and A. S. Peshkov. Chromatographic Recovery of Gadolinium-153 from Irradiated Gadolinium Targets. *Radiokhimiya*, 40: 125–127 (1998).

[kev] Kevlar® aramid fiber technical guide. http://www.dupont.com/content/dam/dupont/products-and-services/fabrics-fibers-and-nonwovens/fibers/documents/Kevlar_Technical_Guide.pdf. Accessed: Feb. 2019.

[Kir98] T. Kirsten. GALLEX solar neutrino results. *Progress in Particle and Nuclear Physics*, 40: 85 – 99 (1998). ISSN 0146-6410. Neutrinos in Astro, Particle and Nuclear Physics, URL http://dx.doi.org/10.1016/S0146-6410(98)00013-1.

[Kor] M. Korzeczek. (KIT, Germany). private communication, 2017.

[Kor16] M. Korzeczek. *eV- & keV-sterile neutrino studies with KATRIN*. Master's thesis, Karlsruhe Institute of Technology (2016).

[KR85] A. Kruglov and A. Rudik. *Reactor production of radioactive nuclides*. Energoatomizdat, Moscow (USSR) (1985).

[Kra87] K. Krane. *Introductory Nuclear Physics*. Wiley (1987). ISBN 9780471805533. URL https://books.google.de/books?id=ConwAAAAMAAJ.

[KSVW13] C. Kraus, A. Singer, K. Valerius, and C. Weinheimer. Limit on sterile neutrino contribution from the Mainz Neutrino Mass Experiment. *Eur. Phys. J.*, C73(2): 2323 (2013). arXiv:1210.4194, URL http://dx.doi.org/10.1140/epjc/s10052-013-2323-z.

[Las18] T. Lasserre. Samak: Matlab Simulation and Analysis for the KATRIN experiment. XXVIII International Conference on Neutrino Physics and Astrophysics (2018).

[Lat16] M. Lattanzi. Planck 2015 constraints on neutrino physics. *Journal of Physics: Conference Series*, 718: 032008 (May 2016). URL http://dx.doi.org/10.1088/1742-6596/718/3/032008.

[Lau56] M. J. Laubitz. Pseudoscalar Interaction in the Decay of ^{144}Pr. *Proceedings of the Physical Society, Section A*, 69(11): 789–798 (1956).

[Lec] P. Lechner. (HLL MPG, Germany). private communication, 2016.

[LEF+12] M. R. Lovell, V. Eke, C. S. Frenk, L. Gao, A. Jenkins, T. Theuns, J. Wang, S. D. M. White, A. Boyarsky, and O. Ruchayskiy. The haloes of bright satellite galaxies in a warm dark matter universe. *MNRAS*, 420: 2318–2324 (Mar 2012). arXiv:1104.2929, URL http://dx.doi.org/10.1111/j.1365-2966.2011.20200.x.

[Lei36] A. I. Leipunski. Determination of the Energy Distribution of Recoil Atoms During β Decay and the Existence of the Neutrino. *Mathematical Proceedings of the Cambridge Philosophical Society*, 32(2): 301–303 (1936). URL http://dx.doi.org/10.1017/S0305004100001869.

[LFH+01] P. Lechner et al. Silicon drift detectors for high count rate X-ray spectroscopy at room temperature. *Nucl. Instr. and Meth. A*, 458(1): 281 – 287 (2001). ISSN 0168-9002.

[LNS04] R. Lewis, P. Nithiarasu, and K. Seetharamu. *Fundamentals of the Finite Element Method for Heat and Fluid Flow.* Wiley (2004). ISBN 9780470020814. URL https://books.google.de/books?id=dzCeaWOSjRkC.

[Lok18] A. Lokhov. A model for a keV-scale sterile neutrino search with KATRIN: SSC-sterile (Jun 2018). XXVIII International Conference on Neutrino Physics and Astrophysics, URL http://dx.doi.org/10.5281/zenodo.1300735.

[LPF08] M. Lépy, J. Plagnard, and L. Ferreux. Measurement of ^{241}Am L X-ray emission probabilities. *Applied Radiation and Isotopes*, 66(6): 715 – 721 (2008). ISSN 0969-8043. Proceedings of the 16th International Conference on Radionuclide Metrology and its Applications, URL http://dx.doi.org/10.1016/j.apradiso.2008.02.078.

[LS85] V. M. Lobashev and P. E. Spivak. A method for measuring the antielectron-neutrino rest mass. *Nucl. Instrum. Meth.*, A240: 305–310 (1985). URL http://dx.doi.org/10.1016/0168-9002(85)90640-0.

[M+19] S. Mertens et al. (KATRIN). A novel detector system for KATRIN to search for keV-scale sterile neutrinos. *J. Phys.*, G46(6): 065203 (2019). arXiv:1810.06711, URL http://dx.doi.org/10.1088/1361-6471/ab12fe.

[MAC+93] J. L. Mortara, I. Ahmad, K. P. Coulter, S. J. Freedman, B. K. Fujikawa, J. P. Greene, J. P. Schiffer, W. H. Trzaska, and A. R. Zeuli. Evidence against a 17 keV neutrino from ^{35}S beta decay. *Phys. Rev. Lett.*, 70: 394–397 (Jan 1993). URL http://dx.doi.org/10.1103/PhysRevLett.70.394.

[MAD+09] B. Märkisch, H. Abele, D. Dubbers, F. Friedl, A. Kaplan, H. Mest, M. Schumann, T. Soldner, and D. Wilkin. The new neutron decay spectrometer Perkeo III. *Nuclear Instruments and Methods in Physics Research Section A: Accelerators, Spectrometers, Detectors and Associated Equipment*, 611(2): 216 – 218 (2009). ISSN 0168-9002. Particle Physics with Slow Neutrons, URL http://dx.doi.org/10.1016/j.nima.2009.07.066.

[Mad19] J. Madsen (IceCube). Ultra-High Energy Neutrinos. In *38th International Symposium on Physics in Collision (PIC 2018) Bogotá, Colombia, September 11-15, 2018* (2019). arXiv:1901.02528.

[MDK+15] S. Mertens, K. Dolde, M. Korzeczek, F. Glück, S. Groh, R. D. Martin, A. W. P. Poon, and M. Steidl. Wavelet approach to search for sterile neutrinos in tritium β-decay spectra. *Phys. Rev.*, D91: 042005 (2015). arXiv:1410.7684, URL http://dx.doi.org/10.1103/PhysRevD.91.042005.

[MFL+11] G. Mention, M. Fechner, T. Lasserre, T. A. Mueller, D. Lhuillier, M. Cribier, and A. Letourneau. Reactor antineutrino anomaly. *Phys. Rev. D*, 83: 073006 (Apr 2011). URL http://dx.doi.org/10.1103/PhysRevD.83.073006.

[MGO+10] A. Michalowska, O. Gevin, O.Lemaire, F. Lugiez, P. Baron, H. Grabas, F. Pinsard, O. Limousin, and E. Delanges. IDeF-X HD: A low power multi-gain CMOS ASIC for the readout of Cd(Zn)Te detectors. In *Nuclear Science Symposium Conference Record (NSS/MIC)*, pages 1556–1559. IEEE (Oct 2010).

[MK02] T. Mayer-Kuckuk. *Kernphysik: Eine Einführung.* Teubner-Studienbücher: Physik. Vieweg+Teubner Verlag (2002). ISBN 9783519132233. URL `https://books.google.de/books?id=kfo03uPI7ocC`.

[ML16] D. Maier and O. Limousin. Energy calibration via correlation. *Nucl. Instrum. Meth.*, A812: 43–49 (2016). `arXiv:1512.04584`, URL `http://dx.doi.org/10.1016/j.nima.2015.11.149`.

[MLG+15] S. Mertens, T. Lasserre, S. Groh, G. Drexlin, F. Glück, A. Huber, A. Poon, M. Steidl, N. Steinbrink, and C. Weinheimer. Sensitivity of next-generation tritium beta-decay experiments for keV-scale sterile neutrinos. *Journal of Cosmology and Astroparticle Physics*, 2015(02): 020 (2015).

[MSTD18] K. Møller, A. M. Suliga, I. Tamborra, and P. B. Denton. Measuring the supernova unknowns at the next-generation neutrino telescopes through the diffuse neutrino background. *JCAP*, 1805(05): 066 (2018). `arXiv:1804.03157`, URL `http://dx.doi.org/10.1088/1475-7516/2018/05/066`.

[N+18] A. Nucciotti et al. Status of the HOLMES Experiment to Directly Measure the Neutrino Mass. *J. Low. Temp. Phys.*, 193(5-6): 1137–1145 (2018). `arXiv:1807.09269`, URL `http://dx.doi.org/10.1007/s10909-018-2025-x`.

[Neu16] B. Neumair (Borexino/SOX). SOX : Short Distance Neutrino Oscillations with Borexino. *PoS*, ICHEP2016: 475 (2016). URL `http://dx.doi.org/10.22323/1.282.0475`.

[NM16] A. Neronov and D. Malyshev. Toward a full test of the νMSM sterile neutrino dark matter model with Athena. *Phys. Rev.*, D93(6): 063518 (2016). `arXiv:1509.02758`, URL `http://dx.doi.org/10.1103/PhysRevD.93.063518`.

[NRVR71] T. Nagarajan, M. Ravindranath, and K. Venkata Reddy. The 0-→0+ Decay of ^{144}Pr and the Pseudoscalar Interaction. *Il Nuovo Cimento A*, 3(3): 699–708 (1971). ISSN 0369-3546. URL `http://dx.doi.org/10.1007/BF02813571`.

[nuf] NuFIT 4.0 (2018). `www.nu-fit.org`. Accessed: May. 2019.

[Nyq28] H. Nyquist. Thermal Agitation of Electric Charge in Conductors. *Phys. Rev.*, 32: 110–113 (Jul 1928). URL `http://dx.doi.org/10.1103/PhysRev.32.110`.

[O+01] A. Osipowicz et al. (KATRIN). KATRIN: A Next generation tritium beta decay experiment with sub-eV sensitivity for the electron neutrino mass. Letter of intent (2001). `arXiv:hep-ex/0109033`.

[OSS+93] T. Ohshima et al. No 17 keV neutrino: Admixture $< 0.073\%$ (95% C.L.). *Phys. Rev. D*, 47: 4840–4856 (Jun 1993). URL http://dx.doi.org/10.1103/PhysRevD.47.4840.

[OW08] E. W. Otten and C. Weinheimer. Neutrino mass limit from tritium beta decay. *Rept. Prog. Phys.*, 71: 086201 (2008). arXiv:0909.2104, URL http://dx.doi.org/10.1088/0034-4885/71/8/086201.

[Pan] V. Pantuev. (INR RAS, Russia). private communication, May 2018.

[Par18] Particle Data Group (Particle Data Group). Review of Particle Physics. *Phys. Rev. D*, 98: 030001 (Aug 2018). URL http://dx.doi.org/10.1103/PhysRevD.98.030001.

[PBB+92] A. Picard et al. A solenoid retarding spectrometer with high resolution and transmission for keV electrons. *Nuclear Instruments and Methods in Physics Research Section B: Beam Interactions with Materials and Atoms*, 63(3): 345 – 358 (1992). ISSN 0168-583X. URL http://dx.doi.org/10.1016/0168-583X(92)95119-C.

[PD59] F. T. Porter and P. P. Day. 0- to 0+ Beta Transition $Pr^{144} \rightarrow Nd^{144}$. *Phys. Rev.*, 114: 1286–1296 (Jun 1959). URL http://dx.doi.org/10.1103/PhysRev.114.1286.

[PF99] F. Perotti and C. Fiorini. Observed energy dependence of Fano factor in silicon at hard X-ray energies. *Nuclear Instruments and Methods in Physics Research Section A: Accelerators, Spectrometers, Detectors and Associated Equipment*, 423(2): 356 – 363 (1999). ISSN 0168-9002. URL http://dx.doi.org/10.1016/S0168-9002(98)01264-9.

[Pon58] B. Pontecorvo. Mesonium and Antimesonium. *Soviet Journal of Experimental and Theoretical Physics*, 6: 429 (1958).

[R+16] E. Richard et al. (Super-Kamiokande). Measurements of the atmospheric neutrino flux by Super-Kamiokande: energy spectra, geomagnetic effects, and solar modulation. *Phys. Rev.*, D94(5): 052001 (2016). arXiv:1510.08127, URL http://dx.doi.org/10.1103/PhysRevD.94.052001.

[Rad] D. Radford. (LBNL, USA). private communication, 2018.

[RCJ+65] F. Reines, M. F. Crouch, T. L. Jenkins, W. R. Kropp, H. S. Gurr, G. R. Smith, J. P. F. Sellschop, and B. Meyer. Evidence for High-Energy Cosmic-Ray Neutrino Interactions. *Phys. Rev. Lett.*, 15: 429–433 (Aug 1965). URL http://dx.doi.org/10.1103/PhysRevLett.15.429.

[Ren11] P. Renschler. *KESS - A new Monte Carlo simulation code for low-energy electron interactions in silicon detectors*. Ph.D. thesis, Karlsruher Institut für Technologie (2011).

[RFB+18] R. Razouk, G. Failleau, O. Beaumont, S. Plumeri, and B. Hay. A Heat-Flux Calorimeter Prototype for Measuring the Thermal Power Released by Radioactive Waste Packages. *IEEE Transactions on Nuclear Science*, PP: 1–1 (Jul 2018). URL http://dx.doi.org/10.1109/TNS.2018.2856277.

[RS92] J. R. H. R. Siegel. *Thermal Radiation Heat Transfer - 3rd ed.* Hemisphere Publishing Corporation (1992). ISBN 0891162712.

[S+19] A. Serebrov et al. (NEUTRINO-4). The first observation of effect of oscillation in Neutrino-4 experiment on search for sterile neutrino. *JETP Letters*, 109(4): 213–221 (Feb 2019). ISSN 1090-6487. URL http://dx.doi.org/10.1134/S0021364019040040.

[Sau18] H. Saul. *Energy Dependence of the Beta Asymmetry in Neutron Beta Decay.* Ph.D. thesis, Technische Universität München and TU Wien (2018).

[SBD+13] M. Slezák, S. Bauer, O. Dragoun, M. Erhard, K. Schlösser, A. Špalek, D. Vénos, and M. Zbořil. Electron line shape of the KATRIN monitor spectrometer. *Journal of Instrumentation*, 8(12): T12002–T12002 (Dec 2013). URL http://dx.doi.org/10.1088/1748-0221/8/12/t12002.

[Sch19] L. Schlüter. *Development of New Methods to Include Systematic Effects in the First Tritium Data Analysis and Sensitivity Studies of the KATRIN Experiment.* Master's thesis, Technical University of Munich (2019).

[SCvF83] K. Schreckenbach, G. Colvin, and F. von Feilitzsch. Search for mixing of heavy neutrinos in the β^+ and β^- spectra of the ^{64}Cu Decay. *Physics Letters B*, 129(3): 265 – 268 (1983). ISSN 0370-2693. URL http://dx.doi.org/10.1016/0370-2693(83)90858-4.

[SHi16] SHiP Collaboration. A facility to Search for Hidden Particles at the CERN SPS: the SHiP physics case. *Rept. Prog. Phys.*, 79(12): 124201 (2016). arXiv:1504.04855, URL http://dx.doi.org/10.1088/0034-4885/79/12/124201.

[Sie19] D. Siegmann. *Investigation on the Detector Response of Electrons in the TRISTAN Prototype Detectors.* Master's thesis, Technical University of Munich and Max-Planck-Institute for Physics (2019).

[Sim81] J. J. Simpson. Measurement of the β-energy spectrum of ^{3}H to determine the antineutrino mass. *Phys. Rev. D*, 23: 649–662 (Feb 1981). URL http://dx.doi.org/10.1103/PhysRevD.23.649.

[Sim85] J. J. Simpson. Evidence of Heavy-Neutrino Emission in Beta Decay. *Phys. Rev. Lett.*, 54: 1891–1893 (Apr 1985). URL http://dx.doi.org/10.1103/PhysRevLett.54.1891.

[Siy18] K. Siyeon (NEOS). First Result of NEOS Experiment. *PoS*, ICRC2017: 1024 (2018). URL http://dx.doi.org/10.22323/1.301.1024.

[SOH+96] S. Schönert, L. Oberauer, C. Hagner, F. Feilitzsch, K. Schreckenbach, Y. Declais, and U. Mayerhofer. Experimental limits for heavy neutrino admixture deduced from Lu-177 beta decay and constraints on the life time of a radiative neutrino decay mode. *Nucl. Phys. Proc. Suppl.*, 48: 201–203 (1996). URL http://dx.doi.org/10.1016/0920-5632(96)00238-1.

[SOX13] SOX Collaboration. SOX: Short distance neutrino Oscillations with BoreXino. *Journal of High Energy Physics*, 2013(8): 38 (2013). URL http://dx.doi.org/10.1007/JHEP08(2013)038.

[SP54] F. H. Spedding and J. E. Powell. The Separation of Rare Earths by Ion Exchange. VIII. Quantitative Theory of the Mechanism Involved in Elution by Dilute Citrate Solutions. *Journal of the American Chemical Society*, 76(9): 2550–2557 (1954). URL http://dx.doi.org/10.1021/ja01638a074.

[Spi05] H. Spieler. *Semiconductor Detector Systems*. Series on Semiconductor Science and Technology. OUP Oxford (2005). ISBN 9780198527848.

[Spi12] C. Spiering. Towards high-energy neutrino astronomy. A historical review. *European Physical Journal H*, 37: 515–565 (Aug 2012). arXiv:1207.4952, URL http://dx.doi.org/10.1140/epjh/e2012-30014-2.

[SRS+13] M. Schlösser, S. Rupp, H. Seitz, S. Fischer, B. Bornschein, T. M. James, and H. H. Telle. Accurate calibration of the laser Raman system for the Karlsruhe Tritium Neutrino Experiment. *Journal of Molecular Structure*, 1044: 61 – 66 (2013). ISSN 0022-2860. MOLECULAR SPECTROSCOPY AND MOLECULAR STRUCTURE 2012, URL http://dx.doi.org/10.1016/j.molstruc.2012.11.022.

[Sue15] F. Suekane. *Neutrino Oscillations*. Springer Japan (2015). ISBN 9784431554615.

[Sup98] Super-Kamiokande Collaboration. Evidence for Oscillation of Atmospheric Neutrinos. *Phys. Rev. Lett.*, 81: 1562–1567 (Aug 1998). URL http://dx.doi.org/10.1103/PhysRevLett.81.1562.

[SV83] G. Schenter and P. Vogel. A Simple Approximation of the Fermi Function in Nuclear Beta Decay. *Nuclear Science and Engineering*, 83(3): 393–396 (1983).

[WDB+99] C. Weinheimer, B. Degenddag, A. Bleile, J. Bonn, L. Bornschein, O. Kazachenko, A. Kovalik, and E. W. Otten. High precision measurement of the tritium β spectrum near its endpoint and upper limit on the neutrino mass. *Phys. Lett.*, B460: 219–226 (1999).

[Zra98] M. Zralek. From kaons to neutrinos: Quantum mechanics of particle oscillations. *Acta Phys. Polon.*, B29: 3925–3956 (1998). arXiv:hep-ph/9810543.

[Zsi18] A. J. Zsigmond. New results from GERDA Phase II (Jun 2018). XXVIII International Conference on Neutrino Physics and Astrophysics, URL http://dx.doi.org/10.5281/zenodo.1287604.

[ZWA15] F. Zandanel, C. Weniger, and S. Ando. The role of the eROSITA all-sky survey in searches for sterile neutrino dark matter. *JCAP*, 1509(09): 060 (2015). arXiv:1505.07829, URL http://dx.doi.org/10.1088/1475-7516/2015/09/060.

Acknowledgments

I would like to thank my supervisors **Thierry Lasserre** and **Stefan Schönert** for giving me the opportunity to pursue a PhD on sterile neutrinos and their guidance. Also, to Thierry I would like to apologize for the traumatic experience at the TUM Campuslauf 2017, but I guess you got a satisfying revenge in 2019.

In the SOX group I am especially grateful to **Lea di Noto** and **Laszlo Papp** with whom (among others) I worked on the calorimeter. I enjoyed very much our fruitful and complementary team work. My thanks also go to the entire calorimeter team, only together we made the technological success possible! Many thanks also to **Vasily Kornoukhov**, who gave insightful details about the SOX source production process. At LNGS I want to thank **Chiara Ghiano**, who was very helpful during my Borexino shifts and gave valuable tips for outdoor activities at Gran Sasso.

I am thanking everyone in the TRISTAN group for the many beneficial discussions and the productive and pleasant environment, but especially **Susanne Mertens** for her extensive supervision, even though she is not my formal supervisor. Special thanks go also to the TRISTAN crew at Troitsk: **Tim Brunst**, **Anton Huber**, **Tobias Bode**, **Thibaut Houdy**, **Daniel Siegmann** and again **Susanne** and **Thierry**. The stays at Troitsk were not only very educational but also extremely fun thanks to you (and with the help of Pelmeni, Vodka, Baltika beer, dried fish, smoked cheese and Pizza Dodo)! Many thanks also to the Russian team, in particular to **Alexander Nozik** and **Vlad Pantuev**. Vlad's encouraging comments as "you are quite old, you should defend" I will not forget (by the way, for German PhD students I am not so old...).
I am grateful also to **David Radford**, who always has a helpful answer to any difficult problem.

At CEA Saclay, I very much want to thank **Olivier Limousin** and **Daniel Maier**, who were always extremely helpful and taught me a lot about semiconductor detectors and electronics. It was a pleasure working with you! Many thanks also to **Victoria Wagner**, **Matthieu Vivier** and **Guillaume Mention** for ensuring a pleasant stay at DPhP and especially their help when French was needed. I also would like to thank **Yann Reinert** and **Olivier Cloue**, who were working in parallel at LNGS on the CEA calorimeter, for their company and interesting dinners.

At my home institute at TUM I would like to thank my long-term office comrades **Birgit Neumair** and **Marc Tippmann**, who made our office a place, where I enjoyed to be. Also, Birgit helped me a lot through her expertise in statistics and data analysis, for which I am very grateful. Also many thanks to the colleagues and friends at E15, especially **Elizabeth Mondragon** for sharing the newest entertaining gossip during coffee breaks ("super secrets") and **Lothar Oberauer** for telling fascinating

anecdotes about neutrino physics. Also, many thanks again to **Birgit**, **Thibaut** and **Eli** for proof-reading parts of this thesis, to Thibaut additionally for translating the abstract to French.

I also thank my family and friends for filling the gap between work and sleep with entertainment, distraction and support.